Development of robust modelling and experimental methods to advance mechanistic insights into the supercritical water gasification of biomass

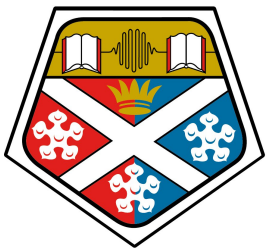

University of Strathclyde Glasgow

Robert Sait-Stewart

Department of Chemical and Process Engineering

University of Strathclyde

A thesis submitted for the degree of

Doctor of Philosophy

August 2025

In loving memory of a childhood friend,

Thieu Khang "Jacky" Truong

1998 – 2017

Thinking of you always

Declaration of Auhthorship

This thesis is the result of the author's original research. It has been composed by the author and has not previously been submitted for examination which has led to the award of a degree.

Robert Sait-Stewart
February 27, 2026

Acknowledgements

I would like to begin by giving thanks to my supervisors, Dr Jun Li and Dr Leo Lue, for their invaluable guidance and expertise. The past few years have been among the most formative of my life, and I am confident that the lessons I have learned under their supervision will continue to support me through challenges I may face in the future.

I extend this thanks to Dr Lewis MacDonald who provided me with invaluable expertise in the lab and always selflessly offered help when needed.

I would also like to mention Klara Grenier, a visiting master's student, whose valuable assistance and optimism were always greatly appreciated.

My PhD experience as a whole was made immeasurably better through the friends I made along the way. So to Stuart, Nisha, Jordan, Elliot, Tom, Tam, James, and everyone else, I wish to thank you all so much for your friendship over the years, wish you all the best for the future, and say that I hope to see you all again soon.

I'd like to thank my mum and dad, Angela and John, and my brother and sister, Edgar and Kirsty. Your support and encouragement means the world to me and I love you all very much.

And last, but by no means least, thank you to Hazel. Your unwavering support, patience, and love kept me believing in myself and I could not have completed this PhD without you. I hope you know how much you are loved and appreciated.

Research Output

Publications

- Sait-Stewart, R., Lue, L. and Li, J., 2026. Optimising supercritical water gasification of biomass: exploring heating strategy through a quantitative kinetic modelling approach. Sustainable Energy & Fuels, 10(1), pp.375-385.
- Sait-Stewart, R. Li, J. Lue, L. 2025. "A Thermodynamic Framework for the Thermochemical Valorization of Biomass". *Energy Conversion and Management*. Submitted/Under Review
- Sait-Stewart, R. Lue, L. Li, J. 2025. "Mechanistic Insights into SCWG: A Kinetic Sensitivity Approach for optimising end- and intermediate products". Drafted

Conferences

- 32^{nd} European Biomass Conference and Exhibition (EUBCE 2024). 2024. Marseille, France. "Optimising Supercritical Water Gasification of Biomass: Exploring Heating Strategy Through Quantitative Kinetic Modelling Approach". Oral Presentation
- 15^{th} International Green Energy Conference (IGEC-XV). 2023. Glasgow, UK. "A Thermodynamic Analysis of Integrated Supercritical Water Gasification and Supercritical CO2 Brayton Cycle: A Novel Approach for Power Generation from Real-World Wet Biomass". Oral Presentation
- ETP 12th Annual Conference. 2023. Glasgow, UK. "A Detailed Kinetic Model for the Supercritical Water Gasification of Real-World Wet Biomass: A Sensitivity Analysis". Oral Presentation. Best Presentation Award for Bioenergy Session
- ETP 11th Annual Conference. 2022. Edinburgh, UK. "An Integrated Kinetic Model to Evaluate the Quality and Composition of Syngas from the Supercritical Water Gasification of Wet Biomass". Oral Presentation. Best Presentation Award for Bioenergy Session

Abstract

Wet biomass is a classification of high-moisture organic materials that are challenging to handle, and the current conventional treatment of these materials contributes significantly to greenhouse gas emissions and local environmental damage. These materials arise from multiple sources; many of which are wastes such as sewage sludge and agricultural slurries, while others are purposely produced, such as microalgae. A commonality amongst them is their high water content which can be upwards of 90 wt.% water. Supercritical water gasification is a novel high temperature, high pressure treatment technique that uses conditions above the critical point of water (374°C and 22.1 MPa) to rapidly and effectively convert wet biomass into syngas fuel with water in-situ. The full-scale commercialisation of supercritical water gasification hinges upon overcoming present challenges which inhibit the efficiency and cost-effectiveness of gasifying biomass in supercritical water. This includes issues relating to poor gasification efficiencies, char formation, high energy demands, and salt deposition. A major problem is that there is currently a poor understanding of the mechanistic processes that underpin supercritical water gasification, and therefore it becomes ultimately harder to overcome the aforementioned challenges if it is not possible to make reference to an accurate, well-established portfolio of biomass reactions in supercritical water. The contents of this thesis aim to progress supercritical water gasification by presenting a series of novel methodologies that can be used to provide useful mechanistic insights into the fundamental processes which govern reactions of biomass molecules in supercritical water. A detailed kinetic model was updated and improved to explore the potential in enhancing syngas yields and carbon gasification efficiency, and mitigating char formation by changing sub-critical heating rates and heating profiles (e.g., linear, accelerating, decelerating). Slow sub-critical heating rates are found to be beneficial for increasing the yield of H_2 from the SCWG of cellulose and hemicellulose compounds. The gasification of lignin could be enhanced by using faster heating rates, as it minimises the formation of char in the sub-critical region. This can guide potential tailored improvements to SCWG by controlling the sub-critical heating regime in accordance with the feedstock to optimise syngas yield and char formation. Secondly, a chemical kinetic sensitivity analysis

of the biomass SCWG mechanism was conducted to present a methodology that can be used to discern the most influential reactions on the formation of target species. Here, the formation of H_2 and acetic acid (a refractory intermediate) from cellulose were investigated as examples, and the rate-determining steps of their formation were determined. A thermodynamic model was developed using a novel perspective of elemental chemical potentials to produce a framework that could be used to evaluate and comparatively analyse any thermochemical or hydrothermal biomass conversion process. Here, ternary diagrams were used to illustrate how operating conditions (e.g., temperature and pressure) and additive agents (e.g., water and CO_2) would influence chemical and phase equilibria. The ternary diagrams offer a unique visualisation of thermodynamic equilibrium and are robust, useful tools for revealing the optimum reaction conditions needed to convert any feedstock, without the need for further calculations or simulations. Finally, experimental methodologies were developed and demonstrated for a newly acquired batch reactor. This process included designing rigorous safety controls, calibrating analytical equipment, and testing the reactor with different feedstocks. The aim of this work was to establish a reliable experimental rig that could be used by the University of Strathclyde and external partners to conduct research into supercritical water gasification and other hydrothermal processes. Given the scarcity of experimental research in this field, the development of the rig is highly valuable, as the data obtained can both validate computational models and support groundbreaking research.

Contents

List of Figures **xvii**

List of Tables **xxiii**

List of Abbreviations **xxv**

1 Introduction **1**

2 Review **9**

2.1 Supercritical Water 10
2.1.1 Density 11
2.1.2 Viscosity 11
2.1.3 Dielectric Constant 11
2.1.4 Ionic Product 12
2.2 Operating Conditions 14
2.2.1 Temperature 14
2.2.2 Pressure 14
2.2.3 Feedstock Concentration 16
2.2.4 Reaction Time 16
2.2.5 Catalysts 17
2.2.6 Heating rate 18
2.3 Biomass Feedstocks for SCW 19
2.4 Reactions of Biomass Model Compounds 24
2.4.1 Cellulose 25
2.4.2 Hemicellulose 25
2.4.3 Lignin 26
2.4.4 Protein 26
2.4.5 Lipids 27
2.5 Modelling Approaches 27
2.5.1 Thermodynamic Modelling 27
2.5.2 Kinetic Modelling 30

2.5.3 Other Modelling Techniques . . . 33
2.6 Experimental Approaches . . . 34
2.7 Conclusions and Recommended Research Areas . . . 35

3 Exploring Heating Strategy in SCWG Through a Quantitative Kinetic Modelling Approach 41
3.1 Introduction . . . 41
3.2 Modelling Concepts and Development . . . 43
3.2.1 Cellulose . . . 43
3.2.2 Hemicellulose . . . 44
3.2.3 Lignin . . . 45
3.2.4 Protein . . . 46
3.2.5 Modifications and Developments . . . 46
3.2.6 Simulation Approach . . . 48
3.3 Results and Discussion . . . 51
3.3.1 Advances and validation of the updated kinetic model . . . 51
3.3.2 The Effect of Heating Rate . . . 53
3.3.3 The Effect of Heating Profile . . . 61
3.4 Conclusions . . . 63

4 Mechanistic Insights into SCWG: A Kinetic Sensitivity Approach for Optimising End- and Intermediate products 65
4.1 Sensitivity Analysis Methods . . . 71
4.1.1 Local Sensitivity . . . 71
4.1.2 Heuristic Sensitivity . . . 73
4.2 Results and Discussion . . . 73
4.2.1 H_2 Heuristic Sensitivity . . . 73
4.2.2 H_2 Local Sensitivity . . . 76
4.2.3 Acetic Acid Sensitivity . . . 85
4.3 Conclusions . . . 90

5 Development of a Thermodynamic Framework for the Thermochemical Valorisation of Biomass 93
5.1 Introduction . . . 93
5.2 Gibbs Free Energy Minimisation Calculation . . . 95
5.3 Chemical reaction equilibria and element chemical potentials . . . 97
5.4 Ternary Diagrams . . . 105
5.4.1 Influence of temperature on the char formation boundary . . . 109
5.4.2 Influence of pressure on the char formation boundary . . . 110

5.5 Influence of Elemental Composition . . . 113
5.5.1 The Addition of Water . . . 115
5.5.2 CO_2 Addition . . . 121
5.6 Optimising Supercritical Water Gasification . . . 127
5.6.1 Acetic acid . . . 129
5.6.2 Wheat straw . . . 131
5.7 Conclusions and Future Work . . . 133

6 Designing Experimental Methods to Support SCWG Modelling 135
6.1 Introduction . . . 135
6.2 The Experimental Rig . . . 137
6.3 Standard Operating Procedure . . . 138
6.3.1 Pre-Experiment Checks and Set-Up . . . 138
6.3.2 Pressure-Cycle Purging . . . 140
6.3.3 Experimental Run . . . 140
6.3.4 Post-Experiment . . . 141
6.4 Safety Considerations . . . 142
6.5 Pressure Cycle Purging . . . 144
6.6 Syngas Analysis . . . 145
6.6.1 Principles of Gas Chromatography . . . 146
6.6.2 Methods . . . 148
6.6.3 General GC-TCD Operation . . . 150
6.6.4 Calibration . . . 153
6.6.5 Uncertainty in Measurement . . . 154
6.7 Design for Validating Models . . . 157
6.7.1 Case 1: H_2 production from the SCWG of hemicellulose with fast heating. . . . 158
6.7.2 Case 2: Kinetics of acetic acid gasification in SCW. . . . 162
6.8 Conclusions . . . 168

7 Overall Conclusions 169
7.1 Conclusions . . . 169
7.2 Future Work . . . 172

References 175

Appendices

List of Figures

1.1 Schematic showing the main features of SCWG and the methodologies used in this thesis. 3

2.1 Pressure versus temperature plot for pure water. 10
2.2 Properties of supercritical water as predicted by IAPWS-95. . . . 13
2.3 Proportion of SCWG publications by feedstock type. 21
2.4 Cumulative number of SCWG publications per feedstock by year. 21

3.1 Schematic diagram showing the main unit operations in a continuous SCWG process. 43
3.2 The configuration of reactors used in simulations 49
3.3 The different SUB-HEX heating profiles studied. 50
3.4 Validation results for lignocellulosic biomass including experimental data [25], the reference model [36], and the results of this work. . 51
3.5 Validation results for protein-containing biomass. 52
3.6 Syngas yields and CGEs from the SCWG of 10 wt.% a) cellulose, b) hemicellulose, c) lignin, and d) protein at 500°C and 600°C with linear SUB-HEX heating rates of 690, 69, and 6.9 °C min^{-1}. 54
3.7 Maximum yields of intermediates formed during the SCWG of cellulose with linear SUB-HEX heating rates of 690, 69, and 6.9 °C min^{-1}. 56
3.8 Maximum yields of intermediates formed during the SCWG of hemicellulose with linear SUB-HEX heating rates of 690, 69, and 6.9 °C min^{-1}. 57
3.9 Total dry mass fraction of lignin and protein derived char, and temperature, versus reaction time at linear sub-critical heating rates of 690, 69, and 6.9 °C min^{-1}. Final reaction temperatures of 500°C (solid) and 600°C (dashed) 59
3.10 Total dry mass fraction of lignin and protein derived char, and temperature, versus reaction time at an accelerating, decelerating, and linear sub-critical heating rate 69 °C min^{-1}. Final reaction temperatures of 500°C (solid) and 600°C (dashed) 60

3.11 Syngas yields and CGEs from the SCWG of 10 wt.% a) cellulose, b) hemicellulose, c) lignin, and d) protein at 500°C and 600°C with linear, accelerating, and decelerating 69 °C min^{-1} `SUB-HEX` heating rates. 62

4.1 Decomposition mechanism for cellulose in supercritical used in kinetic model. Exclusivley supercritical reactions demarcated with red arrows (→). 67
4.2 The configuration of reactors used in simulations 68
4.3 Decomposition profile for cellulose operating under normal conditions. 69
4.4 H_2 formation from cellulose with extended 1000 s `SUP-RCT` residence time. 70
4.5 Heuristic sensitivity of sub-critical cellulose mechanism on H_2 formation at reaction temperatures of 500°C and 600°C. 77
4.6 Heuristic sensitivity of supercritical cellulose mechanism on H_2 formation at reaction temperatures of 500°C and 600°C. 77
4.7 Local sensitivity of H_2 formation to `wshs.gas`. 78
4.8 Local sensitivity of H_2 formation to `acet.aa`. 79
4.9 Local sensitivity of H_2 formation to `la.acet`. 80
4.10 Local sensitivity of H_2 formation to `f.ga1`. 81
4.11 Local sensitivity of H_2 formation to `pa.ga`. 82
4.12 Local sensitivity of H_2 formation to `acry.pa`. 82
4.13 Local sensitivity of H_2 formation to `wgs`. 83
4.14 Local sensitivity of H_2 formation to `f.ga2`. 84
4.15 Local sensitivity of H_2 formation to `fu.wshs` 84
4.16 Heuristic sensitivity analysis results for acetic acid formation from decomposition of cellulose in the sub-critical mechanism. 86
4.17 Local sensitivity of acetic acid formation to `e.acid`. 87
4.18 Local sensitivity of acetic acid formation to `glycol.acid`. 88
4.19 Local sensitivity of acetic acid formation to `a.acid`. 89
4.20 Local sensitivity of acetic acid formation to `acet.aa` 90

5.1 Illustration of Gibbs free energy (G) as a function of reaction extent (ξ). The minimum corresponds to the equilibrium state of the system. 97
5.2 The standard elemental chemical potential of carbon at 1 bar as pure graphite (blue line), in CO / CO_2 (orange line), CH_4 (green line), and CO_2 (red line). 102

5.3 The standard elemental chemical potential of oxygen at 1 bar as molecular oxygen (blue line), in CO_2 / CO (orange line), in water (green line), and in CO_2 (red line). 103
5.4 Standard elemental chemical potential of hydrogen at 1 bar as molecular hydrogen (blue line), CH_4 from conversion of carbon monoxide to CO (orange line), water (green line), and CH_4 from binding with solid carbon (red line). 104
5.5 Ternary diagrams at $T = 500°C$ and pressure $p = 1$ bar showing (a) the char formation phase boundary and feasible region, and (b), the application of the lever rule to ternary diagrams. 106
5.6 Ternary diagram showing the region of feedstock compositions considered in this work. 108
5.7 Ternary diagram showing the effect temperature has on the char phase boundary at $p = 1$ bar. 111
5.8 Ternary diagram showing the effect pressure has on the char phase boundary at 800°C. 112
5.9 Ternary diagram showing the effect pressure has on the char phase boundary at 500°C. 113
5.10 Ternary diagram section demonstrating the range of possible total system compositions attainable by adding water and/or CO_2 to a mixed straws (32 mol% C, 47 mol% H, and 21 mol% O) feedstock. 115
5.11 Equilibrium product yields from mixed straws feedstock (32 mol% C, 47 mol% H, and 21 mol% O) versus weight percentage water at 400°C, 600°C, and 800°C and pressures of 1 bar (solid), 10 bar (dotted), 100 bar (dashed), and 300 bar (dashdot). The production/consumption of water is plotted as moles out minus moles in. 116
5.12 Minimum weight fraction water required to suppress char formation from the thermochemical treatment of biomass and plastics at different temperatures and pressures. 122
5.13 Equilibrium product yields from (i) 0 wt.% water, (ii) 50 wt.% water, mixed straws feedstock (32 mol% C, 47 mol% H, and 21 mol% O) versus weight percentage CO_2 at 400°C, 600°C, and 800°C and pressures of 1 bar (solid), 10 bar (dotted), and 100 bar (dashed). The production/consumption of water and CO_2 is plotted as moles out minus moles in. 124
5.14 Minimum weight fraction CO_2 required to suppress char formation from the thermochemical treatment of biomass and plastics at different temperatures and pressures. 126

5.15 Maximum char yields and weight fraction of CO_2 added during thermochemical treatment of biomass and plastics. 127
5.16 Variation of the net heating value of acetic acid gasification/SCWG versus weight fraction of added water (solid) and CO_2 (dashed) at different operating temperatures and pressures. 130
5.17 Variation of the net heating value of wheat straw gasification/SCWG with the weight fraction of added water (solid) and CO_2 (dashed) at different operating temperatures and pressures. 131

6.1 Labelled picture of the experimental set-up. 137
6.2 PID of the reactor. 138
6.3 Isochoric pressure versus temperature plots for the reactor predicted by IAPWS-95. 143
6.4 Concentration of gas in reactor after N purges predicted by ASTM G-124, and after 3 purges with 10 bar N_2 experimentally. 145
6.5 An a) annotated picture, and b) labelled schematic of the GC-TCD. 147
6.6 Schematic of a two-cell thermal conductivity detector (TCD) . . . 148
6.7 GC-TCD signal for mixed gas (N_2, H_2, CO, CO_2, CH_4) using Method 1 (He carrier) 151
6.8 GC-TCD signal for mixed gas (N_2, H_2, CO, CO_2, CH_4) using Method 2 (Ar carrier) 152
6.9 Two GC-TCD signals with 10 mol.% and 100 mol.% CH_4. Obtained using method 2 153
6.10 Calibration curve for CO concentration using GC-TCD. 155
6.11 a) Calibration curve and b) Monte-Carlo uncertainty for N_2 concentration using GC-TCD. 156
6.12 a) Calibration curve and b) Monte-Carlo uncertainty for H_2 concentration using GC-TCD. 156
6.13 a) Calibration curve and b) Monte-Carlo uncertainty for CH_4 concentration using GC-TCD. 157
6.14 a) Calibration curve and b) Monte-Carlo uncertainty for CO_2 concentration using GC-TCD. 157
6.15 Temperature and pressure versus time in reactor heater to 500°C for 240 min. 159
6.16 Temperature versus time with `fast` and `slow` heating rates employed. 160
6.17 Kinetically predicted concentrations of xylose, H_2, and CO_2 in reactor with `fast` and `slow` heating rates employed. 161
6.18 Kinetically predicted final yields of H_2 and CO_2 using `fast` and `slow` heating rates. 161

6.19 Kinetic data for gasification of acetic acid in SCW from Meyer, Marrone, and Tester [143] 163
6.20 Postulated acetic acid decomposition mechanism in SCW. 165
6.21 Acetic acid conversion versus time at different constant temperatures as predicted by kinetics. 167
6.22 Acetic acid conversion versus time with reactor 400°C heating profile as predicted by kinetics. 167

A1 Total dry mass fraction of lignin and protein derived char, and temperature, versus reaction time at an accelerating, decelerating, and linear sub-critical heating rate 690 °C min^{-1}. Final reaction temperatures of 500°C (solid) and 600°C (dashed) 191
A2 Total dry mass fraction of lignin and protein derived char, and temperature, versus reaction time at a accelerating, decelerating, and linear sub-critical heating rate 6.9 °C min^{-1}. Final reaction temperatures of 500°C (solid) and 600°C (dashed) 192
B1 Sensitivity of H_2 formation to `fal.ga`. 198
B2 Sensitivity of H_2 formation to `glyco.ga`. 198
B3 Sensitivity of H_2 formation to `hpa.glyco`. 199
C1 GC SOP 209
C2 Figure C1 continued. 210

List of Tables

2.1 Summary of experimental SCWG research conducted by active groups in the last five years. 39

3.1 Updated kinetic model reactions 47
3.2 Arrhenius parameters for hemicellulose decomposition in sub-critical water 48

4.1 Arrhenius parameters for H_2 producing and consuming reactions in the cellulose mechanism. 74
4.2 Arrhenius parameters for acetic acid producing reactions in the cellulose mechanism. 86

6.1 Maximum operating temperatures, pressures of the reactor and corresponding maximum water loading. 143
6.2 Thermal conductivities of permanent gases at 25^{o}C and 1 atm [168]. 149
6.3 Calibration gases used for GC-TCD analysis. 154

A1 Arrhenius parameters for reactions of cellulose in sub- and supercritical water 193
A2 Arrhenius parameters for reactions of hemicellulose in sub-critical water 193
A3 Arrhenius parameters for reactions of hemicellulose in supercritical water 193
A4 Arrhenius parameters for reactions of lignin in sub-critical water . 194
A5 Arrhenius parameters for reactions of lignin in supercritical water 194
A6 Arrhenius parameters for reactions of protein in sub-critical water 195
A7 Arrhenius parameters for reactions of protein in supercritical water 195
A8 Arrhenius parameters for reactions of intermediates in sub- and supercritical water 196
A9 Nomenclature of Chemical Species in Kinetic Model 196
C1 N_2 GC-TCD calibration data. 200
C2 H_2 GC-TCD calibration data. 201

C3 CH_4 GC-TCD calibration data. 202
C4 CO_2 GC-TCD calibration data. 203
C5 CO GC-TCD calibration data. 203

List of Abbreviations

AI . . . . . Artificial Intelligence.

CCS . . . . . Carbon Capture & Storage.

CMC . . . . . Carboxymethylcellulose.

CFD . . . . . Computational Fluid Dynamics.

CGE . . . . . Carbon Gasification Efficiency.

EA . . . . . Environmental Assessment.

EOS . . . . . Equation of State.

FTS . . . . . Fischer-Tropsch Synthesis.

GE . . . . . Gasification Efficiency.

GFM . . . . . Gibbs Free Energy Minimisation.

GWP . . . . . Global Warming Potential.

HHV . . . . . Higher Heating Value.

HTC . . . . . Hydrothermal Carbonisation.

HTG . . . . . Hydrothermal Gasification.

HTL . . . . . Hydrothermal Liquefaction.

LCA . . . . . Life Cycle Assessment.

ML . . . . . Machine Learning

NSM . . . . . Non-Stoichiometric Model.

ODE . . . . . Ordinary Differential Equation.

P&ID . . . . . Piping and Instrumentation Diagram.

SAF . . . . . Sustainable Aviation Fuel.

SCW . . . . . Supercritical Water.

SCWG . . . . Supercritical Water Gasification.

SM . . . . . Stoichiometric Model.

SOP . . . . . Standard Operating Procedure.

TEA . . . . . Techno-Economic Assessment.

TRL . . . . . Technological Readiness Level.

"But man is a part of nature,
and his war against nature is inevitably a war against himself."

— Rachel Carson, *Silent Spring* (1962)

1 Introduction

For millions of years human beings relied upon the fire of burning biomass to heat their homes, cook their food, and stave off the darkness of night. The rapid rate of technological advancement provided by our devotion to fossil fuels is undeniable. However, as we, the global community, return to nature looking for solutions to our climate disaster, we can see with hindsight that perhaps we should not have been so quick to turn our back on the natural world after all.

Biomass wastes arise in various forms, including wastewater and sewage sludge, organic fraction of municipal solid waste, agricultural waste, and food industry waste [1]. A significant portion of these biomass wastes are wet in their original forms, being composed of as much as 80 wt.% water in some cases [2]. Wet biomass wastes present a unique set of challenges in their processing, and are viewed as materials which pose problems in their management and disposal. These waste materials are rich in organics (e.g. cellulose, hemicellulose, protein, and lipids) and other useful nutrients (e.g. phosphorous). Forecasting suggests the UK may have access to over 9400 GWh worth of food waste by 2030 [3].

Traditional disposal methods like landfilling fail to recover any value from the wet biomass material stream, and also contribute to global greenhouse gas emissions as well as local environmental damage from leaching. Anaerobic digestion is a more

popular biological treatment with gaining popularity, however, its slow processing time (weeks), poor conversion efficiency, and high sensitivity means it faces many challenges and is unlikely to be robust enough to handle all forms of wet biomass [4]. Conventional thermochemical options such as gasification and pyrolysis typically operate at faster rates and greater conversion efficiencies than AD. Unfortunately, this type of process is hindered by the presence of water and thus an energy intensive feedstock drying stage would be necessary, which makes wet biomass treatment via conventional thermochemical methods uneconomical [5, 6].

Hydrothermal processing refers to a group of three high-pressure, high-temperature thermochemical conversion processes which are differentiated based upon their operating conditions and product distribution. The key advantage of hydrothermal treatments is their ability to process waste with water in-situ which comes with significant energy savings. In increasing operating temperature and pressure order, hydrothermal carbonisation (HTC), liquefaction (HTL), and gasification (HTG) produce predominantly solid, liquid, and gas biofuel products, respectively [7]. Operating at temperatures in the range of 360°C to 700°C, HTG is capable of rapidly (seconds/minutes) and efficiently (>90 %) converting wet biomass into syngas [8]. When operating conditions are in excess of the critical point of water (22.1 MPa and 374°C), HTG boasts its highest conversion efficiency and the ability to produce a H_2-rich fuel in a process also termed supercritical water gasification (SCWG) [7, 9].

Figure 1.1 shows a schematic of a HTG/SCWG process conceptualised by Muhlke et al. [8]. The process starts by pumping a wet biomass feedstock - typically composed of around 10 wt.% solids - to supercritical operating pressure above 22.1 MPa. This pressurised stream is then heated to the desired reaction temperature after which it enters the SCWG reactor where the heterogeneous mixture of relatively large biomass molecules is broken down via a series of reactions into smaller organics and finally synthesis gas (syngas), composed primarily of H_2, CO, CO_2, and CH_4. This is obviously a simplified representation of a SCWG

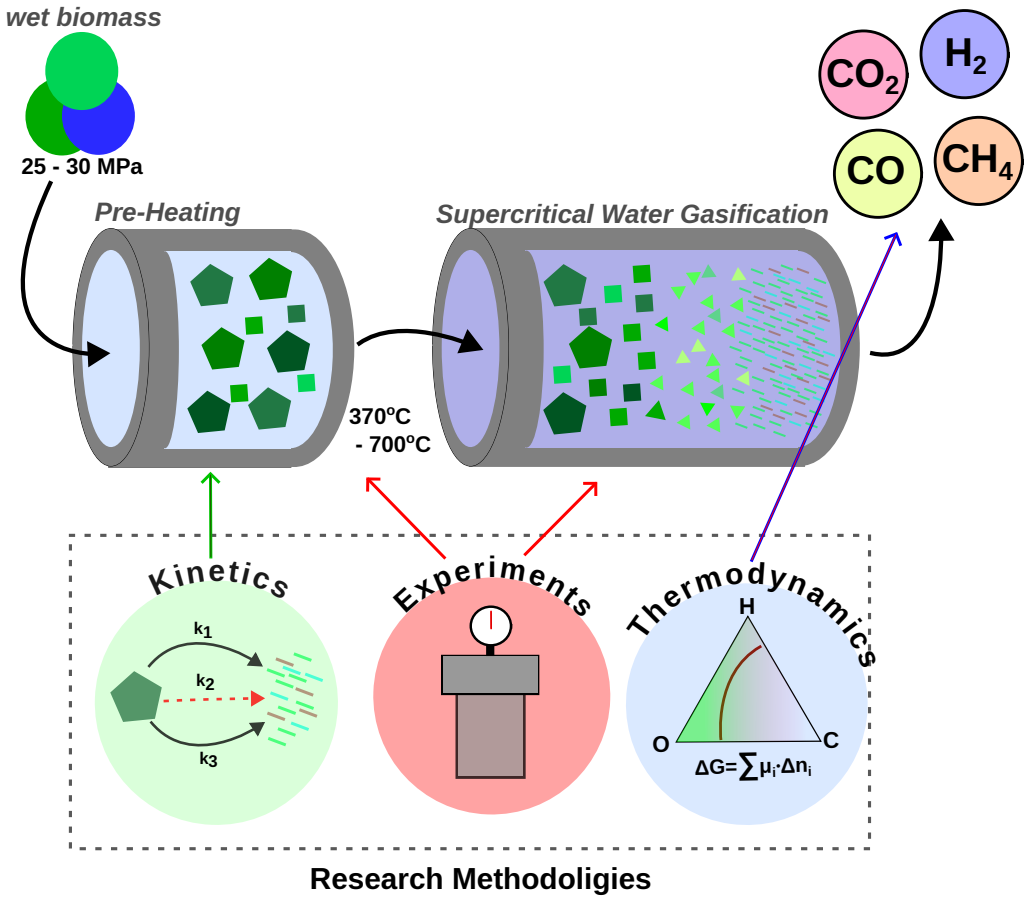

Figure 1.1: Schematic showing the main features of SCWG and the methodologies used in this thesis.

process - in reality other functions would be included, such as salt removal during pre-heating, catalytic reactors, downstream syngas upgrading, etc. However, the general objective remains, which is to use elevated temperatures and pressures to convert high-moisture biomass wastes into syngas with water in-situ, thus negating the need for energy intensive feedstock drying.

There are multiple potential sources of revenue from SCWG, which combined with its ability to both rapidly and effectively treat wet biomass waste make it an appealing, lucrative waste management technique. The syngas can serve to supply multiple functions, whether it is combusted for power generation; upgraded to pure CH_4 or H_2; or sequestered downstream into other useful chemicals,

such as sustainable aviation fuels (SAFs) via a Fischer-Tropsch synthesis (FTS). The separated salts are also marketable as fertiliser additives and the post-SCWG liquid fraction could be sold as a source of industrial/agricultural, or potentially even potable water.

Life cycle assessments (LCAs) are a frequently employed methodology used to provide quantitative comparisons between competing technologies. Dong et al. [10] used an LCA to assess the economic viability and environmental impact of processing food waste via SCWG; where H_2 yield was the main performance indicator. The global warming potential (GWP) of this process was calculated to be $13.4\,\mathrm{kg_{CO_2\text{-}eq}\,kg_{H_2}^{-1}}$. This is comparable to the GWP an alternative food waste biotreatment (enzymatic hydrolysis and fermentation) which had a GWP of $10.1\,\mathrm{kg_{CO_2\text{-}eq}\,kg_{H_2}^{-1}}$, but considerably lower than water electrolysis which comes out closer to $28.4\,\mathrm{kg_{CO_2\text{-}eq}\,kg_{H_2}^{-1}}$ [11]. Coupling SCWG with carbon capture and storage (CCS) has the potential to reduce the GWP further to $0.9\,\mathrm{kg_{CO_2\text{-}eq}\,kg_{H_2}^{-1}}$, and seeing as it is able to process waste much faster than biological treatments, SCWG is a front-runner for future wet biomass treatment and valorisation.

Supercritical water gasification is at an exciting stage of pre-commercialisation. Currently, the only industrial installation is the *SCW Systems* plant in Alkmaar, Netherlands. Launched in 2022, this process uses four modules to treat a total of $16\,\mathrm{tonnes\,h^{-1}}$ of real-world wet biomass waste using high temperature, non-catalytic SCWG [8]. With a technology readiness level (TRL) of 8, it has successfully demonstrated the process through testing and demonstration [12]. This is testament to the current level of understanding, which is fairly good in terms of appreciating how key process variables like temperature and feedstock concentration can be tailored to optimise the conversion of certain biomass. To push SCWG towards TRL 9 and full scale commercialisation, further optimisation of the process is required to make it financially viable in comparison to other methods of waste disposal (e.g., anaerobic digestion, landfilling) and fuel production (e.g. natural gas). Frequently cited in literature are the key bottlenecks preventing

full-scale commercialisation of SCWG. These include the high energy demand of the process; plugging from char formation; and salt precipitation/corrosion [2, 13]

Also highlighted on Fig. 1.1 are the research methodologies used in this thesis. As is shown, both computational and experimental techniques can be used to advance SCWG. In many instances simulations are preferred, as SCWG experiments are generally time-consuming, expensive, and relatively hazardous due to its operating conditions. Thermodynamic and kinetic models are two common types of computational model prolifically explored in literature relevant to SCWG. They have a wide variety of application, ranging from process modelling to reactor design. This work reviews and advances both thermodynamic and kinetic modelling techniques to further optimise SCWG.

The first objective of this thesis focused on employing and improving a detailed SCWG kinetic model. This type of modelling requires the input of experimentally-derived Arrhenius parameters, which in this particular case were obtained from a wide variety of literature sources. Kinetic models are capable of describing the consumption and formation of species involved in a chemical process versus time, and see extensive application in many elements of chemical reaction engineering (e.g., reactor design). The kinetic model described in this thesis was reproduced from literature and improved in this work. Here, this versatile modelling methodology was firstly used to study the main pre-heating stage of SCWG, with particular focus paid to how sub-critical heating regimes alter the gasification of different feedstock molecules in supercritical water (SCW). This is annotated on Fig. 1.1 which shows how this thesis focused on applying the kinetic modelling methodology to the pre-heating section of SCWG. Heating rate has seldom been researched in the field of SCWG, however, it has been demonstrated in other thermochemical processes, such as fast pyrolysis, that this operating parameter can drastically alter the predominant phase and composition of products [14].

Kinetic models, especially detailed ones as used in this thesis, utilise many input variables (e.g. activation energies, pre-exponential factors, etc.) to describe the rate of change of species in a reactive system. The conclusions from the first objective provide useful insight into the feedstock-dependent effect heating rate can have on SCWG. However, little can be hypothesised with regard to the cause of these observed effects without more detailed investigations. The second objective of this thesis therefore presents a sensitivity analysis methodology that can be used to determine the influence rate-limiting reactions in the global kinetic mechanism have on response variables such as product concentration. Sensitivity analyses are powerful tools but have yet to be implemented in relation to SCWG nor have they been employed frequently to study thermochemical processes in general.

The next methodology shown on Fig. 1.1 is thermodynamic modelling. Prolifically reported in literature, this type of model is used to determine equilibrium yields and energy balances of a process. Its application is also frequently expanded to conduct process modelling and techno-economic analyses (TEA) [15, 16], as well as other applications. The Gibbs free energy minimisation calculations necessary to produce a thermodynamic model are typically conducted using a commercial software, such as Aspen Plus. The third objective of this thesis sought an alternative means of performing these calculations and developed a subroutine in Python to produce a thermodynamic model. Given that thermodynamics is time independent, Fig. 1.1 shows that the thermodynamic methodology was only employed here to study the final, equilibrium products from the SCWG of biomass. The novel perspective of element chemical potentials, which is mostly ignored in published literature, was used to justify the chemical and phase equilibrium of SCWG and other thermochemical processes. A comprehensive framework was then developed using ternary diagrams which could be used to ascertain how temperature, pressure, and additive agents (water and/or CO_2) could be used to optimise the thermochemical conversion of any biomass feedstock.

Given the demanding operating conditions of SCWG, experimental data in the field is relatively scarce and therefore highly valuable when it can be obtained. Figure 1.1 shows that experimental methodologies offer the benefit of being able to study all elements of SCWG, whether that be pre-heating rates, or equilibrium gas yields, for example. The commencement of this doctoral research project coincided with the procurement of a high-pressure, high-temperature batch reactor. Consequently, the final objective of this thesis focused on developing a robust experimental methodology for conducting SCWG experiments. The overarching aim was to establish a proficient experimental rig at the University of Strathclyde that could generate high-quality data to validate and support computational SCWG research, as well as other hydrothermal and thermochemical processes.

The remainder of this thesis is structured as follows. Chapter 2 contains a detailed review of SCWG. This section begins by highlighting the fundamental physicochemical properties of supercritical water which underpin the process, before which the effects of the key operating parameters are summarised and the major reactions of biomass. This section finishes by reviewing the major modelling and experimental methodologies reported in recent SCWG publications, and then summarising the main research recommendations for this thesis.

Chapter 3 is the first results chapter, wherein heating rates are studied using a detailed kinetic model. The methodology here revolves around investigating sub-critical heating rates only (i.e., below 374°C), and different heating profiles such as linear and non-linear ones are also tested. The conclusions focus on identifying how the sub-critical heating regime influences the SCWG of the major compounds found in wet biomass: cellulose, hemicellulose, lignin, and protein.

Chapter 4 continues with the kinetic modelling methodology to describe a sensitivity analysis approach that can be used to ascertain a more detailed understanding of the global decomposition mechanism. This chapter employs

the sensitivity analysis to reveal the major formation pathways of H_2 (a desired gas-phase product), and acetic acid (a refractory intermediate) from the SCWG of cellulose.

In Chapt. 5, a general thermodynamic framework is developed that provides a unified perspective to analyse hydrothermal and thermochemical biomass valorisation processes, such as SCWG, HTC, and conventional gasification. The results are compactly summarised in terms of ternary diagrams, which can display information such as when char will form and the relative syngas yield. The framework was used to explore the use of water and CO_2 as a co-media for the gasification of different feedstocks to avoid char formation at high temperatures and to improve product yields and alternatively as co-carbonisation agents to increase char yields at low temperatures.

The final results chapter begins by detailing an experimental methodology designed for a newly acquired batch reactor. This includes a standard operating procedure and the calibration a gas chromatograph necessary for gas-phase detection. The second half of Chapt. 6 describes methodologies that can be used to obtain experimental data to supplement the findings of the preceding computational chapters.

The main conclusions of the thesis are laid out in Chapt. 7 and recommendations made for future work.

2
Review

Supercritical water gasification is a waste treatment technique that draws upon many scientific subject areas. At its simplest, this process can be described as the decomposition of biomass into syngas in SCW. However, upon further investigation it becomes evident that there is an expanse of associated complexity, as there are contributing factors from organic and physical chemistry; reaction engineering; transport phenomena, and other fields of science and engineering. It is not imperative that the reader has a comprehensive understanding of all these principles in order to understand the content of this thesis - nor is much of it fully understood anyway. Instead, this review chapter proceeds with a brief scientific background that touches upon the main features of SCW that allow for the gasification of biomass in a high-moisture system. Following this, a thorough literature review has been conducted. Here, the major operating conditions and feedstocks used in SCWG are reviewed, and then details pertaining to the reactions of major biomass molecules are also described. The intention is to give the reader a good understanding of the main processes at play during SCWG, and how the reaction environment influences the evolution of biomass into syngas products. Following this, research methods are reviewed in two sections which focus on

computational and experimental techniques. This review chapter concludes by summarising findings and stating the recommended research areas of this thesis.

2.1 Supercritical Water

Figure 2.1 shows a pressure versus temperature diagram for pure water. The stoppage of the curve occurs at the critical point - 22.1 MPa and 374°C. At conditions exceeding both these values, water enters a new phase referred to as SCW. The properties of SCW are colloquially said to be like a vapour and liquid hybrid, although, many of the physicochemical properties of this phase are also entirely unique to SCW [17]. Additionally, many properties of SCW, like density, can be drastically changed without phase change occurring [18]. This section describes properties of SCW that are pertinent for the reader to be aware of in order to appreciate the fundamental principles of SCWG. The IAPWS-95 [1] Python package was used to calculate each property. This equation of state (EOS) is an optimised formulation that was developed for scientific use and is able to accurately predict conditions in proximity to the critical point [19].

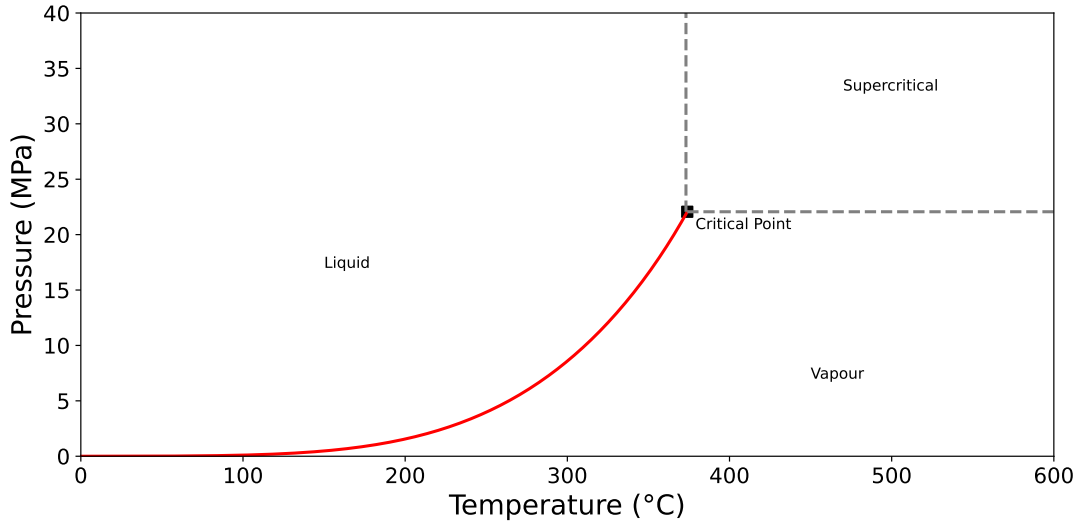

Figure 2.1: Pressure versus temperature plot for pure water.

[1] Source code: https://iapws.readthedocs.io

2.1.1 Density

Figure 2.2a shows how the density of SCW changes with temperature at a series of isobars. Temperature and pressure can be used to great affect to influence the density of SCW. In particular, the initial increase in temperature from the critical point to around 500°C leads to a significant decrease in density at all pressures shown. At 600 bar and 374°C, the density of SCW sits at around 650 $\mathrm{kg\,m^{-3}}$ which is equivalent to a light, hydrocarbon liquid at room temperature, such as butane. Increasing temperature and lowering pressure can reduce the density to around 50 $\mathrm{kg\,m^{-3}}$ which is similar to supercritical CO_2. Density effects on the SCWG of biomass are relatively unknown. Whilst lower densities make SCW a more effective solvent with lower mass transfer resistances, some studies have shown that higher densities expedite the gasification of biomass molecules in SCW [20].

2.1.2 Viscosity

Viscosity is a transport property that is a measure of its resistance to flow. Lower viscosities generally correlate to a greater molecular mobility which enables higher diffusion coefficients for rapid rates of reaction [21, 22]. Figure 2.2b shows how dynamic viscosity in the supercritical region is affected by temperature and pressure. At a constant pressure, viscosity decreases with temperature to a minimum - much like a liquid, after which it increases with temperature - like a gas. Supercritical water has a viscosity that is higher than low pressures gases, but still two orders of magnitude smaller than liquids. For example, saturated steam at 100°C and 1 bar has a viscosity of 0.0135 cP whereas water at ambient conditions has a viscosity of around 1 cP

2.1.3 Dielectric Constant

The relative dielectric permittivity, or dielectric constant, is a measure of the dissolving power of solvents. Under normal conditions, water has a high dielectric constant of around 80. Increasing the pressure and temperature to the critical

point reduces disrupts hydrogen bonds and reduces the dielectric constant to around 5 [21]. This lower dielectric constant is equivalent to non-polar organics, and thus SCW unlike normal water has a great dissolving power for organic compounds. The side effect of this reduced polarity is that polar substances such as salts that would otherwise dissolve readily in normal water precipitate out of solution in SCW. Figure 2.2c shows how lower pressures and higher temperatures correspond to a lower dielectric constant.

2.1.4 Ionic Product

Under normal conditions, the dissociation of water into its cation and anion products can be represented by the equilibrium shown in Eq. 2.1.

$$2H_2O \rightleftharpoons H_3O^+ + OH^- \tag{2.1}$$

Where the ion product, K_w, can be defined using the concentrations of the hydronium (H_3O^+) and hydroxide (OH^-) ions (Eq. 2.2). Ambient water has a K_w of essentially 10^{-14}, which is often represented as its $-log(K_w)$ value of 14.

$$K_w = [H_3O^+][OH^-] \tag{2.2}$$

Under supercritical conditions, the accuracy of this approach comes into question, and more often than not, the dissociation of water is characterized using an H^+ cation and activities, a, as opposed to concentrations [19, 22].

$$K_w = a(H^+)a(OH^-) \tag{2.3}$$

Figure 2.2d shows how the negative log (base 10) of the ion product changes with temperature at ambient pressures (1 bar), and two supercritical pressures. It is shown that increasing temperature up to the critical point increases the value of K_w. The ionic product is marginally higher at subcritical temperatures for the

higher pressure cases. A rapid decrease in K_w occurs at supercritical temperatures, significantly more so however at 1 bar than the supercritical pressures.

The dissociation of water creates an environment that promotes acid- and base-catalysed reactions [21]. The ionic product varies greatly over a range of supercritical conditions, therefore temperature and pressure can be varied to produce a reaction medium that favours homolytic (pK_w>14) or heterolytic (pK_w<14) reactions [18].

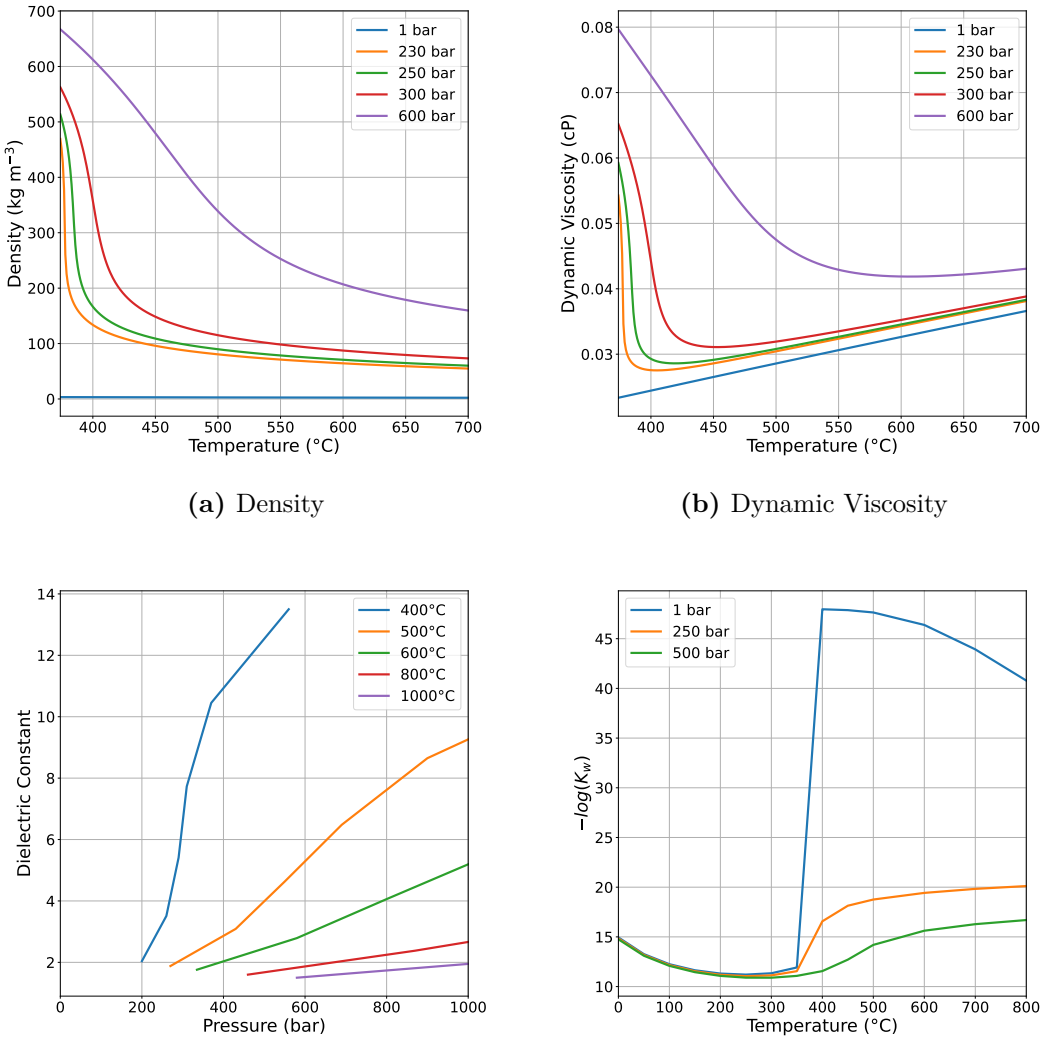

(a) Density

(b) Dynamic Viscosity

(c) Dielectric constant

(d) Ionic Product

Figure 2.2: Properties of supercritical water as predicted by IAPWS-95.

2.2 Operating Conditions

2.2.1 Temperature

Temperature is regarded as the driving force for SCWG. It is with elevated temperatures that the endothermic, rate-limited reactions that make up the global reaction network for biomass gasification are allowed to proceed to any discernible extent.

Generally, two modes of operation are considered for SCWG. Gasification in the high temperature region uses temperatures in the range 550°C to 700°C in a non-catalytic environment. On the other hand, low temperature gasification operates between 360°C to 450°C with a catalyst to help achieve the same conversion efficiency of high temperature gasification [8]. The objective of low temperature gasification is to minimise the capital and operating costs.

The two modes of operation are also divided by the reaction mechanisms that govern gasification in these two temperature regions. Lee, Conradie, and Lester [2] described how low temperature gasification is governed by ionic-product-controlled mechanism, whereas during HTG the mechanism becomes dominated by a free radical mechanism. Figure 2.2d shows that at temperatures close to the critical point of water, the value of K_w is lower than at ambient conditions which means there is a relatively high density of the ion products of water in the SCW. This favours greater yields of CH_4 and char formation. Increasing temperature into the region of high temperature gasification suppresses yields of char and increases the production of H_2.

2.2.2 Pressure

Pressure is a little studied operating parameter in SCWG, and tends to be kept constant whilst other factors are explored [2]. Consequently, the influence of pressure on gasification in SCW is poorly understood. From a thermodynamic perspective, Le Chatelier's principle states equilibrium will shift to the side of the

reaction with fewer gas molecules. The effect of pressure on equilibrium is therefore the cumulative response of methanation, water-gas shift, steam-reforming, and Boudourd reactions [23, 24]. Pressure effects from the physicochemical properties of water can also be taken into consideration. Higher pressures increase the ionic product, density, and dielectric constant of water - see Fig. 2.2. This suggests that for a given temperature, increasing pressure in the supercritical region (e.g., from 250 bar–500 bar) will shift the decomposition mechanisms to being more ionic-product-controlled than free radical [24].

Experimental studies in literature that focus specifically on the influence of pressure on SCWG are few and far between. Within the discourse, there are often conflicting conclusions drawn regarding the influence pressure has on biomass gasification in SCW. For example, Lu et al. [25] and Demirbas [26] demonstrated that higher pressures can increase yields of H_2 from SCWG; on the other hand Güngören Madenoğlu et al. [27] found higher pressures reduced gas yields, and Jin et al. [28] found pressure to have no observable effect.

Whilst there is a discrepancy in literature between the effect of pressure on yields of syngas species and gasification efficiencies, it is consistently observed that temperature is by far the more influential SCWG process variable than pressure. An example of this would be from the study of Lu et al. [25] where increasing the reaction temperature by only 50°C to 650°C from 600°C increased H_2 yields by nearly 30 %. In the same study, reaction pressure was increased significantly from 22.1 MPa to 30 MPa, a range typical of SCWG studies, and it was reported that H_2 yields increased by merely 10 %. Other syngas species in this publication experienced similarly small changes to their yield versus the same change to operating pressure. This type of result typifies why pressure is seldom studied in comparison to temperature in SCWG.

To summarise, pressure effects on the SCWG of biomass are clearly more nuanced than other process variables like temperature, but also less influential as a whole once the critical pressure is surpassed. Literature offers no clear consensus

on the net effect of pressure, largely because pressure simultaneously affects several interdependent variables such as the physicochemical properties of SCW and the thermodynamics of the reactive system. This makes it challenging to isolate a singular global trend between pressure and SCWG, and more research is required to understand the influence pressure has on the SCWG of different biomass types.

2.2.3 Feedstock Concentration

Feedstock concentration is another parameter that strongly influences SCWG. It is typically represented as a dry weight percentage in literature. Supercritical water gasification is a process designed with the intended purpose of treating wet biomass wastes which are typically composed of over 90 wt.% water. Lee, Conradie, and Lester [2] found in their review of SCWG that most experimental publications tend to use feedstock concentrations in the range of 1 wt.%–5 wt.% biomass, although some go up to around 20 wt.% biomass.

There is generally a unanimous agreement in literature in relation to the effect of feedstock concentration of SCWG. At lower feedstock concentrations, there is a greater availability of water per amount of biomass in the system. Since SCW acts as both a solvent and reactant, the increased concentration of water promotes higher gasification efficiencies and greater concentrations of H_2, whereas yields of char and CH_4 are reduced per amount of dry feedstock [2, 13, 24].

2.2.4 Reaction Time

Supercritical water gasification reactions are generally rate-limited, and consequently, longer reactor residence times (to a point) results in higher gasification efficiencies and greater yields of syngas. As a rule of thumb, batch experiments reported in literature usually use a residence times in the range of minutes to tens of minutes, whereas it is seconds to tens of seconds for continuous operation [2]. Longer reaction times favour the cracking of organic intermediates and enable the highest gasification efficiencies to be achieved. It is also generally found that

longer reaction times allow for the conversion of CO into H_2 via the `wgs` which decreases and increases the yields of these two species, respectively [24].

Experiments of SCWG generally employ rapid heating profiles that bring the process stream to temperature in a matter of seconds. There is little understanding of how this heating profile, or other temperature-time profiles for that matter, influence the evolution of gasification reactions in SCW [25].

2.2.5 Catalysts

Catalysts can be deployed in SCWG to target greater H_2 yields and GEs at lower reaction temperatures [8]. A techno-economic assessment was conducted by Lee, Conradie, and Lester [2] using Aspen Plus to provide an initial comparison of catalytic and non-catalytic SCWG conducted at 400°C and 600°C, respectively. A wheat-straw feedstock was used and a constant pressure of 22.1 MPa. The catalytic case used different types of nickel-impregnated heterogeneous catalyst. The results from this preliminary test suggested that operating in the catalytic, low-temperature region offers a more economic approach to SCWG. As despite there being an added cost associated to the procurement of catalysts, this was not as significant as the extra heating cost in the high temperature scenario, or the greater capital expenditure required for the expensive heat and corrosion resistant reactor materials necessary for SCWG at 600°C. These initial findings promote the case for catalytic SCWG, but more research is necessary to reveal the full benefits and limitations of their application in practice.

Vadarlis et al. [29] conducted a comprehensive review of catalytic SCWG. Their conclusions suggest that the most effective catalysts are heterogeneous nickel types supported on magnesia, ceria, zirconia, and alumina, as they offer both a high catalytic activity and stability. The option to boost H_2 selectivity is also possible via doping with promoters like ruthenium and cobalt. The main problem associated to heterogeneous catalysts is their susceptibility to sintering and fouling in SCW. Aqueous alkali salt homogeneous catalysts, such as NaOH, KOH, and K_2CO_3,

have also received significant attention in the subject area and have been shown to offer the same improvements to H_2 selectivity [30]. Homogeneous catalysts on the other hand are difficult to recover and recirculate post-SCWG, which means a constant supply of fresh catalysts would be required at great expense [24].

2.2.6 Heating rate

Heating rate is another important variable in the thermochemical treatment of organic waste. So much so that sub-processes have been created and named purely based off their heating strategy, the example here being fast-pyrolysis. There is a poor understanding of the effect of heating rate on SCWG.

Experimentally, the first mention of heating rate effects on SCWG came from Antal Jr et al. [31]. Here, the continuous SCWG of real biomasses such as potato starch and wood sawdust was conducted at temperatures in excess of 700°C. It was concluded that heating the process stream at a faster rate at temperatures below the critical point would reduce the yield of stable intermediates like acetic acid and increase the overall GE and yield of H_2.

Sınağ, Kruse, and Rathert [32] used a batch reactor to explore the effect of heating rate on glucose. Two heating rates of $1\,^{\circ}\mathrm{C\,min^{-1}}$ and $3\,^{\circ}\mathrm{C\,min^{-1}}$ were used, and it was found that using faster heating rates increased the GE and formation of small carboxylic intermediates like acetic and formic acid. Slower heating rates promoted the formation of more complex intermediates like furfural which can be a precursor to char formation.

Matsumura et al. [33] investigated how the continuous SCWG of glucose, and cabbage slurry is altered by changing heating rates between $10\,^{\circ}\mathrm{C\,s^{-1}}$ and $30\,^{\circ}\mathrm{C\,s^{-1}}$. For both feedstocks, the results clearly demonstrate that faster heating rates favor a greater GE, although there was no observed effect on the distribution of syngas products.

Farobie et al. [34] investigated the heating rate effect on glucose/guaiacol mixtures. Using a fixed final temperature of 600°C and pressure of 25 MPa.

Heating rates were varied between $8°C\,s^{-1}$ and $60°C\,s^{-1}$ by using two feed flow rates of $1\,g\,min^{-1}$ and $2\,g\,min^{-1}$ and pre-heater section lengths between 0.45 m and 1.8 m. Gasification efficiencies were increased by using faster heater rates in the $1\,g\,min^{-1}$ case, whereas slower heating rates improved GEs when using a feed flow rate of $2\,g\,min^{-1}$. This was attributed to interactions between glucose and guaiacol being promoted at higher flow rates. The authors also found that the heating rate had little effect on the distribution of products in the gas phase.

Mainil and Matsumura [35] used the same experimental rig to explore phosphorous deposition during the SCWG of palm oil mill effluent. They found that faster heating rates resulted in lower yields of H_2, higher gasification efficiencies, and less phosphorous precipitation.

Yakaboylu et al. [36] made brief mention to heating rate in the supplementary information of their publication of a detailed kinetic model for the SCWG of biomass - discussed further in Sec. 2.5. As part of their results, the authors tested paper pulp, micro algae, and manure wet biomasses with different two sub-critical (i.e., 25–374°C) heating times of 1 mins and 5 mins, and also tried three heating profile: linear, slow, and rapid.

The findings presented in this subsection demonstrate that heating rate is a process variable that can significantly influence the conversion of feedstocks into syngas during SCWG. The suggestion here is that the successful commercial deployment of SCWG could partly depend on the development of tailored heating regimes that maximise product yields. There are still many unknowns in terms of the exact effects that heating rates and profiles have on the reactions of biomass in hydrothermal conditions, and a greater degree of understanding is required in order to begin to develop optimised heating regimes.

2.3 Biomass Feedstocks for SCW

Broadly speaking, SCWG is a hydrothermal treatment technique that can be applied to any organic waste composed of biomass and/or plastics. In practice,

researchers tend to focus their investigations on a much smaller pool of potential feedstocks. In each case, feedstocks are selected based upon their demand for valorisation and suitability for SCWG.

A systematic review was conducted to quantify the amount by which the SCWG of biomass feedstocks are studied experimentally. The Web of Science [2] database was used to search and refine publications using the following the boolean operators: "supercritical water gasification" OR "hydrothermal gasification" AND "experiment". Papers that used feedstocks derived from fossil fuels or fossil fuel industries, like oily wastewater, were excluded from the review. Figure 2.3 shows SCWG feedstocks with more than one occurrence in publications that were in the list the literature search returned. The most frequently studied feedstocks are the model compounds glucose and glycerol. Glucose is used frequently to represent polysaccharide materials in biomass like cellulose as it is a known to form prolifically during its decomposition. Likewise, glycerol is used to represent lipid and oil-like compounds. Phenol is also used as a representative of the decomposition products of lignin and are known precursors of char formation. In terms of real biomass, the most commonly researched include sewage sludge, food waste, black liquor, and microalgae.

There is a general preference to study model compounds over real biomass. This is mainly because it is easier to appreciate the chemistry of gasification of singular compounds. However, as SCWG advances there is a greater need to study real biomass to appreciate how a commercialised process will behave with industrial feedstocks. Figure 2.4 shows that model compounds dominated experimental literature in earlier publications between 2000 and 2015, with a particular jump in interest in glycerol occurring between 2010 and 2015. However, more recently, there has tended to be a broader range of real biomasses that dominate the majority of experimental SCWG publications.

[2] https://www.webofscience.com

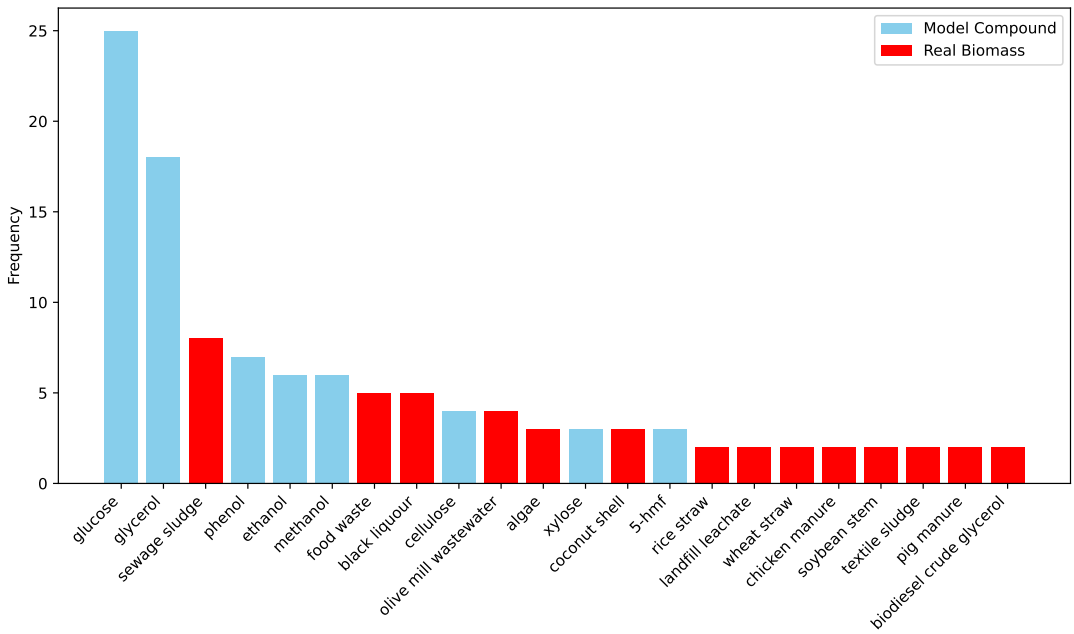

Figure 2.3: Proportion of SCWG publications by feedstock type.

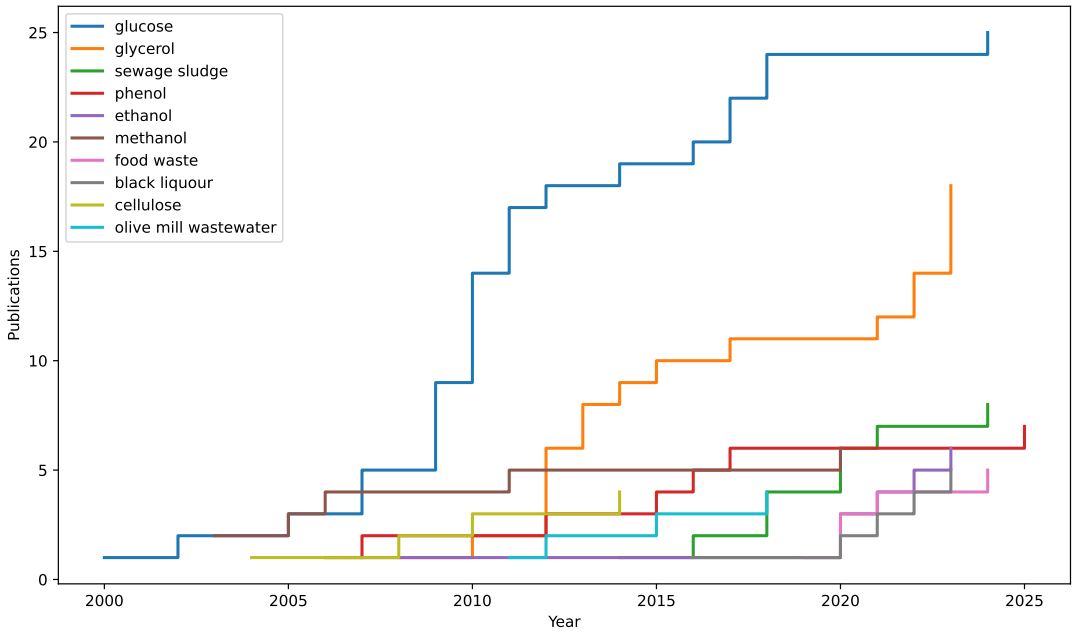

Figure 2.4: Cumulative number of SCWG publications per feedstock by year.

Sewage sludge is the most researched real-world feedstock for experimental SCWG experiments. Its popularity is chiefly due to how appropriate it is for valorisation via SCWG. Sewage sludge is a high-moisture feedstock with a moderate to high calorific value, and also a higher content of inorganics, such as potassium, nitrogen, phosphorous, and calcium compounds that could be used as a fertiliser additives [37]. The composition of sewage sludge varies greatly from source-to-source, however, on a dry basis it can be expected to have 50 wt.%–70 wt.% organic matter and 30 wt.%–50 wt.% mineral components, where the organic matter is typically constituted of proteins, fats, and cellulitic materials [38]. Historically, sewage sludge was disposed of via landfill, however, an understanding of the problems causes by the leachates and CO_2 emissions this causes means the majority of sewage sludge produced in the European Union (EU) is disposed of via incineration or agricultural spreading [38]. In more recent years, advanced treatment techniques have been sought as issues with agricultural spreading like phytotoxicity and long-term soil damage have come to light [39], as have the poor recovery, emissions of GHGs and other pollutants, and high energy cost of sewage sludge incineration [40]. Anaerobic digestion has been applied to sewage sludge, but several challenges remain. These include slow processing times, the formation of hydrogen sulfide (H_2S), and most critically, the sensitivity of the process to inhibitors such as ammonia and heavy metals, which are either present in or formed during digestion of sewage sludge [41]. The rapid, robust treatment offered by SCWG, in addition to the fuel value and nutrient content recovered, make SCWG a prosperous method of sewage sludge treatment. Examples of recent experimental publications investigating the SCWG of sewage sludge have explored the migration of heavy metals (e.g., Ni, Cr, Cu) during gasification [42]; the recirculation of contaminated post-SCWG liquids as a homogeneous catalyst [43]; and the effect of sewage sludge composition on the formation of chars and tars during SCWG [44]. In short, sewage sludge is a calorific, nutrient-dense material stream that has been demonstrated to be suitable for valorisation for SCWG. Notable challenges are the

proclivity of sewage sludge to form chars and tars during gasification due to the complex mixture of organics present; and the development of effective inorganic removal techniques to regain the full nutrient value in the sludge.

Food waste is another example of wet biomass that has reportedly been treated and valorised using SCWG. Globally, landfilling remains the main method of food waste management, although there is increasing interest in a range of other techniques like AD, composting, and thermochemical treatments like HTC [45]. Similarly to sewage sludge, food waste can have a very varied composition, which adds complexity to feedstock-sensitive treatments such as composting and AD. A recent publication explored using H_2 produced from the SCWG of food waste to run a fuel-cell for heating applications [46]. Other experiments studies using food waste have demonstrated how a lower-temperature liquefaction region prior to gasification could be used to save energy consumption by reducing residence times in the supercritical region [47]. Another study focused on how operating parameters (temperature, residence time, etc.) and homogeneous additives such as NaOH can be used to increase yields of H_2 from the SCWG of food waste [48].

Black liquor, also known as Kraft black liquor, is a by-product of the Kraft process used in the paper industry to convert wood into cellulose fibers. Unlike sewage sludge and food waste whose compositions are highly variable, black liquor is an industrial effluent with a more consistent and predictable composition. Around 1.3 billion tonnes of dilute black liquor are produced globally every year; the composition can vary slightly depending on the type of wood used (e.g., softwood, hardwood, straw), or on process-specific additives, like bleaches, but generally the black liquor is anywhere up to 15 wt.% solids of which is mainly lignin, polysaccharides, carboxylic acids, and phenolic compounds [49]. Conventionally, black liqour is dewatered to around 65 wt.% solids and then incinerated. The ashes are recovered and reprocessed to generate chemicals that are necessary additives to the Kraft process, like NaOH and CaO [49]. The recovery of these chemicals via incineration is critical to the economic viability of the process,

however, it leads to the formation of hazardous pollutants like chlorophenolics - and also fails to recover any value from the organic fraction of the black liquor [50]. Integrating the Kraft process with SCWG is a plausible method of effectively treating black liquor whilst recovering the additive chemicals and valorising the organic waste fraction. Themes of research using this feedstock include the study of H_2 production from black liquor via an integrated HTL and catalytic SCWG process [51]. Similar studies studied how H_2 yields from the SCWG of black liquor are affected by the addition of heterogeneous catalysts (e.g., MnO_2), lignocellulosic biomass (polar wood residue) and formic acid [52]; and how short residence times and high temperatures could be used to expedite H_2 formation [53].

The conversion of microalgae via SCWG differs significantly from that of conventional feedstocks. Microalgae biorefineries are based on cultivating algae using biomass-derived nutrients (e.g., sugarcane bagasse), sunlight, and CO_2. The resulting biomass can be used in various downstream applications, including biodiesel production, extraction of high-value proteins and lipids, or, in the case of SCWG, gasification to produce syngas [54]. Additionally, microalgae growth sequesters atmospheric CO_2, offering the potential for negative GHG emissions. Recent experimental research relating to the SCWG of microalgae has explored a variety of subject areas. Heeley et al.(2024) [55] for example studied the influence gasifying *Chlorella vulgaris* in algal growth water, which contains inorganic nutrients, as opposed to deionised water has on gasification efficiencies. Nurcahyani et al.(2020) [56] compared the gasification performance of *Chlorella vulgaris* with and without a hexane lipid extraction pre-treatment. Elsewhere, Xu et al.(2019) [57] explored the integrated HTL and catalytic SCWG of *N. chlorella*.

2.4 Reactions of Biomass Model Compounds

Model compounds represent the building blocks of biomass. Waste feedstocks in particular are highly heterogeneous, however, for most part their molecular

composition can be categorised in terms of the following species. The following subheadings summarise the decomposition and gasification reaction pathways of the major biomass components in sub- and supercritical water.

2.4.1 Cellulose

Cellulose constitutes around 40 wt.%–55 wt.% (dry) of all lignocellulosic biomass [13]. Obviously the products of cellulose SCWG vary greatly upon the operating conditions used, but generally it is a favourable feedstock as it gasifies with relative ease. Cellulose and its derivative compounds are one of the most studied in SCWG-related literature, and as shown on Fig. 2.3 it is common to use derivative model compounds such as glucose. Okolie et al. [24] proposed a detailed mechanism for cellulose decomposition in SCW. It was reported that the primary hydrolysis products of cellulose are monosaccharide sugars like glucose and fructose. Species such as erythrose, and glycolaldehyde are also formed from this primary hydrolysis. Decomposition proceeds via the formation of organic species such as levoglucosan, lactic acid, and 5-hydroxymethylfurfural which go on to decompose into simple organics like acetic acid, formic acid, formaldehyde. Char formation from cellulose is minimal, and would likely come from agglomeration of furfural-type precursors.

2.4.2 Hemicellulose

Hemicellulose is another major component of lignocellulosic material, comprising roughly 15 wt.%–35 wt.% (dry) [13]. Xylose is a monomer unit of hemicellulose that is often used as a representative model compound in studies. Hemicellulose decomposes readily in sub-critical conditions into a mixture comprised of mostly furfural, methyl formate, and glyceraldehyde. These intermediates further decompose into a mixture of propionic, acrylic, and lactics acids [23]. Hemicellulose is thought to be a component of biomass the gasifies with relative ease at temperatures between 200°C–300°C with negligible char formation [2].

2.4.3 Lignin

Lignin is the remaining component in lignocellulosic biomass, typically accounting for 20 wt.%–40 wt.% (dry) [13]. Lignin is far more recalcitrant to gasification than cellulose or hemicellulose, and its presence in biomass is associated with lower GEs [2]. Different types of lignin exist (hardwood, softwood, etc), however, they are alike in their make-up of aromatic compounds, which results in significant, unwanted char formation via the linkage reactions of lignin hydrolysis products such as phenol and catechol [13]. Studies have shown that lignin can decompose easily in sub-critical conditions to form a mixture of stable products, including guaiacol and oCresol. The subsequent decomposition and gasification of these compounds is difficult, resulting in low GEs [58].

2.4.4 Protein

Besides the components found in lignocellulosic materials, wet biomass may also contain considerable amounts of other organic species. Sewage sludge, for example, can include upwards of 40 wt.% protein [59]. Microalgae can contain over 60 wt.% protein as well, and interest in integrating microalgae cultivation with hydrothermal processes for biofuel production has grown in recent years [60].

Amino acids are frequently used as model compounds of protein as they are the direct hydrolysis products of proteins [61]. Experiments with glycine suggested that in a continuous operation with a residence time of 188 s, CGE of roughly 20 % and 80 % would be achieved when using reaction temperatures of 500°C and 600°C, respectively [62]. Alanine behaved similarly to glycine under the same reaction conditions, although glycine produced predominantly CO_2 and H_2 whereas CH_4 and CO were the main syngas species from the SCWG of alanine [63]. Other amino acids such as valine and leucine were found to be more recalcitrant to gasification [64].

In general, SCWG studies using protein are less common than other types of biomass model compound. Amino acids are more difficult to gasify than cellulose and hemicellulose derived species.

2.4.5 Lipids

Lipids are another significant component found frequently in wet biomass in significant amounts. Sewage sludges are a particular example of waste that can have up to 30 % of its total solids accounted for by lipids [65]. The SCWG of lipids is relatively unreported in literature. They are known to hydrolyse readily in sub-critical conditions into their fatty acid and alcohol constituents [13].

Oleic acid has been used in literature as a fatty acid model compound. Experiments show that this compound is stable in conditions typical of LTG, requiring catalysts to decompose, but gasify readily at higher temperatures in excess of 500°C [66]. As shown in Fig. 2.3, glycerol has also been extensively studied as a SCWG feedstock. Guo et al. [67] found that glycerol gasifies readily at temperatures above 487°C. A kinetic investigation by Guo et al. [68] suggested that glycerol directly gasifies but also decomposes into a number of intermediates including propionic acid, acetaldehyde, and propionaldehyde.

2.5 Modelling Approaches

2.5.1 Thermodynamic Modelling

Thermodynamic models are frequently the first option for researchers and operators when studying a new or modified process. Many variations relating to SCWG but also other thermochemical processes as well have been published in literature. Thermodynamic models provide useful information pertaining to the theoretical maximum yields of a reaction, and can be used to appreciate the amount of energy required to perform this conversion [69]. They see a broad range of

extended application in literature ranging from process modelling and techno-economic analyses (TEAs) to heat-recovery pinch analysis and environmental assessments (EAs).

Thermodynamic calculations generally adopt one of two possible approaches: stoichiomtric (SM) and non-stoichiometric (NSM). In SMs, the concentrations of species at equilibrium is determined by calculating the equilibrium constants for a set list of reactions. On the other hand, NSMs use a Gibbs free energy minimisation (GFM) calculation to predict the composition of a pre-defined list of species. Mathematical proofs have demonstrated that for simple organic species (e.g., acetic acid), where gasification can be described in few reactions, SM and NSMs yield the exact same results [70]. Commercial software programs, such as Aspen Plus, are frequently cited methods of producing thermodynamic models in published literature. Alternatively, the calculation can be completed by the user themselves but this requires prior experience in thermodynamics and programming.

Literature contains an abundance of papers using thermodynamic models to investigate SCWG. The continual publication of such articles which are still frequently published in the present day demonstrates the value thermodynamic models offer as a research tool. To give just a few examples, thermodynamic modelling was used to study the SCWG of sewage sludge by Ruya, Purwadi, and Lim [71], Hu et al. [72], and Hantoko et al. [15] who explored autothermal operations, power and H_2 production, and combined-cycle with H_2 production, respectively. Likewise, black liquor was investigated as a feedstock in publications by Chen et al. [73], Qi et al. [74], and Qiu et al. [75] where SCWG thermodynamic models were used to study SCWG combined direct iron reduction, online salt recovery, and gasification versus oxidation, respectively. Food waste is another common feedstock and Dong et al. [76], Macri et al. [77], and Peng et al. [78] investigated power and H_2 production, energy consumption, and integrated in-situ H_2 separation, respectively. Thermodynamic models are not only used to study the

SCWG of real biomass feedstocks, as publications like that of have been used [79] to study the SCWG of model compounds like methanol, ethanol, glycerol, and glucose.

The most common application of thermodynamic models in literature is through larger studied which use process models combined with different methods of assessment to analyse the performance of a newly conceptualised process. More often than not, the novelty of these thermodynamic-based studies comes from integrating two or more different sub-processes together, such as integrated SCWG and steam reforming for H_2 production [80]. Different methods of assessing the performance of these processes are reported. One of the most common are TEAs; this method aims to assess the economic viability of a process by attributing monetary costs to the capital and running demands of a process, and then weighing these against the worth of the product/service produced.

Rahbari et al. [16] undertook a TEA of an integrated microalgae 'solar fuel' plant with SCWG and FTS, where microalgae is produced using solar energy and then gasified in SCW after which the syngas is upgraded via steam-reforming and the converted into liquid fuels via FTS. Here, Aspen Plus was used to model SCWG in a RGibbs (GFM) block. The author's concluded that this process would not be economically competitive with conventional means of fuel production unless incorporated in-part with a fossil fuel feedstock, i.e. supplement H_2 production with natural gas. Another example of a SCWG TEA conducted using a thermodynamic model was published by Khandelwal and Dalai [81]. The objective of this study was to assess the economic viability of a SCWG process designed to produce H_2 from canola straw. Separation of the H_2 product using pressure swing adsorption and CCS was combined into a conventional SCWG process modelled in Aspen Plus using an RGibbs block. The concluded economic feasibility for this process, although it hindered greatly on the high net present value of H_2 (which is subject to fluctuation).

Besides TEAs, another method of assessing thermodynamic-based SCWG process models is through an energy and/or exergy analysis. The general objective

of this study type is to investigate how a process can be optimised to obtain the greatest useful work (exergy) from SCWG with the lowest input of energy (work). One example was published by Cao et al. [82] who explored variables such as reaction temperature and feedstock concentration could be optimised to maximise the exergy efficiency during the SCWG of black liquor.

Each of the papers mentioned in this subsection presents a novel contribution by investigating a different proposed advancement to SCWG. However, a common feature among most published SCWG thermodynamic models is the similarity of a particular graph that is presented in each results section. Typically, these graphs illustrate how variations in operating temperature, pressure, and feedstock concentration influence the equilibrium yields of syngas species (H_2, CO, CO_2, CH_4), and in some cases, char as well, for a given feedstock.

It was Castello and Fiori [83] who highlighted in their work that it is reaction temperature and pressure, and the elemental composition of the biomass feedstock that influence equilibrium yields of products, i.e., not the type of molecules in the feedstock. This concept was extended further by the same authors when they developed a thermodynamic model to describe the SCWG of a biomass pseudo-compound specified only in terms of $C_xH_yO_z$ [84].

2.5.2 Kinetic Modelling

Kinetic models are tools that are employed to describe the consumption of reagents and formation of products versus time. Accurate kinetic models are versatile and see use in many elements of chemical reaction engineering including reactor design, computational fluid dynamics, process simulation, and more. Unlike thermodynamic models which are derived from first principles, kinetic models are inherently more challenging to produce - especially in the field of SCWG - as they rely upon the input of experimentally-derived kinetic data. However, in most cases this makes kinetic models inherently more valuable as they are better at predicting the behavior of real-world scenarios.

The most common type of kinetic modeling used to simulate the decomposition of biomass in SCW is known as the 'lumped' first-order model. This is where the number of reactions requiring modelling is greatly reduced by approximating all intermediates into a single pseudo-compound. The kinetic model then describes the decomposition of the feedstock into the single intermediate, followed by the conversion of that intermediate into the product species (e.g., syngas). In many cases, the objective of a kinetic model is to appreciate the rates at which final products are formed, and how starting material(s) are consumed. In such cases, modelling the formation of a complex mixture of intermediates is superfluous to requirement, and the lumped kinetic model is satisfactory. Lumped kinetic models have been produced for a variety of types of biomass, including model compounds like acetaldehyde [85], microcrystalline cellulose [86], and 5-hydroxymethylfurfural (5-HMF) [87]; and for real biomasses such as horse dung [88], algae [89], and kraft black liqour [74]. The main limitation specific to lumped first order kinetic models is that generally these models are only valid for the specific feedstocks they simulate and thus lack versatility or robustness.

Detailed kinetic models for the thermochemical conversion of real-world organic wastes are few and far between in literature. The complex composition of biomass waste streams, and the large variety of reaction pathways and intermediates that are present in the global mechanism makes modelling every single reaction a near-impossible challenge. For SCWG, the kinetic model published by Yakaboylu et al. [36] is, to the author's knowledge, the only example in literature of a model which attempts to simulate the detailed decomposition pathways from starting molecule to syngas species for the major components found it wet biomass. This model uses 55 sub-critical and 74 supercritical reactions to model the SCWG of real-world biomass. The model describes the biomass in terms of mixtures of cellulose, hemicellulose, lignin, and protein - which are represented using the model compounds cellobiose, xylose, guaiacol, and aspartic acid, respectively. The model was successfully validated against experimental data and shown to have fair

accuracy. However the detailed kinetic model is not without limitations. Firstly, it is pseudo-first order meaning the effect the concentration of water has is not taken into account. This assumption is fine for large excesses of water, but becomes weak as the concentration of biomass increases. Hence, the authors purport the model only to be valid at 10 wt.% biomass or less. Pressure effects are also not taken into account in the model; the quoted pressure range is $25 - -30\,MPa$ which relates to the range of pressures used by the experiments used to derive the kinetic data.

Another limitation of kinetic models are that the reaction kinetics are generally only reliable at the range of reaction conditions used in the experiments from which the kinetic data was obtained. For example, if a SCWG reaction was studied at temperatures and pressures between 400°C–500°C and 25°C–30°C, respectively, using the rate constant to model the reaction at conditions outside this range would introduce significant uncertainty into the results. Experiments also have many additional uncontrollable variables and nuances that are often completely unnoticed. This can affect the accuracy of the kinetic model and the ability of other researchers to reproduce the original results. A good example in the field of SCWG is the catalytic influence of the reactor material. It is understood that Hastelloy (C-276) has a significant catalytic activity that can drastically alter the final syngas product composition from the SCWG of biomass. This has been demonstrated clearly when studying the SCWG of acetic acid, where researchers using Hastelloy report significant H_2 yields [90, 91], but researchers using SS 316 do not [92–94].

There has been limited use of the detailed kinetic model in literature. The study by Ochieng and Sarker [95] used the kinetic model to conduct a TEA to assess the feasibility of combining wood fast-pyrolysis with sewage sludge SCWG, the idea being that gasifying bio-oil in SCW with sewage sludge increases overall yields in comparison to conducting the two processes separately. The authors concluded that from an economic perspective, this process has the potential to be a viable means of H_2 production at a price lower than standalone processes like SCWG and electrolysis.

2.5.3 Other Modelling Techniques

More recently, techniques other than thermodynamics and kinetics have been used to study the SCWG of biomass. This includes computational fluid dynamics (CFD) and machine learning (ML) based approaches, however, the most common is process models [96]. These are used to evaluate the performance of pre-existing or newly thought up chemical processes. They typically incorporate thermodynamic and/or kinetic models in sub-processes to perform the main operations that occur in a chemical process, e.g., plug-flow reactors, flash separators, etc. The majority of process models published in literature use some form of licensed commercial software, such as Aspen Plus. Open-source chemical process simulators like DWSIM [3] are also becoming more popular though and have been used to study the SCWG of biomass [97].

Computational fluid dynamic studies are relatively uncommon for SCWG, partly due to the complexity of modelling thermodynamic and transport properties of fluids near and above the critical point of water [96]. Yoshida and Matsumura [98] were concerned with the deposition of char particles during the SCWG of glucose, and thus used a discrete phase model to simulate the transport of solid spheres in SCW. Goodwin and Rorrer [99] used a 2D, finite-volume CFD simulation to study the SCWG of xylose in a channel. By modeling fluid-flow with the laminar Navier-Stokes equation, investigations into the temperature, velocity, and xylose conversion profiles across the channel were conducted. Caputo et al. [100] used a 3D, finite-volume CFD simulation to study mixing and heat transfer during the SCWG of glucose in a tubular reactor with varied inlet positions.

There are a handful of other modelling techniques like that are beginning to become more prevalent, especially with the recent explosion of artificial intelligence (AI). A number of papers have been published for example that use ML techniques to predict H_2 yields from the SCWG of biomass based off of key process variables like feedstock concentration, temperature, and biomass hydrogen content [101–104].

[3] https://dwsim.org/

The advantage offered by adopting this type of methodology is that experimental data points can be correlated to many input variables to produce models that effectively describe complex, non-linear processes like SCWG.

2.6 Experimental Approaches

A standard experimental methodology does not exist in the field of study for SCWG. Literature reveals that researchers use a wide range of techniques to investigate this process. Experimental rigs can vary significantly between research groups. Key differences include the use of batch versus continuous operation; catalytic versus non-catalytic reactions; self-fabricated versus procured reactors; and the choice of the reactor material. This thesis aims to develop an experimental SCWG methodology, and thus it was pertinent to include a section in this review that collates the common experimental SCWG techniques used by active research groups elsewhere.

A considerable amount of experimental SCWG research originates from Chinese academic institutions, notably Xi'an Jiaotong University. Experiments at this institution are typically conducted using in-house fabricated 'mini' batch reactors with an internal volume of approximately 4 mL, constructed from stainless steel 316. These reactors have been employed to investigate a wide range of topics, including novel catalysts and feedstock pre-treatments (e.g., pulping) [105–107]. The primary focus of research at Xi'an Jiaotong University is coal and crude-oil valorisation via SCWG [108, 109]. Since this focus does not pertain to biomass, these studies were not considered further in this review.

Table 2.1 collates research from other active groups who have published experimental SCWG research in the last five years.

Summarising the contents of Tab. 2.1, it is evident that current experimental trends in SCWG research favour continuous systems, particularly when investigating the catalytic gasification of real-world biomass feedstocks. This is largely due to the greater relevance continuous operations have as a means of replicating

a commercial-scale process. Across the majority of surveyed research groups, the continuous rigs are self-fabricated, with stainless steel 316 being the most common construction material. Its popularity is likely from the combined effect of its affordability and relative ease of replacing/repairing when plugging or corrosion inevitably occur.

Operating conditions were found to be fairly consistent, with most experiments being conducted within a temperature range of 400–600°C and pressures typically remaining between 25–30 MPa. It was notable that very few of the studies reported varying pressure, or use higher pressures (i.e., above $30, \mathrm{MPa}$).

Catalytic SCWG was a dominant research theme for many of the research groups. A range of approaches were studied including homogeneous alkali catalysts and heterogeneous supported metal catalysts. Catalyst development was frequently explored alongside real-world feedstocks like sewage sludge, agricultural residues, and microalgae. Several groups (e.g., KIT, Hiroshima University) also investigated issues related to reactor fouling, salt precipitation, and heavy metal contaminants.

Some groups, including the University of Saskatchewan and Université Grenoble Alpes, use batch reactors. Additionally, at least one group (CEA/Université Grenoble Alpes) employs a commercially procured reactor.

2.7 Conclusions and Recommended Research Areas

The literature review has shown that SCWG is a novel hydorthermal waste treatment process at an exciting stage of pre-commercialisation. Research into the topic explores a wide range of themes, however, the general objectives are to understand how the gasification efficiencies and H_2 yields from the SCWG of biomass can be increased through optimised process parameters like temperature, residence time, and catalysts.

There is a good understanding of how major operating parameters influence the SCWG of the major compounds found in biomass. To summarise, higher

temperature and lower feedstock concentrations favour greater yields of H_2, with carbohydrate species like cellulose and hemicellulose being known as notable precursors to H_2. On the other hand, methane is generally the dominant product gas when using lower reaction temperatures and greater concentrations of feed, however, this also tends to increase yields of char. Achieving greater gasification efficiencies is also made possible by using hotter temperatures and lower feedstock concentrations. Generally, most species in biomass gasify fairly well with the exception being lignin and its derivatives which are known precursors to char formation.

Modelling is a popular choice for SCWG researchers as it avoids the need to conduct experiments, which given the extreme operating conditions required for SCWG can be expensive and time intensive. Thermodynamic models are reported frequently in literature and are typically employed to demonstrate the dependence of reaction conditions on equilibrium yields of syngas, or to conduct other types of investigation such as process modelling and TEAs. The kinetic modelling of SCWG is in relative infancy. A selection of lumped first-order kinetic models have been published which describe the formation of products from specific feedstocks (under specific reaction conditions) versus time. Additionally, a single detailed kinetic model for SCWG has been published. Other modelling methods are becoming more popular which include approaches like ML and CFD.

Experimental techniques tend to mostly use self-fabricated, continuous reactors manufactured from stainless steel 316. These allow SCWG to be studied with high temperatures, generally up to around 600°C, moderate pressures from 23 to 30 MPa, and homogeneous or heterogeneous catalysts if desired. These studies use a broad range of feedstocks, with most attention being paid to model compounds like glucose and glycerol, but also real-world biomasses like sewage sludge, black liquor, and microalgae.

The literature review identified the importance of heating rate as a process parameter in thermochemical processes. There is little published in literature

exploring through either modelling or experimentation the influence that heating rate has specifically on the SCWG of biomass, however, what is available in literature suggests that faster heating rates can be used to increase gasification efficiencies [32–35]. The heating rate studies used a range of feedstocks such as glucose, guaiacol, and cabbage. However, to date no attempt has been made to systematically correlate the effect of heating rates on the individual major constituents of biomass, i.e., cellulose, lignin, etc. With a greater understanding, it would be possible to optimise a process by tailoring the heating regime to the specific composition of the feedstock. Hence, the first results chapter of this thesis uses a detailed kinetic modelling approach to study exactly this, with particular attention paid to how heating rates and profiles in sub-critical conditions alter the yields of syngas species, the gasification efficiency, and char yields from the major components of real-world biomass.

The second recommended area of research revolves around using a chemical kinetic sensitivity analysis approach to obtain a more detailed understanding of the kinetic mechanism which dictates the formation of products versus time. The detailed kinetic model has proven to be a valuable tool in the field of SCWG, however, very little is known or reported with regard to its key features. The objective of this second results chapter was to present a methodology that could be used to obtain more information about the main pathways and rate-limiting steps which govern the formation of species of interest. In this chapter, cellulose is looked at in detail as a starting molecule, and H_2 and acetic acid are considered as products of interest.

The literature review recognised the principle which has been reported briefly before by [128]. This concept is that all varieties of thermochemical processes can be viewed under the same lens from a thermodynamic perspective because it is only temperature, pressure, and elemental composition that influence the distribution of products at equilibrium. That is to say that at a given temperature and pressure, molecule type has no bearing on equilibrium, only the number of

atoms of each element. The third objective extended this concept to develop a comprehensive thermodynamic framework that could be used to describe the thermochemical conversion of any real-world biomass.

The final research objective of this doctoral thesis was therefore to develop an experimental methodology that could be used to conduct SCWG research to validate the computational findings of this thesis and other future research projects.

Table 2.1: Summary of experimental SCWG research conducted by active groups in the last five years.

Institute	Reactor Type	Operating Conditions	Research Themes	References
Karlsruhe Institute of Technology (KIT)	• Self-fabricated • Nickel-based inconel 625 • continuous with capacity of $ml\,min^{-1}$	• 500–700°C • up to 30 MPa.	• water hydrogen donation • effluent recyling • salt precipitation • heavy metal contaminents • real-world biomass (Reed Canary grass and grape vines)	[110–114]
Hiroshima University	• Self-fabricated • Stainless steel 316 • continuous with capacity of $ml\,min^{-1}$	• 500–600°C • around 25 MPa.	• carbon nanotubes (CNTs) • novel catalyst supports • heating rate • microalgae feedstocks • additive char suppressants	[35, 92, 115–118]
Paul Scherrer Institut (PSI)	• Self-fabricated • Stainless steel 316 • continuous with capacity of tens of $ml\,min^{-1}$	• 400–500°C • up to 30 MPa.	• glycerol and sewage sludge feedstocks • catalyst deactivation • carbon decomposition mechanisms	[119–121]
University of Saskatchewan	• Self-fabricated • Stainless steel 316 • Batch	• 400–500°C • around 30 MPa.	• Cruce glycerol, soybean, and canola straw feedstocks • nickel-based catalysts • catalyst supports	[23, 81, 96, 122]
CEA/Université Grenoble Alpes	• Purchased (Top-Industrie SA) • 1.4571 stainless steel • 500 ml batch	• Up to 650°C • Up to 40 MPa.	• Nickel catalysts • Kraft black liqour and PET feedstocks • Integration with hydrothermal liquefaction	[51, 123, 124]
University of Birmingham	• Self-fabricated batch and continuous • 10 ml (batch) • tens of $ml\,min^{-1}$ (continuous) • Stainless steel 316	• 400–550°C • 23–28 MPa.	• coconut shell and microalgae feedstocks • homogeneous and heterogeneous catalysts	[55, 125–127]

3

Exploring Heating Strategy in SCWG Through a Quantitative Kinetic Modelling Approach

The inherently challenging nature of SCWG experimentation makes the collection of kinetic data particularly difficult, which by extension means all experimentally obtained information is highly valuable. The detailed kinetic model reproduced and improved in the following chapter is a prime example of the importance of such data. By accurately predicting the conversion of feedstocks, intermediates, and products over time, the model is a powerful tool which provides deep insights into SCWG processes and enables the investigation of many aspects of chemical reaction engineering with minimal physical experimentation necessary. Here, the model is applied to investigate biomass-specific relationships between sub-critical heating rates and the formation of syngas and char during SCWG.

3.1 Introduction

Figure 3.1 shows a schematic resembling a conceptualised, commercialised SCWG process [8]. To bring the process stream up to the desired SCWG reaction temperature, a pre-heater zone is utilised. Whilst its primary function is to

act as a heat exchanger, the pre-heater also represents a low-temperature, sub-critical reaction region where the initial degradation of biomass will commence. There is very little information available regarding how the operation of the pre-heater affects the overall production of syngas. Given that the purpose of the pre-heater is to provide a temperature change, the main user-changeable operating variable is the heating rate.

The commercialisation of SCWG is hindered by several key challenges including char formation, salt plugging/corrosion, and a high energy demand [2, 129, 130]. The limited but valuable experimental data available shows that heating rate can influence the transformation of biomass into syngas during SCWG [33, 34]. This work theorises that SCWG heating regimes could be tailored according to the composition of a specific biomass feedstock in order to enhance the formation of syngas, suppress char formation, and ultimately improve the economic viability of the process. In addition to the heating rate, non-linear heating profiles are also studied within this work to investigate if and how they can be used to optimise SCWG.

This chapter aims to holistically analyse the affect of operational heating rate and profile in the sub-critical region on the SCWG of biomass. The predicted yields of syngas species (CO, CO_2, CH_4 and H_2); the formation of char; and the generation of key intermediate compounds are used as key indicators of the process and are thoroughly analysed and discussed. The results provide a comprehensive guide for optimal SCWG operations to help tailor heating regimes based on the requirement of feedstock variation to maximise syngas production and process efficiency.

To conduct the systematic analysis of heating regime, an upgraded kinetic model based upon that of Yakaboylu et al. [36] was used. This model used 55 and 74 sub- and supercritical reactions, respectively, and characterises the wet biomass feedstock using four major constituent compounds: cellulose, hemicellulose, lignin, and protein. The modelling chapter to follow acts as a methodology where the kinetic model is first qualitatively described and then the modifications made

in this work are explicitly described and justified. The results section is divided into two sections to separately demonstrate the influence that sub-critical heating rate and profile has on SCWG.

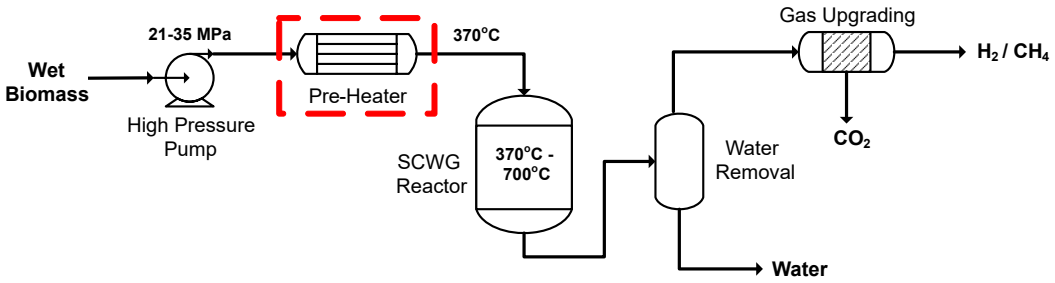

Figure 3.1: Schematic diagram showing the main unit operations in a continuous SCWG process.

3.2 Modelling Concepts and Development

The full kinetic model including Arrhenius parameters, molecule names, and reaction IDs is included in the Appendix A. Cellobiose, xylose, guaiacol, and aspartic acid are used in the model to represent the major organic constituents of wet biomass: cellulose, hemicellulose, lignin, and protein, respectively. In each case, the model compound is a primary hydrolysis product of the biomass component. The following subheadings describe the decomposition of the four model compounds as predicted by the kinetic model.

3.2.1 Cellulose

Glucose, erythrose, and glycolaldehyde are the main products formed from the primary hydrolysis of cellobiose, and are generated directly through reaction 3 or via a glucosyl intermediate in one of the two-step reactions, 1•ge.g or 2•gg.g. Glucose decomposes further into either erythrose (g.e) or one of four other secondary products: levoglucosan (g.a), 5-HMF (g.5), fructose (g.f), or glyceraldehyde (g.gly). Pyruvaldehyde is then formed from glyceraldehyde directly (gly.p)

or via dihydroxyacetone (`gly.dih•dih.p`). The intermediates formed thus far decompose into a mixture composed of predominantly acetic and lactic acid; with the former being produced from erythrose (`e.acid`), glycolaldehyde (`glyco.acid`), and levoglucosan (`a.acid`), and lactic acid being produced from fructose (`f.acid`) and pyruvaldehyde (`p.acid`). These simple organic compounds will either gasify directly or after undergoing further decomposition reactions. Acetic acid for example gasifies to CO_2 and CH_4 (`aa.ga`) in exclusively supercritical conditions, whilst formic acid will be gasified into a mixture of CO2, H_2, CO and H_2O (`fa.ga1` and `fa.ga2`) in both the sub- and supercritical region. Lactic acid decomposes via a pathway composed of 8 reactions and 3 intermediates (acyrlic acid, 3-HPA, and acetaldehyde) to produce 3 simple organic acids: acetic, propionic, and glycolic. In supercritical conditions, propionic and glycolic acid gasify to form mixtures of CO and H_2, and CO_2 and H_2, respectively Formaldehyde also gasifies in the supercritical region to produce CO and H_2 (`fal.ga`) whereas levulinic acid decomposes into a mixture of lactic acid and acetaldehyde (`levu.lacet`). Furfural is the only remaining simple organic in the cellulose decomposition mechanism. In sub-critical conditions, furfural decomposes via `fu.aa` into a mixture of acetic and acrylic acid, termed water-soluble humic species (WSHS). The stoichiometry of this reaction was not specified in the reference source hence the need to group this two species under the single moniker, WSHS. Under supercritical conidtions, WSHS can gasify into CO and H_2 (`aa.gas`), and char formation from furfural is also possible (`fu.ch`). The water-gas shift (WGS) reaction, which produces H_2 and CO_2 from CO and H_2O was the only "gas-phase" reaction included the model. The decomposition mechanism for cellulose is the most detailed of the four model compounds in wet biomass as it includes the most intermediates and reactions.

3.2.2 Hemicellulose

Xylose is a monomer unit and primary hydrolysis product of hemicellulose; it has a comparatively simpler decomposition pathway in the kinetic model compared

to cellulose. In sub-critical conditions, hemicellulose will decompose into furfural (`xy.fu`) and a mixture of glyceraldehyde and methyl formate. Like in the cellulose mechanism, furfural will produce WSHS (`fu.aa`) whereas glyceraldehyde will ultimately form lactic acid (`p.acid`) after decomposing into pyruvaldehyde (`gly.p` and `gly.dih•dih.p`). Under supercritical conditions, methyl formate decomposed into acetic acid (`mf.aa`); WSHS gasifies into CO and H_2 (`aa.gas`); and char formation can occur from furfural (`fu.ch`). Hemicellulose gasifies the most readily of the four biomass components, and it is expected to have high yields of H_2 and to achieve near-complete gasification [36].

3.2.3 Lignin

Lignin is the most complex of the three lignocellulosic materials and produces a wider distribution of products upon first decomposition. Guaiacol was selected as the lignin-representative model compound, which has also been done in other publications with the reasoning being that it has a similar structure and functional groups to lignin.

In sub-critical conditions, guaiacol forms diphenyl directly (`gu.t`) or via catechol and oCresol. Diphenyl can react to form phenol (`t.p`), benzene (`t.b`), char (`t.ch`) or gas (`t.ga`). Guaiacol can also gasify directly in sub-critical conditions (`gu.ga`) or form benzene (`gu.b`) which will go onto produce char (b.ch). In supercritical conditions, benzene can also gasify (`b.ga`), produce phenol (`b.p`), or form naphthalene (`b.na`) which will subsequently form char (`na.ch`). Phenol can also form catechol (`p.c`), gasify (`p.ga`), or form char (`p.ch`) in supercritical conditions.

Due to a lack of data available, the stoichiometry of the gas forming reactions in the lignin decomposition pathway were determined using a Gibbs free energy minimisation (GM) calculation (i.e. thermodynamically) by defining a pre-defined list of gas products: CO, CO_2, CH_4, H_2, N_2, NH_3.

3.2.4 Protein

Protein is modelled on albumin because extensive research has been carried out using it as a model protein [36]. Aspartic acid was chosen as the model compound for protein because its decomposition products, alanine and glycine, are common amino acids obtained from the hydrolysis of albumin.

In the sub-critical region, protein will decompose into alanine (`as.a`) and glycine (`as.g`) and produce acetic acid, propionic acid and char as by-products. These amino acids decompose into ethylamine (`al.et`) and methylamine (`g.met`), respectively, with lactic acid, glycolic acid, NH_3, and CO_2 produced as side-products. In supercritical conditions, the amino acids can gasify directly (`al gas`) and (`g.gas`), or they will form amines which gasify (`et.gas`) and (`met.gas`). Similarly to lignin, in each reaction where direct gasification occurs the stoichiometry is calculated using a GM calculation.

3.2.5 Modifications and Developments

The model reported by Yakaboylu et al. [36] was able to reproduce the carbon gasification efficiency of biomass, however there is a notable disparity in the under-predictions of the yields of H_2, and overprediction of CH_4. It was suggested that these inaccuracies were likely due to incorrect lignin gasification stoichiometries. Given that the biomass mixture of wood sawdust and carboxymethylcellulose (CMC) used for lignocellulosic validation is composed mainly of cellulose, it is unlikely that the disparity in H_2 and CH_4 yields can be attributed solely to inaccurate lignin gasification stoichiometry. This work also considers the possibility that the main source of error is from the cellulose decomposition mechanism.

Acetic acid is a key intermediate during the SCWG of cellulose which is formed via five separate pathways from molecules including erythrose and levoglucosan. Acetic acid gasifies directly via only one route in the global mechanism (`aa.ga`) to form CO_2 and CH_4. On the other hand, formic acid is produced from the decomposition of 5-HMF (`5.lf`) only and will gasify directly to produce CO_2, CO

and H_2 (`fa.ga1`, `fa.ga2`). It is therefore theorised that the kinetic model over and underpredicts the formation of acetic and formic acids, respectively, which subsequently causes inaccurate yields of CH_4 and H_2.

The basis for this hypothesis comes from the experiments of Kabymela et al.[131]. Despite detecting both formic and acetic acids from the hydrothermal decomposition of these two intermediates, only acetic acid was included as a product in the reference model. Excluding formic acid as a product from these reactions was possibly due to the uncertainty in reaction stoichiometry, which is not yet well understood [132]. It is well known that of both formic acid and acetic acids are major products from the hydrothermal decomposition of erythrose, levoglucosan, and other cellulitic materials [131–133].

To further improve the kinetic model and allow for formic acid production from erythrose and levoglucosan, the reactions `e.acid` and `a.acid` were modified as shown in Table 3.1

Table 3.1: Updated kinetic model reactions

Reaction	Reference Model	This Work
`e.acid`	$C_4H_8O_4 \rightarrow 2C_2H_4O_2$	$C_4H_8O_4 + 2H_2O \rightarrow C_2H_4O_2 + 2CH_2O_2 + (4H)$
`a.acid`	$C_6H_{10}O_5 + H_2O \rightarrow 3C_2H_4O_2$	$C_6H_{10}O_5 + 3H_2O \rightarrow 2C_2H_4O_2 + 2CH_2O_2 + (4H)$

Due to ambiguity in the mechanism, the new stoichiometries of `e.acid` and `a.acid` were estimated to give roughly equal yields of formic and acetic acid. It was also necessary to balance the equation using H atoms on the product side of both reactions.

Another modification to the model related to the Arrhenius parameters for xylose decomposition reactions. Yakaboylu et al. [36] cites Qi and Xiuyang [134] as the source of activation energies and pre-exponential factors for xylose decomposition in the reference model. However, a discrepancy exists in the Arrhenius parameters listed by the two authors - as shown in Table 3.2. The reference model kinetic data predicts xylose to be very resistant to decomposition in the sub-critical region, with only 2 mol.% conversion achieved under normal

Table 3.2: Arrhenius parameters for hemicellulose decomposition in sub-critical water

	Qi and Xiuyang [134]		Yakaboylu et al. [36]	
	Activation Energy, E_a ($\mathrm{kJ\,mol^{-1}}$)	Pre-Exponential Factor, A ($\mathrm{s^{-1}}$)	Activation Energy, E_a ($\mathrm{kJ\,mol^{-1}}$)	Pre-Exponential Factor, A ($\mathrm{s^{-1}}$)
`xy.fu`	111.47	2.26×10^{10}	76.6	1230
`xy.gm`	143.14	5.03×10^{13}	153.8	7.38×10^{8}
`fu.aa`	58.84	1.19×10^{5}	24.2	2.95×10^{-14}

operating conditions. This is in disagreement with the work of Qi and Xiuyang [134], who observed 95.8 % conversion of xylose after 50 min at 220°C. Other works have also demonstrated that xylose behaves similarly to glucose under hydrothermal conditions [9]. The results of this work show the model to predict that glucose decomposes readily in supercritical conditions, and thus it is expected that xylose would to. The kinetic model of this work was therefore updated to use the kinetic data from Qi and Xiuyang [134] as it produced an expected, gradual conversion xylose into furfural, glyceraldehyde, and methyl formate in the sub-critical reactor.

3.2.6 Simulation Approach

The SCWG process presented on Fig. 3.1 was emulated using three plug-flow reactors in series.

Labelled on Fig. 4.2 as `SUB-HEX`, `SUP-HEX`, and `SUP-RCT`, these reactors simulate (i) sub-critical reactions while linearly heating the process stream from 25°C to 374°C in 300 sec , (ii) supercritical reactions while linearly heating from 374°C to the target temperature (500°C or 600°C) in 20 sec , and (iii) supercritical reactions while holding at the target temperature for 60 sec , respectively.

The report focuses exclusively on the effect of sub-critical heating, and thus changes were made to the `SUB-HEX` reactor only. The benchmark `SUB-HEX` residence time of 300 sec corresponds to a heating rate of 69 $^{\circ}\mathrm{C\,min^{-1}}$; this was decreased and increased by an order of magnitude to 6.9 and 690 $^{\circ}\mathrm{C\,min^{-1}}$ to reveal how

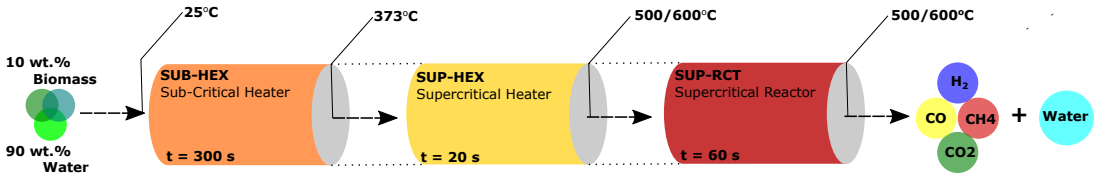

Figure 3.2: The configuration of reactors used in simulations

slower and faster heating rates in SUB-HEX affect the overall transformation of biomass into syngas. Additionally, non-linear sub-critical heating profiles were also investigated. The accelerating and decelerating profiles shown on Fig. 3.3 were also tested having been reproduced from Yakabolyu et al.[36]. A decelerating profile is a common feature of heating water into the supercritical region as heat transfer properties tend to deteriorate, particularly at temperatures approaching the critical point [135]. This is partly attributed to the heat capacity of water which increases exponentially as temperatures rise from 300°C to 374°C [136]. Temperature is widely considered the most important SCWG variable, and thus two final reaction temperatures of 500°C and 600°C are presented for each result to demonstrate how the effect of sub-critical heating rate is altered by reaction temperature.

The decomposition of a feedstock(s) via a network of more than one reaction is mathematically consistent with a series of ordinary differential equations (ODEs) that can be solved as an initial value problem (IVP). Here, the kinetic model was solved in Python using the *scipy.integrate.solve_ivp* package [137]. Source code for the script used to solve the kinetic model is available from mjksill/ReactionNetworks.git [1] This particular package allows the user to choose from a variety of different integration methods to solve the IVP; here the LSODA method was selected as it is a good universal option. [REF]

Similarly to Yakaboylu et al [36], three plug-flow reactors in series were used to emulate the reactions of a real-world, continuous SCWG plant. A standard feedstock of 1000 kg h^{-1}, 10 wt.% biomass was used. Whilst the kinetic model is unaffected by changes to feedstock concentration as water is a zero-order

[1] https://github.com/mjksill/ReactionNetworks

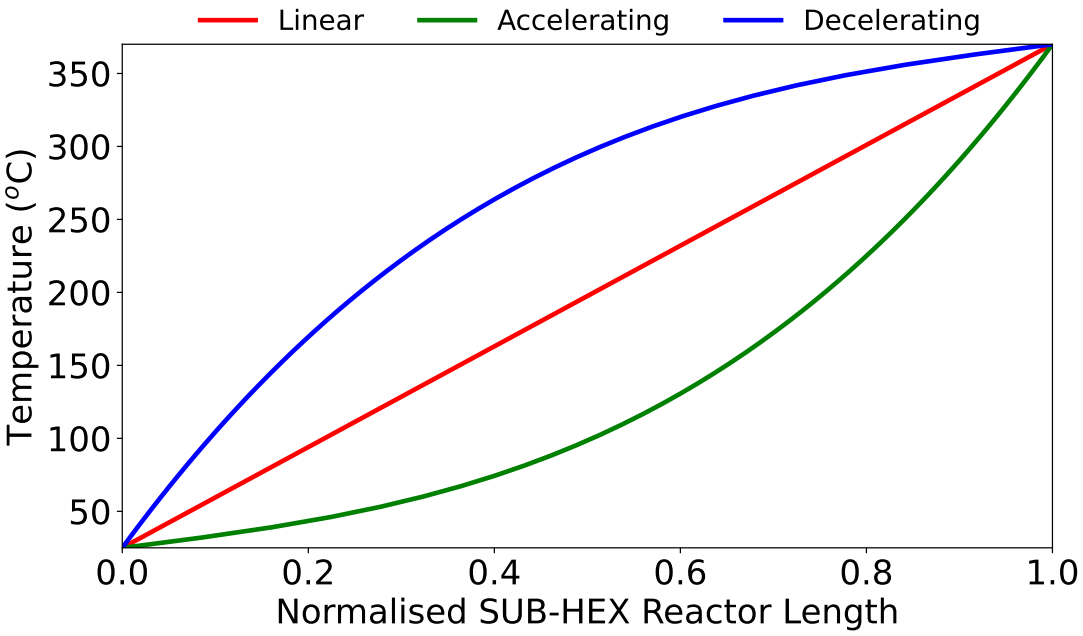

Figure 3.3: The different `SUB-HEX` heating profiles studied.

reagent, simulations using greater concentrations of biomass would not be valid as the kinetic data was obtained from experiments using 90 wt.% water or higher. Similarly, the kinetic model operates independently of pressure, but is assumed to be accurate in the range of 25 to 30 MPa [36].

The carbon gasification efficiency (CGE) is a useful indicator for the evaluating the efficacy of a gasification process. It denoted the conversion efficiency of biomass carbon into gas species carbon (i.e., CO, CO_2, and CH_4), and is calculated as shown in Eq. 3.1.

$$\text{CGE}(\%) = 100 \cdot \left(\frac{n_{CO} + n_{CO_2} + n_{CH_4}}{n_{\text{feed}}} \right) \tag{3.1}$$

where n_i is the moles of carbon in species i.

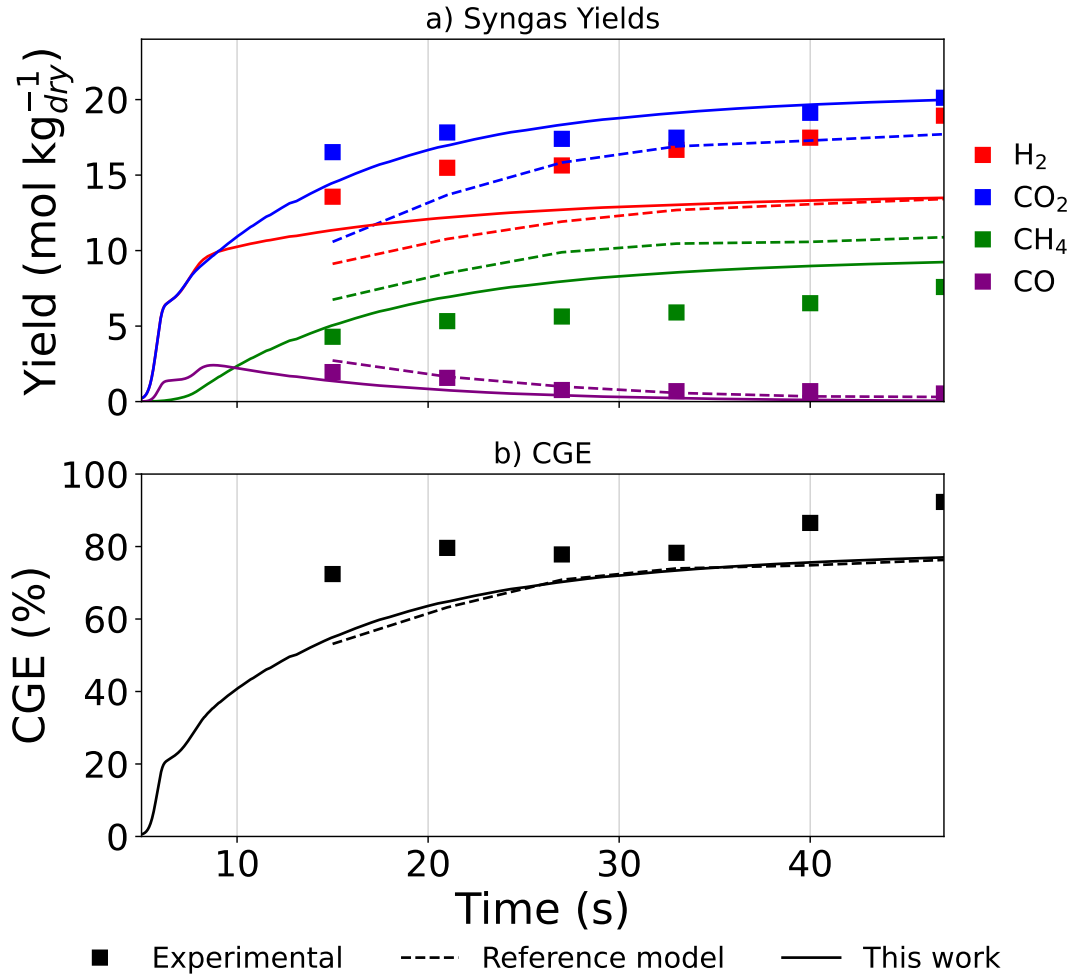

Figure 3.4: Validation results for lignocellulosic biomass including experimental data [25], the reference model [36], and the results of this work.

3.3 Results and Discussion

3.3.1 Advances and validation of the updated kinetic model

Lignocellulosic Biomass

Validation of the kinetic model for lignocellulosic biomass (i.e., cellulose, hemicellulose, and lignin only) was completed using the experimental data of Lu et al.[25]. The residence times and heating conditions were not explicitly stated by Lu et al., but they were estimated based upon the high CGEs achieved [36]. Using the same configuration of reactors presented in Fig. 3.1, a 4 wt.%$_{dry}$ sawdust feedstock was linearly heated across 5 sec from 25°C to 370°C in `SUB-HEX`; linearly

heated further to 650°C in 3 sec in SUP-HEX; and held at 650°C for a further 39 sec . The sawdust was modelled using 74.75 wt.%$_{dry}$ cellulose, 11.75 wt.%$_{dry}$ hemicellulose, and 13.25 wt.%$_{dry}$ lignin [36].

Figure 3.4 presents the results for the validation of lignocellulosic biomass. The yields of H_2, CO_2, CH_4, and CO are plotted on Fig. 3.4a and the CGE on Fig. 3.4b. The graphs show the experimental results of Lu et al., the Yakaboylu et al. model, and the model of this work. The error between experimental and modelling results for the final gas phase composition was calculated. For CO_2 and CH_4, the model of this paper reduced the error from 12 % to 0.5 % and 43 % to 22 %, respectively, versus the Yakaboylu et al. model. The error in H_2 yield was maintained at roughly 29 %, and the CGE error reduced marginally from 17 % to 16 %. Overall, it can be concluded that the kinetic model has been successfully validated for lignocellulosic biomass, and the updates improve the accuracy of gas yield predictions.

Protein-Containing Biomass

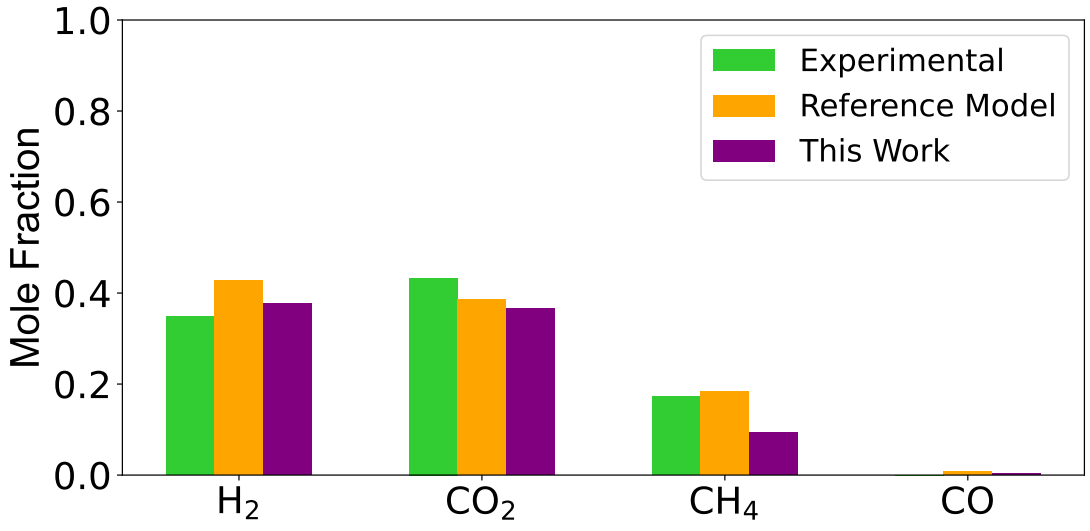

Figure 3.5: Validation results for protein-containing biomass.

A separate experimental study was used to validate the model for protein-containing biomass. Nakmamara et al. [138] conducted a liquefaction-gasification type treatment of a 1.97 wt.%$_{dry}$ chicken manure feedstock. The composition of

the dry biomass was based upon data provided by the *Phyllis* [139] database; and was modelled as 12.00 wt.%$_{dry}$ cellulose, 8.76 wt.%$_{dry}$ hemicellulose, 12.14 wt.%$_{dry}$ lignin, and 43.10 wt.%$_{dry}$ protein [36]. Fig. 3.5 shows the experimental syngas yields from Nakmamara et al. [138]; and those predicted by the models of Yakaboylu et al.[36] and this work.

Figure 3.5, which plots mole fractions (dry) of the product gas shows that generally the model predicts the SCWG of protein-containing biomass well. There are deviations between the experimental results and the gas yields predicted by both models. The model of this work was able to improve the estimation accuracy for H_2 yields, but it worsened it for CO_2 and CH_4. This error can likely be attributed to the GM calculation which was used to obtain the gasification stoichiometry for protein. Overall, there is good agreement between the experimental data and results of this model.

3.3.2 The Effect of Heating Rate

Syngas Yields and CGE

Figure 3.6 shows how sub-critical heating rate influences the yields of syngas and the CGE during the SCWG of cellulose, hemicellulose, lignin, and protein. There are clustered bar plots for each syngas species which are plotted on the left y-axis, plus the CGE plotted on the right y-axis. Three sub-critical heating rates of 690, 69, and 6.9 °C min^{-1} are presented for each of the aforementioned values, and also two different cases for final reaction temperature are shown. This is to illustrate how the product composition is affected differently by sub-critical heating rate depending on whether low temperature (500°C) or high temperature (600°C) gasification is being conducted. To demonstrate the affect of sub-critical heating rate on CO yield, as opposed to plotting the final product composition, Fig. 3.6 plots the maximum observed yields of each syngas species and the CGE. For all species bar CO, the maximum yield is equivalent to the final product composition as the kinetic model does not include reactions which consume them.

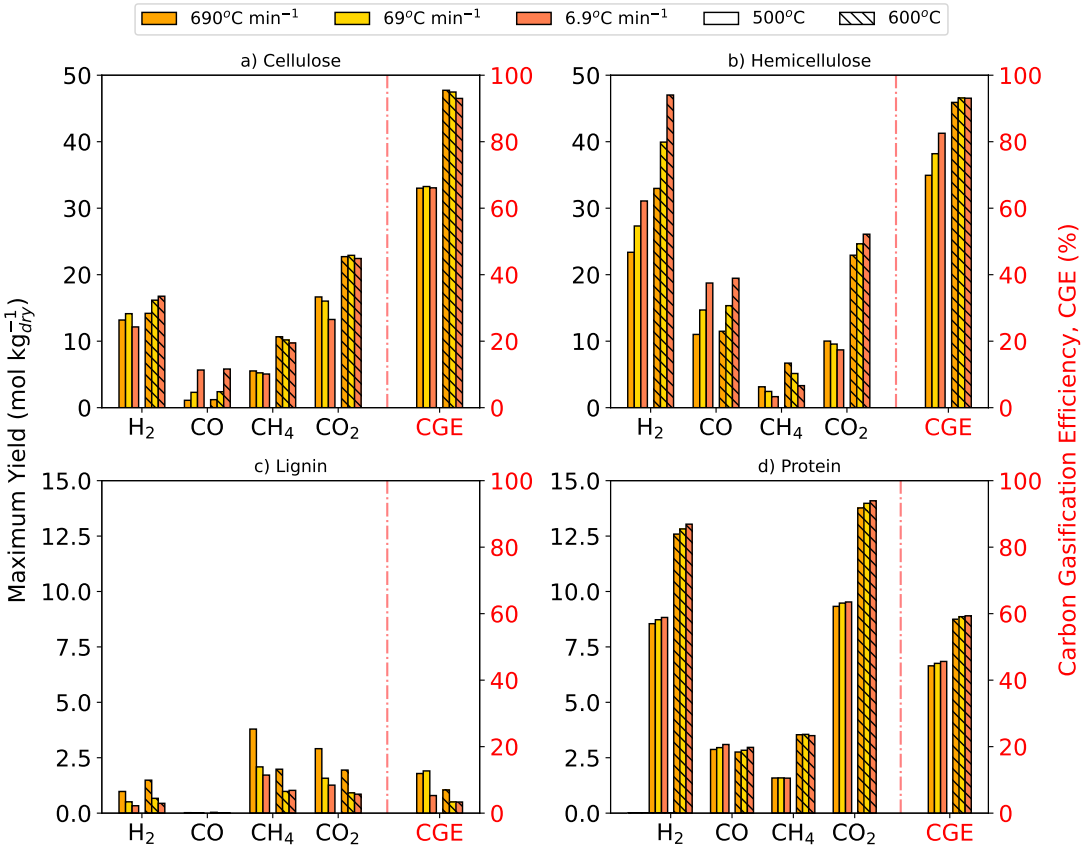

Figure 3.6: Syngas yields and CGEs from the SCWG of 10 wt.% a) cellulose, b) hemicellulose, c) lignin, and d) protein at 500°C and 600°C with linear `SUB-HEX` heating rates of 690, 69, and 6.9 °C min^{-1}.

However, CO is consumed via the only gas-phase reaction included in the model, the water-gas shift reaction, and thus to demonstrate how sub-critical heating rate affects its generation, it is necessary to plot its yield prior to consumption at the instance when it is highest.

The results for cellulose are shown in Fig. 3.6a. The yield of H_2 is negligibly affected by heating rate in the 500°C case, however, it can be seen that at 600°C slowing the heating rate from 690 to 6.9 °C min^{-1} correlated with an increase in H_2 yield from 14.2 to 16.8 mol kg$_{dry}^{-1}$. The maximum yield of CO also increased steadily as heating rate was slowed in both temperature cases. The yields of CH_4 and CO_2 from the SCWG of cellulose are also largely unaffected by changes to the sub-critical heating rate, with the exception being a reduction in CO_2 yield from

16.7 to 13.4 mol kg_{dry}^{-1} as the heating rate is slowed in the 500°C case. Moreover, sub-critical heating rate was demonstrated to produce little change in the CGE, though slowing the heating rate at 600°C did reduce the CGE from 95.5 % to 93 %. It can be concluded from Fig. 3.6a that the SCWG of cellulose is most significantly governed by reaction temperature, however, a discernible increase to H_2 yield can be achieved by slowing the sub-critical heating rate.

Figure 3.6b clearly shows that a far greater correlation exists between the SCWG of hemicellulose and the sub-critical heating rate. Yields of H_2 increase drastically as the heating rate is slowed from 690 to 6.9 °C min^{-1}. Notably, in the 600°C case the H_2 yield increased by over 42 % from 33.0 to 47.0 mol kg_{dry}^{-1} as the heating rate was slowed from 690 to 6.9 °C min^{-1}. A steady increase and decrease in the yields of CO and CH_4, respectively, was also observed for the same change to heating rate. Similarly to cellulose, slowing the heating rate in the 500°C case appears to decrease yields of CO_2; however, the converse of this happens at 600°C. Figure 3.6b also indicates that whilst the CGE from the SCWG of hemicellulose is largely unaffected by sub-critical heating rate at 600°C, in the 500°C case a slower heating rate can be used to increase the CGE. In all, the results here suggest that the SCWG of high-hemicellulose, wet biomass wastes (e.g., brewing wastes [139]) could be optimised by slowing the sub-critical heating rate to expedite H_2 production.

Figure 3.6c indicates that lignin achieves a far lower CGE compared to cellulose and hemicellulose, and that slowing the heating rate reduces the CGE and yields of all syngas species. Protein gasifies more readily than lignin, reaching a CGE of nearly 60 % at 500°C, however, it is shown on Fig. 3.6d how temperature is a much more important variable and sub-heating rate has a negligible effect on the CGE and yields of all syngas species from the SCWG of protein.

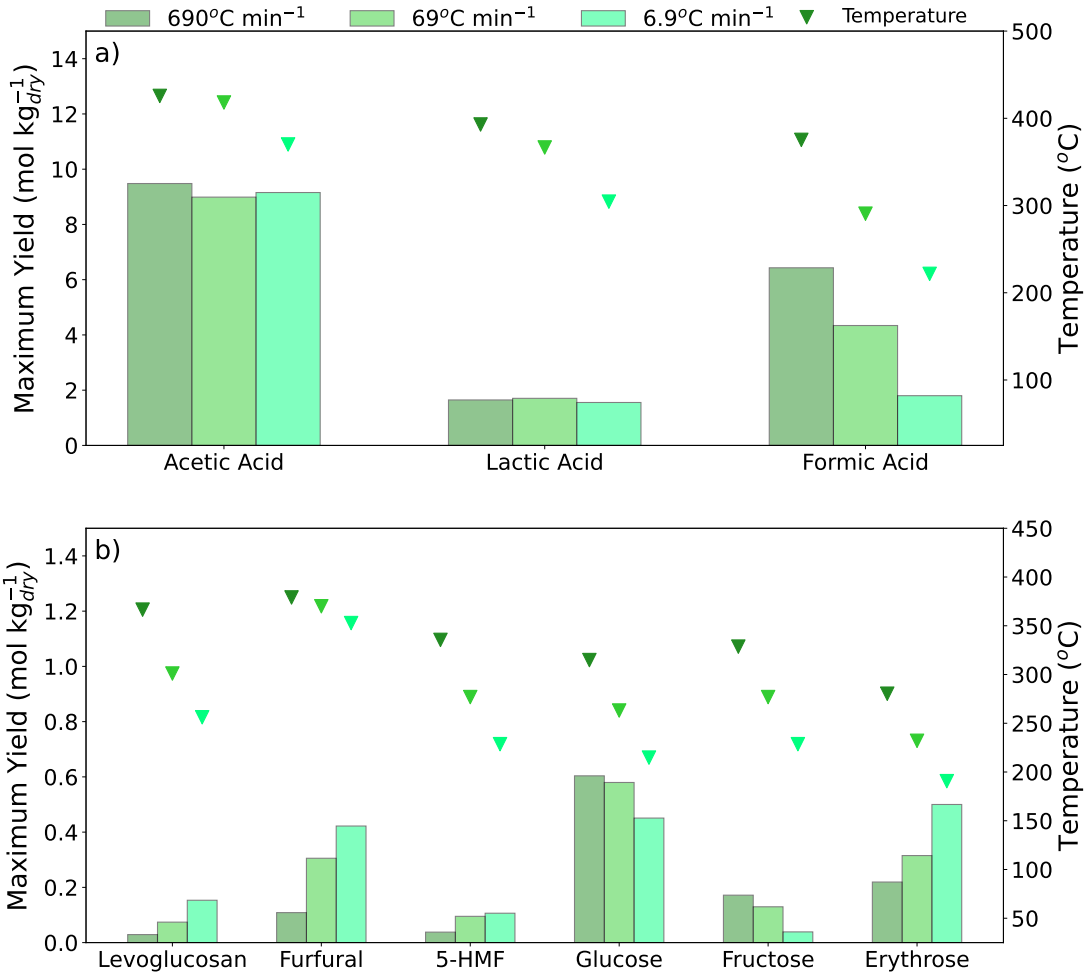

Figure 3.7: Maximum yields of intermediates formed during the SCWG of cellulose with linear SUB-HEX heating rates of 690, 69, and 6.9 °C min^{-1}.

Intermediate Compounds

Figure 3.7 indicates how intermediate species produced during the hydrothermal decomposition of cellulose are affected by changes to sub-critical heating rate. Since the intermediate species are consumed, yields of each species presented are plotted at the instance when they are highest. Moreover, the right-hand axis shows plots the temperature at which the maximum yield occurs, to indicate how this is affected by heating rate. Not all intermediates are presented on Fig. 3.7, only those that occur in non-trace amounts. Figure 3.7a shows that acetic, lactic, and formic acid are the most prolifically formed intermediates from the SCWG

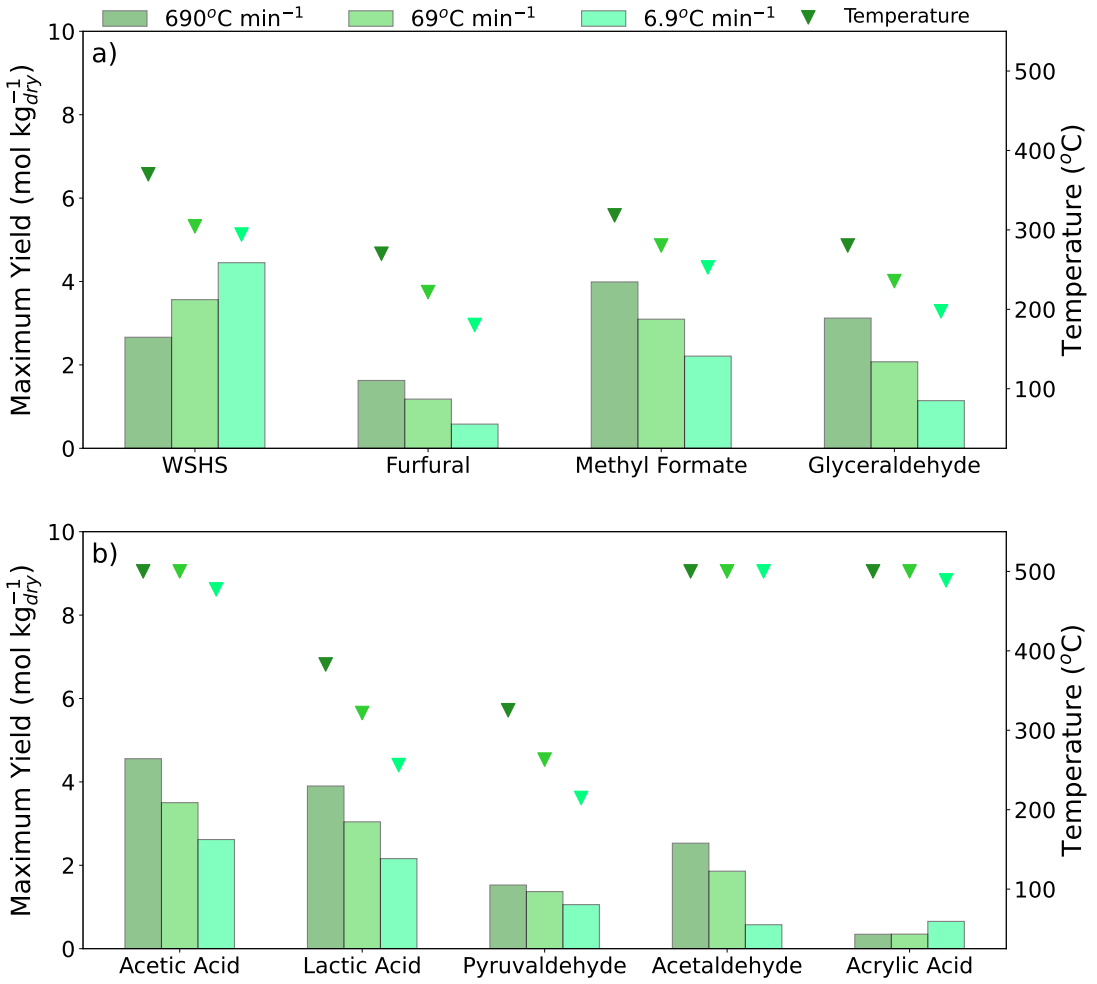

Figure 3.8: Maximum yields of intermediates formed during the SCWG of hemicellulose with linear `SUB-HEX` heating rates of 690, 69, and 6.9 °C min^{-1}.

of cellulose. Both the yields of acetic and lactic acid are mainly unaffected by changes to sub-critical heating rate, whilst the yield of formic acid reduces as the heating rate is slowed. For all three species on Fig. 3.7a, slowing the heating rate reduces the maximum yield temperature.

Figure 3.8a shows that furfural, methyl formate, and glyceraldehyde all decrease in yield as the heating rate is slowed, whilst the maximum yield of WSHS increases. Additionally, slowing the sub-critical rate reduces the temperature at which the maximum yield of all species on Fig. 3.7a occur. Figure 3.8b indicates that the formation of acetic and lactic acids is more sensitive to heating rate

from a hemicellulose feedstock than what was observed for cellulose. These two species, alongside acetaldehyde, steadily decrease in yield as the heating rate is slowed. Figure 3.8b also shows that the peak yield temperature of lactic acid and pyruvaldehyde are particularly affected by `SUB-HEX` heating rate, as it is shown that slower heating rates can be used to generate these species at lower temperatures. The peak yield temperatures of acetic and acrylic acid, and acetaldehyde are less affected by heating rate which means the production of these species is dependent on reaching higher temperatures approaching 374°C at the end of `SUB-HEX`.

The intermediate compounds formed during the SCWG of lignin and protein were also studied, however, little effect was observed.

Char Formation

Figure 3.9 plots the total char formation for lignin and protein at sub-critical heating rates of 690, 69, and 6.9 °C min^{-1}, with two cases of final reaction temperature, 500°C and 600°C, are presented. The formation of char is plotted as a dry mass percentage versus total reaction time, and the reaction temperature is also plotted on the opposite y-axis. The time-scales (x-axis) of Figures 3.9a through c is varied to ignore regions where no char formation occurs. Whilst char can be formed from cellulose and hemicellulose via a furfural intermediate (`fu.ch`), the generation of char from these biomass components is negligible in comparison to lignin and protein, and thus they were not discussed in this subsection.

The occurrence of char during the hydrothermal decomposition of protein is accounted for by a single reaction in the kinetic model, `as.g`, where aspartic acid is converted into glycine. Figure 3.9 shows that the quantity of char produced from protein is unaffected by final reaction temperature, as the 500°C and 600°C plots are superimposed on top of each other. A marginal reduction to char yield can be made by slowing the heating rate, as the final dry mass fraction of char from protein decreased from 38.2 % to 37.3 % to 36.5 % as the heating rate was slowed from 690 though to 69 and 6.9 °C min^{-1}. Figure 3.9a shows that with a heating rate of

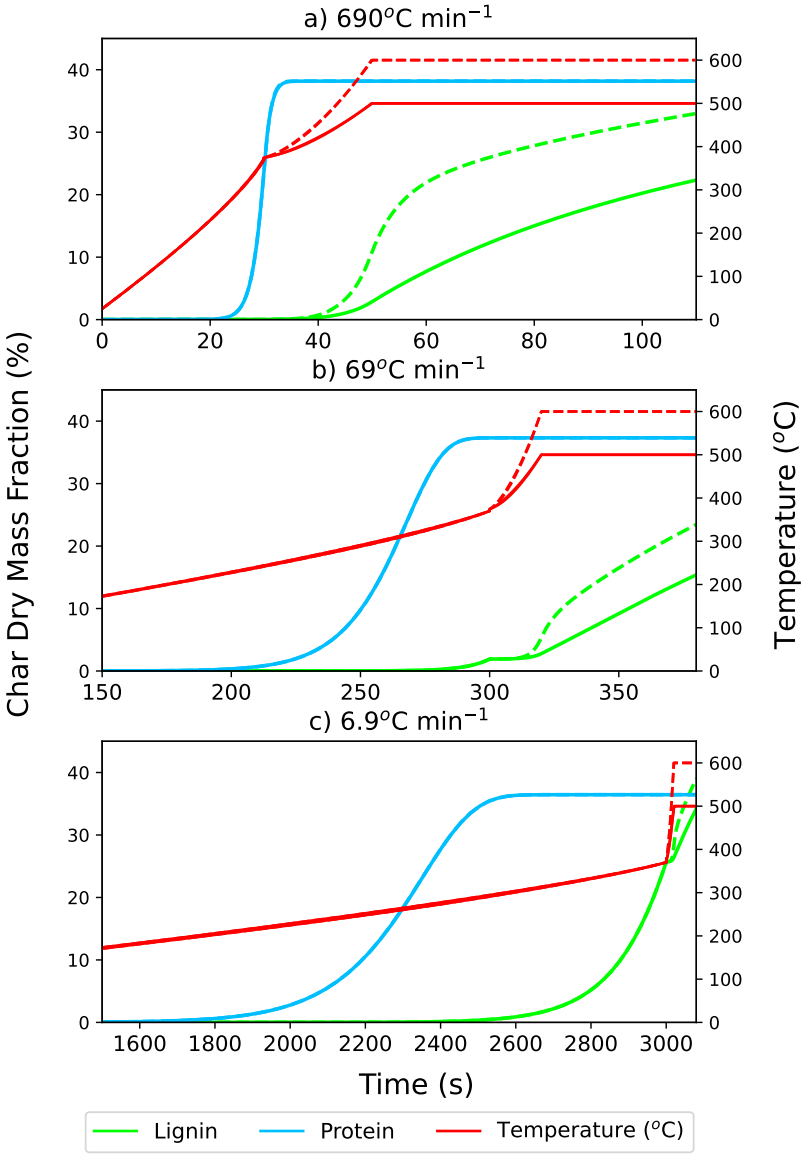

Figure 3.9: Total dry mass fraction of lignin and protein derived char, and temperature, versus reaction time at linear sub-critical heating rates of 690, 69, and 6.9 °C min^{-1}. Final reaction temperatures of 500°C (solid) and 600°C (dashed)

690 °C min^{-1} a maximum yield of char from protein is achieved at a temperature of around 390°C; Figs. 3.9b and 3.9b show that this peak yield temperature reduces to around 375°C and 320°C as the heating rate is slowed to 69, and 6.9 °C min^{-1}, respectively. This demonstrates that char formation from protein occurs almost exclusively in the sub-critical region for the operating conditions tested, and explains why no discrepancy was observed between the 500°C and 600°C cases.

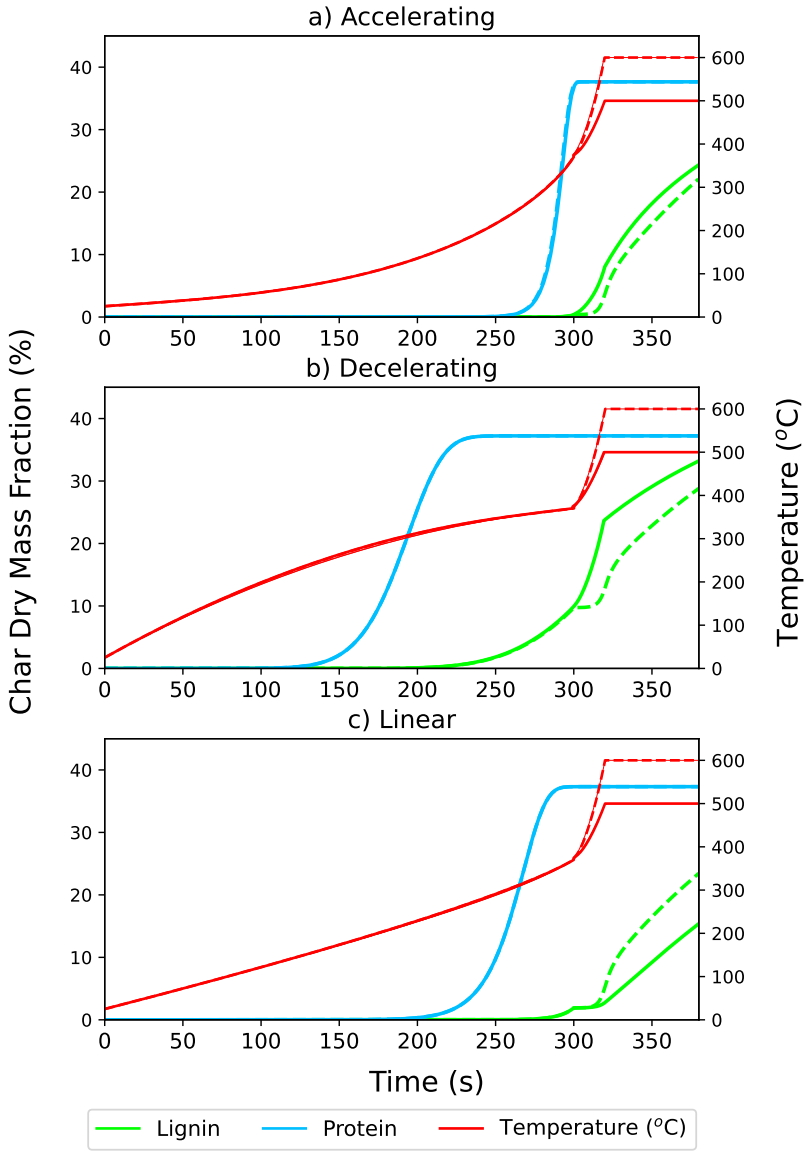

Figure 3.10: Total dry mass fraction of lignin and protein derived char, and temperature, versus reaction time at an accelerating, decelerating, and linear sub-critical heating rate 69 °C min^{-1}. Final reaction temperatures of 500°C (solid) and 600°C (dashed)

The formation of char from lignin is far more complex in the kinetic model with contributions coming from five precursor molecules. benzene (`b.ch`), diphenyl (`t.ch`), guaiacol (`gu.ch`), napthalene (`na.ch`), and phenol (`p.ch`). Figure 3.9a shows that with a fast sub-critical heating rate of 690 °C min^{-1}, in the 600°C case the total formation of char increases rapidly as temperatures surpass the

critical point and then steadily increase to a dry mass percentage of 33.0 %. At 500°C, the rise in char formation also commences in the supercritical region but occurs less abruptly and reaches a smaller total dry mass fraction of 22.3 %. When the sub-critical heating rate is slowed to 69 °C min^{-1}, Fig. 3.9b again shows that char formation in notable quantities only occurs once supercritical conditions are met. At both 500°C and 600°C, the increase in dry mass fraction of lignin-derived char is less abrupt in comparison to the faster, 690 °C min^{-1} scenario; additionally, smaller final dry mass fractions of 15.4 % and 23.4 %, respectively, are achieved for the two temperature cases. Figure 3.9c interestingly shows that slowing the heating rate further to 6.9 °C min^{-1} promotes the formation of char in the sub-critical region in notable quantities, with a total char dry mass fraction of over 25 % occurring after 3000 sec at the end of the sub-critical zone. This slowest heating rate resulted in the greatest yield of char of all the heating rates studied, with final dry mass fractions of 39.1 % and 34.2 % char being reached for the 500°C and 600°C cases, respectively.

3.3.3 The Effect of Heating Profile

Syngas Yields and CGE

Figure 3.11 shows how the yields of syngas species from each biomass component are affected by changes to the sub-critical heating profile at a fixed heating rate of 69 °C min^{-1}. Both Fig. 3.11a and 3.11b show very clearly that the CGE and yield of syngas from the SCWG of cellulose and hemicellulose, respectively, are largely unaffected by changes to heating profile at reaction temperatures of 500°C and 600°C. Figure 3.11d similarly shows that sub-critical heating profile appears to have no influence on the SCWG of protein. Lignin was the only biomass component to demonstrate any dependence between syngas yields and heating profile. Figure 3.11c suggests that at 500°C an accelerating profile favours a greater yield of CH_4 and CO_2, whilst the CGE is highest with a linear heating at 500°C.

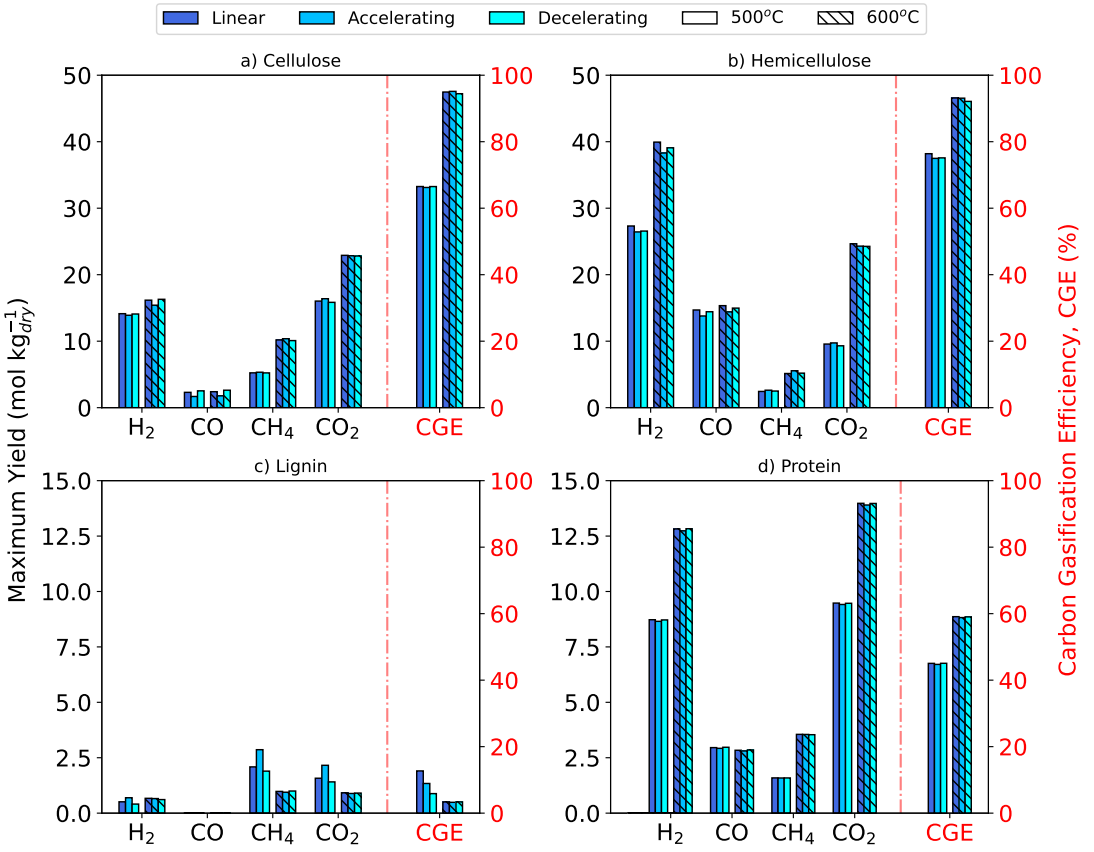

Figure 3.11: Syngas yields and CGEs from the SCWG of 10 wt.% a) cellulose, b) hemicellulose, c) lignin, and d) protein at 500°C and 600°C with linear, accelerating, and decelerating 69 °C min^{-1} `SUB-HEX` heating rates.

Char Formation

Figure 3.9 shows that the formation of char from protein occurred exclusively in sub-critical conditions for the three heating profiles studied and a fixed heating rate of 69 °C min^{-1}, meaning no difference in result was observed between the 500°C and 600°C cases. There was also no significant effect of heating profile on the final yield of char from protein, with the dry mass fraction plateauing at around 37 % on all three Fig. 3.9 plots. The maximum protein char yield was reached at a shorter residence time when using the decelerating profile as it reaches temperatures necessary for char formation sooner. The effect of heating profile on char formation was also studied at heating rates of 6.9 °C min^{-1} and 690 °C min^{-1} - see Appendix A. Again, the only noteworthy influence was that the decelerating

profile reduces the time required to reach the maximum char yield, although this effect was minimised at the faster heating rate of 690 °C min^{-1}.

Figure 3.9a shows that when using an accelerating profile, a greater yield of lignin-derived char is achieved at 500°C (22.4 %) case than 600°C(22.1 %). The same effect is presented on Fig. 3.9b for the decelerating profile with final char dry mass fractions of 33.2 % and 28.8 % being reached at 500°C and 600°C, respectively. Whilst the linear profile yields the lowest overall amount of char from lignin (15.4 % and 23.4 %), the results presented on Fig. 3.9 demonstrate that heating profile can be used to adjust the yield of char depending on the reaction temperature. This however was not the case for heating rates of 690 and 6.9 °C min^{-1} (see Appendix A), where neither the decelerating nor the accelerating heating profile produced greater yields of char at 500°C.

3.4 Conclusions

This work has successfully further advanced a detailed kinetic model and used it to investigate how the heating rate and profile in sub-critical conditions can be used to enhance syngas yields and mitigate char formation from the SCWG of four major constituent species in real-world wet biomass: cellulose, hemicellulose, lignin, and protein.

The heating rate was found to most significantly affect the SCWG of hemicellulose where at both 500°C and 600°C slower sub-critical heating rates increased H_2 yields. Longer sub-critical residence times were also found to increase the CGE in the 500°C case. Cellulose is less sensitive to heating rate, however, slower heating rates were found to marginally increase H_2 yields at 600°C. Faster heating rates generally increased gas yields from the SCWG of lignin. Studying char formation from lignin revealed that using too slow a heating rate can lead to sub-critical char formation which results in a greater overall yield of char. However, using unnecessarily fast heating rates also lead to an increase in char yield. Determining an optimal sub-critical heating rate that minimises char formation based upon

the composition of the biomass feedstock should be considered in future work. Heating rate was found to have no overtly obvious effect on the final yield of syngas species or char from the SCWG of protein.

For the heating profiles studied in this work, the only obvious influence of this operating parameter was that the decelerating heating profile was found to increase the formation of char from the SCWG of lignin.

4

Mechanistic Insights into SCWG: A Kinetic Sensitivity Approach for Optimising End- and Intermediate products

It has been demonstrated in relevant literature that there is a good macroscopic understanding of how the key SCWG operating variables, such as temperature, residence time, and feedstock concentration, influence the product distribution from biomass gasification in SCW. For example, lower feedstock concentrations increase H_2 yields, higher temperatures reduce CH_4 yields, and as it is now hypothesised from the findings of the previous chapter, faster sub-critical heating rates increase yields of H_2 from the SCWG of hemicellulose, and so forth.

The detailed kinetic model described in Chapt. 3 was used with great effect to investigate how heating regimes in the sub-critical regime alter product yields from the SCWG of individual biomass constituents. The model was validated against experimental data and thus there is confidence that it is sufficiently accurate. However, the kinetic model contains numerous reactions and many input variables, namely rate constants which themselves are a function of temperature, activation

energies, and pre-exponential factors. Whilst this degree of complexity is necessary to describe biomass gasification kinetics in SCW, an unavoidable consequence of this is that it is more challenging to pinpoint the causal effect on the observed outputs of the kinetic model. In essence, it is difficult to say *why* - using the Chapt. 3 example again - a faster heating rate at temperatures from 25°C to 374°C increases H_2 yields from hemicellulose gasification in SCW.

A sensitivity analysis describes any approach used to ascertain the influence an input variable has on the response of an output variable [140]. In chemical kinetics, this is typically employed to study the influence reaction rates have on the formation of species of interest and then rank the reactions based on how significantly they govern a chosen output variable [141]. There are numerous practical applications of sensitivity analysis in chemical reaction engineering. Those highlighted by Turányi [142] include model reduction, where unimportant reactions in a mechanism can be removed from a model; the identification of rate-limiting reactions, which could be expedited to increase overall conversion of a chemical process; and honing in on weak areas of the reaction network (in terms of accuracy) and require improvement for the betterment of the model.

The aim of this chapter was to present and implement a methodology that could be used to determine the sensitivity of reaction rates on the formation of any species in the global SCWG mechanism. This chapter considers only examples using cellulose as a feedstock. A major component of most forms of biomass, cellulose is both a good representative molecule for biomass in general, but it also has the most complex decomposition mechanism in the kinetic model meaning there is more uncertainty in relation to the major pathways which govern decomposition and gasification. The full reaction network for cellulose is listed in Appendix A, however, Fig.4.1 has been produced for this chapter to aid with the discussion. Reactions that occur exclusively in supercritical conditions (as opposed to sub-critical ones) are demarcated on Fig. 4.1 using red reaction arrows.

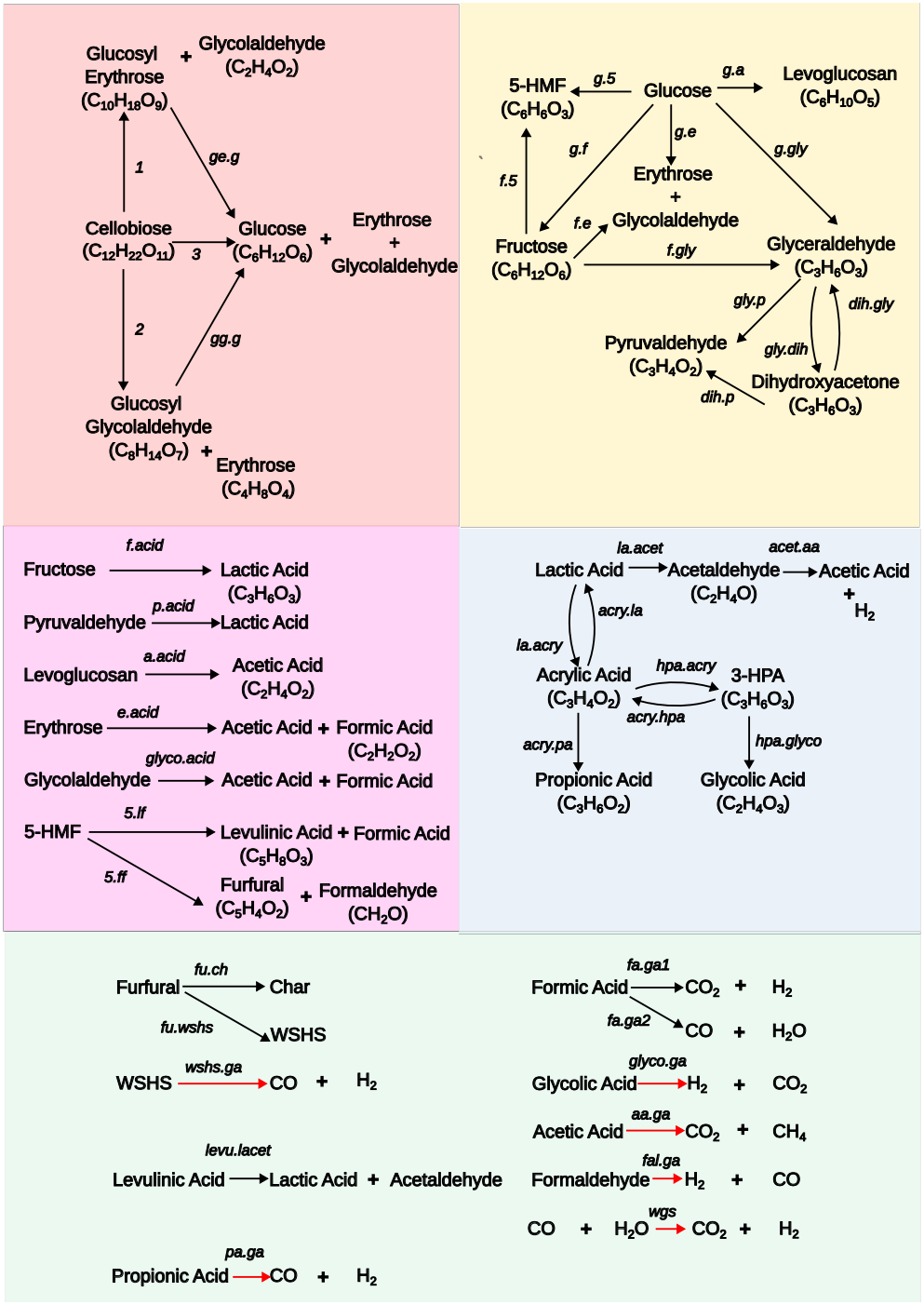

Figure 4.1: Decomposition mechanism for cellulose in supercritical used in kinetic model. Exclusivley supercritical reactions demarcated with red arrows (→).

Two molecules were used as example output variables in the results section of the sensitivity analysis chapter. Firstly, H_2 was studied as this gas-phase product is a desirable species to increase the concentration of in syngas given its

high heating value and other uses. The literature review in Chapt. 2 highlighted some recent SCWG research, and found that optimising H_2 yields was a common objective of many if these papers. Studies explored how homogenous catalysts [55], heterogeneous catalysts [51] and heating rates [31] could be used to expedite H_2 production. In the previous results chapter, the influence of subcritical heating rates on H_2 yields was a major talking point of the results section.

Acetic acid was the second species studied in this sensitivity analysis. Acetic acid is known to be a refractory intermediate compound formed during the decomposition of many types of biomass under hydrothermal conditions. Its stability in sub- and supercritical conditions, in both oxidative and non-oxidative environments means it represents a rate-limiting step in the overall conversion of biomass into syngas [143].

All the results presented in this chapter were obtained using the detailed kinetic model described in Chapt. 3. For coherency, the same configuration of three plug-flow reactors in series was used to emulate a SCWG process. Figure 4.2 shows a reproduction of this figure for convenience. The sub-critical mechanism is used in `SUB-HEX` where the process stream is linearly heated from 25°C to 373°C in 300 s. The supercritical mechanism is then used in `SUP-HEX` and `SUP-RCT` where the process stream is heated and then maintained for 20 s and 60 s , respectively, at target temperatures of 500°C and 500°C. All of these parameters were kept constant for the results presented in this section, with the exception being the `SUP-RCT` residence time which was varied at points.

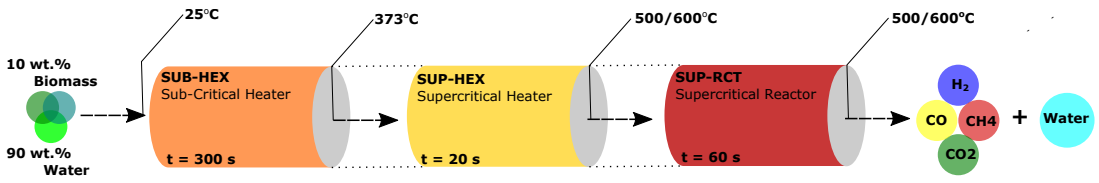

Figure 4.2: The configuration of reactors used in simulations

Figure 4.3a shows how the yields of major intermediates and products evolve as a 10 wt.% cellulose feedstock is fed to the process. Two final temperature cases

are given, 500°C and 600°C, which are represented using solid and dotted lines, respectively. Supplementing this is Fig. 4.3b which shows how the temperature and CGE develop through the course of the three plug-flow reactors. The species 'primaries' on Fig. 4.3a denote the primary decomposition products of cellulose which have been grouped under a single moniker to avoid overcomplicating the Fig. 4.3a plot. The primary molecules consist of species like glucosyl erythrose, glucosyl glycolaldehyde, erythrose, and glycolaldehyde.

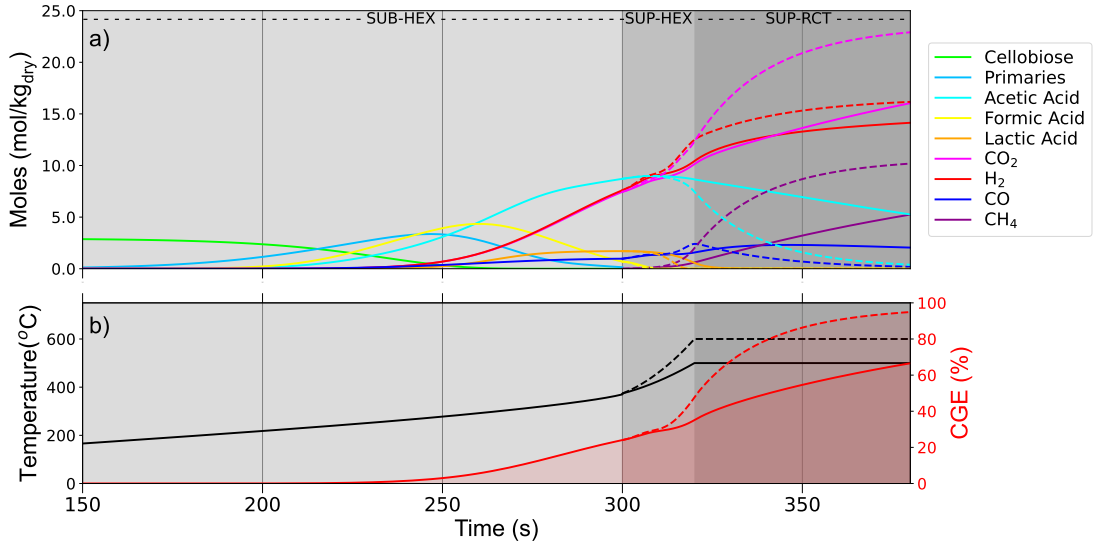

Figure 4.3: Decomposition profile for cellulose operating under normal conditions.

Figure 4.3a shows that acetic acid formation commences after around 200 s in `SUB-HEX`, and rises steadily for the remainder of the sub-critical region becoming the most prevalent intermediate species (by moles). Production of H_2 is first observed after roughly 250 s when temperatures are in excess of 200°C. As the reaction proceeds into `SUP-HEX` where it enters the supercritical regions, H_2 yields increase further, and the disparity in yields between the 500°C and 600°C cases begins. Figure 4.3a shows that after 360 s total reaction time (60 s in `SUP-RCT`), final H_2 yields of around 14.8 and 17.2 $mol\,kg^{-1}$ of cellulose were achieved. Acetic acid yields decrease in the supercritical regions as this species gasifies. At 500°C, the gasification rate is much slower and over 5 $mol\,kg^{-1}$ of acetic acid remain after

60 s in SUP-RCT which corresponds to a CGE of 65 %. On the other hand, using 600°C results in a much quicker gasification of acetic acid and near complete conversion with CGE close to 100 % is achieved in the same time-frame 60 s at this higher temperature.

As was mentioned in Chapt. 3, the 60 s SUP-RCT reaction time was selected to replicate a specific experimental SCWG reactor, as well as to simply represent a supercritical residence time that was in the right order of magnitude for what would be expected during an experimental/industrial process. However, it is worth exploring how longer supercritical residence times affect H_2 yields, especially since the wgs is present, which is the gas-phase conversion of CO into H_2. Figure 4.4 shows how extending the SUP-RCT residence time to 1000 s alters the final yields of H_2 and the CGE. At 600°C, final H_2 yields and CGE of 17.9 $mol\,kg^{-1}$ and >99.7 %, respectively, are reached after around 400 s. It is not until roughly 800 s that the 500°C case meets these same final values of H_2 yields and CGE.

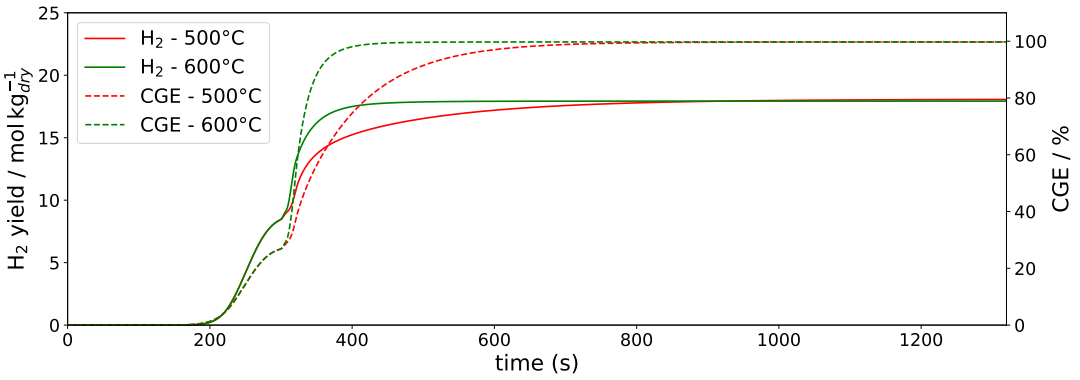

Figure 4.4: H_2 formation from cellulose with extended 1000 s SUP-RCT residence time.

The following section details the sensitivity analysis methodologies used in this chapter. The sensitivity of reactions on H_2 formation are presented first in the results section, followed by the sensitivity of acetic acid production. The final section of this chapter summarises the main findings and makes recommendations in relation to future research along this theme.

4.1 Sensitivity Analysis Methods

4.1.1 Local Sensitivity

There are various types of sensitivity and uncertainty analysis that can be conducted; although, in the field of chemical kinetics what is known as a local analysis is by-in-far the most common type used [144]. In short, local methods refer to when a sensitivity is conducted by making small, incremental changes to usually only one input parameter. Local sensitivity analyses are useful for determining how the output of a model is influenced by the different input parameters [142].

In a local sensitivity analysis, a Taylor-series expansion can be used to define the effect of a parameter change [142].

$$c_i(t, \mathbf{k} + \Delta\mathbf{k}) = c_i(t, \mathbf{k}) + \sum_{j=1}^{n} \frac{\partial c_i}{\partial k_j} \Delta k_j + \frac{1}{2} \sum_{j=1}^{n} \sum_{l=1}^{n} \frac{\partial^2 c_i}{\partial k_j \partial k_l} \Delta k_j \Delta k_l + \cdots$$

Where $c_i(t, \mathbf{k})$ and $c_i(t, \Delta\mathbf{k})$ denotes the concentration of species i at time t, with rate constant of $\mathbf{k}$ and $\Delta\mathbf{k}$, respectively. The expansion contains the partial derivatives ∂c_i and ∂k_j which demonstrate the sensitivity of c_i to local changes in rate constant.

This approach works by approximating a function by an infinite sum of polynomial terms. Each partial derivative in the Taylor series corresponds to a different order sensitivity coefficient, which when combined form a sensitivity matrix. The first term, $\frac{\partial c_i}{\partial k_j}$, is the first order local sensitivity coefficient, the second term, $\frac{\partial^2 c_i}{\partial k_j \partial k_l}$, is the second order local sensitivity coefficient, and so forth.

Numerical methods are generally applied to solve the Taylor series expansion and determine the sensitivity of an output variable to an input. The numerical method applied generally relates to the level of accuracy required and the level of computational expense that is willing to be contributed. The most common and simplest method in chemical kinetics is known as a brute force, or first order

approximation. This is where the sensitivity coefficient, Φ_{ij}, is approximated to the first order local sensitivity coefficient, $\frac{\partial c_i}{\partial k_j}$.

$$\Phi_{ij} = \frac{\partial c_i}{\partial k_j} \approx \frac{c_i(t, \mathbf{k} + \Delta\mathbf{k}) - c_i(t, \mathbf{k})}{\Delta\mathbf{k}} \tag{4.1}$$

The sensitivity coefficient can then be normalised to a dimensionless value that can be used to compare the sensitivity of different reactions.

$$S_{ij} = \Phi_{ij} \frac{k_j}{c_i} \tag{4.2}$$

Φ_{ij} is undefined at zero perturbation and consequently so is S_{ij}. The multiplication of S_{ij} by the ratio k_j/c_i means that this dimensionless value is shifted to reflect the overall sensitivity of k_j on c_i.

The most important consideration when conducting a local sensitivity analysis is the magnitude of perturbation made to the input variable. If $\Delta\mathbf{k}$ is too large, the resulting change to the outputs are no longer local to the chosen input variable and reflect a larger, global change. Equally, if $\Delta\mathbf{k}$ is too small then round-off errors will occur which can lead to noisy or unstable results [145]. In chemical kinetics, a proportionate value of $\pm 1\,\%$ for $\Delta\mathbf{k}$ is a commonly used value in brute force sensitivity analysis [142, 146]. Here, a series of perturbations were made to each rate constant ranging from $\pm 1 - 50\,\%$. By doing so, linearity testing of the chemical system's response can be undertaken. In chemical kinetics, linearity testing refers to determining whether the response (e.g., H_2 concentration) is linearly related to the small changes to input parameters (e.g., rate constant). If linearity is confirmed, it validates the local sensitivity of the response variable to the input parameter. If linearity is lost, then a global sensitivity approach may be required to understand the sensitivity of the reaction [147].

4.1.2 Heuristic Sensitivity

A second, more 'heuristic' approach to sensitivity analysis was also conducted in this chapter. This is where an input parameter is altered by a fixed, generally larger value such as 0, 1 or 5, for example [142]. Heuristic sensitivity analysis results show neither local or global sensitivity, but they have been used effectively by authors such as Cao, Li, and Zhang [148] to identify the major reaction pathways that tend towards the formation/consumption of target species.

The initial step to conduct a heuristic sensitivity analysis involves executing a baseline simulation using the complete, unmodified reaction mechanism, where all rate constants $\mathbf{k}_0$ are active. Following this, each reaction r is systematically deactivated by setting its corresponding rate constant k_r to zero. For each modified mechanism, the simulation is re-run, and the resulting concentration of a target species i at time t is compared to the baseline case.

The influence of reaction r on species i is quantified using the heuristic sensitivity score shown in Eq. 4.3.

$$S_{i,r}(t) = 100 \times \frac{c_i(t;\mathbf{k}_0) - c_i(t;\mathbf{k}_r = 0)}{c_i(t;\mathbf{k}_0)} \tag{4.3}$$

where $S_{i,r}(t)$ is the sensitivity score for species i due to reaction r at time t, $c_i(t;\mathbf{k}_0)$ is the concentration of species i using the full mechanism, and $c_i(t;\mathbf{k}_r = 0)$ is the concentration when reaction r is removed (i.e., $k_r = 0$). The score $S_{i,r}(t)$ provides a dimensionless percentage indicating the influence of each reaction on the concentration of species i.

4.2 Results and Discussion

4.2.1 H_2 Heuristic Sensitivity

From the full mechanism shown on Fig. 4.1, those reactions which directly produce (and consume) H_2 are listed in Tab. 4.1 along with their Arrhenius

Table 4.1: Arrhenius parameters for H_2 producing and consuming reactions in the cellulose mechanism.

Name	**A** (s^{-1})	**Ea** ($kJ\,mol^{-1}$)	**Region***	**Equation**
la.lacet	2.37e+09	1.48e+05	both	LacticAcid →Acetalde + CO_2 + H_2
acet.aa	0.0325	0	both	Acetalde + H_2O →AceticAcid + H_2
acry.pa	0.6	3.49e+04	both	AcryAcid + H_2 →PropAcid
hpa.glyco	0.00131	0	both	HPA + $2H_2O$ →GlyAcid + CO_2 + $3H_2$
f.ga1	1.6e+06	8.5e+04	sub	FormicAcid →CO_2 + H_2
f.ga1	4.8e+12	1.68e+05	sup	FormicAcid →CO_2 + H_2
wshs.gas	3.5e+08	1.43e+05	sup	WSHS + H_2O →5CO + $5H_2$
pa.ga	1.4e+05	8.94e+04	sup	PropAcid + H_2O →3CO + $4H_2$
glycol.ga	2.5e+04	9.4e+04	sup	GlyAcid + H_2O →$2CO_2$ + $3H_2$
fal.ga	4.8e+12	1.68e+05	sup	Formalde →CO + H_2
wgs	3.8e+05	1.16e+05	sup	CO + H_2O →CO_2 + H_2

*Reaction present in either sub-critical ('sub') or supercritical ('sup') region only, or both regions

parameters. There is a single reaction in the mechanism which consumes H_2, `acry.pa`, which represents the formation of propionic acid from acrylic acid. Figure 4.3a shows that H_2 formation commences in sub-critical conditions in `SUB-HEX` shortly before 250 s when the reaction temperature is between 200°C and 250°C. The gradual consumption of formic acid coincides roughly with the commencement of H_2 formation which suggests that formic acid is the main precursor to sub-critical H_2 production.

Figures 4.5 and 4.6 show the heuristic sensitivity of the sub-critical and supercritical cellulose decomposition mechanisms on H_2 yields, respectively. In each case, the bar chart in plot `a` of the figures shows the sensitivity scores, $S_{i,r}(t)$, for the reactions where $S_{i,r}(t)$ exceeded 5 %; plots `b` and `c` show H_2 yield versus time plots in the supercritical reactors (`SUP-HEX` and `SUP-RCT`) for these corresponding reactions at 500°C and 600°C, respectively. Figures 4.5a shows a clear dependence on three early-stage reactions: `3`, `g.f`, and `f.5`. Removing these reactions decreased the H_2 yield at 600°C by roughly 10 %, 13 % and 20 %, respectively. The sensitivities of these reactions were less at 500°C than 600°C in equal proportions which reflects the greater route competitiveness that occurs

when reaction rates are faster at hotter temperatures. It can be inferred that the predominant route for H_2 formation from cellulose proceeds via the direct decomposition of cellulose into glucose (`3`) and the subsequent formation of fructose (`g.f`) and then 5-HMF (`f.5`). The positive percentage change that occurs with the removal of `g.e` or `5.lf` shows that these two reactions detract from the formation of H_2. Erythrose and glycolaldehyde formed via `g.e` competes directly with the formation of fructose from glucose. Both erythrose and glycolaldehyde subsequently decompose into mixtures of predominantly acetic acid which is not a precursor to H_2 in the kinetic model. The reaction `5.lf` represents the production of levulinic acid and formic acid from 5-HMF, and despite both these molecules being predisposed to H_2 formation in their subsequent decomposition, its evident that `5.ff` must be the more lucrative pathway for H_2 production as the removal of this competing reaction of 5-HMF resulted in a negative percentage change. Furfural and formaldehyde which are produced from `5.ff` are therefore the main H_2 precursors in the later stage decomposition of cellulose.

Also presented on Fig. 4.5a are the reactions `f.ga1` and `f.ga2` which represent the formation of CO_2 and H_2, and CO and H_2O from formic acid, respectively. There is a substantial negative sensitivity to `f.ga1`, but only at the lower temperature case of 500°C. Conversely, `f.ga2` has a moderate positive sensitivity, again exclusively at 500°C. It is suspected that `f.ga1` becomes a less prominent route for H_2 formation at higher temperatures when alternative routes via furfural make up a larger proportion. Regarding `f.ga2`, unlike `f.ga1` this reaction does not directly lead to H_2 formation and can be regarded as a competing formic acid gasification reaction, which explains the positive change when this reaction was removed at 500°C. Increasing the temperature to 600°C shifts the H_2 formation route away from formic acid, as previously mentioned, but it also expedites `wgs` kinetics which converts CO into H_2 and turns `f.ga2` into a H_2 producing route. To verify this, the residence time in `SUP-RCT` was increased from 60 s to 1000 s to see if increasing the reaction time would allow the slower `wgs` kinetics at 500°C to

increase H_2 production from `f.ga2`. It was found that the sensitivity of `f.ga2` decreased from $+5.7\,\%$ to $+0.2\,\%$ which proves the hypothesis.

Figure 4.6a shows the sensitivity of the cellulose supercritical decomposition mechanism to H_2 production. The strong dependence of reactions `fu.wshs` and `wshs.gas` on H_2 yields validates what was observed regarding the sensitivity of the sub-critical mechanism, as it is clear that the majority of H_2 comes from furfural. The reactions `fu.wshs` and `wshs.gas` have identical sensitivities as WSHS is produced only via `fu.wshs` in the global cellulose mechanism, which means nullifying `fu.wshs` also nullifies `wshs.gas`. It is seen that there is also a dependence on the reactions `acry.pa` and `pa.ga` which are the formation and gasification of propionic acid from lactic acid. The conversion of acetaldehyde into acetic acid via `acet.aa` also produces H_2 as a by-product which contributes significantly to overall yields. The reversal of the dependence on `la.acet` - a reaction where lactic acid forms acetaldehyde - is another interesting result on Fig. 4.6a At 500°C, the removal of `la.acet` negatively affects H_2 yields which suggests that a large proportion of H_2 comes from the reaction decomposition of acetaldehyde via `acet.aa`. Conversely, at 600°C a positive change occurs when `la.acet` is removed. This suggests that at higher temperatures the majority of H_2 is formed via alternative routes (e.g., `la.acry`) and `la.acet` is a competing reaction. As expected, the `wgs` is the final reaction to significantly govern H_2 yields, and at 600°C in particular contributes majorly to H_2 yields.

4.2.2 H_2 Local Sensitivity

The following subheadings contain a series of figures pertaining to the results of the H_2 local sensitivity analysis. In each figure, plot *a* shows how H_2 yields vary in the final two reactors (`SUP-HEX` and `SUP-RCT`) at two different temperatures of 500°C and 600°C when the rate constant was perturbed between $\pm 1 - 50\,\%$. This graph provides a useful visualisation of how H_2 yields are affected by the changes made to the rate constant versus the unperturbed case (shown as the solid black line).

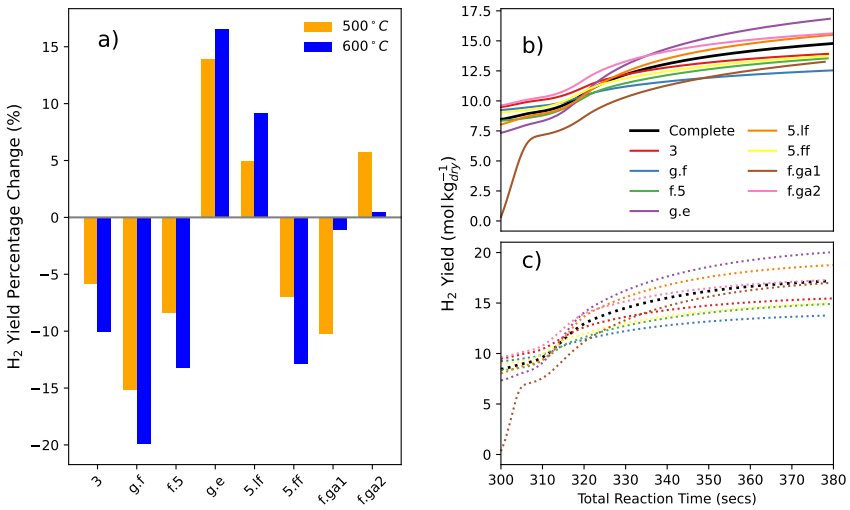

Figure 4.5: Heuristic sensitivity of sub-critical cellulose mechanism on H_2 formation at reaction temperatures of 500°C and 600°C.

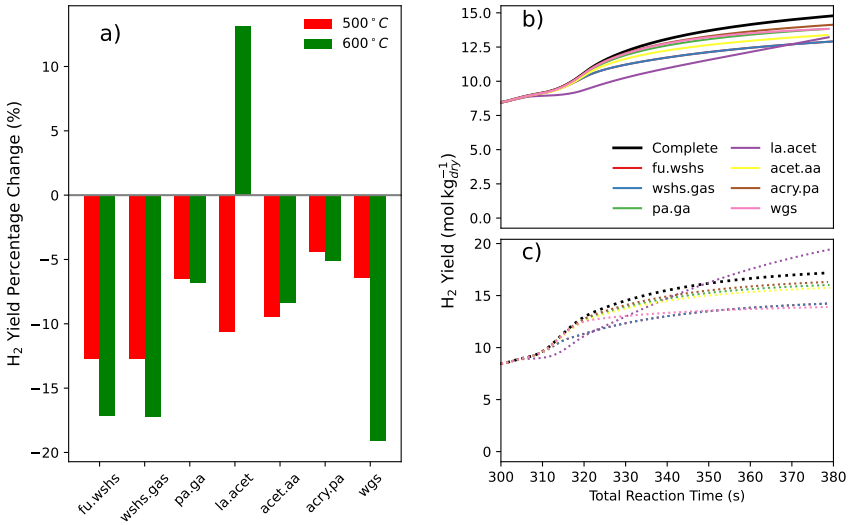

Figure 4.6: Heuristic sensitivity of supercritical cellulose mechanism on H_2 formation at reaction temperatures of 500°C and 600°C.

Plots *b* and *c* in the figures show the sensitivity analysis results at temperatures of 500°C and 600°C, respectively. In each case, the sensitivity coefficient, S, is plotted versus the rate constant, k, at two different residence times: 320 s and 350 s. The reasoning for this was to show how the sensitivity of a reaction changes

as it progresses. At 320 s, the process stream has just entered `SUP-RCT`, and at 350 *s* it is midway through `SUP-RCT`. Figure 4.4 increased the residence time in `SUP-RCT` to 1000 s and it was shown that a near-100 % CGE was achieved after 600 s at reaction temperatures of both 500°C and 600°C. This provides good indication that the global mechanism has reached a point of completion with all reagents consumed; and therefore there is little reason to investigate the sensitivity at a longer residence time (e.g., 600 s) as the reaction rates will be zero.

Smooth curves on the local sensitivity analysis figures demonstrate that the rate of reaction directly affects the H_2 yield at the specified time. The breakdown of this smooth relationship means the reaction no longer has a direct influence on yields of H_2. When this is the case, small perturbations to rate constant can result in seemingly random sensitivity coefficients which is represented as noise.

WSHS + H_2O → 5H_2 + 5CO (`wshs.gas`)

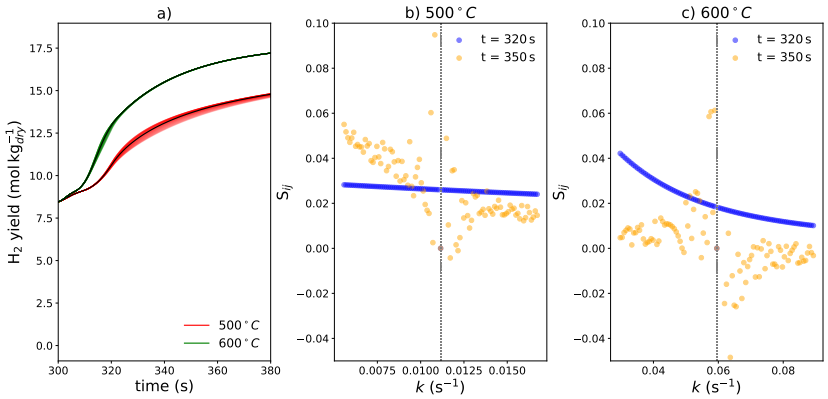

Figure 4.7: Local sensitivity of H_2 formation to `wshs.gas`.

The reaction `wshs.gas` represents the gasification of WSHS (water-soluble humic species) - a mix of acetic and acrylic acids as discussed in Chapt. 3. This mixture of compounds is formed from the decomposition of furfural via `fu.wshs`. Figure 4.7a shows a spread about the normal curves which demonstrates a sensitivity of H_2 concentration to this reaction. The results of the linearity tests at 500°C and 600°C are shown on Fig. 4.7b and c, respectively. At 500°C

and 320 s, there is a linear negative correlation between sensitivity coefficient and rate constant. The strength of the correlation shows a direct local sensitivity between H_2 yields and the rate of `wshs.gas` at this time. The reduction in sensitivity coefficient with faster rate constants shows the reaction is tending towards completion as there is no more WSHS being produced. At 600°C and 320 s, sensitivity dramatically increases as the rate constant is reduced which suggests at these higher temperatures, the yield of H_2 at 320 s is greatly controlled by `wshs.gas`. At both temperatures, the correlation between sensitivity coefficient and rate constant is largely lost which at 350 s which suggests `wshs.gas` has a less significant influence at longer supercritical residence times.

Acetaldehyde + H_2O → Acetic Acid + H_2 (`acet.aa`)

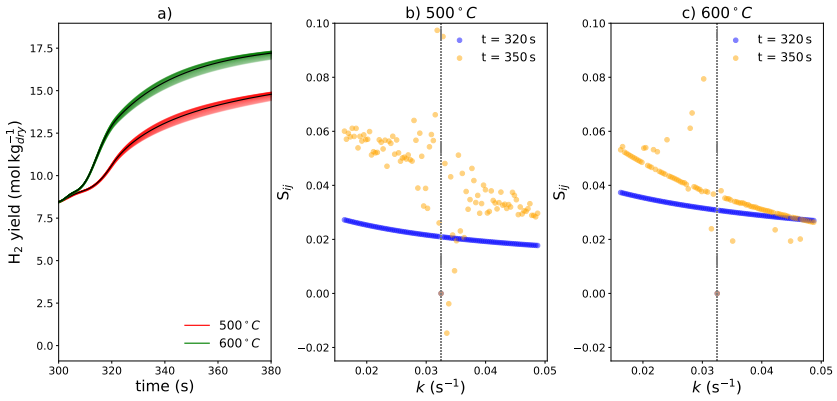

Figure 4.8: Local sensitivity of H_2 formation to `acet.aa`.

Despite only producing one mole of H_2, we see that `acet.aa` has similar degree of sensitivity to H_2 yields as `wshs.gas`. Negative correlations at both 500°C and 600°C at 320 s demonstrate that this reaction is also locally sensitivity to the yields of H_2 at this time stamp. The magnitude of the sensitivity coefficients increases at higher temperatures which suggests it is a more prevalent route for H_2 production in hotter conditions. Interestingly, whilst the correlation is mostly lost at 500°C at 350 s, at 500°C and the same time there is still a fairly strong non-linear correlation between sensitivity coefficient and rate constant.

This suggests that hotter reaction temperatures increase yields of acetaldehyde and `acet.aa` is not completed at 350 s.

Lactic Acid → Acetaldehyde + H_2 + CO_2 (`la.acet`)

Following on from `acet.aa`, the acetaldehyde-producing reaction `la.acet` also produces a mole of H_2. Figure 4.9a shows that at both 500°C and 600°C, the majority of sensitivity to H_2 formation from this reaction comes in the later stages of `SUP-HEX` and early stages of `SUP-RCT` (roughly 310–340 s). The linearity test at 500°C shows a strong negative correlation between sensitivity coefficient and rate constant at 320 s which demonstrates the local sensitivity of H_2 yields to this reaction at this time. THe sensitivity is greater than `acet.aa` because this reaction governs H_2 production from `la.acet` and subsequently through `acet.aa` as well. The sensitivity is lower at 600°C which suggests this reaction loses importance in hotter conditions. At both temperatures, the sensitivity at 320 s is near-zero and/or uncorrelated which suggests no effect from it at longer reaction times.

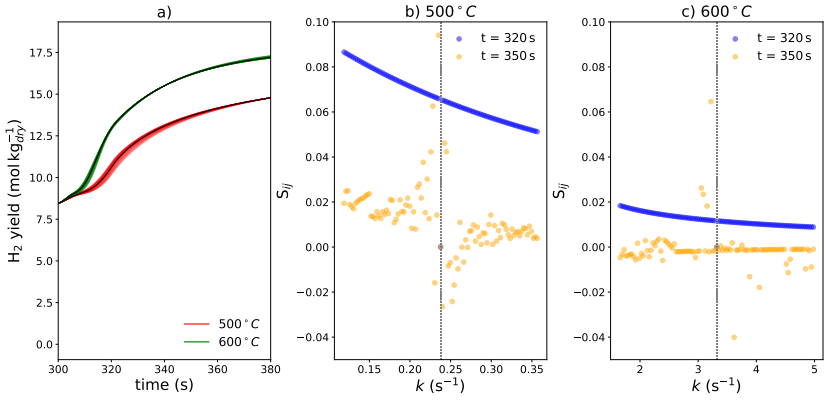

Figure 4.9: Local sensitivity of H_2 formation to `la.acet`.

Formic Acid → H_2 + CO_2 (`f.ga1`)

Figure 4.10a shows the sensitivity analysis produced a considerable spread about the normal values at both 500°C and 600°C. At first inspection, there is greater variability in the earlier part of the supercritical region which is indicative of

formic acid gasifying readily in supercritical conditions. The sensitivity results on Fig. 4.10b show that at 500°C there is a non-linear, negative correlation between sensitivity coefficient and rate constant. Although weaker, there is still correlation between sensitivity coefficient and rate constant at 350 s which suggests formic acid still dictates H_2 yields at longer residence times.

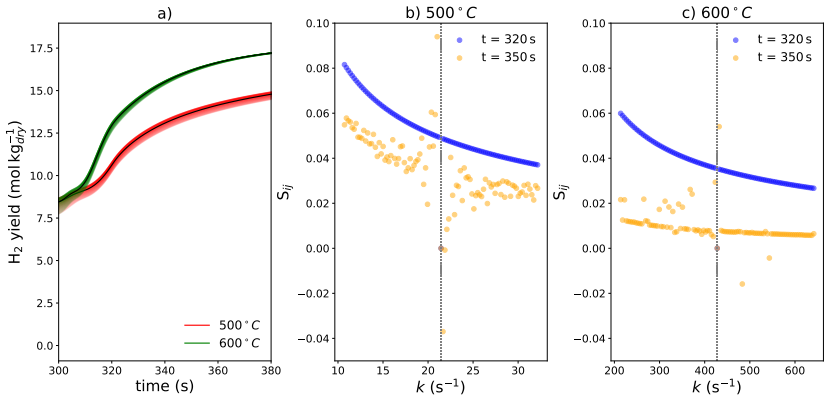

Figure 4.10: Local sensitivity of H_2 formation to `f.ga1`.

Propionic Acid + H_2 → 3CO + 4H_2 (`pa.ga`)

Figure 4.11a shows there is only a slight sensitivity to `pa.ga`, and that there is a greater spread at 500°C than 600°C. Four moles of H_2 are produced via this route per mole of propionic acid that is gasified, however, the low sensitivity suggests this is not a prevalent route for H_2 production.

Acrylic Acid + H_2 → Propionic Acid (`acry.pa`)

The reaction `acry.pa` is the only example in the cellulose mechanism of a reaction which consumes H_2. Despite consuming H_2, Fig. 4.12 shows that sensitivity coefficients of this reaction are in fact positive. This makes sense since `pa.ga` produces four moles of H_2 per mole of propionic acid, whereas `acry.pa` consumes only one mole of H_2 to produce one mole of propionic acid. There is minimal local sensitivity at 500°C, whereas increasing the temperature to 600°C presents notable sensitivity at 350 s in particular.

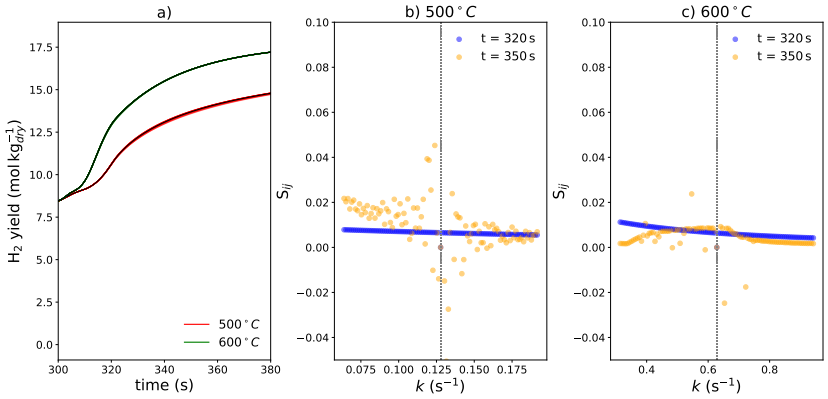

Figure 4.11: Local sensitivity of H_2 formation to `pa.ga`.

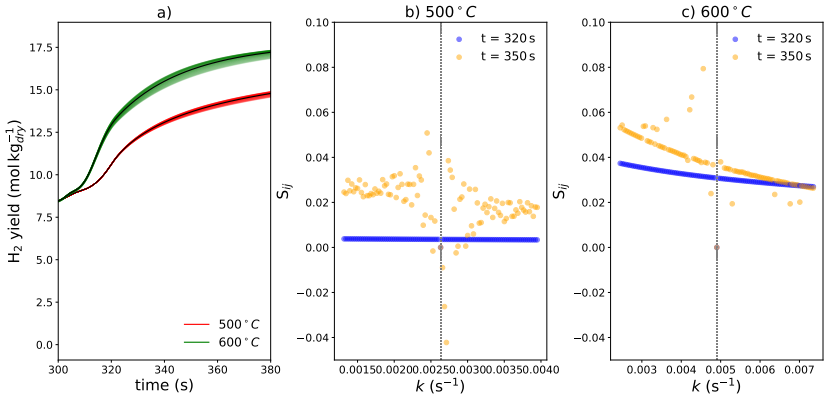

Figure 4.12: Local sensitivity of H_2 formation to `acry.pa`.

$CO + H_2O \rightarrow H_2 + CO_2$ (`wgs`)

Figure 4.13 shows the sensitivity results for the `wgs` reaction. Initial impression from Fig.4.13a show a large spread about the normal case which suggests a strong dependence of H_2 yields on `wgs`. Sensitivity coefficients are much lower at 320 s which suggests it is only until the later stages of the supercritical reactor that H_2 formation via `wgs` becomes prevalent. At 600°C and 350 s, there is a strong negative correlation between sensitivity coefficient and rate constant. This is indicative of the conditions which promote CO formation, as hotter reaction temperatures and longer reaction times allow for a greater CGE and thus the amount of H_2 that can be produced via `wgs` increases as a consequence.

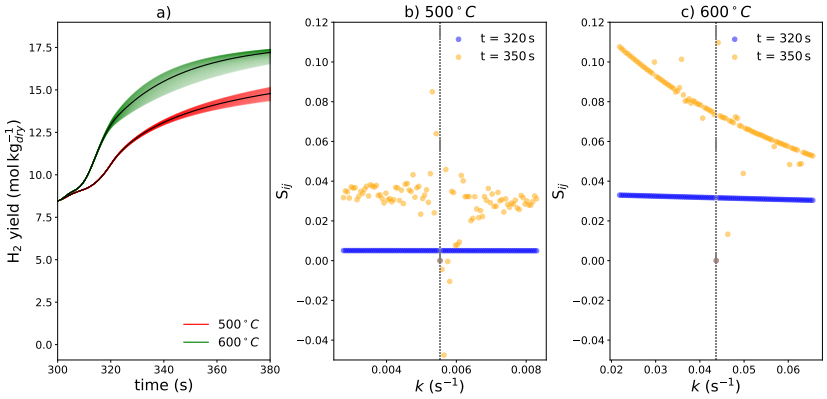

Figure 4.13: Local sensitivity of H_2 formation to `wgs`.

The remaining undiscussed reactions involving H_2 are the gasification of formaldehyde (`fal.ga`) which produces equimolar amounts of H_2 and CO; the gasification of glycolic acid (`glyco.ga`) to produce H_2 and CO_2; the conversion of HPA into glycolic acid (`hpa.glyco`) where H_2 is also formed. The sensitivty analysis revealed no significant governance of these reactions on yields of H_2 at any point - the results are shown in Appendix B.

Formic Acid $\rightarrow$ H_2O + CO (`f.ga2`)

A sensitivity analysis was also carried out on a selection of reactions within the cellulose mechanism that do not produce hydrogen directly, but generate species that contribute to its formation. In the preceding section, the conversion of CO through the `wgs` reaction was identified as having a strong local influence on hydrogen yields during the later stages of operation in the supercritical reactor. The impact of CO formation on hydrogen production is therefore of particular interest in this analysis. Four reactions contribute to CO formation: `fal.ga`, `pa.ga`, `wshs.ga`, and `f.ga2`, although `f.ga2` remains untested.

Figure 4.14a shows that there is a significant spread about the H_2 yield curves at both 500°C and 600°C suggesting significant sensitivity to this reaction. The sensitivity coefficients of `f.ga2` are all negative meaning this reaction detracts from H_2 yields at the conditions presented. The reaction `f.ga2` directly competes with

`f.ga1`, and although `f.ga2` leads to H_2 production via the conversion of CO in `wgs` - the rate of H_2 formation from this competing route is slower and less favourable to H_2 production. The negative sensitivity coefficients are larger at 500°C than600°C, which is indicative of the slower kinetics of `wgs` at cooler temperatures.

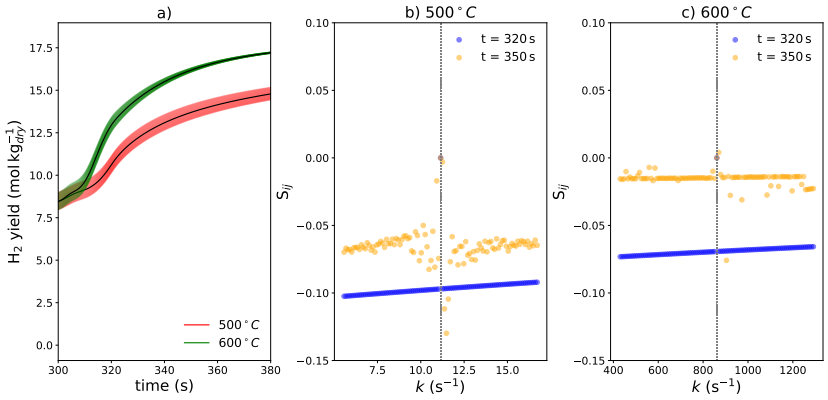

Figure 4.14: Local sensitivity of H_2 formation to `f.ga2`.

Furfural + $2H_2O$ →WSHS (`fu.wshs`)

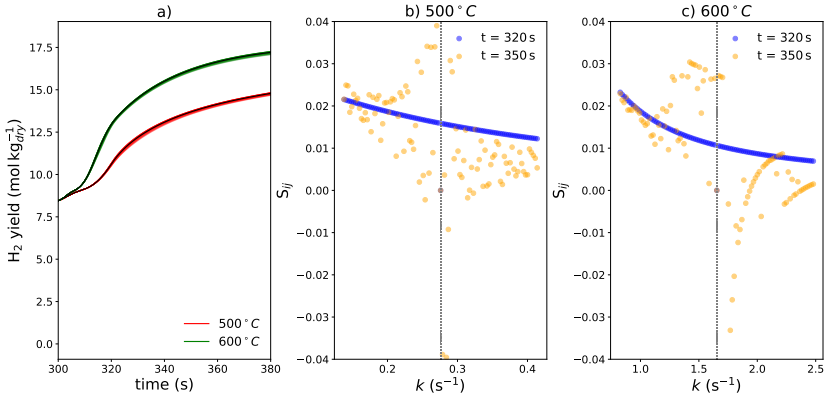

Figure 4.15: Local sensitivity of H_2 formation to `fu.wshs` .

The reaction `wshs.ga` also exhibited measurable sensitivity, and thus the sensitivity of `fu.wshs`, the reaction by which WSHS is produced, was also investigated. This analysis aimed to determine whether the formation of WSHS has an upstream influence on hydrogen production through its downstream gasification.

The results showed that `fu.wshs` does indeed influence H_2 yields, particularly at higher temperatures and later stages of the reaction, indicating that the availability of WSHS is a contributing factor in governing overall H_2 formation. These findings support the hypothesis that precursor-forming reactions can exert indirect but significant control over hydrogen production pathways, reinforcing the importance of intermediate species like WSHS in the supercritical water gasification mechanism.

4.2.3 Acetic Acid Sensitivity

Here the sensitivity analysis results for the refractory intermediate acetic acid are contained. The cellulose decomposition mechanism contains four acetic acid producing reactions: `a.acid`, `e.acid`, `glyco.acid`, and `acet.aa` - they are written in Tab. 4.2 for reference. The reactions `e.acid` and `glyco.acid` represent the decomposition of two primary hydrolysis products of cellulose, erythrose and glycolaldehyde, respectively. Acetic acid is also produced from levoglucosan (anhydroglucose) via `a.acid` which is a possible decomposition pathway for glucose. The reaction `acet.aa` is part of the lactic acid decomposition pathway and occurs later in the mechanism.

The results of the heuristic sensitivity analysis are shown in Fig. 4.16. Acetic acid is predominantly formed in the sub-critical region, hence, only a sensitivity analysis of the sub-critical mechanism was conducted. The sensitivities shown on Fig. 4.16a correspond to the difference in acetic acid concentration at the end of `SUB-HEX` (i.e., at 300 s). Only those reactions which produced a percentage change greater than 5 % are shown.

The reactions `glyco.acid` and `e.acid` demonstrate the greatest sensitivity to yields of acetic acid in the sub-critical region; where reductions of around 50 % and 45 % were observed, respectively. The inference here is that acetic acid is primarily produced from erythrose and glycolaldehyde as opposed to levoglucosan via `a.acid`. This concept is reinforced by the negative sensitivities

Table 4.2: Arrhenius parameters for acetic acid producing reactions in the cellulose mechanism.

Name	A (s^{-1})	Ea ($kJ\,mol^{-1}$)	Equation
e.acid	2.1e+10	1.25e+05	Erythrose + $2H_2O$ →AceticAcid + 2FormicAcid
glyo.acid	2.1e+10	1.25e+05	Glycolal →AceticAcid
a.acid	8e+07	1.09e+05	LevoGluco + $3H_2O$ →2AceticAcid + 2FormicAcid
acet.aa	0.0325	0	Acetalde + H_2O →AceticAcid + H_2

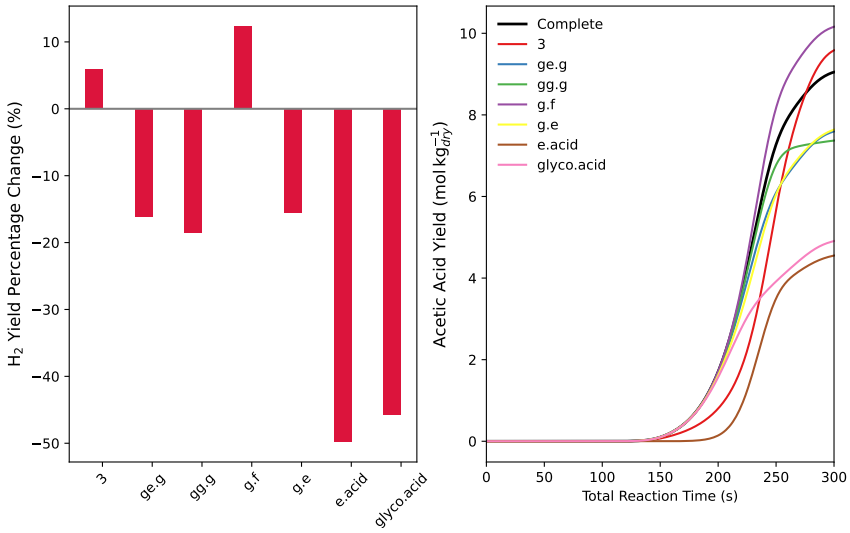

Figure 4.16: Heuristic sensitivity analysis results for acetic acid formation from decomposition of cellulose in the sub-critical mechanism.

of the reactions `g.e`, `gg.g`, and `ge.g` which are all responsible for the production of both erythrose and glycolaldehyde.

The positive sensitivity of the reaction `g.f` suggests this is the only reaction which detracts from acetic acid yields. The formation of erythrose and glycolaldehyde from the initial hydrolysis of cellulose is unavoidable, however, the reaction `g.f` directly competes with `g.e`. Although fructose is also capable of producing erythrose and glycolaldehyde via `f.e`, the suggestion from Fig. 4.16 is that it decomposes preferentially via `f.5` and `f.gly` which are not precursors to acetic acid.

Next, the local sensitivity analysis results for acetic acid are shown. Two time points were used: 150 s and 250 s . The earlier time corresponds to roughly when

acetic acid formation first commences in the sub-critical region. The later time represents a point in `SUB-HEX` when acetic acid concentrations are established but still rising at their fastest increment. Since temperature is changing in this sub-critical reactor where a linear heating profile from 25°C to 373°C is applied, the sensitivty coefficients for the two different times need to be plotted on two different graphs as they occur at different reaction temperatures and have different rate constants.

Erythrose + 2 H_2O →Acetic Acid + 2 Formic Acid (`e.acid`)

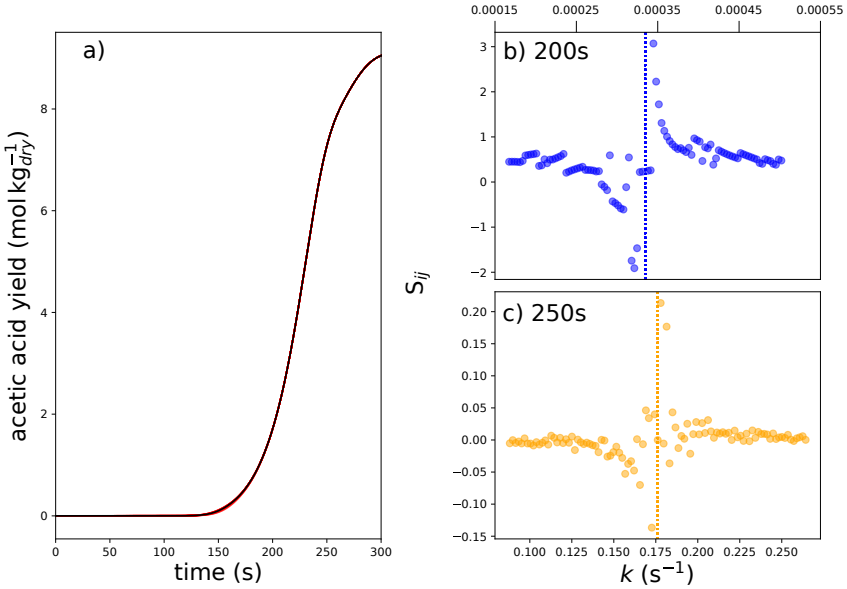

Figure 4.17: Local sensitivity of acetic acid formation to `e.acid`.

The heuristic sensitivity analysis demonstrated that `e.acid` is a major production route for acetic acid from cellulose in SCW. The results of the local sensitivity analysis for this reaction are shown in Fig. 4.17 and demonstrate an almost negligible local sensitivity to this reaction. Figure 4.17a suggest perturbations to the rate constant result in very little spread of yield about the normal curve, with the only notable differences coming at the 150 s mark. The value of S_{ij} sits marginally above 0 at 150 s, and at 250 s it has even less

sensitivity. Neither increasing nor decreasing the rate constant of `e.acid` was found to result in noteworthy changes to acetic acid concentration at the times shown. It is known that `e.acid` is a dominant pathway for acetic acid formation, However, the minimal local sensitivity suggests that this reaction is already sufficiently active that minor changes to rate constant have no influence on acetic acid yield. This effect is exacerbated by the fact that acetic acid is not consumed in the sub-critical region (only in the supercritical region via `aa.ga` - see Fig. 4.1) which means acetic acid accumulates and its concentration becomes less sensitive to local changes to `e.acid`.

Glycolaldehyde →Acetic Acid (`glycol.acid`)

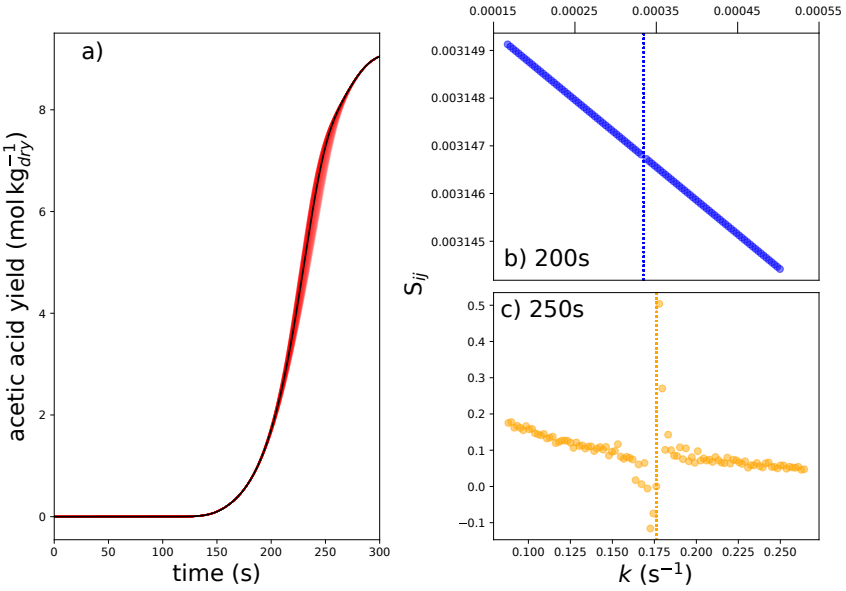

Figure 4.18: Local sensitivity of acetic acid formation to `glycol.acid`.

The reaction `glycol.acid` was the second acetic acid forming reaction shown on Fig. 4.16 to govern yields of this refractory intermediate in the sub-critical region. The local sensitivity results are displayed on Fig. 4.18, where it is shown on plot `a` that perturbing the rate constant of this reaction does produce an observable change to acetic acid yields roughly between 200 s and 250 s . Figure 4.18b shows

a strong, linear relationship between rate constant and S_{ij} at 150 s ; however, the sensitivity coefficients are very small which suggests the effect of changing this parameter at 150 s is very small. At 250 s , the linearity is weaker, but the sensitivity coefficients are two orders of magnitude larger. Similar to `e.acid`, the conclusion here is that although `glycol.acid` contributes significantly to acetic acid formation, its local sensitivity is minimal as acetic acid production in this region of the reactor is prominent and from a variety of pathways. The negative, linear sensitivity at 250 s does suggest that this reaction becomes more tunable to acetic acid at later stages of the sub-critical region.

levoglucosan + 3 H_2O →2 Acetic Acid + 2 Formic Acid (`a.acid`)

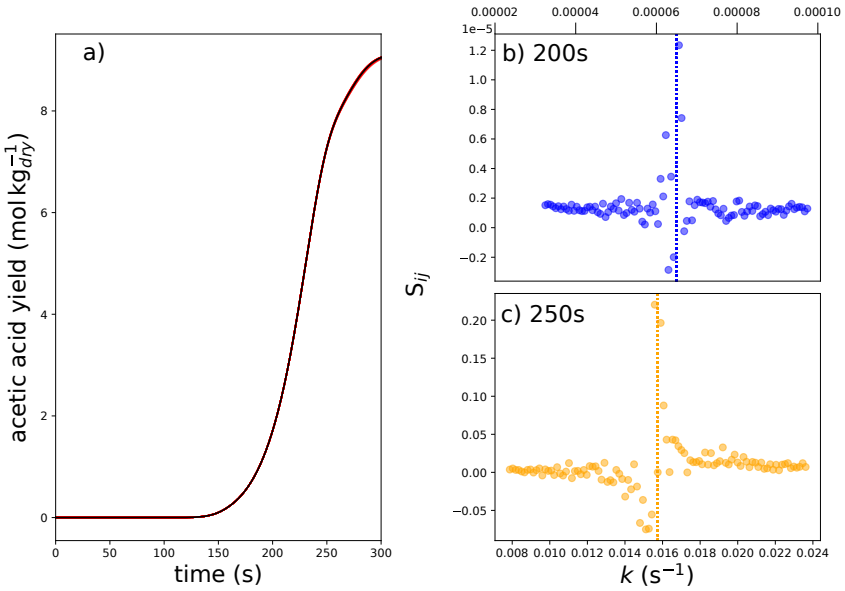

Figure 4.19: Local sensitivity of acetic acid formation to `a.acid`.

The reaction `a.acid` was shown during the heuristic sensitivity analysis to have a less than 5 % sensitivity to sub-critical acetic acid yields upon its removal from the mechanism. Figure 4.19 demonstrates that there is minimal local sensitivity to this reaction at both 150 s and 250 s .

Acetaldehyde + H_2O →Acetic Acid + H_2 (`acet.aa`)

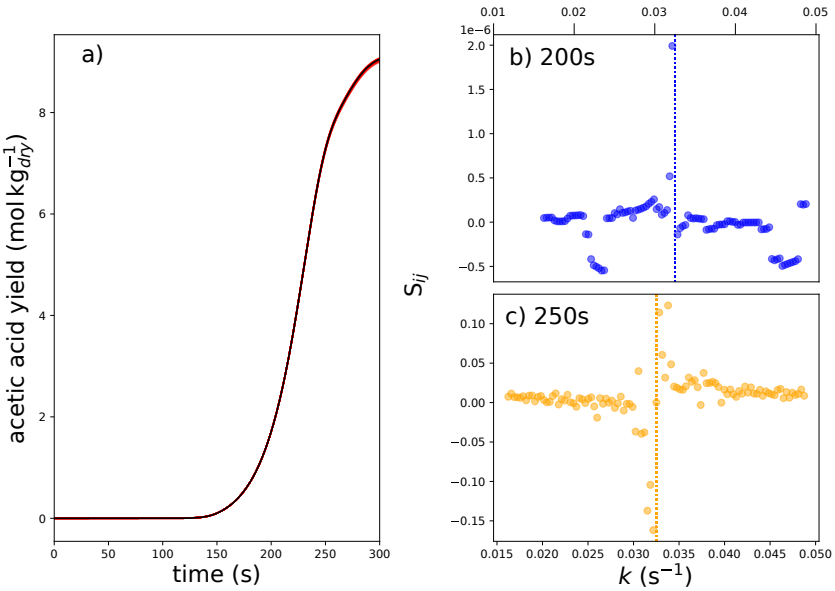

Figure 4.20: Local sensitivity of acetic acid formation to `acet.aa`

The final acetic acid producing reaction is `acet.aa` which was discussed earlier in this chapter since it forms H_2. The heuristic sensitivity analysis suggests that this reaction also has a comparatively minimal influence on the formation of acetic acid as its sensitivity was lower than 5 %.

The local sensitivity analysis shown on Fig. 4.20 suggests negliigible local sensitivity to this reaction. Although, sensitivity coefficents are greater at 250 s than 150 s which suggests this reaction is more prevalent in the later stages of the cellulose decomposition mechanism.

4.3 Conclusions

This chapter used two different sensitivity analysis methodologies to determine how the output of the SCWG detailed kinetic model is sensitivity to input variables. Cellulose was selected as the starting feedstock of choice, and the rate of each reaction in this mechanism was altered to ascertain the response it

had on yields of H_2, and acetic acid (a refractory intermediate). The findings of this chapter identify the reactions that most significantly govern the formation of these species and provide guidance for future optimisation of SCWG and refinement of the kinetic model.

Both local and heuristic sensitivity analyses were conducted. The local sensitivity made a series of minor ($\pm 1\,\%$) perturbations to the rate constant, and the response from the output variables, H_2 and acetic acid concentration, was observed. In the heuristic sensitivity analysis, the step-wise removal of each reaction in turn was used to give a more general indication to the most prevalent formation routes.

The heuristic sensitivity analysis found that the predominant sub-critical route for H_2 formation came from the formation of 5-HMF via glucose and fructose. The conversion of glucose into erythrose and glycolaldehyde was identified as being the main competing route that reduces final yields of H_2 from the SCWG of cellulose. For the supercritical mechanism, the heuristic sensitivity analysis pinpointed the gasification of WSHS, formed from furufural, as a major pathway for H_2 formation. The importance of the `wgs` reaction, at higher temperatures in particular, was also demonstrated to and shown to contribute to nearly 20 % of all H_2 produced at 600°C. The local sensitivity analysis was used to identify where linear relationships exist between reaction rate and H_2 yields. Snapshots were taken at reaction times of 320 s and 350 s to understand the sensitivity of a reaction to H_2 yields at the beginning of the supercritical region, and midway through it, respectively. For most reactions, linearity was observed at 320 s but not 350 s indicating the importance of gasification in the early stages of the supercritical region. In particular, there was a strong correlation between H_2 yields and the rate of reaction `la.acet` at 320 s. At the later time of 350 s, `wgs` was the only reaction to exhibit a linear relationship between its rate and H_2 yields, which was strongest at 600°C.

Comparing the heuristic and local sensitivity results provides interesting insight into the differing influence of reactions. The main difference is that the heuristic analysis quantifies the sensitivity in terms of the absolute difference in H_2 yields at the end of the run, whereas the local sensitivity analysis provides insight into which reactions are significant at different time points throughout the reaction. We have identified through heuristic sensitivity that the majority of H_2 from cellulose is formed through the formation of glucose and fructose, 5-HMF, WSHS, and furfural (in that order). The local sensitivity analysis, on the other hand, demonstrates that upon entry into the supercritical region, H_2 yields are most influenced by the conversion of lactic acid into acetaldehyde (`c`).

The second results section dealt with the sensitivity of acetic acid. This is a prominent intermediate that is stable in SCW, and the gasification of which is seen as an energy barrier to the complete conversion of biomass. The heuristic sensitivity analysis identified erythrose and glycolaldehyde as the two prominent precursors to acetic acid formation. Equally, it was shown that the removal of reaction `g.f` - which converts glucose into fructose - resulted in an increase in acetic acid yields. This suggests that cellulose decomposition via fructose results in a lower concentration if acetic acid in the intermediate mixture. The local sensitivity analysis demonstrated a weak sensitivity to acetic acid forming reactions which is testament to the accumulation of acetic acid in sub-critical conditions, as changing the rate of acetic acid forming reactions had little influence on the concentration of this refractory intermediate.

A recommendation from the sensitivity analysis is to conduct greater experimental research into the decomposition of furfural, and the subsequent gasification of its WSHS products. WSHS is the only 'lumped' term in the whole kinetic model, as it represents an unknown mixture of acrylic and acetic acids. Therefore, ascertaining a more detailed understanding of this reaction pathway will likely have the most impact on the accuracy of predicting H_2 yields from the SCWG of cellulose.

5

Development of a Thermodynamic Framework for the Thermochemical Valorisation of Biomass

Thermodynamic analyses are fundamental in the design and assessment of reactors, separation processes, energy recovery systems, and many other systems [69]. Thermodynamics provides information of equilibrium compositions and limits to product yields, as well as estimates of the costs (in terms of energy, exergy, etc.) of performing the described conversions. Thermodynamic models play a critical role in the conceptualisation and optimisation of all chemical processes. Here, a new thermodynamic framework is produced, and whilst discussion focuses on its use in the context of SCWG, the methodology can be applied to the thermochemical treatment of any biomass feedstock.

5.1 Introduction

The review contained in Chapt. 2 reported an abundance of literature in the field where thermodynamic models had been employed to establish relationships between the equilibrium yields of syngas and char from SCWG, and operating variables like biomass composition, feedstock concentration, temperature, and

pressure. In many instances, the application of these thermodynamic models were extended to fulfill other functions like investigating novel integrated processes or conducting TEAs. This method of research is not unique to SCWG as thermodynamic models are used widely in the general topic of thermochemical waste treatment to study the conversion of biomass (and plastic) in processes like gasification, pyrolysis, HTC, etc.

As mentioned in Chapt. 2, Castello and Fiori [128] demonstrated that from a thermodynamic perspective, all thermochemical process can be viewed from the same lens. This principle stands because it is only temperature, pressure, and elemental composition which influence the distribution of products at equilibrium. That is to say that at a given temperature and pressure, molecule type has no bearing on equilibrium, only the number of atoms of each element. This is demonstrated in the following subsection of this chapter. The aforementioned copious number of publications employed thermodynamic models to study SCWG and other thermochemical processes by and large fail to address this thermodynamic fundamental. As a consequence, there is little paper-to-paper recognition of this similarity shared by thermochemical processses and there is a saturation of disjointed, repetitive publications in literature. The objective of this chapter is to provide a comprehensive conceptual framework that can be used to characterise the thermodynamic behavior of any thermochemical process.

A popular choice for researchers using thermodynamic models to investigate thermochemical treatments is to use a commercial process simulation software, like Aspen Plus. With such tools, simulations can be conducted with relative ease but at greater monetary expense. As an alternative, the method adopted in this thesis to develop a script capable of performing the same thermodynamic calculations that describe the equilibrium state. Source code is available from the following repository: mjksill/ternarydiagrams [1]

[1] https://github.com/mjksill/ternarydiagram

The main limitation of thermodynamics is that it assumes equilibrium has been reached, and thus it has no consideration for the time-dependent change in composition of a system as a feedstock decomposes and tends towards its final equilibrium composition. However, with these limitations in mind, its possible to discuss the thermal conversion of biomass within the context of thermodynamics. Here, the analysis is restricted to systems composed of only the elements C, H, and O, which includes a broad range of organic wastes, and can also be extended to plastics.

The remainder of this chapter is organised as follows. The next section describes the fundamentals of the Gibbs free energy minimisation calculation. Following this, the basic thermodynamic framework from the perspective of element chemical potential is introduced, highlighting how temperature, pressure, and elemental composition influence the tendency for certain molecules to form at equilibrium. Ternary diagrams are presented in Sec. 5.4. These are graphical tools that are used here to demonstrate the influence of carbon, hydrogen, and oxygen content on the thermodynamic behavior of thermochemical systems. This framework is then used to examine how elemental composition can be altered via the addition of two key additives, water and CO_2, commonly used in the thermochemical processing of organic waste to optimise the behaviour of a system at a range of pressures and temperatures. A case study for the gasification of acetic acid, a refractory model compound, is then used to demonstrate how elemental composition effects the efficiency of performing thermochemical conversions. Finally, the chapter concludes with a summary of the main findings and recommendations for directions of future research.

5.2 Gibbs Free Energy Minimisation Calculation

The change in Gibbs free energy of a system, dG, is given by the following.

$$dG \leq V \cdot dP - S \cdot dT + \sum_i \mu_i \cdot dn_i \tag{5.1}$$

where V is the volume of the system, dP is the change in pressure, S is the entropy, dT is the change in temperature, μ_i is the chemical potential of component i, and dn_i is the change in the number of moles of component i.

Here, the objective is to describe an equilibrium state of a closed system at constant temperature and pressure. When such conditions are satisfied, the first two terms of Eq. 5.1 are nullified and the change in Gibbs free energy can be related solely to the chemical potentials of species in the system.

$$dG = \sum_i \mu_i \cdot dn_i \tag{5.2}$$

Consider a system composed of solely CO, CO_2, H_2, and H_2O. Equilibrium here is dictated exclusively by a single reaction, `wgs`.

$$CO + H_2O \rightleftharpoons H_2 + CO_2 \tag{5.3}$$

The extent of reaction, ξ, is a measure of how far a reaction (`wgs` in this case) has progressed. Depending on the stoichiometric coefficient, ν_i, of each component, it determines the number of moles of a component in the system.

$$dn_i = \nu_i \, d\xi \tag{5.4}$$

This relationship is key to defining equilibrium in this chapter. By substituting Eq. 5.4 into Eq. 5.2, dG can be expressed in terms of $d\xi$.

$$dG = \left(\sum_i \mu_i \nu_i \right) d\xi \tag{5.5}$$

Equilibrium is satisfied by the condition at which G is minimised, which occurs at the point when an infinitesimal change in ξ results in no change to G, as represented in Fig. 5.1.

$$\frac{dG}{d\xi} = 0 \tag{5.6}$$

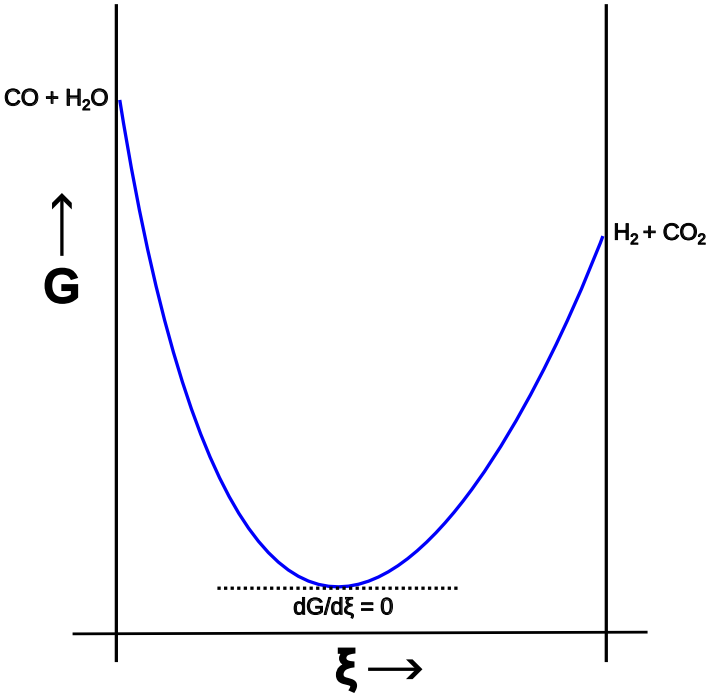

Figure 5.1: Illustration of Gibbs free energy (G) as a function of reaction extent (ξ). The minimum corresponds to the equilibrium state of the system.

This can be extended to also point out that equilibrium occurs when the net-sum of chemical potentials of components in the system is equal to 0, i.e., chemical potential of products equals chemical potential of reagents.

$$\sum_i \mu_i \nu_i = 0 \tag{5.7}$$

In cases of multiple reactions, subject to the constraint of available molecules, reaction extents are adjusted to give an equilibrium composition of components that minimise the value of G.

5.3 Chemical reaction equilibria and element chemical potentials

From thermodynamics, heat naturally flows from high temperature to low temperatures; so temperature can be thought of as driving heat flow. For mass transport,

the key driving force is chemical potential. A compound will diffuse from a region where its chemical potential is high to a region where its chemical potential is low.

The chemical potential of a molecule α in a system at absolute temperature T, pressure p, and composition given by a set of mole fractions $y_{\alpha'}$ can be separated into three main contributions:

$$\mu_\alpha(T,p,y) = \mu_\alpha^{\circ,\mathrm{ig}}(T,p_0) + RT\ln\frac{p_\alpha}{p_0} + RT\ln\phi_\alpha(T,p,y) \tag{5.8}$$

where $\mu_\alpha^{\circ,\mathrm{ig}}(T,p_0)$ is the chemical potential in the ideal gas state at temperature T and reference pressure p_0 (which is typically taken to be 1 bar), p_α is the partial pressure of α, and ϕ_α is the fugacity coefficient for species α. The first term is a formation free energy, which is an indication of the work required to "create" the molecule. The second term is related to the amount of the compound present in the system: the larger the concentration (partial pressure) of the species, the higher its chemical potential. The final term describes the influence of interactions with the environment and represents deviations from the ideal gas law. The less favourable the interactions a molecule has with other components in the system, the greater this term.

The chemical potential of molecules allows researchers to understand the motion through the system (e.g., diffusion). In order to consider chemical reactions, chemical potentials are used for individual elements. From this perspective, a molecule can be considered to be like a solution, and each element/atom within the molecule considered as a separate species in the solution with its own chemical potential.

In this chapter, the focus is on the elements, rather than on the multitude of potential molecular species that they can form. Within a closed system, the elemental composition remains fixed, while the molecular composition may drastically vary due to chemical reactions. From this perspective, the key driving force for changes in the system are the element chemical potentials. As with molecular chemical potentials, there is an ambiguity in how the total Gibbs free

energy is assigned between different species when the system is out of equilibrium. At equilibrium, however, they are uniquely defined.

Molecules can be thought of as containers that atoms can occupy. The chemical potential of a molecule is just the sum of the chemical potentials of the elements from which it is composed. The chemical potential μ_α of a molecule α can be written as the sum of the chemical potentials of its constituent elements e

$$\mu_\alpha = \sum_e A_{\alpha e}\mu_e \tag{5.9}$$

where $A_{\alpha e}$ is the number of elements e that are in a molecule of type α, and μ_e is the chemical potential of element e. As a specific example, consider CO_2. The distinct chemical potential of the molecule is given by the sum of the chemical potential of the individual elements carbon and oxygen:

$$\mu_{CO_2} = \mu_C + 2\mu_O$$

The molecular chemical potential can be uniquely determined from the individual element chemical potentials. That is, given the values of the chemical potentials for a set of elements, the chemical potentials of the molecules. To determine the element chemical potentials μ_e, Eq. (5.9) must be inverted, but, in general, the matrix $A_{\alpha e}$ does not possess an inverse. Consequently, the element chemical potentials are not, in general, uniquely defined in terms of the molecular chemical potentials. For example, the chemical potential of carbon atoms might be written as

$$\mu_C = \mu_{CO_2} - \mu_{O_2}$$

or as

$$\mu_C = \mu_{CH_4} - 2\mu_{H_2}.$$

Different routes of calculating the element chemical potentials will, in general, lead to different values. These different values are, in fact, the driving force

for chemical reactions, as the elements will try to transfer from higher chemical potentials to lower chemical potentials

At chemical equilibrium, however, all these expressions will lead to the same value. This corresponds to formally inverting the matrix $A_{e\alpha}$ using the Moore-Penrose pseudo-inverse $A^{+}_{\alpha e}$ [149–151]. This provides unique values for the element chemical potentials, given the molecular chemical potentials, for a system at equilibrium.

$$\mu_e = \sum_{\alpha} A^{+}_{\alpha e} \mu_\alpha$$

where the summation runs over all molecular species present in the system. So at chemical equilibrium, it is possible to uniquely determine the element chemical potentials from molecular chemical potentials.

In a similar manner to the molecular species chemical potentials, the element chemical potentials can be conceptually divided into separate contributions. In particular, the formation contribution to the chemical potential of an element from the formation free energies of the molecules they are in can be calculated. These element chemical potentials for carbon are relevant to char formation.

$$\mathrm{CO_{2(g)}} + \mathrm{C} \rightleftharpoons 2\mathrm{CO_{(g)}} \qquad \mu_C^{\ominus} = 2\mu^{\circ,\mathrm{ig}}_{\mathrm{CO}}(T, p_0) - \mu^{\circ,\mathrm{ig}}_{\mathrm{CO_2}}(T, p_0)$$

$$2\mathrm{H_{2(g)}} + \mathrm{C} \rightleftharpoons \mathrm{CH_{4(g)}} \qquad \mu_C^{\ominus} = \mu^{\circ,\mathrm{ig}}_{\mathrm{CH_4}}(T, p_0) - 2\mu^{\circ,\mathrm{ig}}_{\mathrm{H_2}}(T, p_0)$$

There is an analogy with half cell reactions in electrochemistry and standard reduction potentials:

$$\mathrm{Cu^{2+}_{(aq)}} + 2e^- \rightleftharpoons \mathrm{Cu_{(s)}} \qquad \phi^{\ominus} = +0.34\,\mathrm{V}$$

$$\mathrm{Zn^{2+}_{(aq)}} + 2e^- \rightleftharpoons \mathrm{Zn_{(s)}} \qquad \phi^{\ominus} = -0.76\,\mathrm{V}$$

The higher the standard reduction potential, the greater the driving force for the electron to be captured.

At the temperatures and pressures considered in this chapter, the most stable species $\mathrm{H_2}$, CO, $\mathrm{CO_2}$, $\mathrm{CH_4}$, $\mathrm{H_2O}$, and $\mathrm{C_{(s)}}$, as they have the lowest chemical

potential of species possible. While larger molecules (e.g., ethane, ethene, etc) could be present, their composition at equilibrium would be negligible, so they are excluded here.

Figure 5.2 plots the standard chemical potentials for the elemental carbon in different forms: by itself as pure solid graphite, bonded with oxygen, either as CO or CO_2 in the gas phase, paired with CH_4 (also in the gas phase), or in the form of CO_2. The standard chemical potentials were calculated using Eq. 5.2 with thermodynamic properties taken from the NASA 9-coefficient polynomial [152]. These are calculated at a pressure of 1 bar and taken with respect to the chemical potential of graphite at $T_0 = 25°C$. Graphite is the stable form of carbon at conditions typical of SCWG hence why it is the only form of carbon considered in this work. For carbon, there are at least three known phases: graphite, diamond, and liquid. In general, each phase of carbon will have a different Gibbs free energy. The stable phase will be the one with the lowest Gibbs free energy. At low temperatures and high pressures (GPa), diamond becomes the stable form. At extremely high temperatures, the stable form of carbon is a liquid. When two phases coexist, this means that both phases have the same Gibbs free energy [153, 154]

The value of these chemical potentials gives insight into which molecular form carbon will want to take on. What is important is not the absolute values of the curves, but their relative positions. The lower the chemical potential of carbon is in that molecule, the more likely that it will form. The red line lies far below the other lines, which means that carbon will readily bind with any molecular oxygen present in the system to form CO_2. As a consequence, there is no expectation of molecular oxygen to be present in the system at any significant concentration.

At low temperatures, it is seen that the prevailing form of gas phase carbon is CH_4 as it occupies the lowest chemical potential for carbon. As temperature is raised, the element chemical potentials of carbon in CH_4 and CO increase and decrease, respectively. At around 600°C, these two curves intersect and cross

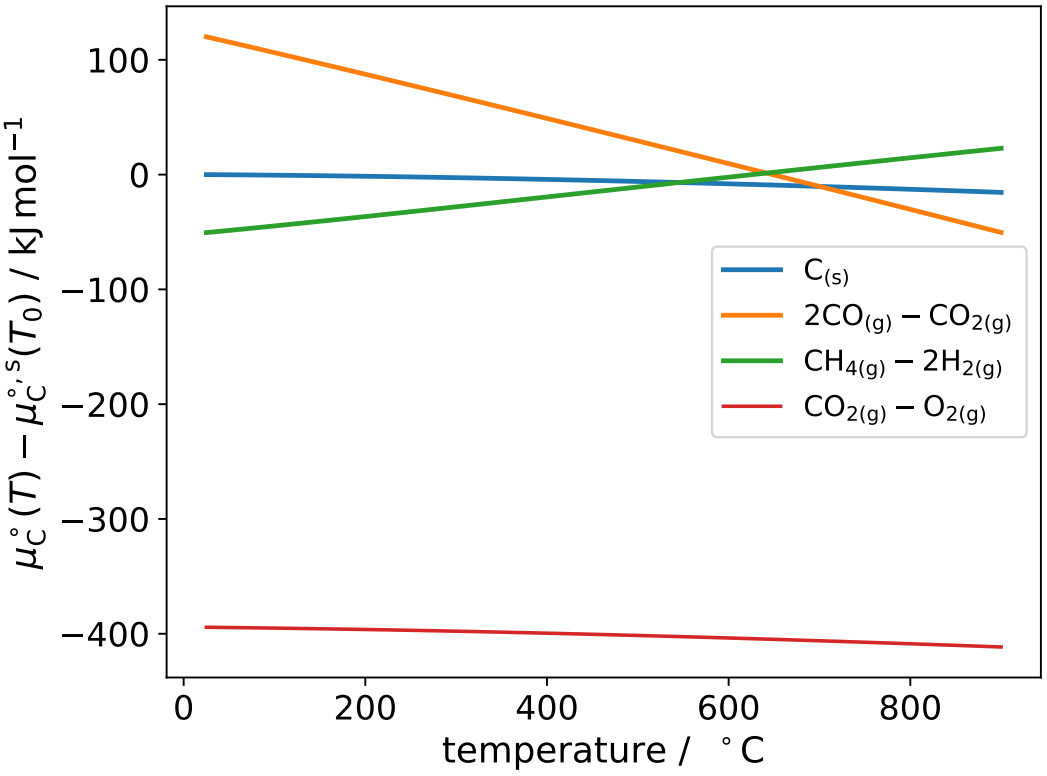

Figure 5.2: The standard elemental chemical potential of carbon at 1 bar as pure graphite (blue line), in CO / CO_2 (orange line), CH_4 (green line), and CO_2 (red line).

and CO becomes the more stable form of carbon in the gas phase. The chemical potential of carbon as solid carbon (blue line) lies between the curves for CO / CO_2 (orange line) and CH_4 (green line) at low and high temperatures. There is a small range of temperatures around 600°C where solid carbon is the most stable form.

In Fig. 5.3, the standard chemical potential is plotted for the element oxygen. In the system, the main stable molecules that oxygen can exist in are with carbon in the form of CO_2 or CO or with hydrogen in the form of water. The chemical potential for elemental oxygen for molecular oxygen (blue line) is much higher than that in either water or when associated with carbon. Consequently, it is seen that molecular oxygen will not be present at any significant amount when the system is at equilibrium.

At low temperatures, oxygen prefers to be bound with carbon in the gas

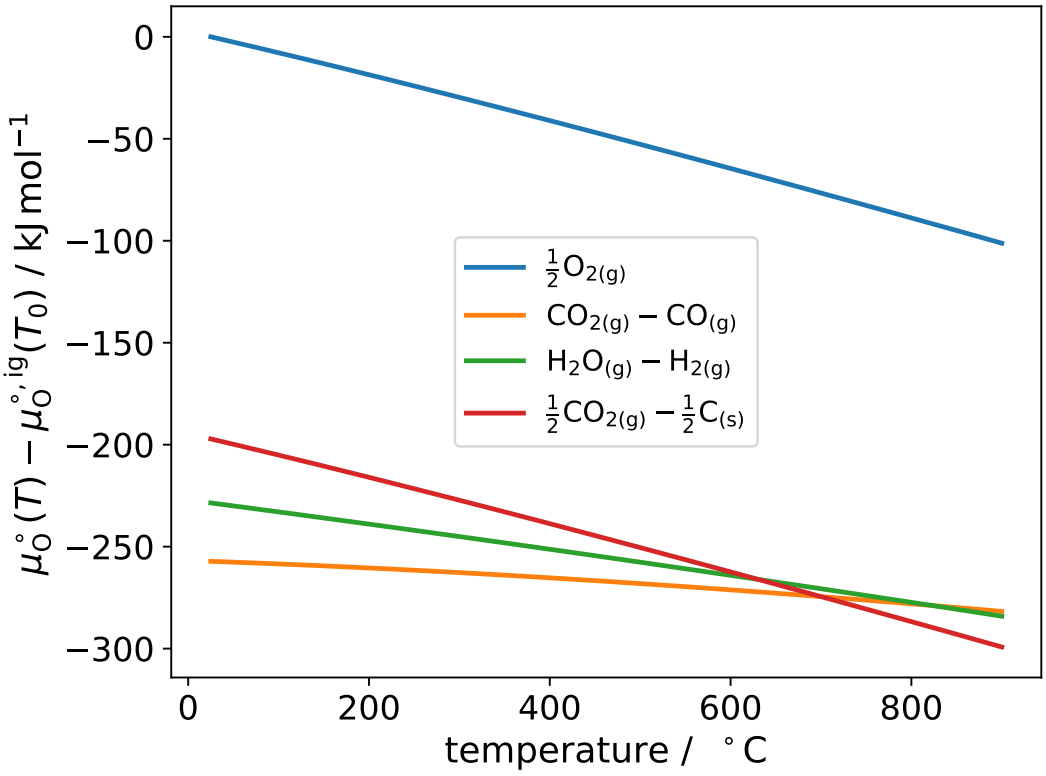

Figure 5.3: The standard elemental chemical potential of oxygen at 1 bar as molecular oxygen (blue line), in CO_2 / CO (orange line), in water (green line), and in CO_2 (red line).

phase, converting CO to CO_2 rather than binding with hydrogen to form water; as temperature increases, they become comparable, with water becoming more stable beyond about 800°C.

The red line represents the binding of oxygen with graphite (solid carbon) to form CO_2. The line decreases as temperature increases, which implies that oxygen has more of a tendency to bind with graphite to form CO_2 at higher temperatures. This line lies above the water curve (green line) and the CO_2/CO curve (orange line) at low temperature, but it becomes lower than both at higher temperatures. This implies that at low temperatures, oxygen would rather bind with other species already in the gas phase, while at high temperatures it would rather bind with solid carbon to form CO_2. This can be interpreted as char

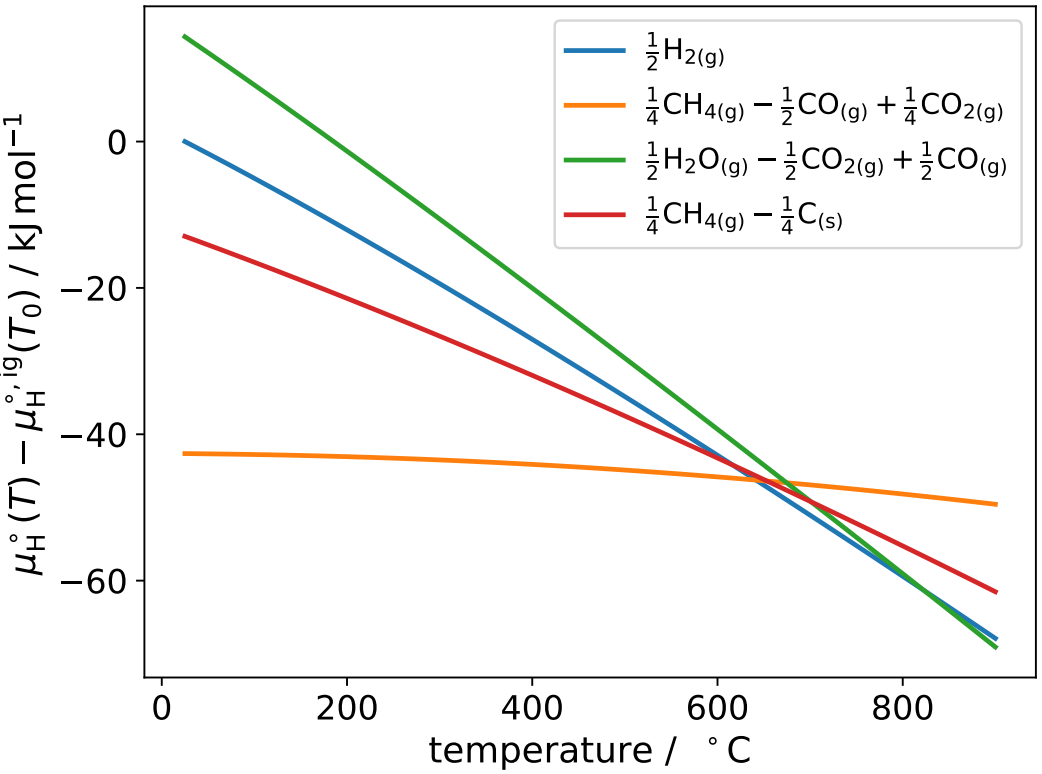

Figure 5.4: Standard elemental chemical potential of hydrogen at 1 bar as molecular hydrogen (blue line), CH_4 from conversion of carbon monoxide to CO (orange line), water (green line), and CH_4 from binding with solid carbon (red line).

being more stable at low temperature.

In Fig. 5.4, the standard chemical potential is plotted for the element hydrogen. Here, elemental hydrogen can either exist as molecular hydrogen, associated with carbon in the form of CH_4, or associated with oxygen in the form of water. At low temperature, the hydrogen is most stable as CH_4, where it prefers to be formed from binding of carbon from the conversion of CO_2 to carbon monoxide (orange line) rather than with solid carbon (red line). At high temperatures, hydrogen prefers to bond with solid carbon rather than carbon from the gaseous species, however, at these temperatures, CH_4 becomes relatively less stable than either molecular hydrogen or water. So, from this, it is seen that CH_4 formation is favored at low temperatures, while hydrogen formation is favored at high temperatures.

In this section, the thermodynamics of thermal processing of biomass from the perspective of the constitutive elements, rather than the molecular species, has been discussed. The advantage of this perspective is that it is only necessary to consider the three elements, rather than the multitude of potential molecular species that may form. The equilibrium state of a system is dependent only on its initial *elemental* composition, and not directly to its initial molecular composition. Consequently, it is possible to analyse the thermal processing of a wide variety of organic wastes from knowledge of only its elemental composition.

Here, element chemical potentials have been introduced, which serves as the driving force for chemical reactions, with elements trying to form molecular compounds which minimise their chemical potentials. The formation contribution to the chemical potentials of elemental carbon, oxygen, and hydrogen in different compounds and their variation with temperature were examined. In the next section, this perspective is used to consider the formation of char and its dependence on system temperature and pressure.

5.4 Ternary Diagrams

The dependence that standard element chemical potentials have on temperature have been shown, and consequently the influence this has on the tendency for carbon, hydrogen, and oxygen to form certain molecules at equilibrium. Here, ternary diagrams are introduced, a graphical tool borne from studies on reactive distillation seeking to interpret and present the dependence of three variable systems [155]. Castello and Fiori [128] used two ternary diagrams in their publication to demonstrate the influence of temperature and pressure on the SCWG of biomass.

Figure 5.5a shows an example of a ternary diagram for a thermochemical system. The mole fractions of carbon, hydrogen, and oxygen are plotted along three faces. For a system at equilibrium composed of entirely molecular hydrogen, CO_2, carbon monoxide, CH_4, water, and solid carbon; the convex hull of the

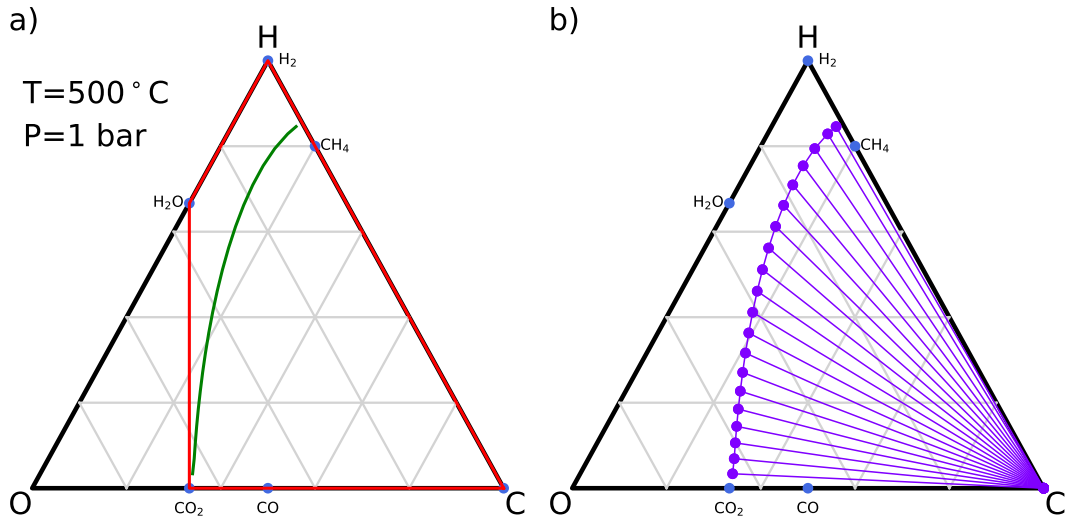

Figure 5.5: Ternary diagrams at $T = 500°C$ and pressure $p = 1$ bar showing (a) the char formation phase boundary and feasible region, and (b), the application of the lever rule to ternary diagrams.

region bound in red represents elemental compositions that are feasible. Given the high chemical potential of elemental oxygen in molecular oxygen (see Fig. 5.3), it is not anticipated that any O_2 to form at equilibrium and thus any oxygen-rich compositions to the left of the line that connect CO_2 to water in Fig. 5.5a are not possible in thermochemical systems without the addition of O_2 to the reaction (which are not considered in this chapter).

The green line in Fig. 5.5a represents the char formation phase boundary, which in this case is at 500°C and 1 bar. If the total elemental composition sits on the left side of this curve, no char is present in the system at equilibrium. A system that falls to the right of the curve will exist in two phases: a solid phase consisting of pure carbon and a gas phase consisting primarily of a mixture of water vapor, CH_4, hydrogen, CO_2, and CO. The phase boundary shifts with temperature and pressure.

The lever rule is used to draw the phase boundary on ternary diagrams, as shown on Fig. 5.5a. A point on the ternary diagram represents the composition of a closed system composed of carbon, hydrogen, and oxygen. If a line is then

extended between the system point and the carbon corner of the ternary, as shown on Fig. 5.5b, moving the system composition along that line towards the carbon corner will cause the fraction of solid phase products ($C_{(s)}$) at equilibrium to increase to a maximum value 1. Whilst moving along this line causes the fraction of equilibrium gas phase products to reduce to 0, the composition of the gas phase (i.e., proportions of CO, CO_2, CH_4, and H_2) will remain unchanged. Moving the system composition along the line in the opposite direction of the carbon corner will increase the fraction of gas phase products to increase to a value of 1 and reduce the solid phase products to 0. This defines a point on the phase diagram. Therefore, by calculating the equilibrium gas phase composition for any point on the ternary, and then determining the composition in terms of carbon, hydrogen, and oxygen of that gas phase product only, a point on the phase boundary will always be defined. By repeating this process for different starting compositions, multiple points along the boundary can be plotted and eventually a full phase boundary drawn.

For a closed system, the composition of a feedstock represents a point on the ternary diagram that does not move during the reaction process. While different operating temperatures and pressures will change the relative quantities of char, hydrogen, CH_4, etc., the elemental composition remains fixed. Figure 5.6 shows some examples of biomass wastes that are appropriate for feedstocks for thermochemical treatment. Their compositions were obtained from the Phyllis2 database [139]. Additionally, the compositions of polystyrene (PS), polyethylene (PE), polyethylene terephthalate (PETE), and polypropylene (PP) plastics are also shown; these were also selected based-upon their applicability for thermochemical valorisation. Note that PE and PP have the same elemental composition; additionally, common plastics containing other elements, such as PVC which contains chlorine, were not included.

The region bound by the green box represents the range of feedstock compositions considered in this work. The boundaries were drawn to allow for a

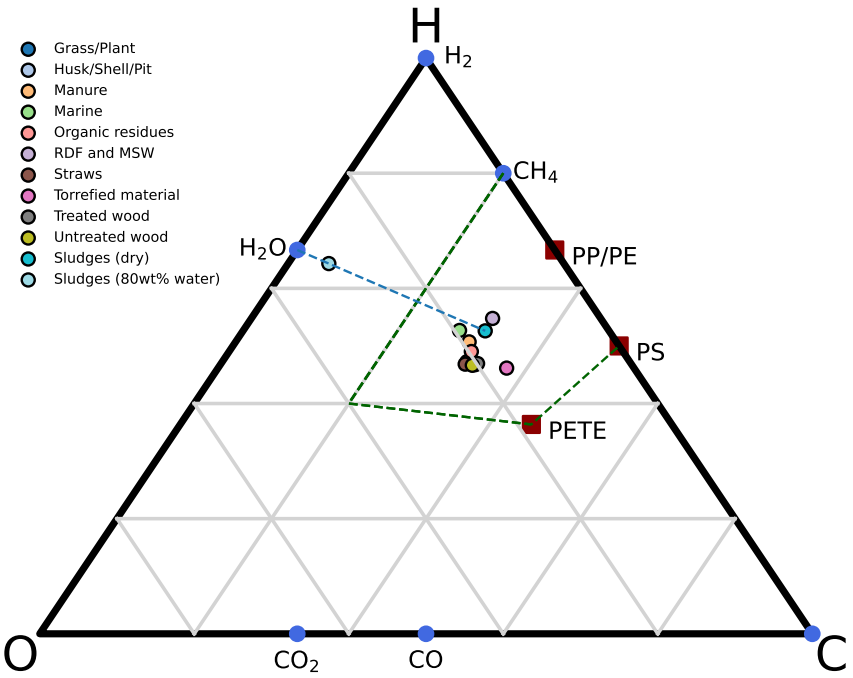

Figure 5.6: Ternary diagram showing the region of feedstock compositions considered in this work.

comprehensive analysis of any feedstock, appropriate for any type of thermochemical conversion. This encompasses biomass, plastics, CH_4 and other hydrocarbon gases. The furthest left corner of the enclosed region stretches towards the oxygen vertex of the ternary as far as it does because this represents formic acid (CH_2O_2), a simple organic frequently found as an intermediate during thermochemical conversions, and at 40 mol.% oxygen is likely the most oxygen-rich species present in thermochemical conversions.

Most real-world feedstocks have an inherent moisture content, which can range from a few wt.% to over 80 *wt.*% in feedstocks like sewage sludge [2]. Two examples of sewage sludge feedstocks are plotted on Fig. 5.6, a dry and an 80 *wt.*% version. Adding water to the system shifts the overall composition along the line connecting water and the initial feedstock on the ternary.

The following section uses the ternary diagrams that have been described here to provide a comprehensive thermodynamic framework of thermochemical systems. Temperature, pressure, and water content are explored as key process variables. Additionally, similar to water, the influence and potential benefit that the addition of CO_2 can have on the thermochemical treatment of waste is shown.

5.4.1 Influence of temperature on the char formation boundary

Here the influence of temperature is described. In Fig. 5.7, the variation of the char formation boundary with temperature for systems at a pressure of 1 bar is plotted. As temperature increases, the phase boundary gradually straightens from a curve that connects a coexisting gas of nearly pure carbon dioxide at low elemental hydrogen content to a gas mixture of molecular hydrogen and CH_4 at low elemental oxygen content to a nearly straight line that connects a gas consisting mainly of carbon monoxide to one containing mainly hydrogen.

For systems with a low hydrogen content (near the bottom of the ternary diagram), increasing temperature moves the char formation boundary towards higher values of carbon, reducing the size of the two-phase region where char formation is possible. This implies hotter reaction temperatures result in lower yields of char at equilibrium, and in the gas phase CO becomes the prevailing site for elemental carbon to occupy. This can be explained using the plot of chemical potential for elemental carbon shown in Fig. 5.2.

The element chemical potential of carbon in CO is consistently lowest which makes it the most stable form for gas phase carbon at all temperatures shown. However, increasing temperature reduces the element chemical potential of carbon in CO, and increased it for carbon in CH_4 and CO_2. At roughly 600°C, the intersection of the CH_4 and carbon monoxide carbon chemical potentials occurs, and at temperatures above this CO becomes a favourable site for carbon to occupy in the gas phase.

For systems with a high hydrogen content (near the top of the ternary diagram), increasing temperature moves the char formation boundary towards higher values of elemental hydrogen, where molecular hydrogen becomes a more preferential gas phase site for elemental hydrogen to occupy versus CH_4. This can be explained using the plot of chemical potential for elemental hydrogen shown in Fig. 5.4. As temperature increases, the element chemical potential of hydrogen in CH_4 increases significantly. There is a slight decreasing trend for the elemental chemical potential of molecular hydrogen for the same temperature change. At around 600°C, the two curves intersect and the chemical potential of elemental hydrogen in CH_4 becomes the larger of the two and thus molecular hydrogen becomes the preferential form of gas phase hydrogen. At a similar temperature, the curves for chemical potentials of hydrogen in water and CH_4 also cross meaning there is a greater tendency for elemental hydrogen to bond with oxygen as opposed to carbon.

5.4.2 Influence of pressure on the char formation boundary

Here the influence of pressure is discussed. The shift of the char formation boundary with pressure at a temperature of 800°C is shown in Fig. 5.8. For systems with low hydrogen content, increasing pressure moves the char formation boundary to lower values of carbon in the system, widening the region where char forms and implying that it becomes easier for char to form. The coexisting gas switches to mainly consisting of CO to mainly consisting of CO_2, as pressure increases.

This behavior can be rationalised in terms of Le Chatelier's principle. When solid carbon reacts with CO_2 to enter the gas phase, two moles of CO are formed:

$$CO_{2(g)} + C_{(s)} \rightleftharpoons 2CO_{(g)}$$

Consequently, the pressure of the system will tend to increase as solid carbon enters the gas phase, so increasing pressure will tend to favor char formation.

For systems with low oxygen content and relatively high hydrogen content (near the top corner of the ternary diagram), increasing pressure moves the char

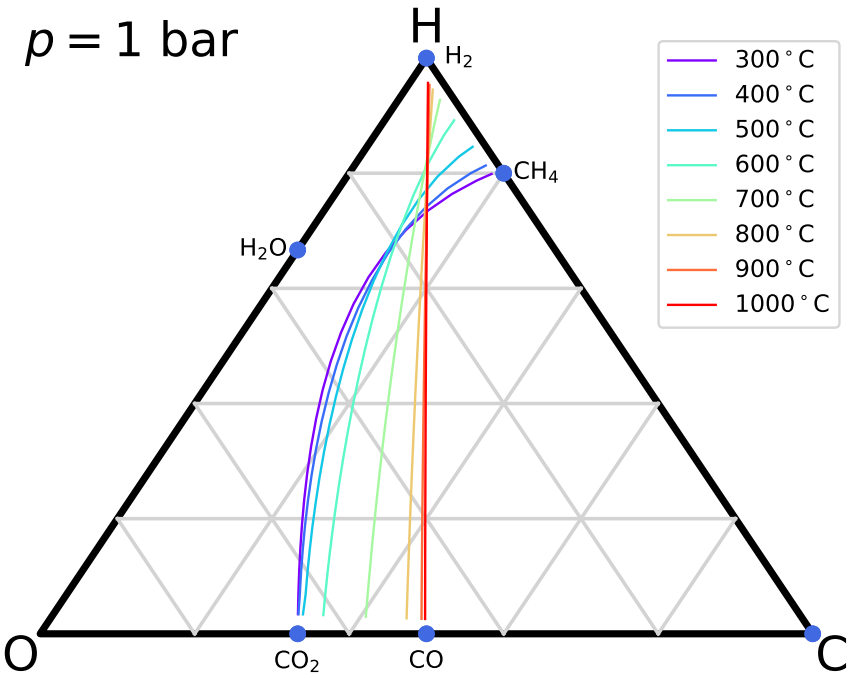

Figure 5.7: Ternary diagram showing the effect temperature has on the char phase boundary at $p = 1\,\mathrm{bar}$.

formation boundary to higher values of carbon in the system, shrinking the region where char forms and implying that it becomes more difficult for carbon to precipitate from the gas phase. The coexisting gas switches to mainly consisting of hydrogen to mainly consisting of CH_4, as pressure increases.

This behavior can also be rationalised in terms of Le Chatelier's principle. When solid carbon reacts with hydrogen gas to form CH_4, two moles of molecular hydrogen are removed from the gas phase and replaced by one mole of CH_4, thereby tending to reduce the pressure of the system.

$$2H_{2(g)} + C_{(s)} \rightleftharpoons CH_{4(g)}$$

Thus, increasing pressure is shown to tend to shift the reaction equilibrium to the right, making char formation more difficult.

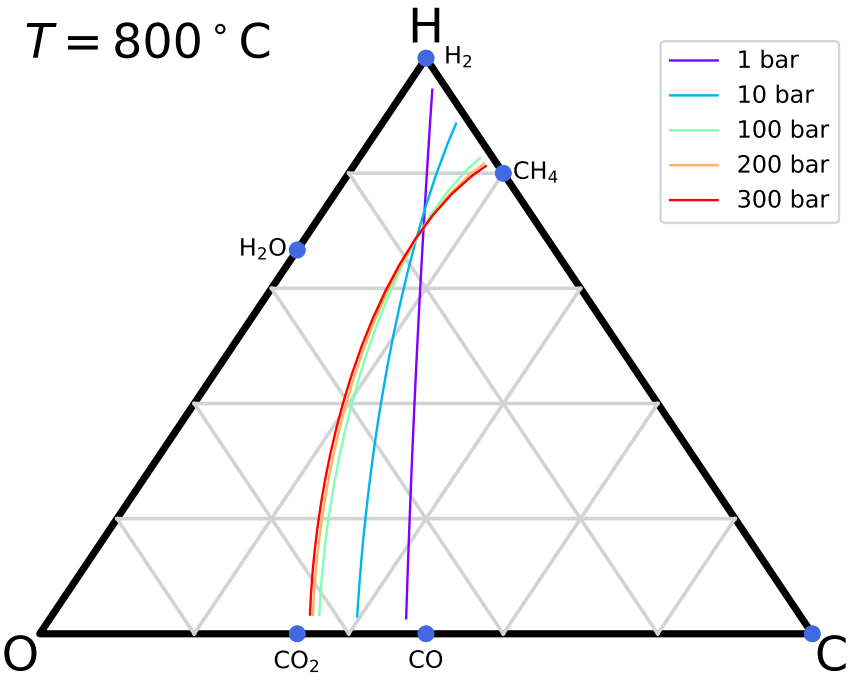

Figure 5.8: Ternary diagram showing the effect pressure has on the char phase boundary at 800°C.

In Fig. 5.9, the variation of the char formation boundary with pressure is shown at a temperature of 500°C. At this lower temperature, it is shown that the influence of pressure is qualitatively the same at the higher temperature of 800°C, although the effect is not as significant.

At low temperatures, CH_4 is favored over molecular hydrogen, which tends to make char formation more difficult, while at high temperatures, hydrogen is favored, which makes char formation easier. Equally, at low temperatures, CO_2 is favored over CO, which tends to make char formation easier, while at high temperatures, CO is favored, which makes char formation more difficult.

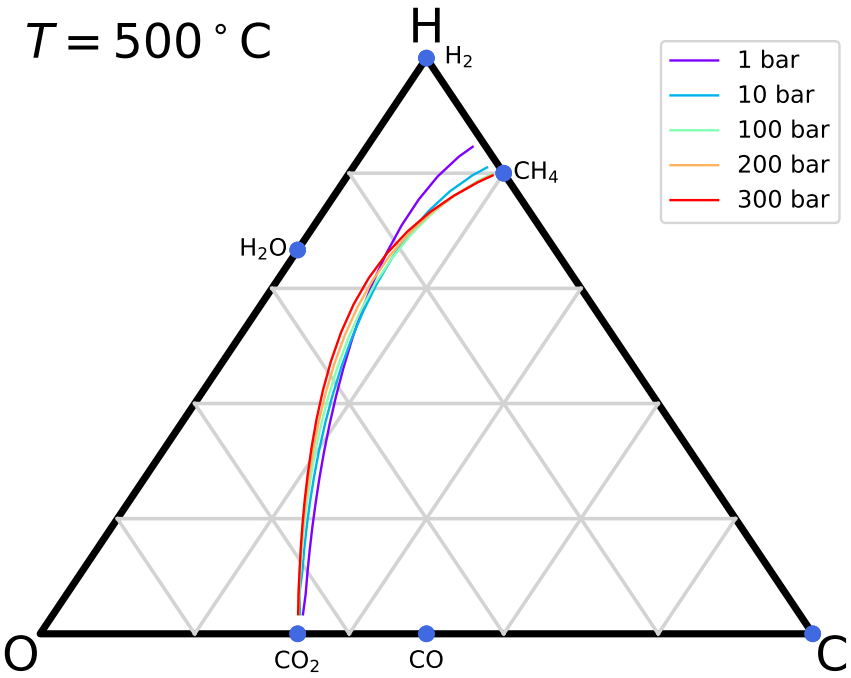

Figure 5.9: Ternary diagram showing the effect pressure has on the char phase boundary at 500°C.

5.5 Influence of Elemental Composition

Isobaric formation chemical potentials and Le Chatelier's principle have been used to demonstrate how temperature and pressure, respectively, alter the two-phase behavior and gas composition of thermochemical systems at equilibrium. The second term in Eq. (5.8) shows the dependence of chemical potential on the concentration/partial pressure of a species. Increasing the concentration of a species increases its chemical potential and therefore makes its formation in thermochemical processes at equilibrium less favourable. In this section, how the elemental composition of a system can be adjusted is explored, in much the same way temperature and pressure conventionally are, in order to achieve a desired response. Here, the main process indicator considered was char formation, and the

location of the phase boundary that separates the two regions where its formation is possible and infeasible. In processes like torrefaction and HTC, char is the desired product and operators seek to increase yields of this solid form of elemental carbon. On the other hand, when gases are the intended products during gasification and HTG/SCWG, char formation is avoided as it can cause damage, plugging, and taring of process equipment and signifies a loss in waste-to-gas conversion.

The addition of two agents is considered in this section: water and carbon dioxide. Water is present in varying concentrations in most forms of organic wastes, and as illustrated on Fig. 5.6 its presence shifts the composition of a dry system along towards the location of water on the ternary. Hydrothermal processes are specifically designed to treat high-moisture feedstocks by taking advantage of superior reaction kinetics that are only attainable at elevated pressures [2]. The addition of water/steam to other processes like gasification is a well-established means of increasing hydrogen yields and suppressing the formation of solids [156]. CO_2 is another cheap, abundant, non-toxic process fluid that is considered here as a potential additive to thermochemical processes. Although its affects are not as well understood as water, there are numerous publications in literature demonstrating the benefits that can be brought about by use of CO_2 as a reaction co-medium. Moreover, the utilisation of carbon dioxide in chemical processes is a field of research of increasing interest globally given the potential for neutral or negative carbon emissions.

Figure 5.10 shows a section of a ternary diagram where the location of an example biomass, mixed straws (32 mol% C, 47 mol% H, and 21 mol% O), is plotted. The blue and green lines show how the composition of the mixed straw system will change as water and CO_2 are added, respectively. In each case, an example composition is plotted representing the composition when 1 mole of water or CO_2 is added per mole of carbon in mixed straw. The region shaded in blue represents all possible compositions that could be attained by adding a mixture of water and CO_2 to mixed straw.

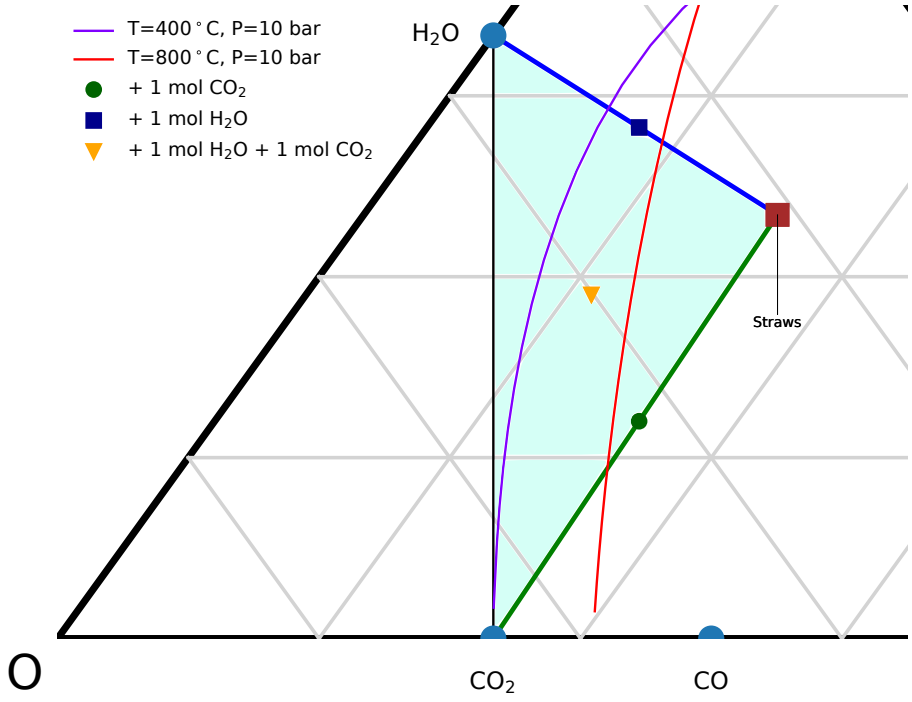

Figure 5.10: Ternary diagram section demonstrating the range of possible total system compositions attainable by adding water and/or CO_2 to a mixed straws (32 mol% C, 47 mol% H, and 21 mol% O) feedstock.

The following results use ternary diagrams to provide a set of comprehensive visual aids that can be used to ascertain the critical relationship between water or CO_2 addition and char formation from the thermochemical processing of any foreseen composition of organic waste (dry), at the likely range of reaction temperatures and pressures.

5.5.1 The Addition of Water

Figure 5.11 plots equilbrium yields of syngas and char from the thermochemical processing of mixed straws for a range of process conditions. The x-axis in each plot is the added amount of water to a fixed amount of dry feedstock, in terms of weight percentages. The yields are in units of mmol per gram of mixed

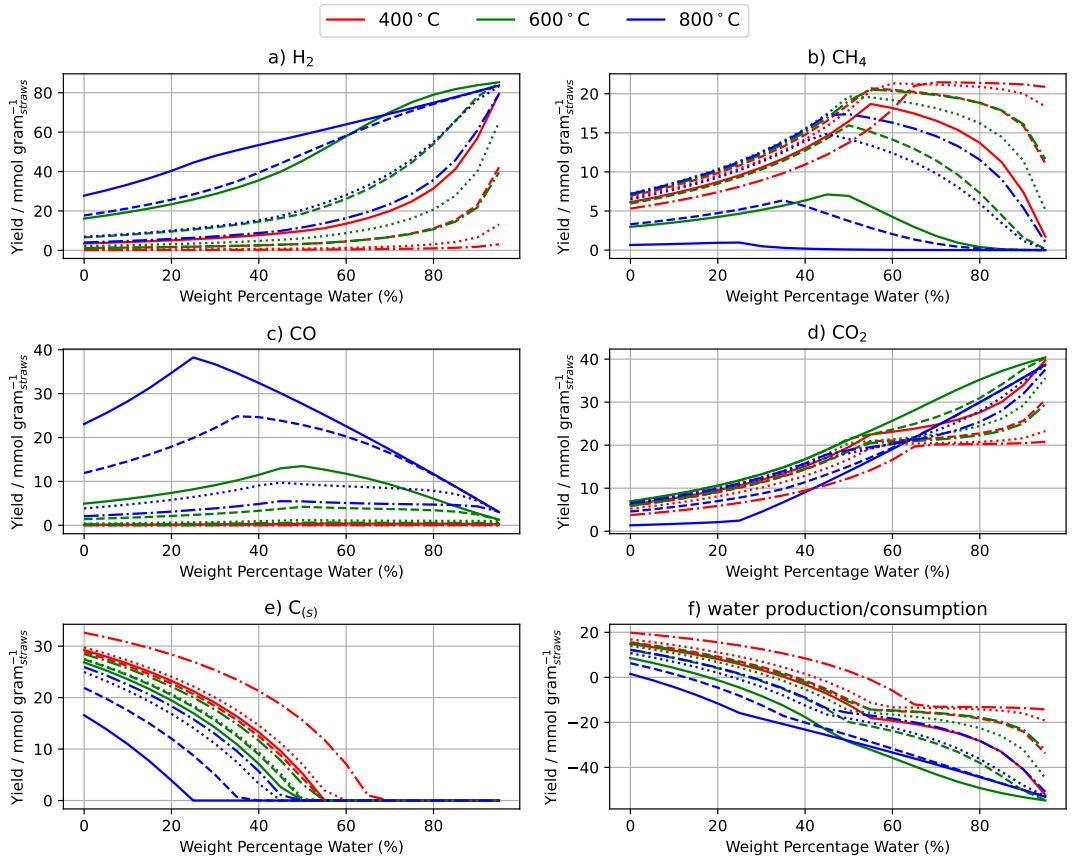

Figure 5.11: Equilibrium product yields from mixed straws feedstock (32 mol% C, 47 mol% H, and 21 mol% O) versus weight percentage water at 400°C, 600°C, and 800°C and pressures of 1 bar (solid), 10 bar (dotted), 100 bar (dashed), and 300 bar (dashdot). The production/consumption of water is plotted as moles out minus moles in.

straws (mmol $\text{gram}^{-1}_{\text{straw}}$). Similar graphs have been reported in the literature, as Gibbs reactors have been used numerous times to demonstrate the influence temperature, pressure, and moisture content have on equilibrium yields of char and syngas from the thermochemical processing of organic waste. It is generally understood that higher reaction temperatures and moisture contents favour a greater yield of molecular hydrogen and CO_2 at equilibrium, but a lower yield of CH_4 and solid char [128, 157]. Here, the objective was to report the same findings but to also offer some unique insight into the observed trends occur from the perspective of element chemical potentials.

Figure 5.11a shows that, in general, higher temperatures lead to a higher

yield of H_2. This can be rationalised by the steady decrease of the element chemical potential of hydrogen in H_2 with increasing temperature (see Fig. 5.4). At temperatures above roughly 600°C in particular, the element chemical potential of hydrogen in H_2 is lower than in CH_4 (see Fig. 5.4), which makes H_2 a more favourable molecule for hydrogen to form. Lower pressures are also seen to favour H_2 yields. This can be explained in terms of Le Chatelier's principle. where the formation of H_2 is defined as. Molecular hydrogen can be formed either by the reaction of CH_4 and CO_2

$$CH_{4(g)} + CO_{2(g)} \rightarrow 2H_{2(g)} + 2CO_{(g)} \tag{5.10}$$

or by the decomposition of CH_4

$$CH_{4(g)} \rightarrow 2H_{2(g)} + C_{(s)} \tag{5.11}$$

resulting in the precipitation of solid carbon. In both cases, the reactions result in the formation of more molecules in the gas phase, and, consequently, it is expected that lowering the pressure will increase the forward extent of these reactions, resulting in more molecular hydrogen.

Figure 5.11a also demonstrates that increasing water to the system increases the yield of H_2 per gram of dry biomass (mixed straws), but most significantly at high temperatures. This can also be explained with reference to Fig. 5.4. Adding water to a system increases the element chemical potential of hydrogen in water. At low temperatures, the added molecular hydrogen preferentially forms CH_4 as it has a lower element chemical potential, however, increasing temperatures makes H_2 the more favourable molecular form for hydrogen to transfer into.

Figure 5.11b shows that lower temperatures favour the formation of CH_4. Increasing temperature does slightly decrease the element chemical potential of hydrogen in CH_4 (see Fig. 5.4), but not as much as H_2 (or water) as mentioned above. Additionally, the chemical potential of carbon in CH_4 increases with temperature, and crosses the curve for CO at around 600°C which makes CH_4

a less favourable molecule for carbon to form at higher temperatures. Higher pressures favour the formation of CH_4. This can be explained by applying Le Chatelier's principle to the reactions for the formation of CH_4, which are given by the reverse of the reactions in Eqs. (5.10) and (5.11). In this case, the formation of CH_4 results in a decrease in the number of gas species, which will be favoured when pressure is increased.

The addition of water to the system first increases, and then decreases yields of CH_4. The maximum yields occur at greater concentrations of water when pressures are higher and temperatures are lower. The subsequent decrease in CH_4 yields is less severe at higher pressures too. At low temperatures (i.e. 400°C), CH_4 has the lowest elemental chemical potential of hydrogen (see Fig. 5.4) and adding water favours the conversion of molecular hydrogen into CH_4. The carbon comes from $C_{(s)}$ which is still formed at these low temperatures and has a higher carbon element chemical potential than carbon in CH_4. At 800°C and 1 bar, the initial addition of water has a negligible effect on CH_4 yields as the chemical potential of hydrogen in CH_4 is too high at these conditions. Beyond the maxima, the decrease in CH_4 yields observed with the addition of water on Fig. 5.11b is a result of the preferential formation of CO and CO_2 over CH_4, which is required to occupy the oxygen that is added via water.

Figure 5.11c the yields of CO are increased by using hotter reaction temperatures. The element chemical potential of carbon in CO steadily decreases as temperature is increased which makes CO a more favourable site for carbon to occupy. Lower pressures favour the formation of CO, which is justified with the formation equation for CO and knowledge of Le Chatelier's principle.

$$C_{(s)} + \frac{1}{2}O_{2(g)} \rightarrow CO_{(g)} \tag{5.12}$$

A greater number of gas-phase moles occur on the right-hand side of the equation and consequently lower pressures shift equilibrium in the forward direction. The addition of water on CO yields has a similar effect as it did on CH_4, although here

the maxima occur at lower weight percentages of water at higher temperatures and lower pressures. At lower concentrations of water, when $C_{(s)}$ formation is prevalent, CO is a favourable site for elemental oxygen. At greater concentrations of water, the increasing concentration of elemental oxygen in the system makes CO_2 become the favourable molecule to form as it has a lower oxygen chemical potential.

Figure 5.11d shows that reaction temperature and pressure have a less obvious relationship with CO_2 yields. The 600°C and 1 bar case has consistently the greatest yield of CO_2. At lower weight fractions of water, the cooler temperature of 400°C has the second highest yield whereas the hotter temperature of 800°C has the lowest. At some point between 60–80 wt.% water, these two curves cross and the 400°C curve yields the lowest CO_2 at $1\,bar$. The formation of CO_2 from its elemental constituents has balanced gas moles meaning the position of equilibrium is unaffected by changes in pressure. The variations of CO_2 yield with pressure shown on Fig. 5.11d are therefore the knock-on effect from other species in competition with CO_2.

$$C_{(s)} + O_{2(g)} \rightarrow CO_{2(g)} \tag{5.13}$$

At all conditions shown, the addition of water has a positive effect on CO_2 yields. This is a direct consequence of the increasing content of elemental oxygen in the system that occurs with water addition. Figure 5.3 shows that the formation of CO_2 from CO at low temperatures, or the formation of CO_2 from $C_{(s)}$ at high temperatures, has a lower oxygen chemical potential than water.

Figure 5.11e definitively shows that higher temperatures and lower pressure favour a reduction in yields of solid $C_{(s)}$. For all conditions shown, the addition of water results in the complete suppression of any char formation. Elemental carbon will preferentially form CO_2 and CO upon the addition of water in order to lower the chemical potential of elemental oxygen in the system. The suppression of char on Fig. 5.11e corresponds to the system composition crossing the phase boundary on the ternary diagram into the single phase region. At lower temperatures and

higher pressures, the phase boundary becomes more curved (see Fig. 5.9), which means more water is required to shift the composition of a dry, organic material across the phase boundary into the single-phase gas region.

The final subplot on Fig. 5.11 plots the production/consumption of water (i.e. moles of water out minus moles of water in). There is a direct correlation between the consumption of water and the production of H_2 shown on Fig. 5.11a. Generally, higher temperatures and lower pressures favour a greater consumption of water, however, as was the case for H_2 the 600°C and 1 *bar* case has the highest yields at concentrations of water above 60 wt.%. Figure 5.4 shows that the element chemical potentials of hydrogen in water and molecular hydrogen are closely matched. The addition of water increases the elemental chemical potential of hydrogen in water and makes molecular hydrogen a more favourable site, particularly at high temperatures.

A key response to the addition of water in thermochemical system is the suppression of char formation. For processes like gasification where the objective is to optimise the production of a fuel-rich syngas, this is a beneficial effect. However, extra work is required to bring the added water up to operating pressure and temperature; and too much water can also inhibit the kinetics of gasification reactions. It is therefore pertinent to minimise the quantity of water required to achieve the desired response. Figure 5.12 plots a series of ternary diagrams which show the minimum amount of water required to move into the char-free region for a given feedstock composition that has been standardised to contain 1 mole of carbon.

At 400°C, the phase boundary is at its most curvaceous and sits far away from the pure carbon vertices of the ternary. Feedstocks positioned in the more oxygen-rich region of the partition (lower left) require the least water, and at 1 bar need as less than 20 wt.% water to enter the char-free region. Increasing pressure extends the distance between the phase boundary and the feedstock region, and at 300 bar those same oxygen-rich feedstock need upwards of 40 *wt.*% water. Those feedstocks

with a high carbon content, such as PS and PETE shown on Fig. 5.6, require as much as 70 wt.% water at 1 bar which goes up to nearly 80 wt.% water at 300 bar

Increasing the temperature of the system straightens the phase-boundary towards the vertical. It can be seen that at 800°C and 1 bar, a significant portion of the oxygen-rich feedstocks lie to the left of the phase boundary and consequently require no added water for char-free gasification. At this condition, the most carbonaceous feedstocks require around 50 wt.% water to cross the phase-boundary which is comparatively low. Increasing pressure at these higher temperatures naturally reduces the portion of feedstocks that sit to the left of the phase boundary.

5.5.2 CO_2 Addition

Within the scope of biomass and plastic thermochemical treatment, widespread attention has been paid to the use of CO_2 as a co-gasification agent [158]. Additionally, research into the utilisation of CO_2 in other processes like pyrolysis [159], and hydrothermal processes like liquefaction [160] and SCWG [161] have also been explored. In each case, it was found that CO_2 assisted thermochemical processes can offer benefits relating to reduced energy consumption, improved product yield, and/or captured carbon. With recent focus being on waste-to-energy processes incorporating carbon capture and utilisation (e.g., BECCUS) [162, 163], CO_2 utilisation in thermochemical processes is becoming an ever-increasingly crucial component of their commercial viability.

Figure 5.13 shows how the addition of CO_2 changes the yields of gas and solid phase products. Three temperatures (400°C, 600°C, and 800°C) and two pressures (10 bar and 300 bar) are plotted for a case study mixed straws feedstock with two different moisture contents: 0 wt.% and 50 wt.% water. Compared to water addition, the influence of added CO_2 on equilibrium has seldom been reported. A thermodynamic model used in literature reported that the addition of CO_2 to a glycerol feedstock will generally reduce H_2 yields and increase the formation of char [164].

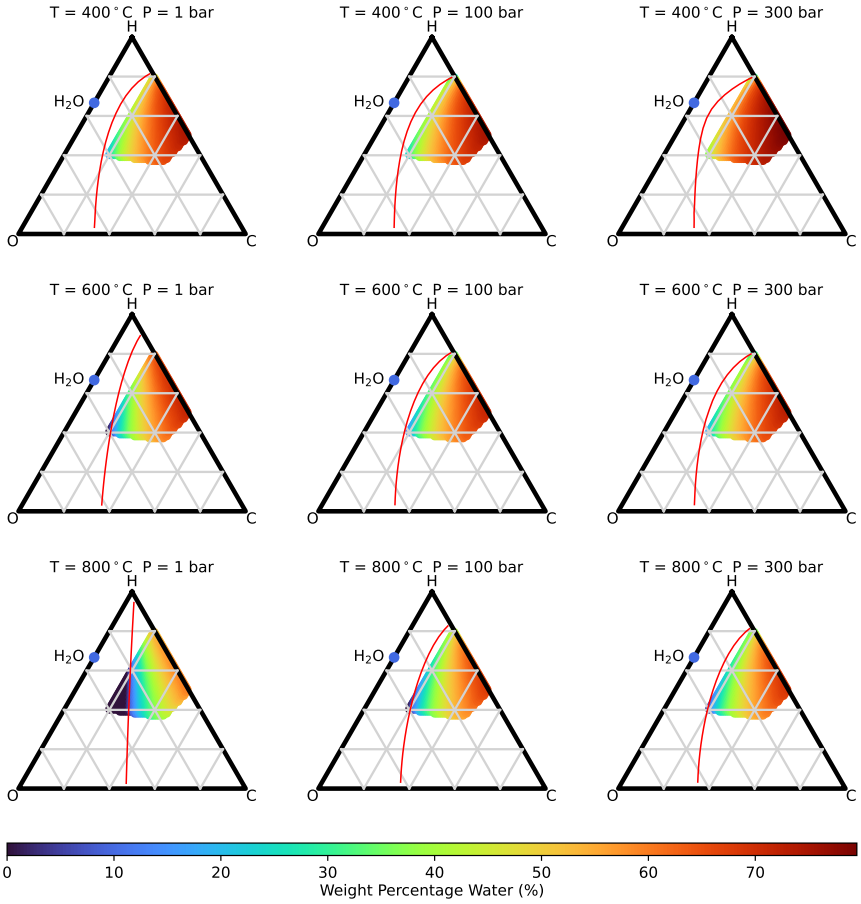

Figure 5.12: Minimum weight fraction water required to suppress char formation from the thermochemical treatment of biomass and plastics at different temperatures and pressures.

At both 0 wt.% and 50 wt.% water, the yield of H_2 is only affected by the addition of CO_2 at temperatures of 600°C or higher, and at 1 bar. Here, a steady decrease is observed upon adding CO_2. This observation can be justified by referencing the element chemical potentials of oxygen and hydrogen in H_2, CH_4, and water. Adding CO_2 increases the element chemical potential of oxygen in this molecule. At lower temperatures and higher pressures, yields of water increase

as it has the next lowest oxygen chemical potential. The hydrogen required to form water comes from CH_4 which is present in greater concentrations at lower temperatures and has a relatively high hydrogen chemical potential. As temperature is increased, H_2 yields are greater than CH_4 as it is a more favourable site for hydrogen. The addition of CO_2 at high temperatures consequently relies upon the conversion of H_2 into water to reduce the overall element chemical potential of oxygen.

The addition of CO_2 increases yields of CO, with a more notable increase occurring in the absence of water at 800°C and 1 bar. Here, adding 20 moles of CO_2 per gram of straw feedstock can quadruple yields of CO from roughly 20 to 80 mmol g_{straw}^{-1}. Comparing this to the plots for CO_2 and $C_{(s)}$ at the same conditions, it is clear that this extra 60 mmol g_{straw}^{-1} came from 40 and 20 mmol g_{straw}^{-1} of elemental carbon from CO_2 and $C_{(s)}$, respectively.

The most interesting of all cases presented is the char yield. In the absence of water at 400°C and at all pressures, the addition of CO_2 increases yields of $C_{(s)}$. At 800°C and all pressures, the addition of CO_2 suppresses the formation of $C_{(s)}$. At 800°C, adding CO_2 initially increases yields of $C_{(s)}$ but then decreases them, with greater yields being obtained at higher pressures. A similar trend is observed at 50 wt.% water, although in all cases less $C_{(s)}$ is produced. From the perspective of chemical potential, these results can be explained using Fig. 5.2. Increasing temperatures reduces the element chemical potential of carbon in CO. At low temperatures, the addition of CO_2 leads to the formation of $C_{(s)}$, however, at high temperature CO is the preferential molecule for carbon to occupy. This temperature-dependent relation between CO_2 addition and char formation can also be linked to the shape of the phase boundary presented in the ternary diagrams. Figure 5.10 shows that at 800°C, the phase boundary aligns more closely with the vertical axis, and consequently the line which connects the composition of organic waste to CO_2 readily crosses this phase boundary. This means CO_2 can be added to a system and these conditions and used to shift the composition into

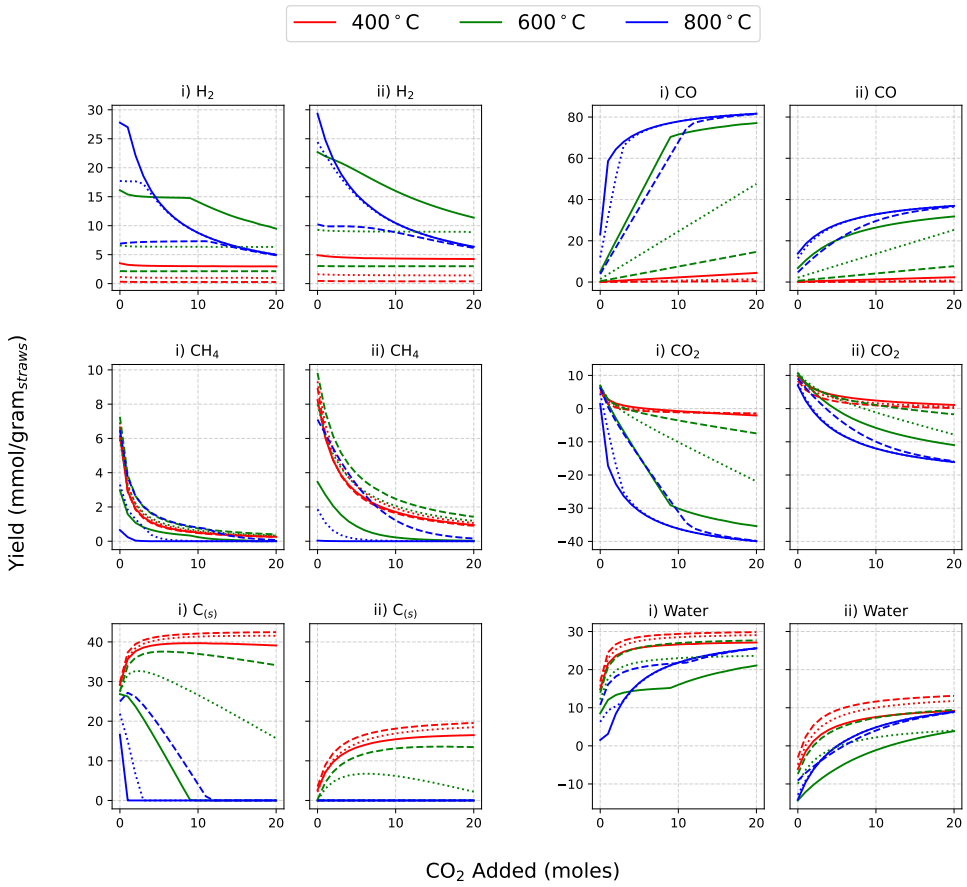

Figure 5.13: Equilibrium product yields from (i) 0 wt.% water, (ii) 50 wt.% water, mixed straws feedstock (32 mol% C, 47 mol% H, and 21 mol% O) versus weight percentage CO_2 at 400°C, 600°C, and 800°C and pressures of 1 bar (solid), 10 bar (dotted), and 100 bar (dashed). The production/consumption of water and CO_2 is plotted as moles out minus moles in.

the single-phase, char-free zone. At lower temperatures, like 400°C, the phase boundary is more curvaceous, the two lines never cross, and this it is not possible to exit the two-phase region via the addition of exclusively CO_2.

It is known from the lever rule, as discussed in relation to Fig. 5.5b, that compositions that lie closer to the carbon corner (bottom-right) of the ternary have a greater proportion of solid carbon in the equilibrium products. The addition of CO_2, which shifts the composition of the system along the line that connects the starting feedstock to CO_2 (green line on Fig. 5.10), can result in

either the decreased or increased char yields depending on the shape of the phase boundary. Figure 5.7 shows that the phase boundary tends to the vertical at high temperatures and the addition of CO_2 therefore readily shifts the composition of the system into the char-free region. This is demonstrated by the suppression of char shown at high temperatures on Fig. 5.13. Conversely, at lower temperatures the phase boundary is curved and located much further away from the carbon corner of the ternary. The addition of CO_2 in this case can bring the composition of the system closer to the carbon corner while still remaining in the two-phase region which corresponds to a greater yield of char at equilibrium. Again, this was shown at 400°C on Fig. 5.13.

To explore the role CO_2 plays as a char-suppresant, Fig. 5.14 plots a series of ternaries which demonstrate the amount of CO_2 required to cross the phase boundary for a feedstock composition that has been standardised to contain 1 mole of carbon. Since Fig. 5.13 indicates that CO_2 can be used to mitigate char formation at high temperatures only, here only high temperatures are investigated.

At 600°C, around 40 wt.% CO_2 can be used to suppress char formation from the most oxygen-rich portion of the feedstocks studied at 1 bar. However, at higher pressures, there is a unanimous requirement of over 80 wt.% CO_2 for all the feedstocks. At 800°C and 1 bar, the clear vertical gradients of color correspond to feedstock compositions that have a fixed difference in carbon and oxygen content. At compositions close to the right-hand side of the boundary, less than 20 wt.% CO_2 is required to cross the phase boundary. As carbon content increases, this increases to around 70 wt.%. Increasing pressure has no benefit and only increases the amount of CO_2. Increasing the temperature further to 1000°C serves only to increase the region of the feedstocks studied where CO_2 can be used to suppress char.

From the perspective of increasing char formation in low temperature thermochemical processes, the ternary diagrams in Fig. 5.15 have been plotted. Here the maximum percentage conversion of carbon in the feedstock into char is shown,

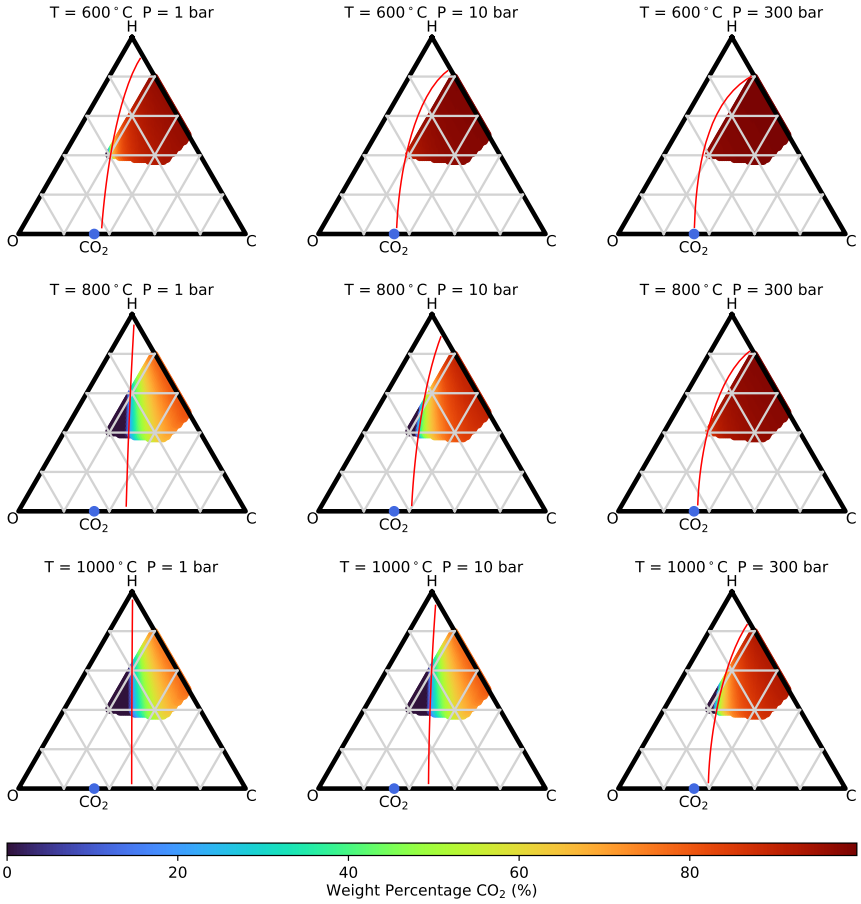

Figure 5.14: Minimum weight fraction CO_2 required to suppress char formation from the thermochemical treatment of biomass and plastics at different temperatures and pressures.

and also the number of moles of added CO_2 required to reach that maximum. Instinctively, Fig. 5.15a shows that feedstocks with a greater content of carbon yield more solid carbon at equilibrium. Reducing the carbon content from its maximum to its minimum reduces the carbon conversion from 40% to below 5%. From Fig. 5.15b, it is shown that a region of feedstocks exists where the amount of CO_2 required to maximise char yields is 0.

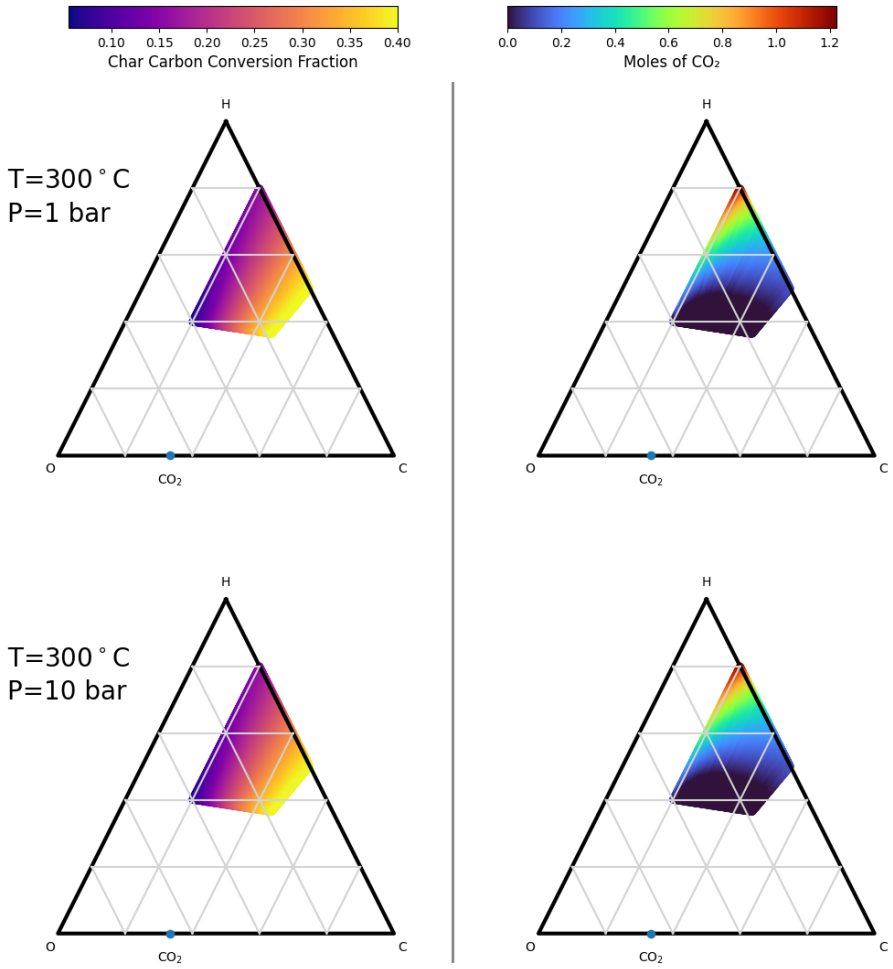

Figure 5.15: Maximum char yields and weight fraction of CO_2 added during thermochemical treatment of biomass and plastics.

Increasing temperature and pressure increases the size of this region. It is shown that for carbonaceous feedstocks, adding small quantities of CO_2 can offer benefits.

5.6 Optimising Supercritical Water Gasification

So far, it has only been examined how the equilibrium solid and gas composition of a system depends on its temperature, pressure, and elemental composition. The efficiency of SCWG or any thermochemical conversion processes is, however,

not solely subject to the quality of the product, as it also depends on the amount of work required to achieve it. To appreciate the energy cost required to reach a certain equilibrium composition, the type of starting biomass molecules must be taken into consideration.

In this subsection, a method is developed to allow operators to optimise the efficiency of the SCWG of specific feedstocks. Here, the SCWG of acetic acid and wheat straw is studied to explore how temperatures and pressures typical of gasification/SCWG and the addition of water and carbon dioxide can be used to optimise the process. Acetic acid is a stable intermediate frequently formed during the thermochemical treatment of biomass [165]. The conversion of acetic acid can be considered a rate-limiting step in the overall process of converting biomass to syngas [143]. Wheat straw is a commonly used feedstock for thermochemical valorisation, and there is fair abundance of experimental data for it in the literature, including ultimate analyses which pertain to its elemental composition. The specific objective here is to maximise the higher heating value (HHV) of gases produced from a particular biomass feedstock.

In order to optimise the conditions for the thermochemical conversion of a particular feedstock material, it is necessary to choose a manner to quantitatively assess the quality of the final product (i.e. syngas) and also the cost of running the process.

It was required to select an appropriate metric to value the quality of syngas in each case. This needed to incorporate the fuel value of the syngas, but also its purity. It is not sufficient to only describe syngas quality in terms of the sum of its combustible components, as this does not factor in the presence of noncombustible permanent gases (i.e. CO_2) which cannot be easily separated and dilutes the final gas product. The higher heating value of the syngas was described using [164]

$$\mathrm{HHV} = C_f(n_{\mathrm{H_2}}\mathrm{HHV}_{\mathrm{H_2}} + n_{\mathrm{CH_4}}\mathrm{HHV}_{\mathrm{CH_4}} + n_{\mathrm{CO}}\mathrm{HHV}_{\mathrm{CO}}) \tag{5.14}$$

where $\mathrm{HHV}_{\mathrm{H_2}} = 147.74\,\mathrm{kJ\,g^{-1}}$, $\mathrm{HHV}_{\mathrm{CH_4}} = 55.74\,\mathrm{kJ\,g^{-1}}$, and $\mathrm{HHV}_{\mathrm{CO}} = 10.11\,\mathrm{kJ\,g^{-1}}$, and the combustible fraction C_f is the mole ratio of the combustible gas species to the total permanent gases.

The choice of cost can be done in many ways (e.g., as measured by money, energy usage, environmental impact, etc.). Here the cost of a process is quantified based on the enthalpy ΔH required to take the initial mixture of biomass and any additives at ambient temperature $T_0 = 25°\mathrm{C}$ and pressure $p_0 = 1\,\mathrm{bar}$ to the operating gasification temperature T and pressure p which results in the equilibrium composition of syngas and char:

$$\Delta H = H(T, p) - H(T_0, p_0) \tag{5.15}$$

where H is the total system enthalpy. Note that in order to calculate the initial enthalpy of a system, the enthalpy of formation of the feedstock and any additives is required.

Finally, the effectiveness of the process is characterized through the net heating value η, defined as

$$\eta = \mathrm{HHV} - \Delta H, \tag{5.16}$$

which is the difference between the heating value of the syngas product and the enthalpy cost of bringing the system to reactor conditions.

5.6.1 Acetic acid

First consider acetic acid ($\mathrm{C_2H_4O_2}$), which has a standard enthalpy of formation of $-483.52\,\mathrm{kJ\,mol^{-1}}$ [166]. The net heating value is plotted in Fig. 5.16. The optimum for the range of conditions examined is at 1 bar and $800°C$. Here, around 20 wt% $\mathrm{CO_2}$ or 15 wt% water can be added to acetic acid to yield around $17.5\,\mathrm{MJ\,kg^{-1}_{acetic}}$. Increasing the pressure of a system into the supercritical region (e.g., $> 22.1\,\mathrm{MPa}$) reduces the efficiency, which suggests in this case there is no thermodynamic benefit to conducting SCWG as opposed to a different, low pressure thermochemical treatment.

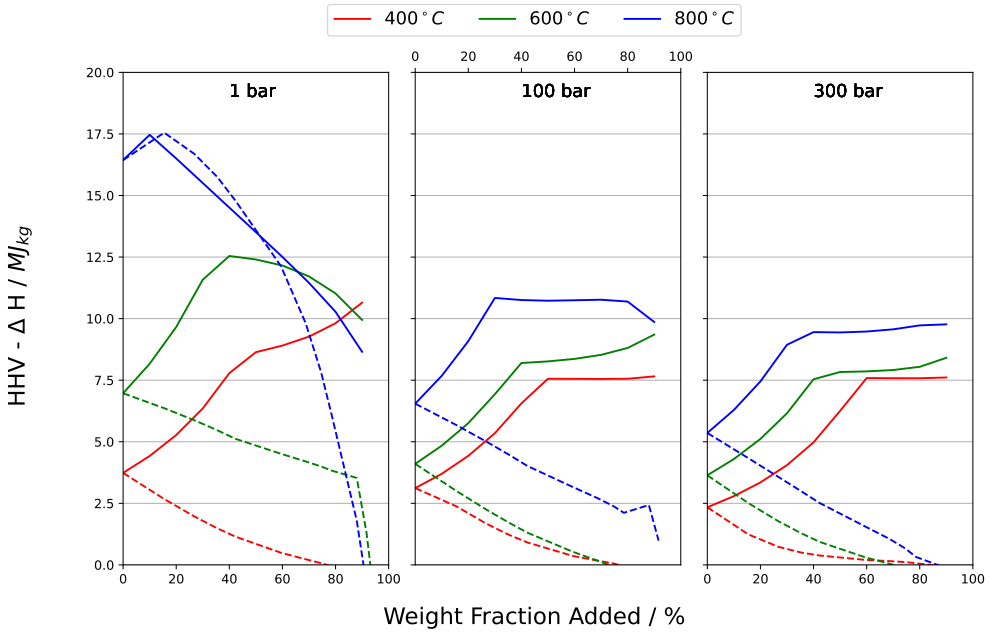

Figure 5.16: Variation of the net heating value of acetic acid gasification/SCWG versus weight fraction of added water (solid) and CO_2 (dashed) at different operating temperatures and pressures.

Without the addition of water, the element composition of the biomass lies in the char-forming region. The main benefit of initially adding water is to reduce the formation of char, thereby increasing the formation of syngas. If sufficient water is added, then the system exits the char-forming region of the ternary diagram (see Fig. 5.7). At 1 bar, around 40 wt% water can be added to maximise efficiency at 600°C, whereas at 400°C increasing water content into the region of 90 wt% produces a steady improvement to efficiency. Conversely, a maximum is reached after adding 60 wt% water to a system at 300 bar and 400°C. The maximum can be reduced to 40 wt% at this SCWG pressure by increasing the temperature to 800°C.

At 1 bar, the maxima of the net heating value at 600°C and 800°C and the kink at 400°C are associated with the system moving from inside to outside the char-forming region. Once outside the char-forming region, whether the addition of water enhances or detracts the net heating value depends on the temperature and pressure of the system. At pressures higher than 1 bar, the maximum net

heating value is lower. Adding water still offers a benefit to efficiency, although the plateau which appears at around 40–50 wt% is likely because all char formation is suppressed beyond this point and no further benefit comes from adding water.

The addition of CO_2 is beneficial only in the region between 0 and 20 wt% at 800°C and 1 bar. The initial increase in the net heating value is associated with the reduction of char formation, and the peak is where the system exits the char-forming region. Outside this region, however, little of the added CO_2 is converted to CO, and so the net heating value is reduced. At higher pressures and lower temperatures, adding CO_2 results in a reduction of the system efficiency.

5.6.2 Wheat straw

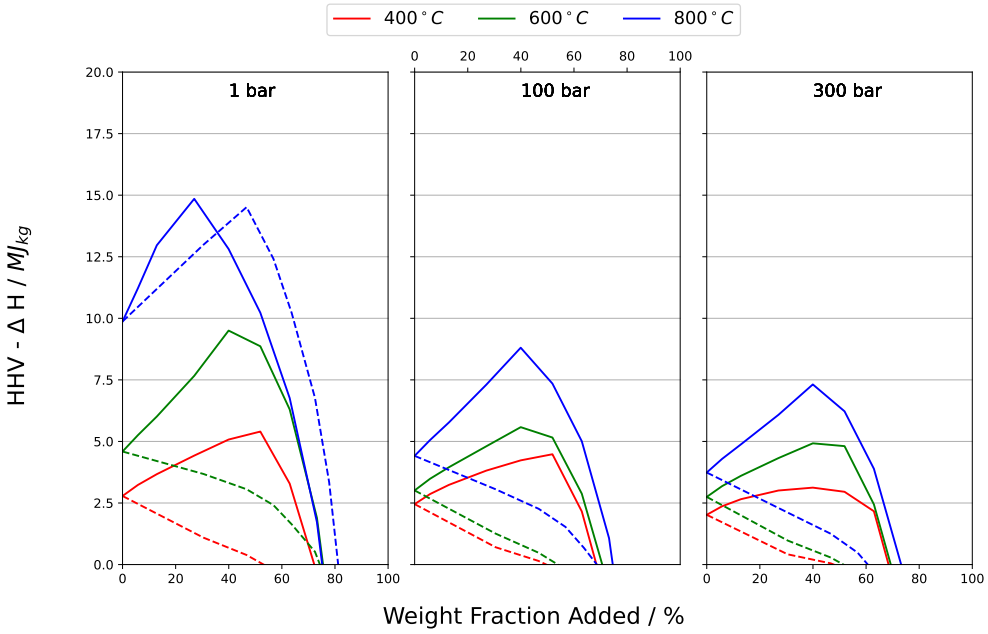

Figure 5.17: Variation of the net heating value of wheat straw gasification/SCWG with the weight fraction of added water (solid) and CO_2 (dashed) at different operating temperatures and pressures.

Now take the SCWG of wheat straw. The Phyllis2 [139] database was used to obtain an average wheat straw elemental composition of 50.1 wt% carbon, 6.17 wt% hydrogen, and 43.8 wt% oxygen, respectively.

As was necessary for acetic acid, the enthalpy of formation of wheat straw is needed in order to determine the heat required to reach equilibrium. The formation enthalpies for real-world biomasses are not commonly reported as they do not possess a fixed molecular structure; however, they can be estimated from their heats of combustion (or, equivalently, their heating value). If experimental combustion data are unavailable, an empirical relationship can be used to estimate the heat of combustion for any biomass, such as that provided by Channiwala and Parikh [167]

$$H_{\text{comb}} = m_{\text{C}} H_{\text{C}} + m_{\text{H}} H_{\text{H}} + m_{\text{O}} H_{\text{O}} \tag{5.17}$$

where H_{comb} is heat of combustion on a dry basis, $H_{\text{C}} = 0.3491\,\text{MJ}\,\text{kg}^{-1}$, $H_{\text{H}} = 1.1783\,\text{MJ}\,\text{kg}^{-1}$, $H_{\text{O}} = -0.1034\,\text{MJ}\,\text{kg}^{-1}$, and m_i is the mass percentage of i in the biomass on a dry basis. With an estimate for the enthalpy of combustion, the thermochemical conversion of any real-world biomass can be optimised in terms of operating temperature, pressure, and additive species by knowing only the elemental composition of the biomass.

Using Eq. 5.17, the heat of combustion for wheat straw was estimated to be $20.2\,\text{MJ}\,\text{kg}^{-1}$. The net heating value is plotted on Fig. 5.17. Similarly to acetic acid, the optimum case for the range of conditions studied occurs at 1 bar and 800°C. Supercritical pressures again offer no thermodynamic benefit when it comes to the thermochemical conversion of wheat straw.

Compared to acetic acid, the maxima for wheat straw occur at notably lower efficiencies. With the addition of just over 20 wt% water, a net heating value just shy of $15\,\text{MJ}\,\text{kg}^{-1}$ is achieved. The wheat straw system requires the addition of roughly 50 wt% CO_2 to obtain a peak net heating value at these conditions. The element composition of the wheat straw puts it slightly deeper in the char-formation region, as compared to acetic acid; so this can rationalise the fact that more water or carbon dioxide is needed to reach the optimum net heating value.

Similarly to acetic acid, at all conditions other than 1 bar and 800°C, the addition of CO_2 has a negative impact on the net heating value. The curves for the addition of water, however, remain peaked at these other conditions.

5.7 Conclusions and Future Work

A two-phase thermodynamic model was built using a Gibbs free energy minimisation calculation to model the thermochemical treatment of biomass. Most attention was given to biomass feedstocks, but the principle can be extended to plastic wastes too.

The previously unreported perspective of chemical potential was used to justify the commonly observed chemical and phase equilibrium behaviour at a wide range of conditions covering all classifications of thermochemical treatments. Ternary diagrams were used as visual aids to give the reader a comprehensive understanding of how exclusively the temperature, pressure, and elemental composition of a system influence equilibrium yields of syngas and char.

Phase boundaries were highlighted on the ternaries and used to demonstrate the two regions that exist where solid char formation is, and is not, possible. Higher temperatures and lower pressures were shown to shift the phase boundary towards the vertical, meaning more carbonaceous feedstocks gasify in the single-phase region. Feedstocks with more carbon tend to form CO, and those with more hydrogen form H_2. At lower temperatures and higher pressures, the phase boundary is more curvaceous and two-phase region is larger. Here, the feedstocks with more carbon tend to form CO_2 and those with more hydrogen will produce CH_4.

The addition of water to thermochemical processes was demonstrated to be a means by which the composition of a system can be shifted from the two phase into the single-phase regions. The effect of water on yields of syngas species and char was discussed from the perspective of element chemical potentials, and a series of ternary diagrams was plotted to show the minimum amount of water required to cross the phase boundary depending on feedstock composition, temperature and pressure.

The framework can also be used to evaluate the efficiency of SCWG. In this chapter, acetic acid and wheat straw were examined and for both systems it was found that the most efficient operating conditions were at high temperatures (i.e. 800°C) and low pressures (i.e. 1 bar). This suggests that using supercritical pressures provides only kinetic benefits to a process, not thermodynamic benefits.

The effect of CO_2 was also discussed as a potentially beneficial additive in thermochemical processes. It was found that at higher temperatures, CO_2 can be used as a gasification additive whereby it can mitigate char by shifting the system composition into the single-phase region. At low temperatures on the other hand, CO_2 can be added to promote yields of char.

It is appreciated that the main drawback of the thermodynamic model is that it assumed equilibrium has been reached, whereas in fact for the most part, this is very unlikely to be true for any thermochemical process. The present model does not consider the formation of liquid phase, bio-oils - a product of pyrolysis. For future work, one recommendation is that the equilibrium model be used to model non-equilibrium scenarios, i.e., when intermediate liquids form. A hypothesis is that elemental compositions in the single-phase region on the ternary diagram will have no tendency to form bio-oils. Compositions closer to the carbon corner in the two-phase region will have a greater propensity to bio-oil production because here liquid species will form as intermediates during the assemblage of carbon atoms into longer-chained and ring molecules as they move towards char at equilibrium.

It is also suggested that investigations into the influence of other elements, like nitrogen, chlorine, or sulphur, which are likely present in biomass and plastic organic wastes. The formation of species like NH_3 will have a bearing on the equilibrium concentrations of other syngas species at equilibrium.

6

Designing Experimental Methods to Support SCWG Modelling

Computational research provides valuable insight into SCWG through kinetic, thermodynamic, and other types of models. However, without experimental validation, the reliability of conclusions drawn from such studies remains unsubstantiated. This penultimate chapter outlines how experiments could be conducted at the University of Strathclyde to validate the findings presented in the preceding modelling-based chapters.

6.1 Introduction

Previously Chapt. 3 employed a detailed kinetic modelling methodology to demonstrate how sub-critical heating regimes can be tailored to biomass composition to favour the formation of desired products (e.g., H_2). Chapter 4 seamlessly continued from this by using a sensitivity analysis approach to demonstrate how rate-limiting reactions can be identified from a complex kinetic mechanism, particularly for H_2 and acetic acid. A thermodynamic modelling approach was developed in Chapter 5, and a series of ternary diagrams were provided which use element chemical potentials to determine the chemical and phase equilibrium

behaviour for the thermochemical processing of any biomass feedstock composed of carbon, hydrogen, and oxygen.

The purpose of a computational model is to emulate a real chemical process, and the models described in this thesis are powerful tools that have been proven to be of great use in conducting SCWG research. However, models are not without limitation and need to be validated appropriately. Thermodynamic models for example are built from first principles, and the major drawback is that they describe an equilibrium state that is unlikely to ever be reached. Kinetic models on the other hand are constructed using experimental data, which for the kinetic model described in this project was obtained from a literature review. The conclusions obtained from computational models always come with the caveat that their accuracy is inherently tied to assumptions and limitations of the model itself. Therefore, the findings of the computational models described in chapters previous require bolstering and validation with experimentation.

A 75 ml non-stirred pressure vessel was acquired from Parr Instruments Ltd. midway through the duration of this doctoral research program. This high pressure, high temperature reaction vessel is rated to a maximum operating pressure of 61.3 MPa at a maximum operating temperature of 540°C. The primary objective was to use the batch reactor to conduct SCWG and HTG type experiments to supplement and expand upon the modelling capabilities developed as part of this thesis. The objective of this final results chapter of the thesis was to create a series of experimental methodologies to validate and support the main findings of the computational content of the report. The chapter is firstly arranged into two sections. The first describes the experimental rig and details the methodology that was established to operate the reactor. There are inherent challenges to conducting experiments in hydrothermal conditions, such as those required for SCWG, and the objective here is to provide a concise methodology that can be replicated to conduct experiments in SCW. The second section demonstrates

methodologies which can be employed to supplement the findings of Chapt. 3 - the kinetic heating rate study, and Chapt. 4 - the kinetic sensitivity analysis.

6.2 The Experimental Rig

Figure 6.1 shows a picture of the experimental rig, where the main components of the set-up are labelled.

Label	Component
1	75 ml high temperature, high pressure vessel.
2	Gauge block assembly.
3	Analogue pressure gauge.
4	Digital pressure transducer.
5	Thermocouple.
6	Heater.
7	Heater and vessel stand.
8	Controller unit.
9	Rupture disc chimney.
10	Reactor barricades.

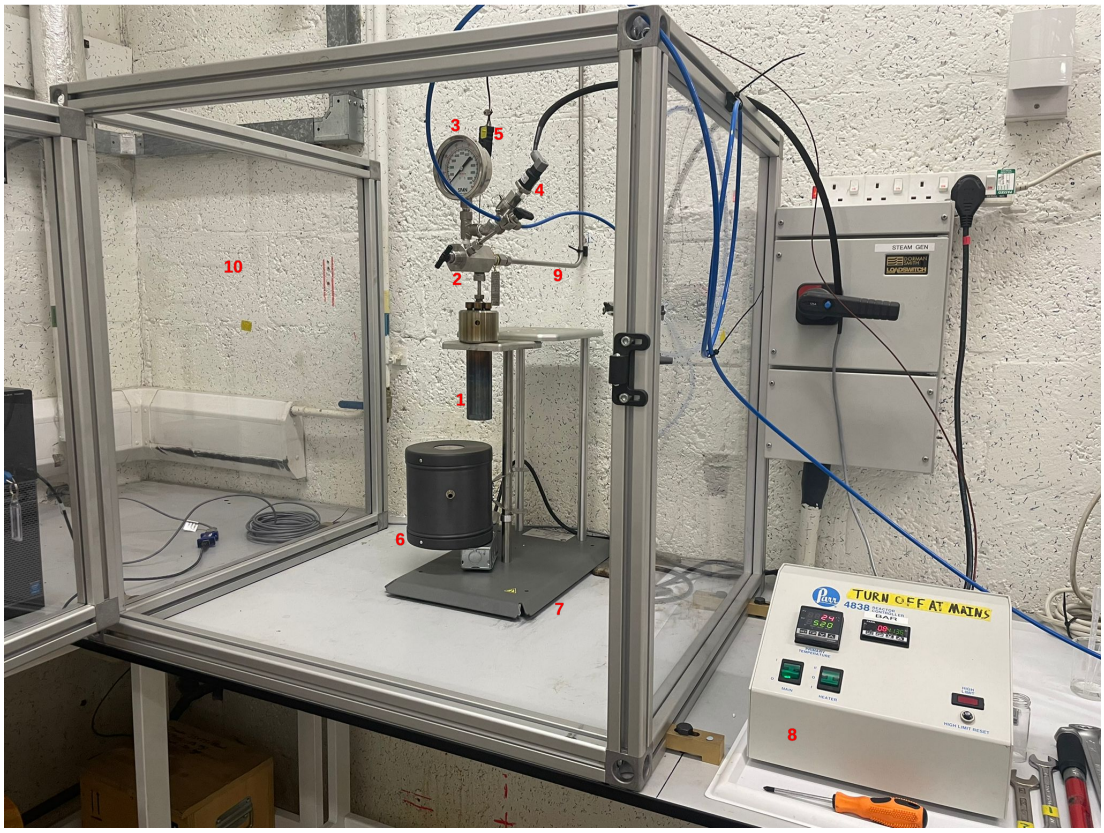

Figure 6.1: Labelled picture of the experimental set-up.

6.3 Standard Operating Procedure

Developing a standard operating procedure (SOP) formed a significant portion of work for this thesis given the novelty of this type of equipment in the department and university. After much testing, the following SOP was designed which should be replicated in order to replicate experiments. The SOP references valves which are labelled on the Fig. 6.2 PID.

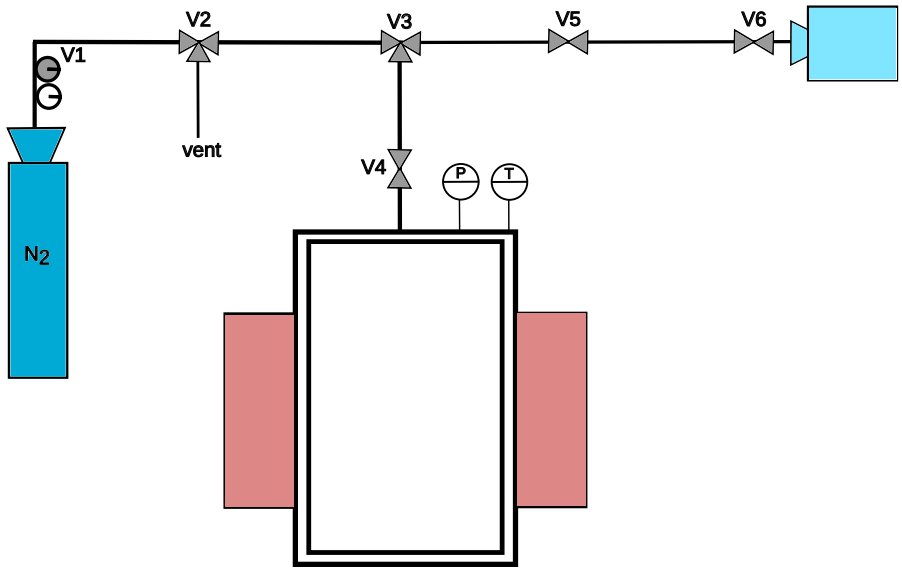

Figure 6.2: PID of the reactor.

6.3.1 Pre-Experiment Checks and Set-Up

1. Ensure pressure vessel is clean, dry and free of debris.

2. Check vessel head, compression ring, compression bolts, and screw cap for signs of wear and damage.

3. Reapply nickel anti-seize to compression bolts and tube bushing if necessary

4. Calculate desired liquid loading using NIST Chemistry WebBook [168] to check isochoric pressure-temperature data of water. Users must also consider pressure evolved from reactions (e.g., gasification) and additional gas added to the vessel. Operating pressures should not exceed allowable maximum at target temperature for given loading - see Sec. 6.4.

5. Secure vessel into bench-top vice and load with sample.

6. Place vessel head onto vessel and firmly push it into the vessel lip ensuring it lays flat.

7. Place compression ring onto vessel head.

8. Place compression bolts into screw cap, ensuring they do not protrude through.

9. Screw the screw cap onto the vessel all the way - then back off 1/8 turn.

10. Use 8mm hex/Allen key to screw the compression bolts in cross-cross pattern until you feel the bolts make contact with the compression ring.

11. Use torque wrench with 8mm hex bit to tighten the bolts to 10 ft-lbs in crisscross pattern.

12. Tighten compression bolts further to 15 ft-lbs in same crisscross pattern.

13. Place gauge-block assembly onto vessel. Ensuring thermocouple is unobstructed.

14. Use torque wrench with 3/8 inch crows foot attachment to tighten tube head screw to 15 ft-lb.

15. Place the vessel into the holder and affix the rupture disc assembly to the chimney.

16. Move the heater into position around the reactor.

17. Attach the inlet/outlet valve to the gauge block assembly. Change the position of the valve to 'outlet'.

18. Connect the thermocouple wire and pressure transducer cable to gauge block assembly. Turn on the 4838 controller.

6.3.2 Pressure-Cycle Purging

1. Fully open the gauge block valve (V4).

2. With the gas delivery valve (V2) in the 'to vessel' position. Use a cylinder key to open the N_2 cylinder (V1) and then the regulator to delivery 10 bar to the vessel.

3. Slowly change the inlet/outlet valve (V3) into its inlet position to charge the vessel with 10 bar.

4. Open the downstream valve (V5). Slowly change the inlet/outlet valve (V3) to outlet position to depressurise the vessel. Close the downstream valve (V5).

5. Repeat steps 3 to 4 twice more.

6. With an atmospheric pressure of N_2 in the vessel, fully close the gauge block valve (V4).

7. Use the cylinder key and regulator to close the N_2 cylinder (V1).

6.3.3 Experimental Run

1. With SpecView V3[1] open and in 'Full Online Run' mode, simultaneously click 'Start Logging' on SpecView and turn the heater switch on the 4838 controller to position ON II.

[1] https://www.specview.com/

2. After the reactor has heated and maintained its temperature for the desired amount of time, turn off the heater on the 4838 controller and use Kevlar oven gloves to move the heater away from the vessel.

3. Position the cooling fan in front of the vessel on the opposite side to the heater and turn it on.

4. Wait for the reactor to cool to 25°C.

5. Attach an empty gas sample bag to the downstream line, open the bag's valve (V6), and then open the downstream valve (V5).

6. Fully open the gauge block valve (V4) to discharge the remnant pressure in the vessel and collect the gases in the bag.

7. Shut the gas sample bag valve (V6) and remove from the downstream line.

6.3.4 Post-Experiment

1. Disconnect the thermocouple and pressure transducer

2. Remove the chimney from the gauge block assembly.

3. Secure the vessel in a bench-top vice. Remove the gauge block assembly by loosening the gauge block screw.

4. Loosen the compression bolts in a crisscross pattern. Unscrew the screw cap, remove the compression ring and vessel head.

5. Decant the reactor contents into a glass sample holder.

6.4 Safety Considerations

Despite its small volume, the extreme pressures and high temperatures make the reactor an inherently dangerous item of equipment to work with. The main fail-safe feature of the reactor is a rupture disc located on the back of the vessel head which breaks before catastrophic failure of the vessel itself. However, in addition to this feature a number of other safety protocols required design and installation in order to minimise the risks associated to it. The controller unit is also fitted with a high-temperature shut off which will stop power to the heater unit in the event a high-temperature alarm is reached, or the thermocouple is detached.

Due to limited availability in the lab, it was not possible to install the experimental rig in a fume hood which would have been the preferred choice. Instead, the rig was assembled in ordinary lab space which meant a chimney system required design to divert expelled gases in the gas that the rupture disc failed. Additionally, as per university guidelines a heat barricade would be necessary to protect laboratory users from the high temperatures of the reactor. The barricade and chimney are labelled on Figure 6.1. The barricade is constructed from an aluminum frame with sheets of 8 mm polycarbonate. The chimney is a stainless steel tubing which diverts to exit of the rupture disc over 3 meters upwards.

The final main safety consideration is not related to an item of equipment, rather a pre-experiment check that should be carried out. The pressure developed in the batch reactor arises almost exclusively from the phase transition of water from a liquid to a gas. The gasification of organic matter will also contribute to system pressure and this must be calculated before any experiment to check it falls within safe operable limits. Isochoric (constant density) calculations should be completed prior to any experiment to determine what the final pressure will be at the set target temperature for a given loading of water. Table 6.1 shows that maximum operating conditions of the reactor and the corresponding maximum water loadings. This does not account for gases produced from reactions. The

NIST Chemistry WebBook [168] is a useful online tool that uses an IPAWS-95 physical property method to perform such calculations. Figure 6.3 has also been provided to give guidelines for pressure versus temperature at different loadings in the 75 ml reactor.

Table 6.1: Maximum operating temperatures, pressures of the reactor and corresponding maximum water loading.

Temperature (°C)	**Pressure** (PSI/MPa)	**Water Loading (g)**
350	9400/64.9	27.75
400	9400/64.9	27.75
450	9400/64.9	27.75
500	9400/64.9	27.75
540	8900/61.3	20.25

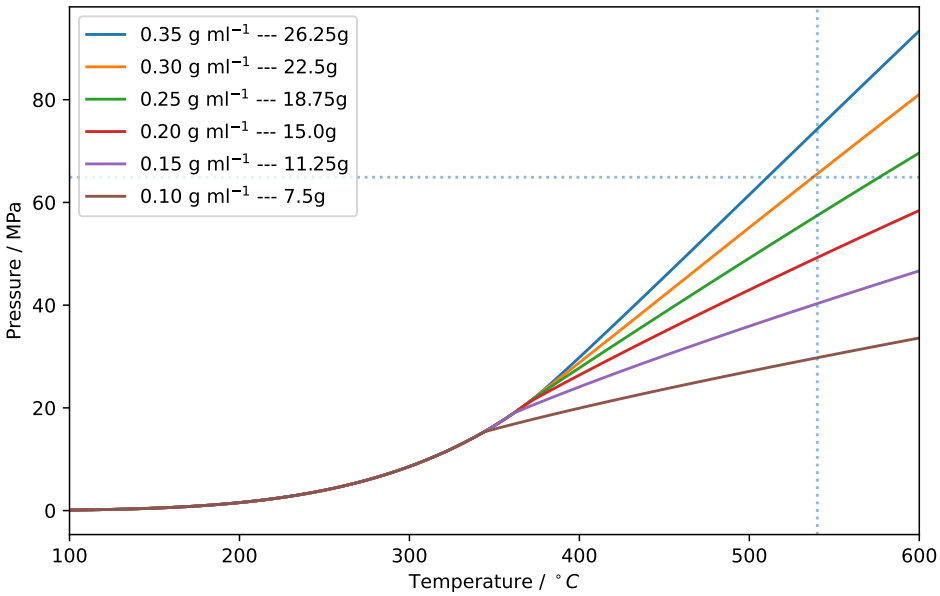

Figure 6.3: Isochoric pressure versus temperature plots for the reactor predicted by IAPWS-95.

In addition to the pressure versus temperature curves, Fig. 6.3 also shows the maximum operating conditions of the vessel - 61.3 MPa at 540°C. Fill volumes of 0.3 and 0.35 $g\,l^{-1}$ result in pressures exceeding 61.1 MPa at the maximum operating temperature and thus should never be used when heating to 540°C.

6.5 Pressure Cycle Purging

Removal of O_2 in the reactor prior to experiments was pivotol to conducting gasification reactions. In oxidative environments, biomass and syngas will combust to produce CO_2 and H_2O which would then constitute the majority of products. The easiest way to prevent this is to remove the air content of the vessel with an inert species, like N_2. The reactor only has one inlet/outlet which means it is not possible to continuously flow N_2 through the vessel to gradually remove remnant O_2. Instead, the pressure-cycle purging routine described in the SOP was employed to drive out the O_2. This is when the vessel is charged and discharged with a pressurised, O_2-free source of N_2 to systematically lower the O_2 content. Equation 6.1 shows the equation provided by ASTM standard G-124 which can be used to calculate the number of purges, N, required to reduce the molarity of air down to 0.01% for a given charging, a, and discharging, P_h, pressure. It was derived from Dalton's Law and the ideal gas Law.

$$N = \frac{-4}{log_{10}(\frac{P_a}{P_h})} \tag{6.1}$$

The equation can be adapted to show the concentration of O_2 after each purge [169].

$$C_{O_2} = \frac{P_a}{P_h} C_{0,O_2} + \left(1 - \frac{P_a}{P_h}\right) C_{h,O_2} \tag{6.2}$$

Where C_{O_2}, C_{0,O_2}, and C_{h,O_2} are the final, initial, and purge gas concentration of O_2. Figure 6.4 shows how Eq. 6.2 predicts the concentration of N_2 in the vessel will change depending on the number of purges and the pressure of the purge gas. The concentration of N_2 was plotted as opposed to O_2 as this gas can be quantitatively analysed with the GC-TCD. The figure also shows the concentration of gas obtained experimentally after the third purge with 10 bar N_2.

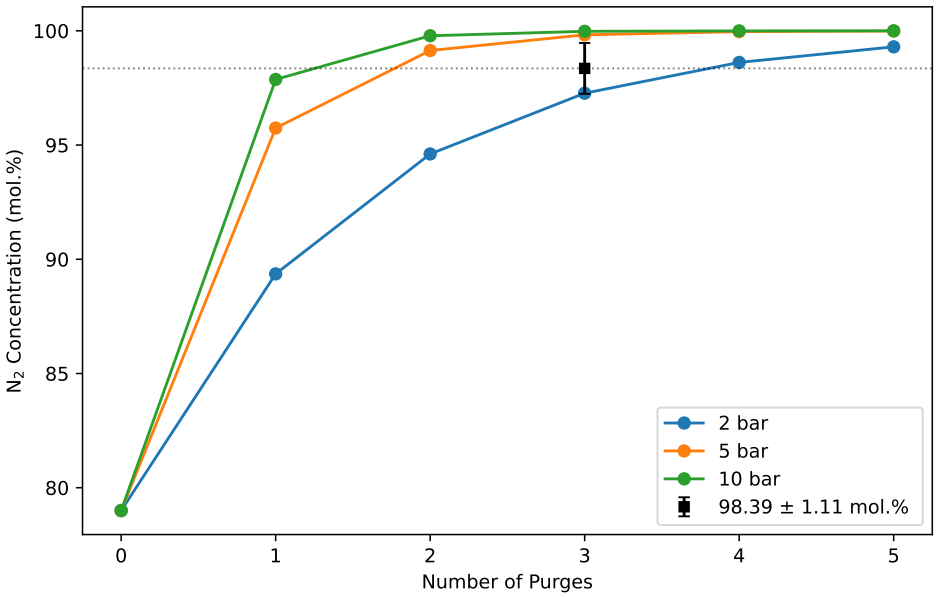

Figure 6.4: Concentration of gas in reactor after N purges predicted by ASTM G-124, and after 3 purges with 10 bar N_2 experimentally.

The graphs show that higher pressures allow for a greater removal of O_2 in fewer purges. The N_2 cylinder regulators have a maximum outlet pressure of 10 bar, hence, this was chosen for the purge gas so as much O_2 as possible could be removed from the vessel. After 3 purges, the final concentration of N_2 was 98.39 ± 1.11 mol.%. This was slightly lower than as predicted by Eq 6.2, however it is suitably high that we can say with confidence that pressure cycle purging is a suitable method of removing O_2 from the reactor.

6.6 Syngas Analysis

Gas analysis is a fundamental component to any series of SCWG experiments. The gas phase composition dictates the quality of the syngas product and the gasification efficiency, which are two main indicators of the efficacy of a SCWG process. Fot the quantitative or qualitative characterisation of syngas, the restoration and calibration of an existing Hewlett-Packard (HP) 6890 series

Gas Chromatograph was required as part of this experimental methodology.

The objective here was to use the GC to determine the concentration of H_2, CH_4, CO, CO_2, and N_2 in the SCWG product gas. The following subheadings summarise some GC fundamentals after which the procedure and results of calibration are presented.

6.6.1 Principles of Gas Chromatography

The GC was fitted with a thermal conductivity detector (TCD), and henceforth is referred to as the GC-TCD. There are several types of detector used in gas chromatography, each with advantages and disadvantages which suit them to different applications, and therefore it is pertinent to make explicit reference to the detector in use. Figure 6.5a and 6.5b show a picture and labelled diagram, respectively, of the GC-TCD used in this work; the images highlight the key components of the GC-TCD.

- Carrier Gas - The mobile phase which transports the sample through the system and acts as the reference point for the TCD. Different carrier gas types are used depending on the gases requiring detection; the work herein used both helium (He) and argon (Ar).

- Sample Injection - The gas sample is injected into the carrier via a pre-heated inlet. A fixed temperature of 230°C. was used for all runs completed.

- Capillary Column - The solid, static phase where the sample separates as a result of partial adsorption of the gases. The column used was a Carboxen$^{\text{ő}}$ 1006 fused silica capillary with a 0.53 mm diameter and 30 m length.

- Oven - Maintains the capillary column at a fixed, elevated temperature to increase the velocity of gases in the column. The oven temperature was varied between 25^{o}C to 35^{o}C.

- Thermal Conductivity Detector - Measures the change in thermal conductivity of the gas stream (sample and carrier) and produces a signal. This was also held at a fixed temperature of 230°C.

(a)

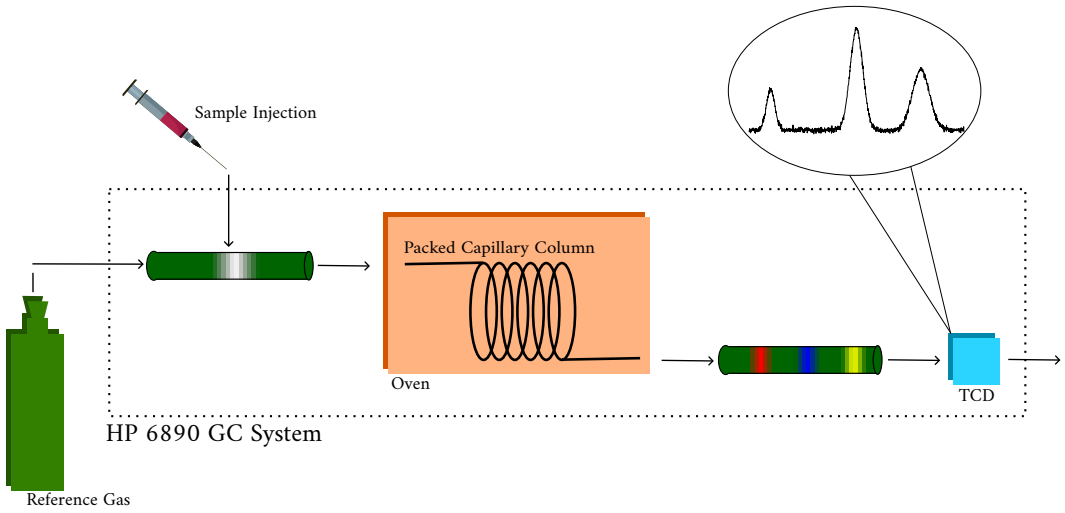

(b)

Figure 6.5: An a) annotated picture, and b) labelled schematic of the GC-TCD.

A TCD works by measuring the change in electrical resistance of two filaments at elevated temperature. Gases have varying thermal conductivities, and therefore the temperature and electrical resistance of a heated filament will change depending on the type of gas flowing over it. Figure 6.6 shows a schematic of an example

two-filament TCD, its operation is based upon the principle of a Wheatstone bridge [170]. By applying a constant voltage across two filament cells - one containing a mixture of the sample and the carrier gas, and the other containing only the carrier gas - a signal peak for each gas in the sample is ascertained by measuring the change in resistance versus the carrier reference.

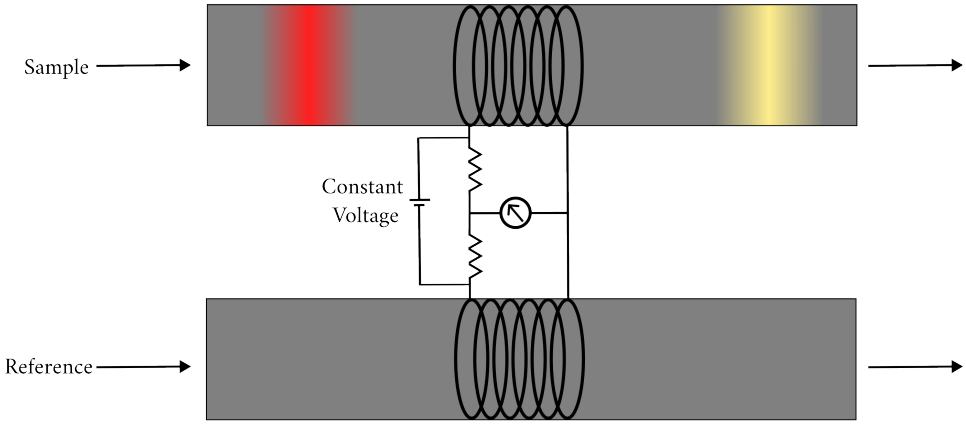

Figure 6.6: Schematic of a two-cell thermal conductivity detector (TCD)

6.6.2 Methods

The operating parameters listed above form part of the overall GC-TCD method. The method refers to a set of user-specified instructions that the GC-TCD follows when setting its operating parameters. It includes variables such as inlet pressure, carrier-sample split ratio, oven temperature and column flow rate. The full details of method 1 and 2 are described in Appendix C.

Methods are designed to produce the best practically possible signal trace for the gas species of interest. Generally, sharp and symmetrical peaks (i.e., Gaussian) are preferred to those that are skewed or have long tailing edges [171]. Sometimes, 'sticky' molecules like CO_2 will have longer column retention times than other species that interact with the internal packing material less (e.g., H_2). In this case, a compromise may be desirable where GC-TCD operating parameters are

changed in order to reduce the retention times of these more absorptive species at the cost of a slightly diminished peak quality.

Table 6.2: Thermal conductivities of permanent gases at 25°C and 1 atm [168].

Gas	Thermal Conductivity($\mathbf{W\,m^{-1}\,K^{-1}}$)
He	0.1553
Ar	0.01775
N_2	0.02584
CO_2	0.01663
CO	0.02490
CH_4	0.03396
H_2	0.1858

Table 6.2 shows the thermal conductivities of the carrier and sample gas species considered in this work. As a rule of thumb, the greater the difference in thermal conductivity between the carrier gas and the species requiring detection, the better the signal trace. He is a popular choice of carrier gas as it has a thermal conductivity roughly an order of magnitude greater than other permanent gases. He and H_2 have very similar thermal conductivities however, and it is necessary to use a different carrier gas to detect H_2. In this case, Ar was used to detect for H_2. Two methods were developed, each of which was designed to work with either an He or Ar carrier gas.

Figures 6.7 and 6.8 show two GC-TCD traces obtained using method 1 with He and method 2 with argon for the same sample of mixed gases containing N_2, H_2, CH_4, CO, and CO_2. An obvious observation is that Figs. 6.7 and 6.8 have reflected peaks. Since He has the highest thermal conductivity, the filament temperature cools as sample gases pass through the TCD. This reduces the electrical resistance and a positive signal change occurs. Ar has a lower thermal conductivity than the sample gases and thus the opposite occurs. The signal peaks are larger in Fig. 6.7 because there is a greater difference in thermal conductivity between the carrier and sample gases.

Method 1 was developed mainly with the intention of CO_2 quantitative detection. Figure 6.8 shows that CO_2 does produce a signal peak with Ar in method 2, but since the thermal conductivities of He and CO_2 have a greater disparity (Tab. 6.2), He was chosen as the best carrier gas for CO_2 detection. Method 1 was also used for CO detection, again because there is a greater difference between the thermal conductivities of CO and He, than CO and Ar. The main feature developed for method 1 was that the carrier gas flow rate was increased after 7 min run time. The reasoning for this was to allow for CO to pass through the detector at roughly 5 min, and then change the GC-TCD parameters in such a way that it would accelerate the velocity of CO_2 through the column and reduce the retention time of this molecule. This can be seen on Fig. 6.7 as the baseline reduces slightly between 8 and 12 min after which it stabilises again and CO_2 passes though at roughly 13 min.

As previously explained, method 2 was used to detect H_2 as this gas species is undetectable in He. When using method 1, notice how Fig. 6.7 shows that the peak for CH_4 occurs when the baseline is destabilised by changing carrier gas flow rates at roughly 9 min. It was therefore decided that CH_4 detection should also be conducted using method 2 with an Ar carrier in order to produce the best quality peak for this species. Method 2 was also used to detect for N_2, the reasoning here being that there were more calibration gases available for mixtures of H_2 and N_2 (see Tab. 6.3) which meant more calibration points could be obtained by detecting N_2 with Ar.

6.6.3 General GC-TCD Operation

The age and incomplete service history of the existing GC-TCD means its operation is nuanced, and the following methodology was developed after undertaking a great deal of trial-and-error testing. A full SOP with descriptive step-by-step instructions and pictures is included in Appendix C.

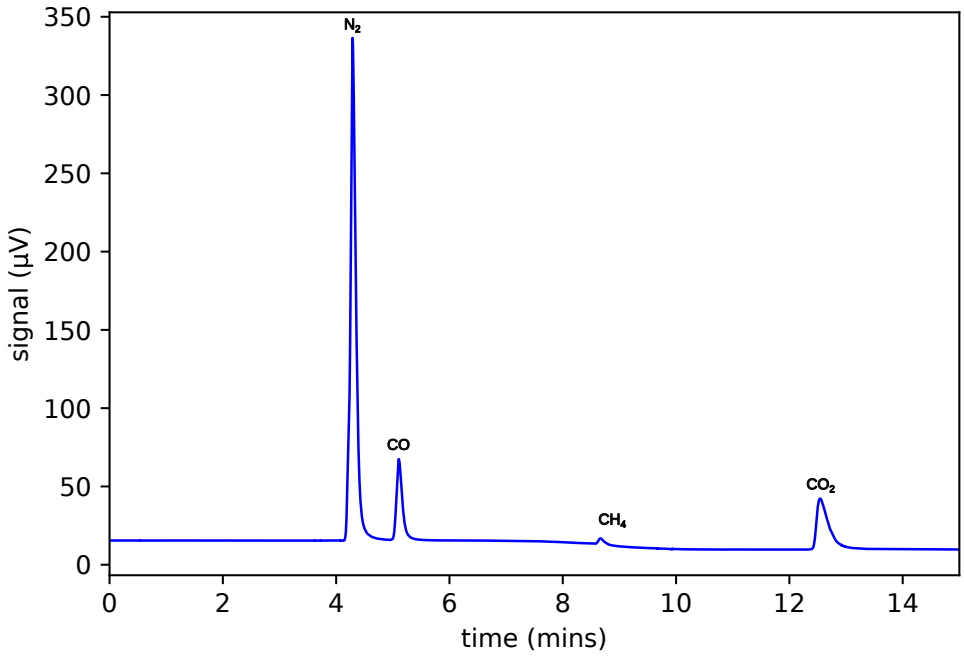

Figure 6.7: GC-TCD signal for mixed gas (N_2, H_2, CO, CO_2, CH_4) using Method 1 (He carrier)

An unavoidable feature of the GC-TCD is the time it takes for the baseline signal to reach a steady state, which after initially turning on the GC-TCD can take anywhere between 40 min to over an hour. Additionally, there is a necessary cool-down period that must be allowed before the GC-TCD can be switched off at the close of day. It is necessary to let the heated components (gas inlet and TCD) to cool down whilst there is still carrier gas flowing through the system to prevent damage and blockage of these components. A cooling period of around 1 hour is needed to allow the heated components to cool to below 100°C after which the carrier gas and GC-TCD switched off for the day. Within a 9 am to 5 pm working day, after the heat-up and stabilisation time at that start of the day and cooling period at the end, there is roughly 6 hours of sample running time available. Each run takes 15 min to complete for both Method 1 and 2, and thus an experienced user can perform 4 runs in an hour, which works out to a maximum of 24 samples a day. This number is an absolute maximum and assumes no failed-runs, delays, etc.

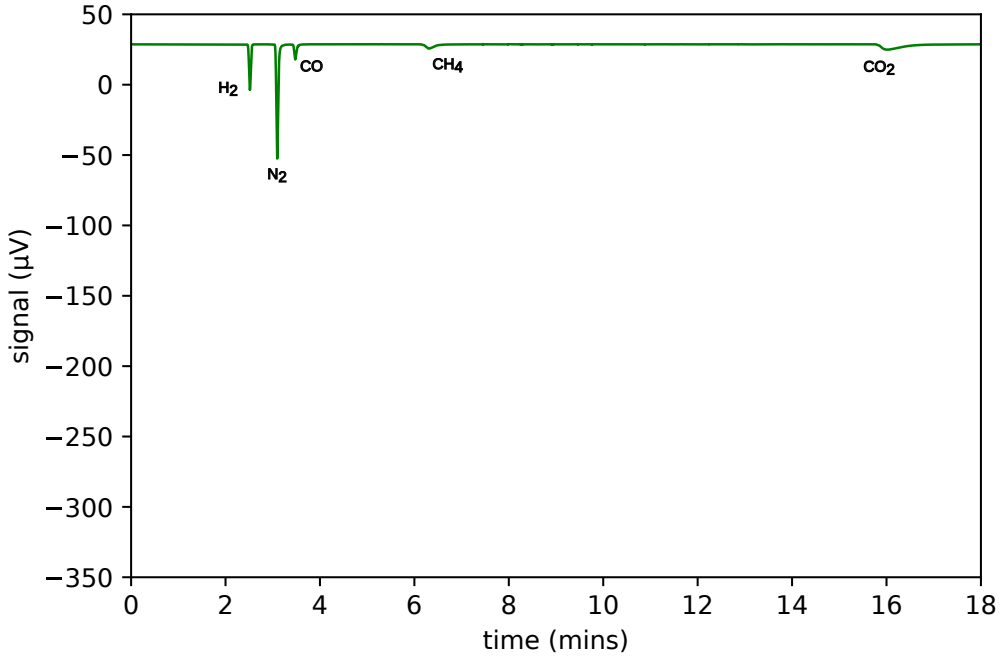

Figure 6.8: GC-TCD signal for mixed gas (N_2, H_2, CO, CO_2, CH_4) using Method 2 (Ar carrier)

Switching from one method to another also incurs a long wait period before a new run can be made as the GC-TCD needs to re-adjust to the new carrier gas and operating parameters. Therefore, changing methods during the working day significantly reduces the number of samples that can be run. For future general operation of the GC-TCD, when it is anticipated that other lab uses will require use of the GC-TCD, it is recommended that methods are allocated to run on different days of the week. For example, Method 1 for CO_2 and CO detection on Tuesday and Thursday, and Method 2 for H_2, CH_4 and N_2 detection on Monday, Wednesday and Friday. This will maximise the number of samples that can be run in a 9 am to 5 pm working week and reduce the amount of intervention needed for experienced researchers and technicians.

Due to problems associated with versioning of the `GC Online` software provided by the original manufacturers of the machine, all post-processing of GC-TCD signals was completed using a Python code developed as part of this doctoral

research. This complete package is available in Appendix C. Building this Python script future-proofs the GC-TCD as it its operation is no longer dependent on the availability of commercial software.

6.6.4 Calibration

The peak area for a component on a GC-TCD chromatogram is directly proportional to the concentration of that gas in the sample [172]. This is demonstrated with Fig. 6.9 which shows the signal trace for samples of pure (>99.99%) and 10 mol.% CH_4 obtained using method 2. The peak area of the 10 mol.% trace is ten times smaller than that of the pure one. Using known concentrations of gases, it is possible to produce calibration curves which directly correlate peak area to gas concentration. Table 6.3 shows the gases procured to carry out the GC-TCD calibration procedure.

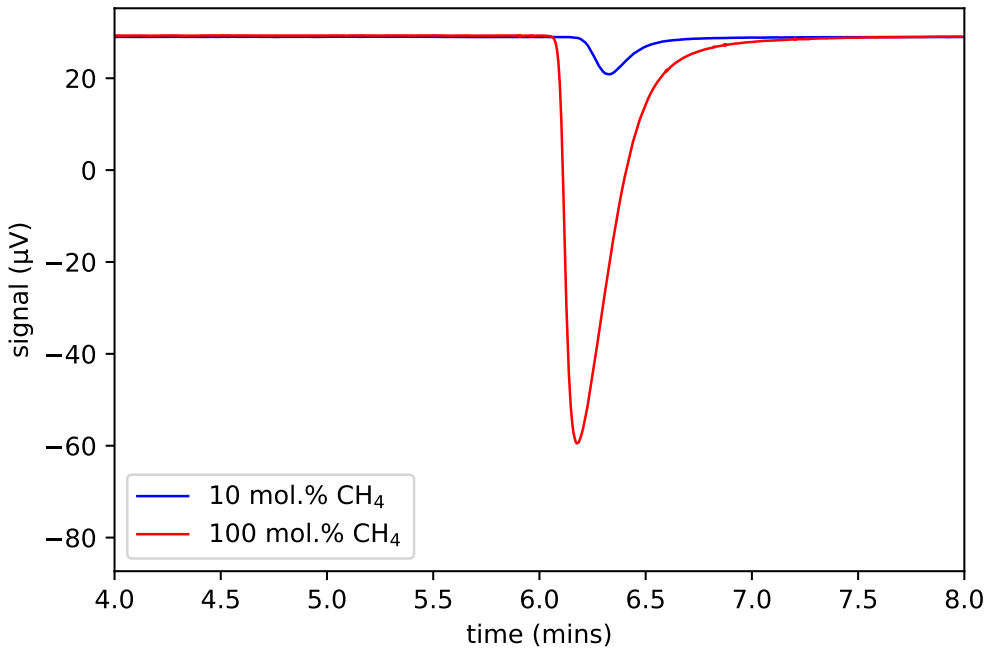

Figure 6.9: Two GC-TCD signals with 10 mol.% and 100 mol.% CH_4. Obtained using method 2

A selection of calibration gases were procured, in addition to cylinders already kept in the lab. The concentration and supplier of these gases is shown in Tab. 6.3.

Table 6.3: Calibration gases used for GC-TCD analysis.

Gas Composition	Tolerance (mol.%)	Supplier
10% H_2	10.005 ± 0.002	CALGAZ^{TM} Ltd
20% H_2	20.001 ± 0.002	CALGAZ^{TM} Ltd
10% CH_4	10.0 ± 0.2	CALGAZ^{TM} Ltd
100% CH_4	99.99	BOC^{TM} Ltd
10% CO_2	10.005 ± 0.002	CALGAZ^{TM} Ltd
100% CO_2	99.99	BOC^{TM} Ltd
100% N_2	99.99	BOC^{TM} Ltd
100% CO	99.99	BOC^{TM} Ltd

The calibration procedure involved conducting a series of at least 10 repeat runs using the GC-TCD for each calibration gas available. The raw data is tabulated in Appendix C.

Figures 6.11 through 6.10 present the calibration curves for the objective gas species. In each case, figure 'a' presents a simplistic calibration curve that correlates peak area to concentration. Outliers were removed if they deviated from the mean of the repeats by more than 3 standard deviations. The calibration curve was then plotted through the means of the calibration points, with (0,0) included as an additional point in every case. An R^2 is provided for each of these calibration curves to indicate the accuracy of the fit. This calibration curve is useful for estimating a gas concentration based upon a measured peak area.

6.6.5 Uncertainty in Measurement

The conventional calibration curve provides the user with a best-fit line with a confidence band that assumes a fixed error. Whilst the error in the calibration gas concentration is fixed, the error in the measurement, which is bought about by variations to the injected gas volume, peak area determination (Gaussian fitting), general GC-TCD performance, etc., is not constant and is random. Consequently,

conventional calibration curves do not fully account for the uncertainty that is brought about by random error in the measurement.

The fitted calibration curve does not provide the user with any indication of the uncertainty in the measurement. Here, two main sources of error were identified which affect the accuracy between the measurement and the expected value. There is random error in peak area (y values) arising from multiple factors including variability in the manually injected volume of gas; the accuracy of the Gaussian fitting used for peak integration; natural variance in the GC-TCD performance and others. There is also a systematic error in the concentration of the calibration gas (x values), which Tab. 6.3 shows were supplied with a specified tolerance.

Monte-Carlo simulations were used to propagate the uncertainty in each of the calibration lines. The results are shown in Figs. 6.11 through 6.10. The code used to conduct the Monte-Carlo simulations is contained in Appendix C. In each case, 10,000 runs were generated by randomly perturbing the linear calibration curves within the specified uncertainty bounds. The distribution of these generated calibration curves could then be used to estimate the probability (i.e., the uncertainty) of each gas measurement.

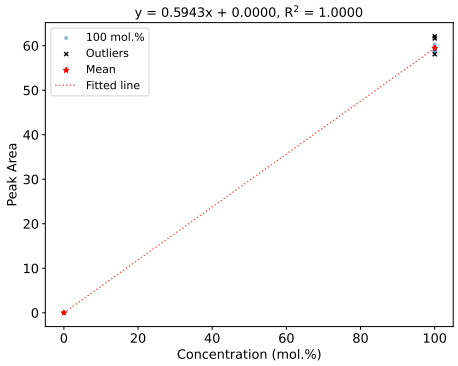

Figure 6.10: Calibration curve for CO concentration using GC-TCD.

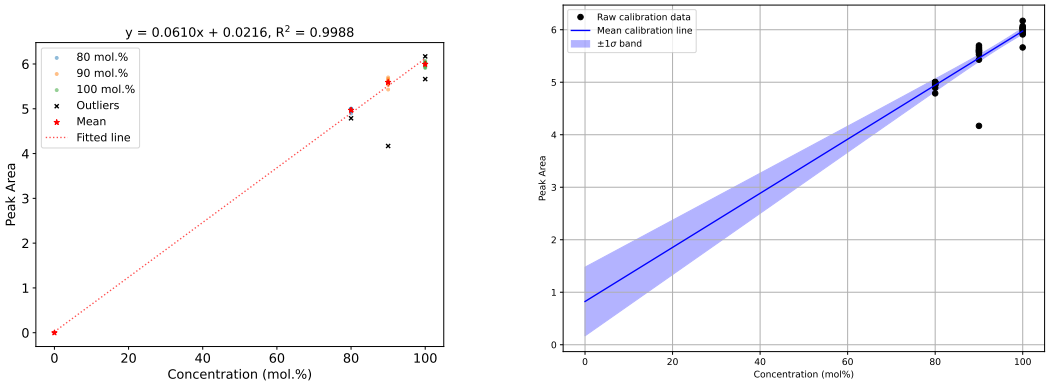

(a) **(b)**

Figure 6.11: a) Calibration curve and b) Monte-Carlo uncertainty for N_2 concentration using GC-TCD.

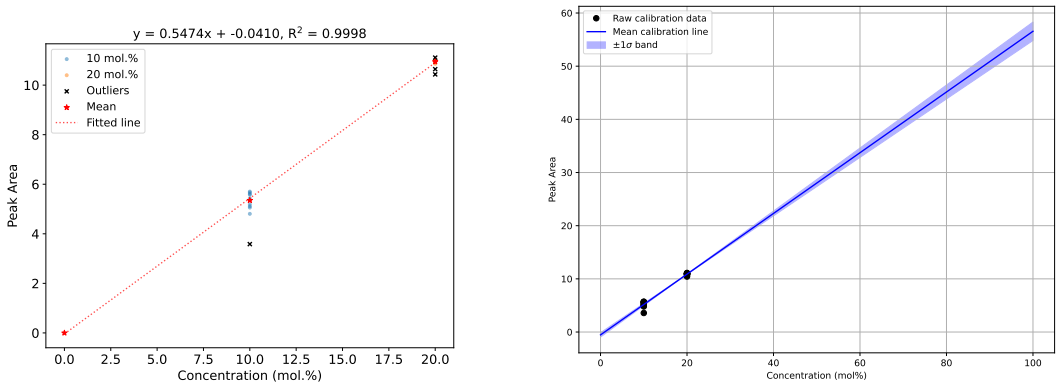

(a) **(b)**

Figure 6.12: a) Calibration curve and b) Monte-Carlo uncertainty for H_2 concentration using GC-TCD.

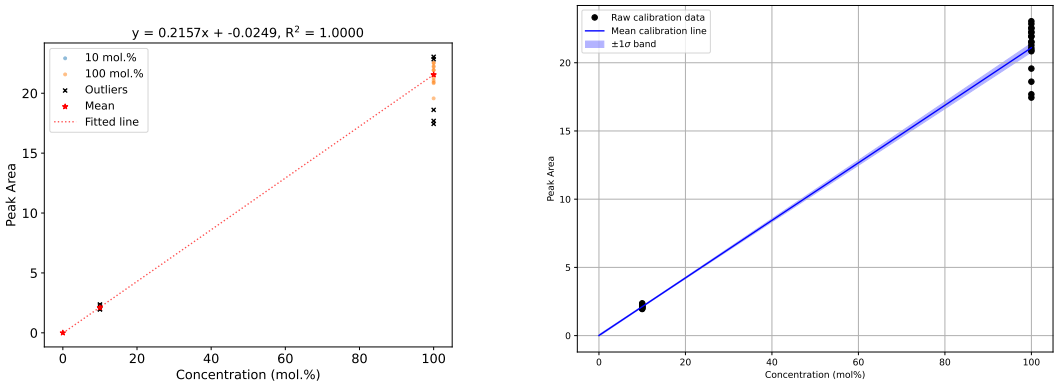

(a) **(b)**

Figure 6.13: a) Calibration curve and b) Monte-Carlo uncertainty for CH_4 concentration using GC-TCD.

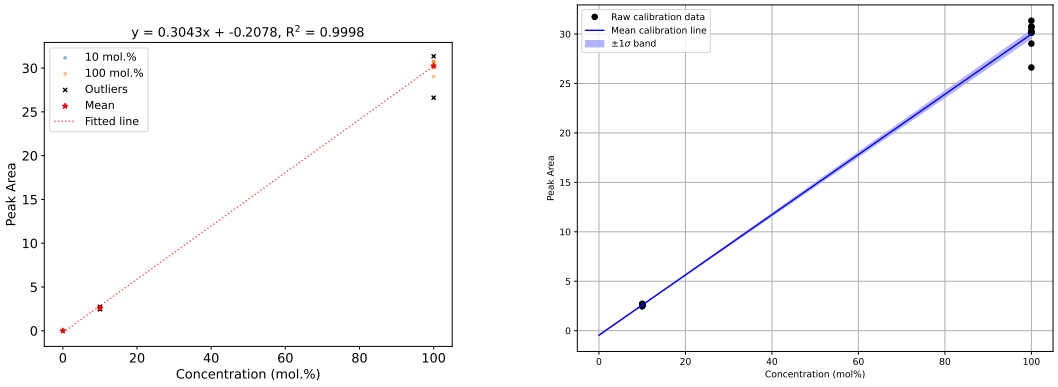

(a) **(b)**

Figure 6.14: a) Calibration curve and b) Monte-Carlo uncertainty for CO_2 concentration using GC-TCD.

6.7 Design for Validating Models

The scope of the experiments described in the following chapter aim to validate the computational conclusions of the other computation results chapters. Here, attention is primarily paid to the kinetic aspects of this thesis over thermodynamics. The reasons for doing so are because SCWG is typically rate-limited in practice and equilibrium is rarely reached; the kinetic model has a significant margin of error

and therefore further experimental data will help to validate results; and finally the batch reactor setup is more conducive to obtaining kinetic information for reactions.

Experiments involving catalysts have been ignored here as the addition of homogenous or heterogeneous inorganic salts could potentially alter the surface chemistry of the inside walls of the Hastelloy reactor. By activating the surfaces, they become catalysts themselves and will affect the SCWG of biomass through a series of experiments making the results unrepeatable.

Model compounds such as hemicellulose (xylose) and acetic acid are chosen preferentially over real biomass at this stage, as the conclusions of the previous chapters highlight an interest in the kinetics of these specific molecules. Additionally, the use of real biomass could introduce inorganic species into the reaction, which could alter the reactor surface chemistry and as described above is currently undesirable.

The remaining sections of this chapter describe two different experimental methodologies. They focus respectively on the effect of heating rate on H_2 yields from the SCWG of hemicellulose; and then the decomposition kinetics of the stable intermediate, acetic acid, in SCW.

Conducting SCWG experiments is time-consuming and costly, requiring commitment to lab work on a full-time basis. Given the significant computational content of this thesis, there was insufficient time and resources for the experiments described as follows to be conducted as part of this doctoral research. The intention here is to lay the foundations of an experimental project that could be commenced by a future researcher.

6.7.1 Case 1: H_2 production from the SCWG of hemicellulose with fast heating.

One of the most notable conclusions from Chapt. 3 was that faster sub-critical heating rates lead directly to an increased yield of H_2 from the SCWG of hemicellulose. This is a promising result to discover, and could lead to conceptualisation of a fast-SCWG process design for hemicellulose rich feedstocks, like corn stalks [139].

In this subsection, a methodology based upon the experimental rig is established with the objective being to consolidate the claims made using the kinetic model regarding heating rate effects on hemicellulose SCWG.

By employing a simple set-point program, the reactor is heated to the target temperature and then maintained about the set-point using a PID control. A test was conducted by loading the reactor with 20 g of water and heating to a set-point of 500°C. After 4 hours of heating, the heater was turned off and the reactor was air fan cooled. Operating using a set-point program demonstrates the fastest possible heating rate that can be employed for a given reactor loading. Figure 6.15 shows a plot where temperature and pressure versus time are plotted on the primary and secondary y-axis, respectively. Pressure measurements were recorded at intervals using the analogue pressure gauge.

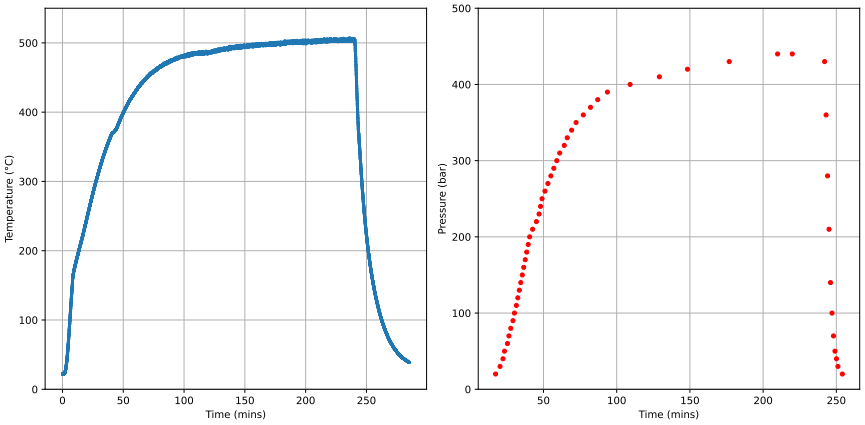

Figure 6.15: Temperature and pressure versus time in reactor heater to 500°C for 240 min.

Figure 6.15 suggests heating is fastest at the start, where in this example a linear increase of roughly 25°C min^{-1}. At around 170°C, the gradient reduces to slower linear heating rate of 7°C min^{-1}. This point represents boil-off in the reactor, i.e., when all the liquid has evaporated. The second change to heating rate occurs at the critical temperature of water, 374°C. The plot shows that for this feedstock loading, the critical pressure (22.1 MPa) is reached at a similar time to the critical temperatures. Hence, the reactor contents become supercritical as

the critical temperature of water is surpassed. Here, the heating rate is slower still, and it reduces further as temperatures approach the set point.

In addition to set point control, a ramp program can be used to manage a lower heating rate. This allows the user to define the time required to reach a chosen set point. Ramp and soak functions can also be used to if it is desirable to ramp to a chosen set point, maintain the temperature at that set point (soak), and then ramp to a subsequent set point.

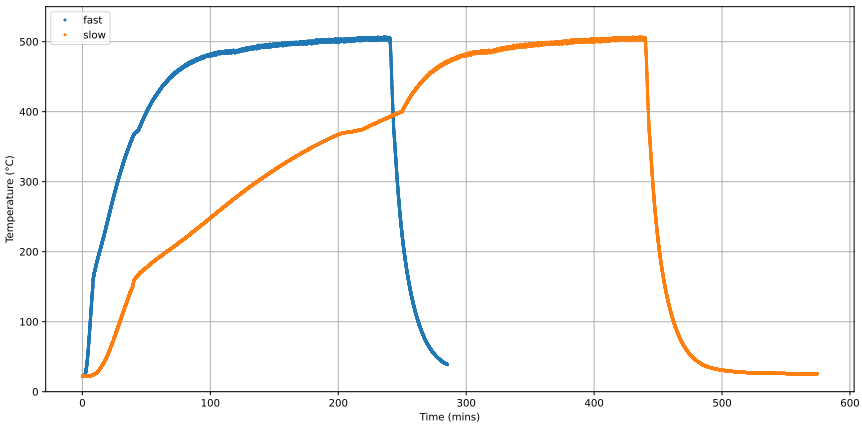

Figure 6.16: Temperature versus time with `fast` and `slow` heating rates employed.

Figure 6.16 shows two different heating profiles for the reactor. The first `fast` profile is the same as is plotted on Fig. 6.15, where 20 g of water was loaded into the vessel and the reactor was heated to a set-point of 500°C. The second, `slow` heating rate used the same feedstock but employed a ramp program to heat to 400°C in 4 hours, after which it would heat to 500°C as quickly as possible. The aim here was to extend the heating time in the subcritical region as long as practically possible.

Simulations were run using the kinetic model with the `fast` and `slow` heating rates shown on Fig. 6.16 with a 10 wt.% hemicellulose feedstock (modelled as Xylose). The results are shown on Fig. 6.17. The plots demonstrate that the kinetic model predicts a higher yield of H_2 from hemicellulose when using the `fast` heating program.

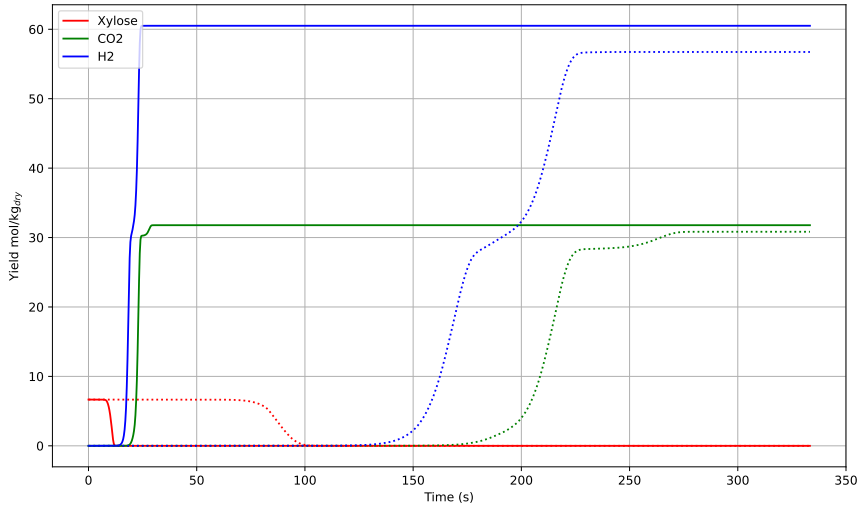

Figure 6.17: Kinetically predicted concentrations of xylose, H_2, and CO_2 in reactor with `fast` and `slow` heating rates employed.

The final yields are plotted on Fig. 6.18. By replicating the two heating profiles in experiments, it is anticipated that using the `fast` heating versus the `slow` one will increase yields of H_2 by nearly 7% from 56.7 to 60.5 mol kg_{dry}^{-1}.

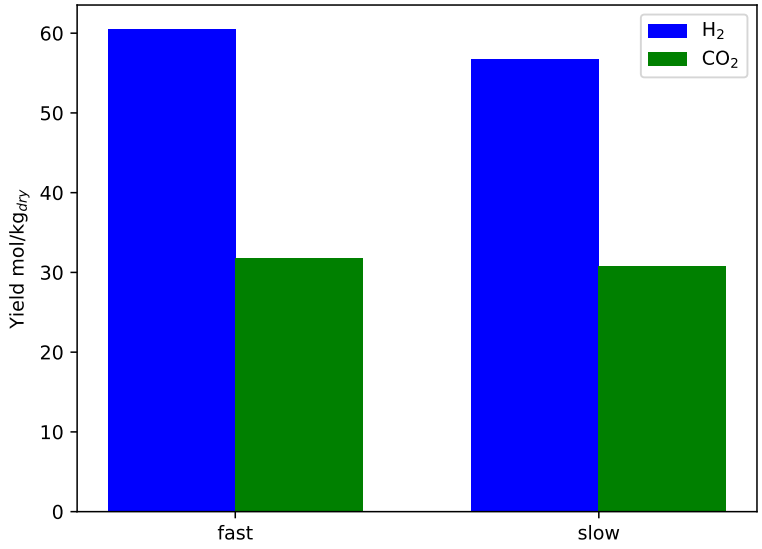

Figure 6.18: Kinetically predicted final yields of H_2 and CO_2 using `fast` and `slow` heating rates.

6.7.2 Case 2: Kinetics of acetic acid gasification in SCW.

The sensitivity analysis in Chapt. 4 identified acetic acid as an important intermediate during the SCWG of cellulose. The full decomposition profile for cellulose plotted on Fig. 4.3 demonstrated the superiority of this small organic compound in the later stages of the sub-critical region. It was found that after 60 s in the supercritical reactor (SUP-RCT), a CGE of 95 % was achieved at 600°C but only 67 % at 500°C. The discrepancy here being directly caused by remnant acetic acid in the system. Conclusions were made highlighting the importance of gasifying acetic acid specifically in order to achieve the complete conversion of biomass during SCWG. Acetic acid is known to be a refractory, rate-limiting intermediate produced during the hydrothermal decomposition of cellulose, glucose, wood tars, waste cooking oil and other types of biomass [143, 173–175].

The detailed kinetic model uses a single reaction to represent the decomposition of acetic acid in SCW.

$$CH_3COOH \rightarrow CO_2 + CH_4 \tag{6.3}$$

$$(-r)_{CH_3COOH} = 2.5 \times 10^4 \cdot \exp\left(-\frac{94}{RT}\right) \cdot [CH_3COOH] \tag{6.4}$$

These kinetics were approximated from Meyer, Marrone, and Tester [143] - the only article in literature that has published kinetic data for SCWG of acetic acid - who used a 4.24 m of 0.635 cm o.d. X 0.211 cm i.d. Inconel 625 tubing to carry out reaction between 475°C and 600°C. The authors used a fixed reaction time, pressure, and feedstock concentration of 8 s, 24.6 MPa, and 1 mmol/l ($\tilde{0}$.006 wt.%) acetic acid, respectively. Figure 6.19 shows reproduced figures from the original work by Meyer, Marrone, and Tester [143], where Fig. 6.19a shows acetic acid conversion versus temperature data, and Fig. 6.19b shows how the Arrhenius kinetics were obtained from data fitting.

The experiments in the low temperature zone produced flow rates of gas that were immeasurable as they were below the lower limit of the apparatus in use. Additionally, the composition of the gas at these low temperatures/conversions

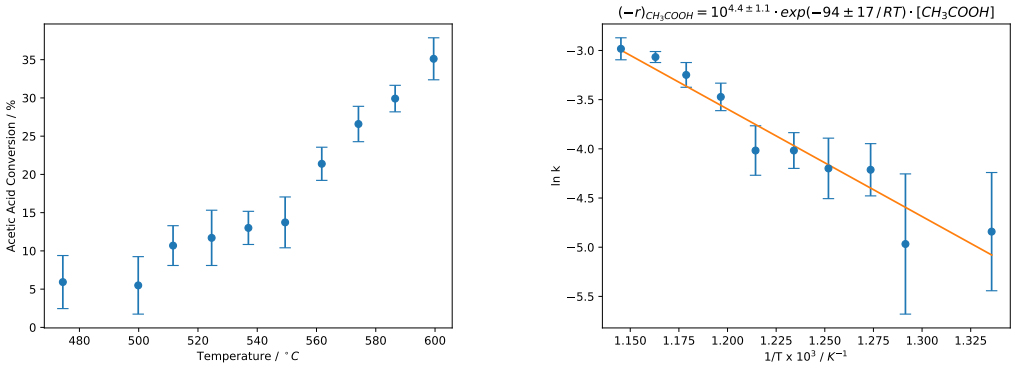

(a) **(b)**

Figure 6.19: Kinetic data for gasification of acetic acid in SCW from Meyer, Marrone, and Tester [143]

consisted of mostly CO_2 and CH_4 but was non-reproducible [143]. Figure 6.19a shows the high-degree of uncertainty in the low temperature experiments, with a particularly peculiar feature being the reduction in conversion observed as reaction temperature was increased from 475°C to 500°C. This translates to a very large uncertainty in $ln\, k$ at these low temperatures as shown in Figure 6.19b. Meyer, Marrone, and Tester [143] admitted in their conclusions that there were doubts surrounding the first-order model used to fit the kinetic data, particularly due to the uncertainty in experiments conducted at 500°C and lower. It was suggested that more rigorous kinetics could be obtained by conducting more experiments at a wider range of temperatures and residence times. Additionally, neither the effect of acetic acid concentration nor reaction pressure was taken into account.

Other SCWG experiments using an acetic acid feedstock have been conducted in literature. Watanabe et al. [93] found that at 400°C, acetic acid was stable in SCW at 25 MPa after 60 min with no catalyst present. Under these same reaction conditions, partial decomposition into CH_4, CO_2, and acetone could be promoted via the addition of KOH, or complete decomposition into CO_2 and acetone with ZrO_2 catalyst. It is purported that temperatures in excess of 450°C are needed to commence the gasification of acetic acid in a non-catalytic environment [143]. It had been previously reported by Watanabe et al. [176] that altering the pressure

of reaction between 25 MPa and 40 MPa had no observable effect on promoting the gasification of acetic acid at 400°C.

Guo et al.(2012) [90] studied the SCWG of acetic acid in a tubular reactor. They found that at 550°C and 25 MPa, around 70 % of a 1 wt.% acetic acid feedstock was gasified after 55 s. This could be increased to over 95 % conversion with the addition of 0.1 wt.% NaOH. The composition of the final gas phase product was 45, 30, and 20 mol.% CO_2, H_2, and CH_4, respectively, in the non-catalytic environment. The addition of 0.1 wt.% NaOH increased the H_2 yield to leave 25, 45, and 15 mol.% CO_2, H_2, and CH_4, respectively.

Caputo et al.(2017) [94] investigated the SCWG of acetic acid at 660°C and 24 MPa in a continuous reactor. After 128 s, a GE of nearly 95 % was achieved, with the gas product consisting of roughly 45, 5, and 50 mol.% CO_2, H_2, and CH_4, respectively.

Wang et al.(2018) [91] used a tubular reactor at 550°C and 25 MPa to study the SCWG of 0.5 to 3.5 wt.% solutions of acetic acid. They found that for all concentrations studied, a GE of nearly 80 % was achieved. The product gas consisted of roughly 66 and 33 mol.% H_2 and CO_2, respectively. They also found that acetic acid could be used as an additive to promote the degradation of other recalcitrant SCWG intermediates like phenol and naphthalene. It was proposed that this was due to acetic acid forming radicals like CH_3COO and CH_3 during its decomposition.

Changsuwan et al.(2020) [92] investigated this concept further by conducting SCWG reactions in a tubular reactor at 25 MPa and 600°C with mixtures of acetic acid and guaiacol - a lignin-dervied char precursor. Gasifying acetic acid on its own, they found increasing the feedstock concentration from 0.5 to 2 wt.% reduced the GE from roughly 100 % to 41 %. In each case, the gas product contained roughly 60 mol.% CO_2, 40 mol.% CH_4, and less than 5 mol.% H_2. It was then shown that acetic acid could be used to completely mitigate char

formation from guaiacol (under the same reaction conditions) by adding around 22 mol.% by carbon acetic acid.

Chakinala et al.(2013) [165] postulated a mechanism for the gasification of acetic acid in SCW. It has been reproduced here in Fig. 6.20. There are a possible three reaction routes which are initiated by the scission of one of following bonds: $O \rightarrow H$, $C \rightarrow H$, or $C \rightarrow O$. Route 1 results in the formation of CH_4 and CO_2 only, whereas Route 2 produces a highly reactive ketene intermediate which leads to the formation of char, CO, and CO_2. Finally, Route 3 results in the possible formation of acetaldehyde, acetone, char, and CO_2; although this has only been observed in the presence of a catalyst.

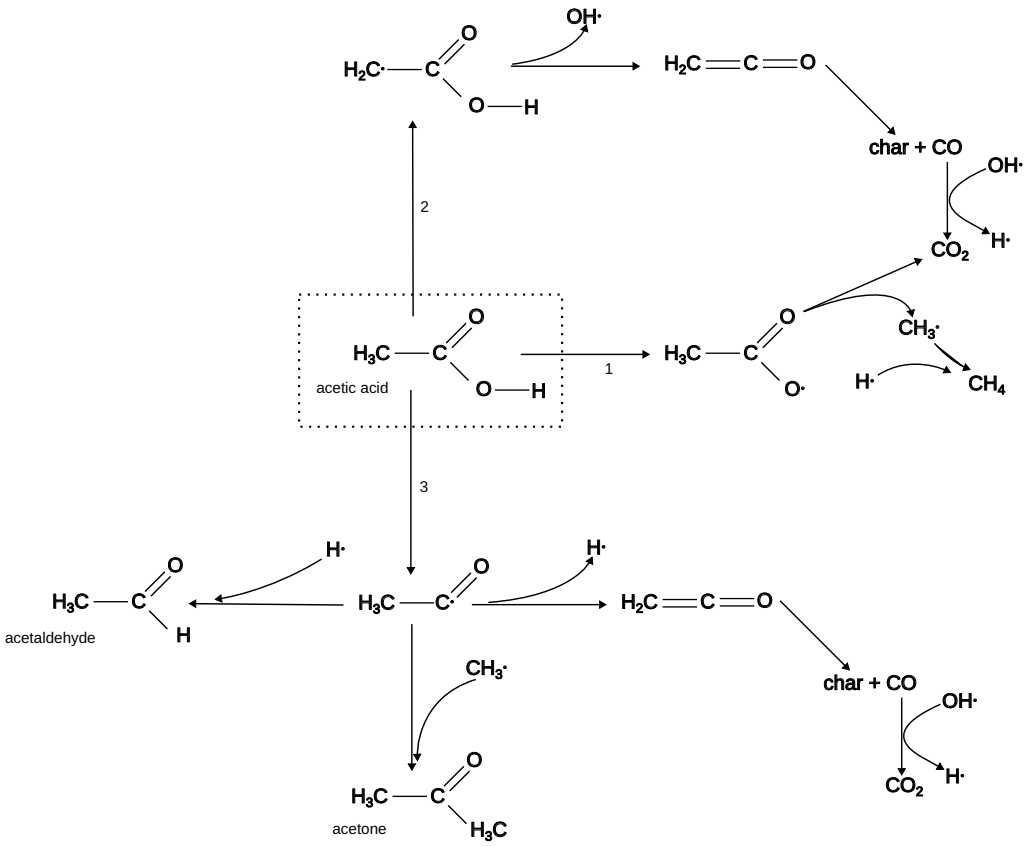

Figure 6.20: Postulated acetic acid decomposition mechanism in SCW.

Experiments suggest that the dominant reaction pathway is Route 1 which

results in the formation of equimolar concentrations of CO_2 and CH_4 via the simplified reaction shown in Eq. 6.4 [165].

Chakinala et al.(2013) [165] conducted SCWG experiments of organic acids and alcohols in a fluidised bed reactor at 600°C and 25 MPa. They found that increasing the feedstock concentration from 10 to 20 wt.% reduced the GE from around 70 to 55%. The ungasified organics in the liquid phase was composed of primarily acetic acid, with a trace amount of acetone. They reported the gas phase to be composed of 50, 5 and 45 mol.% CO_2, H_2, CH_4, respectively - with little difference existing between the 10 and 20 wt.% feedstock concentrations.

A notable discrepancy in the literature data is the yield of H_2. In some cases, it was reported as being a major component of the gas phase product [90, 91], whereas other investigations showed that CH_4 and CO_2 were the dominant products [92–94, 165]. It is possible that this is due to the auto-catalytic influence of the reactor material, as the studies that report significant H_2 yields used reactors constructed from Hastelloy C-276. On the other hand, publications where H_2 yields were low used stainless steel 316, or Inconel 625 in the case of Chakinala et al.(2013) [165].

The objective of this second piece of experimental work would be to increase the understanding of acetic acid gasification in near-critical and supercritical water. Literature shows there are weak kinetics in the temperature region between the critical point of water and 500°C, and there are also discrepancies in the predicted composition of the gas phase product. Given acetic acid's recalcitrance to gasification and high rate of formation during the hydrothermal decomposition of many organic species, obtaining a better understanding of its gasification in SCW is key to maximising the conversion efficiency of SCWG processes.

Figure 6.21 shows how acetic acid is predicted to gasify at fixed temperatures using the Eq. 6.4 kinetics from Meyer, Marrone, and Tester [143]. Even at the lowest temperature plotted, 374°C, complete conversion of acetic acid is predicted to occur after around 150 min. Increasing the temperature to 450°C can reduce this time to less than 25 min.

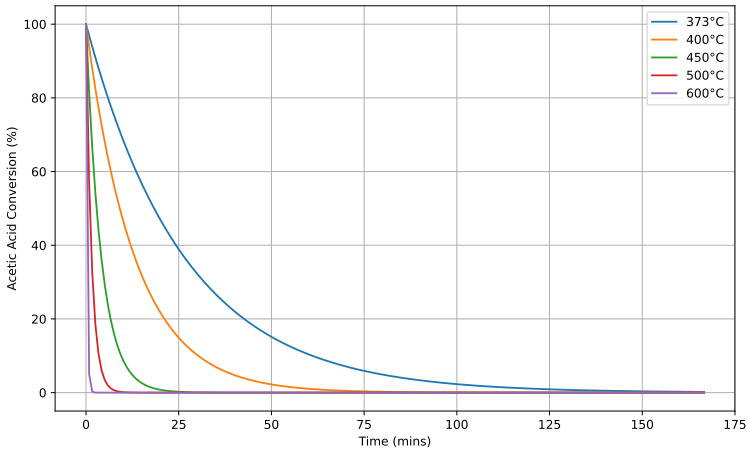

Figure 6.21: Acetic acid conversion versus time at different constant temperatures as predicted by kinetics.

Figure 6.22 shows how acetic acid decomposition is predicted to occur using the kinetics for a 400°C set-point program with the reactor (20 g of water). By tracking both the conversion and temperature plots, it is evident that the current kinetics anticipate complete conversion of acetic acid after 150 min just as the system reaches 400°C.

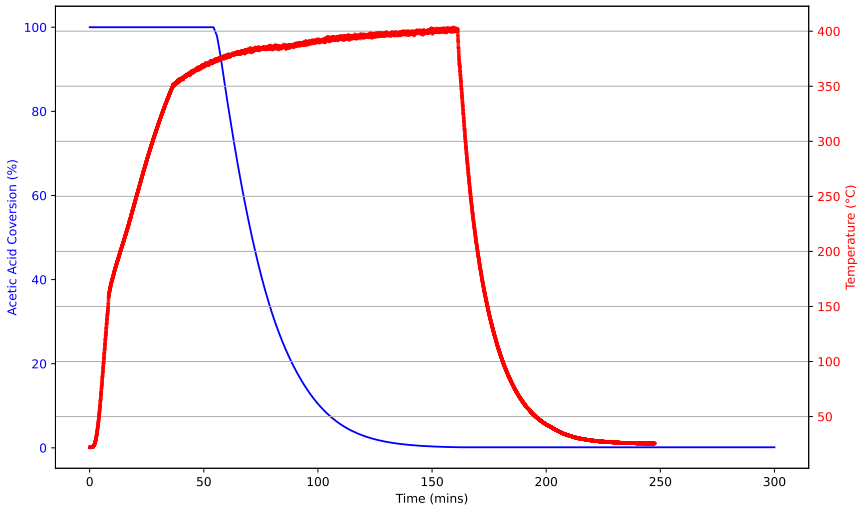

Figure 6.22: Acetic acid conversion versus time with reactor 400°C heating profile as predicted by kinetics.

6.8 Conclusions

This chapter demonstrates a range of experimental approaches associated with the support and development of the SCWG modelling described in this thesis.

A robust experimental methodology was developed which can be implemented to conduct a range of batch-type hydrothermal and supercritical reactions of water and biomass. Calibration of a GC-TCD was also conducted to allow for accurate quantification of syngas in terms of CO, CO_2, CH_4, H_2, and N_2. Monte-Carlo simulations were used to propagate and predict the error in the measurement of each calibration gas.

The final section of this chapter explored different experimental designs that could be used to supplement the computational findings of this thesis. Notably, studies in the effect of heating rate on the gasification of hemicellulose in SCW, and SCWG kinetics of acetic acid.

7 Overall Conclusions

The aim of this doctoral research was to develop and then apply computational and experimental methodologies to increase understanding of the SCWG of wet biomass. Supercritical water gasification is a new technology that shows great promise as a means of effective waste disposal and valorisation. However, its commercial deployment is hindered by several significant hurdles which the objectives of each individual results chapter aimed to help resolve. Here, the knowledge gaps that each results chapter aimed to fulfil and the corresponding conclusions are summarised. Following this, an outlook towards possible directions of beneficial future research is discussed.

7.1 Conclusions

In Chapt. 3, a detailed kinetic model was reproduced from literature, modified, and then validated. The objective of this first results chapter was to establish the kinetic model and then use it to explore the effect of heating rate in the sub-critical region, 25°C to 374°C, have on the SCWG of the major organic constituents of wet biomass: cellulose, hemicellulose, lignin, and protein. Yields of individual syngas species, the CGE, and char formation were used as indicators to assess the

efficacy of the process as a whole. The heating rate was found to most significantly affect the SCWG of hemicellulose, where faster heating rates directly resulted in increased yields of H_2. Cellulose was less responsive to heating rate, although slower heating rates correlated to a marginal increase in H_2 yields when the higher final reaction temperature of 600°C was used. Faster sub-critical heating rates also mitigated char yields from the SCWG and correspondingly increased the CGE, although, increasing the heating rate too much resulted in a return to higher char yields. By studying non-linear heating profiles, it was also found that a 'decelerating' profile could be used to mitigate char yields. The sub-critical heating regime was found to have no influence on the SCWG of protein.

This chapter applied both heuristic and local sensitivity analyses to a detailed kinetic model of cellulose SCWG, identifying key reactions influencing H_2 and acetic acid yields. The analyses revealed that H_2 formation primarily proceeds via the conversion of glucose and fructose to 5-HMF under sub-critical conditions and through WSHS gasification, formed from furfural, under supercritical conditions. The `wgs` reaction was also found to be a major contributor, especially at higher temperatures. Local sensitivity results showed that early-stage supercritical reactions, such as `la.acet`, strongly influence H_2 yields, while `wgs` remains significant later in the process. For acetic acid, erythrose and glycolaldehyde were identified as key precursors, and the conversion of glucose to fructose appeared to reduce its formation. Overall, the limited sensitivity of acetic acid to rate changes highlights its stability in SCW. The findings suggest that improving the kinetic representation of WSHS gasification, particularly the decomposition of furfural, could significantly enhance model accuracy and process optimisation.

A thermodynamic model based on Gibbs free energy minimisation was developed to investigate the equilibrium behaviour of biomass thermochemical treatments. This methodology was unique in that it did not require commercial software to produce the thermodynamic model. Here, the novel perspective of element chemical potentials was used to provide a mechanistic explanation for

the shifting phase and chemical equilibrium observed when changes are made to system temperature, pressure, and elemental composition. Ternary diagrams were used as visual aids to illustrate how these variables alter the relative yields of syngas and char, with focus being paid to the phase boundary on the ternary in particular, which separates the two regions where char formation is possible and not. By adding water and/or CO_2 as co-media to a thermochemical reaction, elemental composition was investigated as an adjustable, optimisable, process variable, like temperature and pressure conventionally are. Water was found to be an effective char-suppressant as the addition of molecuar oxygen shifts the system composition into the single-phase region, whereas CO_2 on the other hand was a more flexible additive as it could be used to either increase char yields in the two-phase region at lower temperatures (below 400°C) or reduce and mitigate char yields at higher temperatures.

The final results chapter focused on designing and developing a series of experimental SCWG methodologies that could be conducted with a newly acquired batch reactor; with focus being paid to experiments that would bolster the computational findings of this thesis. Significant testing was undertaken with the reactor and a robust methodology and operating procedure was established. A GC-TCD was also repaired and calibrated as part of this doctoral research to allow for the accurate quantification of CO, CO_2, CH_4, H_2, and N_2 in the syngas product. Two experiments were designed as part of this final chapter. The first aimed to validate the findings of Chapt. 3 by exploring how heating rate influences H_2 yields from the SCWG of hemicellulose. The second set of experiments looked at acetic acid, a refractory intermediate of SCWG, and sought to determine accurate kinetics and a more detailed decomposition mechanism for this gasification rate-limiting compound.

7.2 Future Work

In addition to the conclusions of each results chapter, various routes of future investigation have been identified that will supplement and advance the findings of this thesis, and progress SCWG as a whole.

The first recommendation is to conduct an experimental heating rate study to validate the findings of Chapt. 3. It was demonstrated in Chapt. 6 how the experimental rig could be used to modify heating rates, and how the kinetic model in such a system would anticipate H_2 yields from the SCWG of hemicellulose to differ when using a slow or fast heating rate. The first objective of this experimental research would be to validate the kinetic model's prediction using a pure hemicellulose (or xylose) feedstock, before which the principle could be tested on hemicellulose-rich real-world feedstocks (e.g. corn stalks).

The sensitivity analysis identified several key areas of the kinetic mechanism that should be improved to deliver the greatest impact. The grouped term 'water-soluble humic species' (WSHS) was used to describe a mixture of acrylic and acetic acid of unknown proportions that significantly contributes to yields of H_2 upon its gasification. To improve the model, experiments should be conducted to establish a far-more detailed, stoichiometric pathway of furfural decomposition into this mixture of acids. This could be obtained using the experimental methodology developed in this thesis to explore how hemicellulose decomposes in a hydrothermal environment into furfural and subsequently WSHS. Analysis of the liquid product would reveal the stoichiometric ratio of acrylic and acetic acid produced from furfural, and any other products that exist in the liquefaction product. The GC-TCD could then also be used to analyse the gas product from WSHS gasification in order to verify the amount of H_2 produced from this purportedly lucrative reaction pathway.

While the thermodynamic framework developed in Chapt. 5 does not apply directly to processes that operate away from equilibrium and that are kinetically

controlled, it does gives an indication of the direction in which the system wants to proceed and the driving forces in the formation of product. It is therefore hypothesised that systems that form char at equilibrium will do so through the formation of longer-chained and ring molecules, leading to liquid bio-oil products as they move towards the final thermodynamic state. Hence, in the future the ternary diagrams should be used to verify if the phase boundary presented also represents the boundary that separates two regions of elemental compositions where char-precursor molecules (e.g., aromatics) will and will not form in a non-equilibrium calculation. This would also help to develop a more holistic understanding of SCWG reaction chemistry by linking the thermodynamic and kinetic models of this thesis, which as it stands are currently entirely disconnected. If it is possible to verify that the ternary diagram phase boundary at a given temperature and pressure dictates whether char-precursor molecules will form for a given system composition or not, then this can be compared to the rate at which those same char-precursors are formed as predicted by the kinetic model for the same reaction temperature and starting molecule.

While the thermodynamic framework developed in Chapt. 5 does not apply directly to processes operating away from equilibrium and under kinetic control, it does provide an indication of the direction in which the system tends to evolve and the driving forces governing product formation. It is therefore hypothesised that systems predicted to form char at equilibrium will do so via the formation of longer-chained and ring-containing molecules, leading to liquid bio-oil products as they progress toward the final thermodynamic state. Hence, in future work the ternary diagrams should be used to verify whether the phase boundary presented also represents the boundary separating two regions of elemental composition in which char-precursor molecules (e.g., aromatics) do and do not form under non-equilibrium conditions. Establishing this connection would contribute to a more holistic understanding of SCWG reaction chemistry by linking the thermodynamic and kinetic models developed in this thesis, which at present remain entirely

disconnected. If it can be verified that the ternary diagram phase boundary at a given temperature and pressure dictates whether char-precursor molecules will form for a given system composition, this prediction can then be compared with the rate at which those same precursors are formed according to the kinetic model under the same reaction temperature and starting composition.

References

[1] David Meek et al. “Comparing Scottish bioenergy supply and demand in the context of Net-Zero targets”. In: (2022).

[2] Chai Siah Lee, Alex V. Conradie, and Edward Lester. “Review of supercritical water gasification with lignocellulosic real biomass as the feedstocks: Process parameters, biomass composition, catalyst development, reactor design and its challenges”. In: *Chemical Engineering Journal* 415 (2021), p. 128837. URL: https://www.sciencedirect.com/science/article/pii/S1385894721004319.

[3] Judith Bates. *Biomass Feedstock Availability: Final Report*. Report. Ricardo Energy & Environment, 2017. URL: https://www.gov.uk/government/publications%20/uk-and-global-bioenergy-resource-model.

[4] Muhammad Usmaan Bin Khawer et al. “Anaerobic digestion of sewage sludge for biogas and biohydrogen production: State-of-the-art trends and prospects”. In: *Fuel* 329 (2022), p. 125416. URL: https://www.sciencedirect.com/science/article/pii/S0016236122022499.

[5] Jorge M. Ribeiro et al. “Future Perspectives of Biomass Torrefaction: Review of the Current State-Of-The-Art and Research Development”. In: *Sustainability* 10.7 (2018), p. 2323.

[6] S. K. Sansaniwal et al. “Recent advances in the development of biomass gasification technology: A comprehensive review”. In: *Renew. Sustain. Energy Rev.* 72 (2017), pp. 363–384.

[7] Koray Alper et al. “Sustainable energy and fuels from biomass: a review focusing on hydrothermal biomass processing”. In: *Sustainable Energy Fuels* 4.9 (2020), pp. 4390–4414.

[8] Robert Muhlke et al. “Hydrothermal gasification-White paper”. In: (2023).

[9] Yulin Hu et al. “Supercritical water gasification of biomass model compounds: A review”. In: *Renew. Sustain. Energy Rev.* 118 (2020), p. 109529.

[10] Runqiu Dong et al. “Thermodynamic analysis and life cycle assessment of the preferred supercritical water gasification coupled system for energy self-sufficiency: From food waste to hydrogen”. In: *Energy* 317 (2025), p. 134553.

[11] Xietian Zheng et al. “Environmental impact assessment of a combined bioprocess for hydrogen production from food waste”. In: *Waste Management* 173 (2024), pp. 152–159. URL: https://www.sciencedirect.com/science/article/pii/S0956053X23006840.

[12] UKRI. *Eligibility of technology readiness levels (TRL)*. Online. 2025. URL: https://www.ukri.org/councils/stfc/guidance-for-applicants/check-if-youre-eligible-for-funding/eligibility-of-technology-readiness-levels-trl/.

[13] Catalina Rodriguez Correa and Andrea Kruse. "Supercritical water gasification of biomass for hydrogen production–Review". In: *The Journal of Supercritical Fluids* 133 (2018), pp. 573–590.

[14] Mohammad-Saeed Safdari et al. "Heating rate and temperature effects on pyrolysis products from live wildland fuels". In: *Fuel* 242 (2019), pp. 295–304.

[15] Dwi Hantoko et al. "Supercritical water gasification of sewage sludge and combined cycle for H2 and power production–a thermodynamic study". In: *International Journal of Hydrogen Energy* 44.45 (2019), pp. 24459–24470.

[16] Alireza Rahbari et al. "A solar fuel plant via supercritical water gasification integrated with Fischer–Tropsch synthesis: Steady-state modelling and techno-economic assessment". In: *Energy Conversion and Management* 184 (2019), pp. 636–648.

[17] M-C Bellissent-Funel. "Structure of supercritical water". In: *Journal of Molecular Liquids* 90.1-3 (2001), pp. 313–322.

[18] Dirk Bröll et al. "Chemistry in supercritical water". In: *Angewandte Chemie International Edition* 38.20 (1999), pp. 2998–3014.

[19] Gerd Brunner. *Hydrothermal and supercritical water processes*. Vol. 5. Elsevier, 2014.

[20] Mitsumasa Osada et al. "Water density effect on lignin gasification over supported noble metal catalysts in supercritical water". In: *Energy & Fuels* 20.3 (2006), pp. 930–935.

[21] Y. Guo et al. "Review of catalytic supercritical water gasification for hydrogen production from biomass". In: *Renewable and Sustainable Energy Reviews* 14.1 (2010), pp. 334–343. URL: https://www.sciencedirect.com/science/article/pii/S1364032109002123.

[22] Hermann Weingärtner and Ernst Ulrich Franck. "Supercritical water as a solvent". In: *Angewandte Chemie International Edition* 44.18 (2005), pp. 2672–2692.

[23] Kapil Khandelwal et al. "Conversion of biomass into hydrogen by supercritical water gasification: a review". In: *Environmental Chemistry Letters* 21.5 (2023), pp. 2619–2638.

[24] Jude A Okolie et al. "Supercritical water gasification of biomass: a state-of-the-art review of process parameters, reaction mechanisms and catalysis". In: *Sustainable energy & fuels* 3.3 (2019), pp. 578–598.

[25] Y.J. Lu et al. "Hydrogen production by biomass gasification in supercritical water: A parametric study". In: *International Journal of Hydrogen Energy* 31.7 (2006), pp. 822–831. URL: https://www.sciencedirect.com/science/article/pii/S0360319905002855.

[26] Ayhan Demirbas. "Hydrogen-rich gas from fruit shells via supercritical water extraction". In: *International Journal of Hydrogen Energy* 29.12 (2004), pp. 1237–1243. URL: https://www.sciencedirect.com/science/article/pii/S0360319903003343.

[27] Tülay Güngören Madenoğlu et al. "Simultaneous effect of temperature and pressure on catalytic hydrothermal gasification of glucose". In: *The Journal of Supercritical Fluids* 73 (2013), pp. 151–160. URL: https://www.sciencedirect.com/science/article/pii/S089684461200321X.

[28] Hui Jin et al. "Hydrogen production by partial oxidative gasification of biomass and its model compounds in supercritical water". In: *International Journal of Hydrogen Energy* 35.7 (2010). 2008 International Hydrogen Forum (HyForum2008), pp. 3001–3010. URL: https://www.sciencedirect.com/science/article/pii/S0360319909009586.

[29] Athanasios A. Vadarlis et al. "Catalytic Biomass Gasification in Supercritical Water and Product Gas Upgrading". In: *ChemBioEng Reviews* 10.4 (2023), pp. 370–398. eprint: https://onlinelibrary.wiley.com/doi/pdf/10.1002/cben.202300007. URL: https://onlinelibrary.wiley.com/doi/abs/10.1002/cben.202300007.

[30] Emmanuel Galiwango, James Butler, and Samira Lotfi. "A Review of Catalyst Integration in Hydrothermal Gasification". In: *Fuels* 5.3 (2024), pp. 375–393. URL: https://www.mdpi.com/2673-3994/5/3/22.

[31] Michael Jerry Antal Jr et al. "Biomass gasification in supercritical water". In: *Industrial & Engineering Chemistry Research* 39.11 (2000), pp. 4040–4053.

[32] Ali Sınağ, Andrea Kruse, and Jens Rathert. "Influence of the heating rate and the type of catalyst on the formation of key intermediates and on the generation of gases during hydropyrolysis of glucose in supercritical water in a batch reactor". In: *Industrial & Engineering Chemistry Research* 43.2 (2004), pp. 502–508.

[33] Yukihiko Matsumura et al. "EFFECT OF HEATING RATE OF BIOMASS FEEDSTOCK ON CARBON GASIFICATION EFFICIENCY IN SUPERCRITICAL WATER GASIFICATION". In: *Chemical Engineering Communications* 193.5 (2006). doi: 10.1080/00986440500440157, pp. 649–659. URL: https://doi.org/10.1080/00986440500440157.

[34] Obie Farobie et al. "Effect of the heating rate on the supercritical water gasification of a glucose/guaiacol mixture". In: *Industrial & Engineering Chemistry Research* 56.22 (2017), pp. 6401–6407.

[35] Rahmat Iman Mainil and Yukihiko Matsumura. "Effect of heating rate on gasification and phosphorus recovery for palm oil mill effluent in supercritical water". In: *The Journal of Supercritical Fluids* 173 (2021), p. 105217.

[36] Onursal Yakaboylu et al. "Supercritical Water Gasification of Biomass: An Integrated Kinetic Model for the Prediction of Product Compounds". In: *Ind. Eng. Chem. Res.* 54.33 (2015), pp. 8100–8112.

[37] Paul T Williams. *Waste treatment and disposal*. John Wiley & Sons, 2005.

[38] Małgorzata Kacprzak et al. "Sewage sludge disposal strategies for sustainable development". In: *Environmental research* 156 (2017), pp. 39–46.

[39] Sezai Delibacak, Lyudmila Voronina, and Ekaterina Morachevskaya. "Use of sewage sludge in agricultural soils: Useful or harmful". In: *Eurasian Journal of Soil Science* 9.2 (2020), pp. 126–139.

[40] Mian Hu et al. "Thermochemical conversion of sewage sludge for energy and resource recovery: technical challenges and prospects". In: *Environmental Pollutants and Bioavailability* 33.1 (2021), pp. 145–163.

[41] Francesco Di Capua et al. "High-solid anaerobic digestion of sewage sludge: challenges and opportunities". In: *Applied Energy* 278 (2020), p. 115608.

[42] Mi Yan et al. "Syngas production and heavy metal dynamics during supercritical water gasification of sewage sludge". In: *Frontiers of Environmental Science & Engineering* 18.12 (2024), p. 149.

[43] H Zhang et al. "Alkali-catalyzed supercritical water gasification of sewage sludge: effect of liquid residue reuse as homogenous catalyst". In: *International Journal of Environmental Science and Technology* 17 (2020), pp. 2845–2852.

[44] Chenyu Wang et al. "Char and tar formation during hydrothermal treatment of sewage sludge in subcritical and supercritical water: Effect of organic matter composition and experiments with model compounds". In: *Journal of Cleaner Production* 242 (2020), p. 118586.

[45] Kelly M Kibler et al. "Food waste and the food-energy-water nexus: A review of food waste management alternatives". In: *Waste management* 74 (2018), pp. 52–62.

[46] Sathish Thanikodi and Atul A Sagade. "Utilizing supercritical water gasification for hydrogen production combined with a waste heat recovery system for domestic households". In: *Results in Engineering* 24 (2024), p. 103432.

[47] Jianyong Liu et al. "A two-step process for energy-efficient conversion of food waste via supercritical water gasification: Process design, products analysis, and electricity evaluation". In: *Science of The Total Environment* 752 (2021), p. 142331.

[48] Wei Su et al. "Supercritical water gasification of food waste: Effect of parameters on hydrogen production". In: *International Journal of Hydrogen Energy* 45.29 (2020), pp. 14744–14755.

[49] Lucía Pola et al. "Kraft black liquor as a renewable source of value-added chemicals". In: *Chemical Engineering Journal* 448 (2022), p. 137728.

[50] Ajay Kumar Singh and Ram Chandra. "Pollutants released from the pulp paper industry: Aquatic toxicity and their health hazards". In: *Aquatic toxicology* 211 (2019), pp. 202–216.

[51] Hary Demey et al. "Hydrogen Production by Catalytic Supercritical Water Gasification of Black Liquor-Based Wastewater". In: *ENERGIES* 16.8 (Apr. 2023).

[52] Ali Karimi et al. "Catalytic supercritical water gasification of black liquor along with lignocellulosic biomass". In: *International Journal of Hydrogen Energy* 47.38 (2022), pp. 16729–16740.

[53] Pau Casademont et al. "Hydrogen production by supercritical water gasification of black liquor: use of high temperatures and short residence times in a continuous reactor". In: *The Journal of Supercritical Fluids* 159 (2020), p. 104772.

[54] Lakhan Kumar and Navneeta Bharadvaja. "A review on microalgae biofuel and biorefinery: challenges and way forward". In: *Energy sources, part A: recovery, utilization, and environmental effects* 46.1 (2024), pp. 16599–16622.

[55] Kieran Heeley et al. "Supercritical water gasification of microalgae: The impact of the algal growth water". In: *The Journal of Supercritical Fluids* 205 (2024), p. 106143. URL: https://www.sciencedirect.com/science/article/pii/S0896844623003078.

[56] Puji Rahmawati Nurcahyani, Soshi Hashimoto, and Yukihiko Matsumura. "Supercritical water gasification of microalgae with and without oil extraction". In: *The Journal of Supercritical Fluids* 165 (2020), p. 104936.

[57] Donghai Xu et al. "Catalytic supercritical water gasification of aqueous phase directly derived from microalgae hydrothermal liquefaction". In: *International Journal of Hydrogen Energy* 44.48 (2019), pp. 26181–26192.

[58] Chuang Yang et al. "Hydrothermal liquefaction and gasification of biomass and model compounds: a review". In: *Green Chemistry* 22.23 (2020), pp. 8210–8232.

[59] Motonobu Goto et al. "Kinetic analysis for destruction of municipal sewage sludge and alcohol distillery wastewater by supercritical water oxidation". In: *Industrial & engineering chemistry research* 38.5 (1999), pp. 1863–1865.

[60] Christopher Jazrawi et al. "Two-stage hydrothermal liquefaction of a high-protein microalga". In: *Algal Research* 8 (2015), pp. 15–22. URL: https://www.sciencedirect.com/science/article/pii/S2211926414001428.

[61] Thachanan Samanmulya, Obie Farobie, and Yukihiko Matsumura. "Gasification characteristics of aminobutyric acid and serine as model compounds of proteins under supercritical water conditions". In: *Journal of the Japan Petroleum Institute* 60.1 (2017), pp. 34–40.

[62] Thachanan SAMANMULYA and Yukihiko MATSUMURA. "Effect of activated carbon catalytic on supercritical water gasification of glycine as a model compound of protein". In: *Journal of the Japan Institute of Energy* 92.9 (2013), pp. 894–899.

[63] Thachanan Samanmulya et al. "Gasification characteristics of alanine in supercritical water". In: *Journal of the Japan Petroleum Institute* 57.5 (2014), pp. 225–229.

[64] Thachanan SAMANMULYA et al. "Gasification characteristics of amino acids in supercritical water". In: *Journal of the Japan Institute of Energy* 93.9 (2014), pp. 936–943.

[65] D. Fytili and A. Zabaniotou. "Utilization of sewage sludge in EU application of old and new methods—A review". In: *Renewable and Sustainable Energy Reviews* 12.1 (2008), pp. 116–140. URL: https://www.sciencedirect.com/science/article/pii/S1364032106000827.

[66] Emhemmed A. Youssef, George Nakhla, and Paul A. Charpentier. "Oleic acid gasification over supported metal catalysts in supercritical water: Hydrogen production and product distribution". In: *International Journal of Hydrogen Energy* 36.8 (2011), pp. 4830–4842. URL: https://www.sciencedirect.com/science/article/pii/S0360319911002060.

[67] Simao Guo et al. "Hydrogen production from glycerol by supercritical water gasification in a continuous flow tubular reactor". In: *International Journal of Hydrogen Energy* 37.7 (2012). XII International Symposium on Polymer Electrolytes: New Materials for Application in Proton Exchange Membrane Fuel Cells, pp. 5559–5568. URL: https://www.sciencedirect.com/science/article/pii/S0360319911028692.

[68] Simao Guo et al. "Supercritical water gasification of glycerol: Intermediates and kinetics". In: *The Journal of Supercritical Fluids* 78 (2013), pp. 95–102.

[69] Jude A. Okolie et al. "Modeling and process optimization of hydrothermal gasification for hydrogen production: A comprehensive review". In: *The Journal of Supercritical Fluids* 173 (2021), p. 105199. URL: https://www.sciencedirect.com/science/article/pii/S0896844621000383.

[70] Sahar Safarian, Runar Unnthorsson, and Christiaan Richter. "The equivalence of stoichiometric and non-stoichiometric methods for modeling gasification and other reaction equilibria". In: *Renewable and Sustainable Energy Reviews* 131 (2020), p. 109982. URL: https://www.sciencedirect.com/science/article/pii/S1364032120302732.

[71] Petric Marc Ruya, Ronny Purwadi, and Siew Shee Lim. "Supercritical water gasification of sewage sludge for power generation— thermodynamic study on auto-thermal operation using Aspen Plus". In: *Energy Convers. Manag.* 206 (Feb. 2020), p. 112458.

[72] Dianqi Hu et al. "Thermodynamic and environmental analysis of integrated supercritical water gasification of sewage sludge for power and hydrogen production". In: *Energy* 299 (2024), p. 131568.

[73] Jingwei Chen et al. "System development and thermodynamic performance analysis of a system integrating supercritical water gasification of black liquor with direct-reduced iron process". In: *Energy* 295 (2024), p. 131094.

[74] Xingang Qi et al. "Hydrogen production by kraft black liquor supercritical water gasification: Reaction pathway and kinetic". In: *Energy* 282 (2023), p. 128839.

[75] Yue Qiu et al. "Thermodynamic analysis and optimization of supercritical water gasification and oxidation systems for papermaking black liquor". In: *International Journal of Hydrogen Energy* 109 (2025), pp. 486–496.

[76] Runqiu Dong et al. “Thermodynamic analysis of an integrated hydrogen and power production system by food waste supercritical water gasification”. In: *Journal of Environmental Chemical Engineering* 13.1 (2025), p. 115092.

[77] Domenico Macri et al. “Supercritical water gasification of biomass and agro-food residues: Energy assessment from modelling approach”. In: *Renewable Energy* 150 (2020), pp. 624–636.

[78] Zhiyong Peng et al. “Thermodynamic and environmental analysis of food waste supercritical water gasification integrated H2 in-situ separation system”. In: *Applied Thermal Engineering* 264 (2025), p. 125460.

[79] FAP Voll et al. “Thermodynamic analysis of supercritical water gasification of methanol, ethanol, glycerol, glucose and cellulose”. In: *International Journal of Hydrogen Energy* 34.24 (2009), pp. 9737–9744.

[80] Dwi Hantoko et al. “Thermodynamic study on the integrated supercritical water gasification with reforming process for hydrogen production: Effects of operating parameters”. In: *international journal of hydrogen energy* 43.37 (2018), pp. 17620–17632.

[81] Kapil Khandelwal and Ajay K. Dalai. “Catalytic Supercritical Water Gasification of Canola Straw with Promoted and Supported Nickel-Based Catalysts”. In: *Molecules* 29.4 (2024). URL: https://www.mdpi.com/1420-3049/29/4/911.

[82] Changqing Cao et al. “Evaluation of effect of evaporation on supercritical water gasification of black liquor by energy and exergy analysis”. In: *International Journal of Hydrogen Energy* 43.30 (2018), pp. 13788–13797.

[83] Daniele Castello and Luca Fiori. “Supercritical water gasification of biomass: Thermodynamic constraints”. In: *Bioresource technology* 102.16 (2011), pp. 7574–7582.

[84] Daniele Castello and Luca Fiori. “Supercritical water gasification of biomass: a stoichiometric thermodynamic model”. In: *International Journal of Hydrogen Energy* 40.21 (2015), pp. 6771–6781.

[85] Liang Zhao et al. “Effects of potassium carbonate on acetaldehyde gasification in supercritical water”. In: *Energy Sources, Part A: Recovery, Utilization, and Environmental Effects* 42.10 (2020), pp. 1286–1298.

[86] Fernando L. P. Resende and Phillip E. Savage. “Kinetic model for noncatalytic supercritical water gasification of cellulose and lignin”. In: *AIChE Journal* 56.9 (2010), pp. 2412–2420. eprint: https://aiche.onlinelibrary.wiley.com/doi/pdf/10.1002/aic.12165. URL: https://aiche.onlinelibrary.wiley.com/doi/abs/10.1002/aic.12165.

[87] Athika Chuntanapum and Yukihiko Matsumura. “Role of 5-HMF in supercritical water gasification of glucose”. In: *Journal of chemical engineering of Japan* 44.2 (2011), pp. 91–97.

[88] Yi Xie, Xinliang Zheng, and Weijun Gao. "Gasification of horse dung in supercritical water". In: *International Journal of Hydrogen Energy* 47.9 (2022), pp. 5871–5878.

[89] Qingqing Guan, Chaohai Wei, and Phillip E Savage. "Kinetic model for supercritical water gasification of algae". In: *Physical Chemistry Chemical Physics* 14.9 (2012), pp. 3140–3147.

[90] Yang Guo et al. "Gasification of two and three-components mixture in supercritical water: Influence of NaOH and initial reactants of acetic acid and phenol". In: *International Journal of Hydrogen Energy* 37.3 (2012). 2010 AIChE Annual Meeting Topical Conference on Hydrogen Production and Storage Special Issue, pp. 2278–2286. URL: https://www.sciencedirect.com/science/article/pii/S0360319911024475.

[91] Yuzhen Wang et al. "Interactive effects of phenol, naphthalene and acetic acid during the supercritical water gasification process". In: *Environmental Progress & Sustainable Energy* 37.3 (2018), pp. 1140–1148.

[92] Pattraporn Changsuwan, Shuhei Inoue, and Yukihiko Matsumura. "Supercritical Water Gasification of Guaiacol with Acetic Acid as a Radical Scavenger: Interaction Effect on Char Formation and Gas Composition". In: *ACS Omega* 5.38 (2020). PMID: 33015500, pp. 24818–24825. URL: https://doi.org/10.1021/acsomega.0c03506.

[93] Masaru Watanabe et al. "Conversions of some small organic compounds with metal oxides in supercritical water at 673 K". In: *Green Chemistry* 5.5 (2003), pp. 539–544.

[94] Giuseppe Caputo et al. "Valorization of waste solvents through supercritical water gasification". In: *CHEMICAL ENGINEERING* 57 (2017).

[95] R Ochieng and S Sarker. "Energy and techno-economic analysis of integrated supercritical water gasification of sewage sludge and fast pyrolysis of wood for power, heat, and hydrogen production". In: *Chemical Engineering Science* (2025), p. 121236.

[96] Jude A. Okolie et al. "Optimization and modeling of process parameters during hydrothermal gasification of biomass model compounds to generate hydrogen-rich gas products". In: *International Journal of Hydrogen Energy* 45.36 (2020). Waste and Biomass-derived Hydrogen Synthesis and Implementation, pp. 18275–18288. URL: https://www.sciencedirect.com/science/article/pii/S0360319919319883.

[97] Thiago Averaldo Bimestre et al. "Energy and exergy analysis of a supercritical water gasification system for the simultaneous production of hydrogen, heat, and electricity from sugarcane bagasse". In: *Next Energy* 8 (2025), p. 100266.

[98] Takuya Yoshida and Yukihiko Matsumura. "Reactor development for supercritical water gasification of 4.9 wt% glucose solution at 673 K by using computational fluid dynamics". In: *Industrial & engineering chemistry research* 48.18 (2009), pp. 8381–8386.

[99] Aaron K Goodwin and Gregory L Rorrer. "Modeling of supercritical water gasification of xylose to hydrogen-rich gas in a hastelloy microchannel reactor". In: *Industrial & engineering chemistry research* 50.12 (2011), pp. 7172–7182.

[100] Giuseppe Caputo et al. "Experimental and fluid dynamic study of continuous supercritical water gasification of glucose". In: *The Journal of Supercritical Fluids* 107 (2016), pp. 450–461.

[101] Sheng Zhao et al. "Interpretable machine learning for predicting and evaluating hydrogen production via supercritical water gasification of biomass". In: *Journal of Cleaner Production* 316 (2021), p. 128244.

[102] Jie Li et al. "Machine learning aided supercritical water gasification for H2-rich syngas production with process optimization and catalyst screening". In: *Chemical Engineering Journal* 426 (2021), p. 131285.

[103] Chengwei Huang et al. "Optimizing H2 production from biomass: A machine learning-enhanced model of supercritical water gasification dynamics". In: *Energy* 312 (2024), p. 133490.

[104] Kapil Khandelwal, Sonil Nanda, and Ajay K Dalai. "Machine learning modeling of supercritical water gasification for predictive hydrogen production from waste biomass". In: *Biomass and Bioenergy* 197 (2025), p. 107816.

[105] Hui Ge et al. "Experiment evaluation and thermodynamic analysis of pulping modification on ordered conversion of bark in supercritical water". In: *Chemical Engineering Journal* 491 (2024), p. 152157. URL: https://www.sciencedirect.com/science/article/pii/S1385894724036441.

[106] Botian Hao et al. "Catalytic gasification of indole in supercritical water with non-noble bimetallic catalysts". In: *Biomass and Bioenergy* 166 (2022), p. 106601.

[107] Lixiao Zheng et al. "A novel biotar-derived porous carbon supported Ru catalyst for hydrogen production from supercritical water gasification of glycerol". In: *Renewable Energy* 212 (2023), pp. 921–927.

[108] Fanrui Meng et al. "Catalytic gasification of anthracene in supercritical water with Ni/TiO2 catalyst: Products distribution and kinetics". In: *Fuel* 358 (2024), p. 130341.

[109] Pai Peng et al. "Supercritical water gasification mechanism of polymer-containing oily sludge". In: *International Journal of Hydrogen Energy* 46.53 (2021), pp. 26834–26847.

[110] Athanasios A. Vadarlis et al. "Supercritical water gasification and subsequent steam reforming of the product gas under elevated temperature and pressure". In: *International Journal of Hydrogen Energy* 111 (2025), pp. 567–580. URL: https://www.sciencedirect.com/science/article/pii/S0360319925007621.

[111] Julian Dutzi et al. “Comparison of Experimental Results with Thermodynamic Equilibrium Simulations of Supercritical Water Gasification of Concentrated Ethanol Solutions with Focus on Water Splitting”. In: *Industrial & Engineering Chemistry Research* 62.32 (2023), pp. 12501–12512. URL: https://doi.org/10.1021/acs.iecr.3c01595.

[112] Julian Dutzi, Nikolaos Boukis, and Jörg Sauer. “Supercritical water gasification of heavy metal contaminated plants with focus on separation of heavy metal contaminants”. In: *Biomass and Bioenergy* 182 (2024), p. 107059. URL: https://www.sciencedirect.com/science/article/pii/S0961953424000126.

[113] Julian Dutzi, Nikolaos Boukis, and Jörg Sauer. “Process Effluent Recycling in the Supercritical Water Gasification of Dry Biomass”. In: *Processes* 11.3 (2023). URL: https://www.mdpi.com/2227-9717/11/3/797.

[114] Julian Dutzi, Nikolaos Boukis, and Jörg Sauer. “Investigating Salt Precipitation in Continuous Supercritical Water Gasification of Biomass”. In: *Processes* 12.5 (2024). URL: https://www.mdpi.com/2227-9717/12/5/935.

[115] Mohammed Ahmed Mohammed Ali, Shuhei Inoue, and Yukihiko Matsumura. “Gasification characteristics of carbon nanotube in supercritical water”. In: *The Journal of Supercritical Fluids* 182 (2022), p. 105532. URL: https://www.sciencedirect.com/science/article/pii/S0896844622000171.

[116] Mohammed Ahmed Mohammed Ali, Shuhei Inoue, and Yukihiko Matsumura. “Carbon nanotube as catalyst support in supercritical water”. In: *The Journal of Supercritical Fluids* 190 (2022), p. 105755.

[117] Mohammed Ahmed Mohammed Ali et al. “Reaction characteristics of homogeneous and heterogenous reactions for glucose gasification in supercritical water using ruthenium catalyst supported on carbon nanotube”. In: *The Journal of Supercritical Fluids* 206 (2024), p. 106156. URL: https://www.sciencedirect.com/science/article/pii/S0896844623003200.

[118] Puji Rahmawati Nurcahyani and Yukihiko Matsumura. “Reutilization of Algal Supercritical Water Gasification Waste for Microalgae Chlorella vulgaris Cultivation”. In: *ACS Omega* 6.19 (2021). PMID: 34056405, pp. 12551–12556. URL: https://doi.org/10.1021/acsomega.1c00476.

[119] Christopher Hunston et al. “Investigating active phase loss from supported ruthenium catalysts during supercritical water gasification”. In: *Catalysis science & technology* 11.22 (2021), pp. 7431–7444.

[120] Christopher Hunston et al. “Particle size effects in Ru/CNF catalysts during supercritical water gasification of glycerol”. In: *Applied Catalysis B: Environmental* 320 (2023), p. 121956. URL: https://www.sciencedirect.com/science/article/pii/S0926337322008979.

[121] Daniil Salionov et al. “The nature of carbon deposits and their formation pathways during catalytic supercritical water gasification of glycerol”. In: *Journal of Catalysis* 426 (2023), pp. 257–269. URL: https://www.sciencedirect.com/science/article/pii/S0021951723002968.

[122] Jude A. Okolie et al. "Catalytic Supercritical Water Gasification of Soybean Straw: Effects of Catalyst Supports and Promoters". In: *Industrial & Engineering Chemistry Research* 60.16 (2021), pp. 5770–5782. URL: https://doi.org/10.1021/acs.iecr.0c06177.

[123] Helene Curmi et al. "Extraction of phenolic compounds from sulfur-free black liquor thanks to hydrothermal treatment before the production of syngas for biofuels". In: *JOURNAL OF SUPERCRITICAL FLUIDS* 181 (Feb. 2022).

[124] Larissa Sepini et al. "Understanding the conversion mechanisms in supercritical water conditions of PET as a model compound of plastic wastes". In: *CHEMICAL ENGINEERING JOURNAL* 488 (May 2024).

[125] Marcela M. Marcelino et al. "Supercritical Water Gasification of Coconut Shell Impregnated with a Nickel Nanocatalyst: Box-Behnken Design and Process Evaluation". In: *Energies* 16.8 (2023). URL: https://www.mdpi.com/1996-1073/16/8/3563.

[126] Marcela M. Marcelino et al. "Effect of Nickel Nanocatalyst Loading on Supercritical Water Gasification of Coconut Shell". In: *Energies* 17.4 (2024). URL: https://www.mdpi.com/1996-1073/17/4/872.

[127] Kieran Heeley et al. "Assessment of Iron(III) chloride as a catalyst for the production of hydrogen from the supercritical water gasification of microalgae". In: *Next Energy* 6 (2025), p. 100198. URL: https://www.sciencedirect.com/science/article/pii/S2949821X24001030.

[128] Daniele Castello and Luca Fiori. "Supercritical water gasification of biomass: Thermodynamic constraints". In: *Bioresour. Technol.* 102.16 (2011), pp. 7574–7582.

[129] Chao He et al. "Hydrothermal gasification of sewage sludge and model compounds for renewable hydrogen production: A review". In: *Renew. Sustain. Energy Rev.* 39 (2014), pp. 1127–1142.

[130] Catalina Rodriguez Correa and Andrea Kruse. "Supercritical water gasification of biomass for hydrogen production – Review". In: *J. Supercrit. Fluids* 133 (2018), pp. 573–590.

[131] Bernard M. Kabyemela et al. "Glucose and Fructose Decomposition in Subcritical and Supercritical Water: Detailed Reaction Pathway, Mechanisms, and Kinetics". In: *Ind. Eng. Chem. Res.* 38.8 (1999), pp. 2888–2895.

[132] T. Flannelly et al. "Non-stoichiometric formation of formic and levulinic acids from the hydrolysis of biomass derived hexose carbohydrates". In: *RSC Adv.* 6.7 (2016), pp. 5797–5804.

[133] Andrew A Peterson et al. "Thermochemical biofuel production in hydrothermal media: a review of sub-and supercritical water technologies". In: *Energy Environ. Sci.* 1.1 (2008), pp. 32–65.

[134] JING Qi and LÜ Xiuyang. "Kinetics of non-catalyzed decomposition of D-xylose in high temperature liquid water". In: *Chin. J. Chem. Eng.* 15.5 (2007), pp. 666–669.

[135] Brian R Pinkard et al. “Supercritical water gasification: practical design strategies and operational challenges for lab-scale, continuous flow reactors”. In: *Heliyon* 5.2 (2019).

[136] Zhi Shen et al. “Experimental and numerical analysis of heat transfer to water at supercritical pressures”. In: *International Journal of Heat and Mass Transfer* 108 (2017), pp. 1676–1688. URL: https://www.sciencedirect.com/science/article/pii/S0017931016314351.

[137] Pauli Virtanen et al. “SciPy 1.0: Fundamental Algorithms for Scientific Computing in Python”. In: *Nature Methods* 17.3 (Mar. 2020), pp. 261–272. URL: https://doi.org/10.1038/s41592-019-0686-2.

[138] Akifumi Nakamura et al. “Gasification of catalyst-suspended chicken manure in supercritical water”. In: *J. Chem. Eng. Jpn.* 41.5 (2008), pp. 433–440.

[139] Phyllis2. “database for (treated) biomass, algae, feedstocks for biogas production and biochar”. In: (2024). URL: https://phyllis.nl/.

[140] M.P.R. Haaker and P.J.T. Verheijen. “Local and Global Sensitivity Analysis for a Reactor Design with Parameter Uncertainty”. In: *Chemical Engineering Research and Design* 82.5 (2004), pp. 591–598. URL: https://www.sciencedirect.com/science/article/pii/S0263876204725319.

[141] Jian An et al. “A new framework of global sensitivity analysis for the chemical kinetic model using PSO-BPNN”. In: *Computers & Chemical Engineering* 112 (2018), pp. 154–164.

[142] Tamás Turányi. “Sensitivity analysis of complex kinetic systems. Tools and applications”. In: *Journal of mathematical chemistry* 5.3 (1990), pp. 203–248.

[143] Jerry C Meyer, Philip A Marrone, and Jefferson W Tester. “Acetic acid oxidation and hydrolysis in supercritical water”. In: *AIChE journal* 41.9 (1995), pp. 2108–2121.

[144] Andrea Saltelli et al. “Sensitivity analysis for chemical models”. In: *Chemical reviews* 105.7 (2005), pp. 2811–2828.

[145] T Turanyi and H Rabitz. “Local methods”. In: *Sensitivity analysis* (2000), pp. 81–99.

[146] Judit Zádor, I Gy Zsely, and Tamás Turányi. “Local and global uncertainty analysis of complex chemical kinetic systems”. In: *Reliability Engineering & System Safety* 91.10-11 (2006), pp. 1232–1240.

[147] M Kavgic et al. “Uncertainty and modeling energy consumption: Sensitivity analysis for a city-scale domestic energy model”. In: *Energy and Buildings* 60 (2013), pp. 1–11.

[148] Wenhan Cao, Jun Li, and Xiaolei Zhang. “Evaluation of the effects and interactions of initial chlorine and sulphur contents on the release of potassium compounds during biomass combustion”. In: *Journal of the Energy Institute* 101 (2022), pp. 178–186.

[149] Eliakim H Moore. “On the reciprocal of the general algebraic matrix”. In: *Bull. Amer. Math. Soc.* 26 (1920), pp. 294–295. URL: https://cir.nii.ac.jp/crid/1573387450082342272.

[150] R. Penrose. "A generalized inverse for matrices". In: *Math. Proc. Camb. Philos. Soc.* 51.3 (July 1955), pp. 406–413.

[151] R. Penrose. "On best approximate solutions of linear matrix equations". In: *Math. Proc. Camb. Philos. Soc.* 52.1 (Jan. 1956), pp. 17–19.

[152] Bonnie J McBride. *NASA Glenn coefficients for calculating thermodynamic properties of individual species*. National Aeronautics and Space Administration, John H. Glenn Research Center . . ., 2002.

[153] Luca M. Ghiringhelli et al. In: *Physical Review Letters* 94.14 ().

[154] Xiaofei Wang, Sandro Scandolo, and Roberto Car. In: *Physical Review Letters* 95.18 ().

[155] Michael F. Doherty and Michael F. Malone. *Conceptual design of distillation systems.* McGraw-Hill chemical engineering series. New York, NY, USA: McGraw-Hill, 2001. URL: https://cir.nii.ac.jp/crid/1130282271096684928.

[156] Vineet Singh Sikarwar et al. "An overview of advances in biomass gasification". In: *Energy Environ. Sci.* 9.10 (2016), pp. 2939–2977.

[157] T. Srinivas, A. V. S. S. K. S. Gupta, and B. V. Reddy. "Thermodynamic Equilibrium Model and Exergy Analysis of a Biomass Gasifier". In: *J. Energy Resour. Technol.* 131.3 (Aug. 2009).

[158] Yunhui Pang et al. "Experimental study on co-gasification of cellulose and high-density polyethylene with CO_2". In: *J. Energy Inst.* 117 (2024), p. 101839.

[159] Eilhann E. Kwon, Soosan Kim, and Jechan Lee. "Pyrolysis of waste feedstocks in CO_2 for effective energy recovery and waste treatment". In: *J. CO2 Util.* 31 (2019), pp. 173–180.

[160] Kiran Raj Goud Burra et al. "Near-Critical CO_2-Assisted Liquefaction-Extraction of Biomass and Wastes to Fuels and Value-Added Products". In: *J. Energy Resour. Technol.* 146.1 (Dec. 2024), p. 011801.

[161] Yaping Hu et al. "CO2-assisted catalytic municipal sludge for carbonaceous biofuel via sub-and supercritical water gasification". In: *Energy* 233 (2021), p. 121184.

[162] Department for Energy Security and Net Zero. *Biomass Strategy 2023.* Tech. rep. 2023. URL: https://assets.publishing.service.gov.uk/media/64dc8d3960d123000d32c602/biomass-strategy-2023.pdf.

[163] Supergen Bioenergy Hub. *Supergen Bioenergy Hub response to consultation on Invest 2035: the UK's modern industrial strategy.* Tech. rep. 2024. URL: https://www.supergen-bioenergy.net/wp-content/uploads/2024/11/Industrial-strategy-consultation-response-Nov-2024.pdf.

[164] Jialing Xu et al. "Thermodynamic analysis of using CO2 as a co-gasification agent in supercritical water gasification of glycerol". In: *Journal of Environmental Chemical Engineering* 11.6 (2023), p. 111359. URL: https://www.sciencedirect.com/science/article/pii/S2213343723020985.

[165] Anand G. Chakinala et al. “Supercritical water gasification of organic acids and alcohols: The effect of chain length”. In: *The Journal of Supercritical Fluids* 74 (2013), pp. 8–21. URL: https://www.sciencedirect.com/science/article/pii/S0896844612003592.

[166] WV Steele et al. “Thermodynamic Properties and Ideal-Gas Enthalpies of Formation for 2-aminoisobutyric acid (2-methylalanine), acetic acid,(Z)-5-ethylidene-2-norbornene, mesityl oxide (4-methyl-3-penten-2-one), 4-methylpent-1-ene, 2, 2 ‘-bis (phenylthio) propane, and glycidyl phenyl ether (1, 2-epoxy-3-phenoxypropane)”. In: *Journal of Chemical & Engineering Data* 42.6 (1997), pp. 1053–1066.

[167] S A Channiwala and P P Parikh. “A unified correlation for estimating HHV of solid, liquid and gaseous fuels”. In: *Fuel* 81.8 (2002), pp. 1051–1063.

[168] P.J. Linstrom and eds. W.G. Mallard. *NIST Chemistry WebBook, NIST Standard Reference Database Number 69*. https://webbook.nist.gov/chemistry/. National Institute of Standards and Technology, Gaithersburg MD, 20899. 2025.

[169] Katherine E Robbins and Samuel Eddie Davis. “Verification of the ASTM G-124 Purge Equation”. In: *Twelfth International Symposium on Flammability and Sensitivity of Materials in Oxygen Enriched Atmospheres*. M09-0198. 2009.

[170] Colin F Poole. “Conventional detectors for gas chromatography”. In: *Gas Chromatography*. Elsevier, 2021, pp. 343–369.

[171] Leonid M Blumberg. “Theory of gas chromatography”. In: *Gas chromatography*. Elsevier, 2021, pp. 19–97.

[172] Shimadzu. *Analysis results of GC*. https://www.shimadzu.com/an/service-support/technical-support/analysis-basics/fundamentals/results.html. 2025.

[173] Lourdes Calvo and David Vallejo. “Formation of organic acids during the hydrolysis and oxidation of several wastes in sub-and supercritical water”. In: *Industrial & engineering chemistry research* 41.25 (2002), pp. 6503–6509.

[174] Colomba Di Blasi et al. “Supercritical gasification of wastewater from updraft wood gasifiers”. In: *Biomass and Bioenergy* 31.11-12 (2007), pp. 802–811.

[175] Sonil Nanda et al. “Hydrothermal catalytic processing of waste cooking oil for hydrogen-rich syngas production”. In: *Chemical Engineering Science* 195 (2019), pp. 935–945.

[176] Masaru Watanabe et al. “Catalytic decarboxylation of acetic acid with zirconia catalyst in supercritical water”. In: *Applied Catalysis A: General* 219.1 (2001), pp. 149–156. URL: https://www.sciencedirect.com/science/article/pii/S0926860X01006779.

Appendices

Appendix A

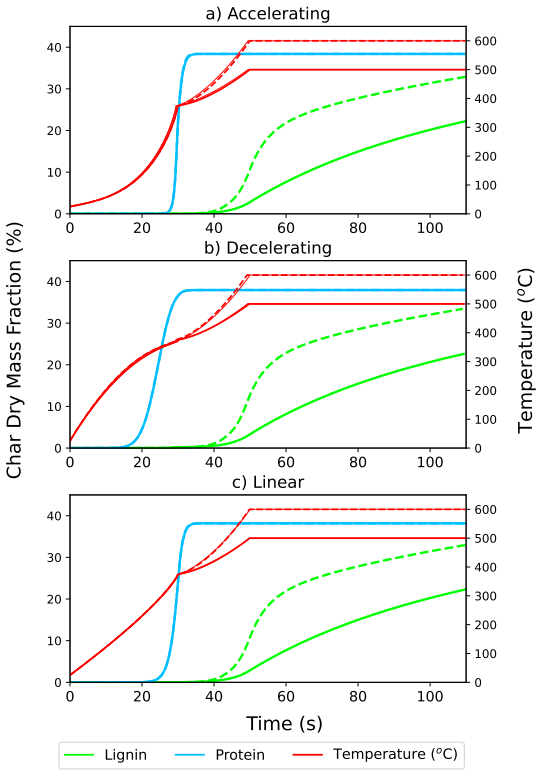

Figure A1: Total dry mass fraction of lignin and protein derived char, and temperature, versus reaction time at an accelerating, decelerating, and linear sub-critical heating rate 690 °C min^{-1}. Final reaction temperatures of 500°C (solid) and 600°C (dashed)

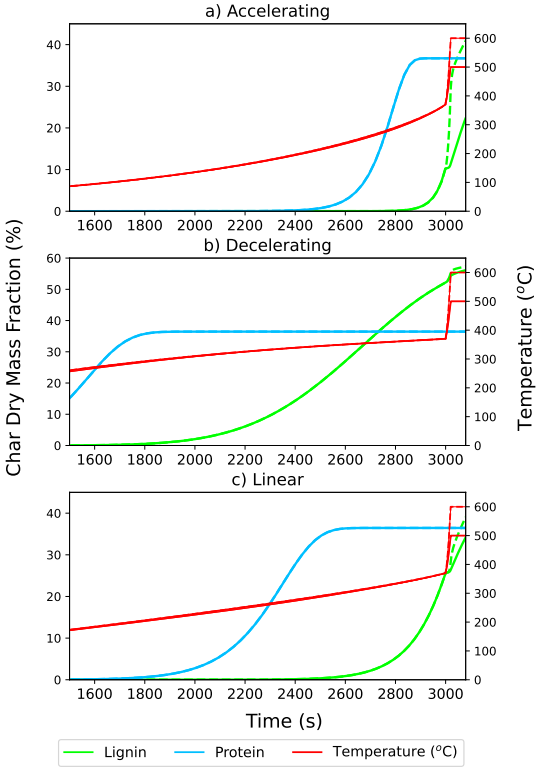

Figure A2: Total dry mass fraction of lignin and protein derived char, and temperature, versus reaction time at a accelerating, decelerating, and linear sub-critical heating rate $6.9\,^{\circ}\mathrm{C}\,\mathrm{min}^{-1}$. Final reaction temperatures of 500°C (solid) and 600°C (dashed)

Table A1: Arrhenius parameters for reactions of cellulose in sub- and supercritical water

Name	**A** (s^{-1})	**Ea** ($kJ\,mol^{-1}$)	**Equation**
1	3.1e+04	6.69e+04	Cellobiose →GlyEryt + Glycolal
2	7.8e+04	6.93e+04	Cellobiose →GlyGly + Erythrose
3	1.4e+09	1.09e+05	Cellobiose + H_2O →Glucose + Glycolal + Erythrose
ge.g	3.6e+08	1.06e+05	GlyEryt + H_2O →Glucose + Glycolal + 0.5Erythrose
gg.g	1.4e+08	1.11e+05	GlyGly + H_2O →0.5Glucose + 0.5Glycolal + Erythrose
g.f	3e+09	1.13e+05	Glucose →Fructose
g.a	9e+03	6.59e+04	Glucose →AnhyGlu + H_2O
g.5	1.48e+08	1.14e+05	Glucose →HMF + $3H_2O$
f.5	1.15e+03	4.23e+04	Fructose →HMF + $3H_2O$
g.e	1.2e+12	1.41e+05	Glucose →Erythrose + Glycolal
f.e	5.3e+11	1.4e+05	Fructose →Erythrose + Glycolal
g.gly	2.5e+07	9.57e+04	Glucose →2Glyceral
f.gly	1.2e+11	1.33e+05	Fructose →2Glyceral
gly.dih	1.5e+13	1.54e+05	Glyceral →Dihydrox
dih.gly	4.6e+05	7.73e+04	Dihydrox →Glyceral
gly.p	7.6e+06	8.26e+04	Glyceral →Pyruval + H_2O
dih.p	1.8e+07	8.87e+04	Dihydrox →Pyruval + H_2O
f.acid	7.4e+10	1.29e+05	Fructose →2LacticAcid
p.acid	6.59e+07	9.4e+04	Pyruval + H_2O →LacticAcid
a.acid	8e+07	1.09e+05	AnhyGlu + $3H_2O$ →2AceticAcid + 2FormicAcid + 4H
e.acid	2.1e+10	1.25e+05	Erythrose + $2H_2O$ →AceticAcid + 2FormicAcid + 4H
glyo.acid	2.1e+10	1.25e+05	Glycolal →AceticAcid
5.lf	8e+07	9.56e+04	HMF + $2H_2O$ →LevuAcid + FormicAcid
5.ff	7.1e+09	1.15e+05	HMF →Furfural + Formalde

Table A2: Arrhenius parameters for reactions of hemicellulose in sub-critical water

Name	**A** (s^{-1})	**Ea** ($kJ\,mol^{-1}$)	**Equation**
xy.fu	2.26e+10	1.11e+05	Xylose →Furfural + $3H_2O$
fu.aa	1.19e+05	5.88e+04	Furfural + $2H_2O$ →WSHS
xy.gm	5.03e+13	1.43e+05	Xylose →Glyceral + MethForm

Table A3: Arrhenius parameters for reactions of hemicellulose in supercritical water

Name	**A** (s^{-1})	**Ea** ($kJ\,mol^{-1}$)	**Equation**
xy.fu	1.3e+13	1.48e+05	Xylose →Furfural + $3H_2O$
xy.wshs	6.6e+14	1.55e+05	Xylose →WSHS + H_2O
fu.wshs	1.7e+06	1.01e+05	Furfural + $2H_2O$ →WSHS
fu.ch	1.37e+04	8.79e+04	Furfural →CharFurf
wshs.gas	3.5e+08	1.43e+05	WSHS + H_2O →5CO + $5H_2$

Table A4: Arrhenius parameters for reactions of lignin in sub-critical water

Name	**A** (s^{-1})	**Ea** ($kJ\,mol^{-1}$)	**Equation**
gu.oc	0.0311	0	Guaiacol →oCresol + O
gu.ga	6.7e+10	1.69e+05	Guaiacol + 4.099H_2O →0.198H_2 + 0.001CO + 3.049CO_2 + 3.95CH_4
gu.c	6.83e+03	8.24e+04	Guaiacol →Catechol + aCH_2
gu.t	0.773	1.01e+05	Guaiacol →0.5Diphenyl + CH_3O + O
c.oc	0.005	8.48e+03	Catechol + aCH_2 →oCresol + O
c.t	0.3	1.09e+04	Catechol →0.5Diphenyl + OH + O
t.ga	0.08	1.82e+04	Diphenyl + 9.637H_2O →0.277H_2 + 0.002CO + 4.817CO_2 + 7.18CH_4
t.p	1.8	3.75e+04	Diphenyl + 2OH →2Phenol
t.b	1.13e+03	7.98e+04	Diphenyl + H_2 →2Benzene
t.ch	3.09e+04	6.69e+04	Diphenyl →CharDiph
gu.b	8.28e+03	8.46e+04	Guaiacol →Benzene + Formalde + O
b.ch	3.4e+22	2.99e+05	Benzene →CharBenz
oc.t	9.5e+10	1.63e+05	oCresol →0.5Diphenyl + CH_3 + O

Table A5: Arrhenius parameters for reactions of lignin in supercritical water

Name	**A** (s^{-1})	**Ea** ($kJ\,mol^{-1}$)	**Equation**
gu.ch	4.4e+17	2.68e+05	Guaiacol →CharGuai
gu.ga*	1.58e+05	9.68e+04	Guaiacol + 4.648H_2O →1.316H_2 + 0.021CO + 3.313CO_2 + 3.666CH_4
gu.ga**	1.58e+05	9.68e+04	Guaiacol + 5.577H_2O →3.253H_2 + 0.098CO + 3.74CO_2 + 3.162CH_4
gu.oc	3.7e+04	8.33e+04	Guaiacol →oCresol + O
gu.c	0.039	0	Guaiacol →Catechol + aCH_2
gu.t	3.38e+03	5.61e+04	Guaiacol →0.5Diphenyl + CH_3O + O
c.oc	0.06	1.85e+04	Catechol + aCH_2 →oCresol + O
t.p	0.001	0	Diphenyl + 2OH →2Phenol
t.ch	8.15e+05	1.1e+05	Diphenyl →CharDiph
t.ga*	3.3	3.78e+04	Diphenyl + 10.324H_2O →1.683H_2 + 0.035CO + 5.145CO_2 + 6.821CH_4
t.ga**	3.3	3.78e+04	Diphenyl + 11.51H_2O →4.184H_2 + 0.164CO + 5.673CO_2 + 6.162CH_4
c.t	44.4	4.78e+04	Catechol →0.5Diphenyl + OH + O
p.c	1.41e+03	8.92e+04	Phenol + O →Catechol
p.t	1.8	2.31e+04	Phenol →0.5Diphenyl + OH
p.ga*	54.8	5.95e+04	Phenol + 4.496H_2O →1.009H_2 + 0.018CO + 2.739CO_2 + 3.243CH_4
p.ga**	54.8	5.95e+04	Phenol + 5.21H_2O →2.503H_2 + 0.083CO + 3.063CO_2 + 2.853CH_4
p.ch	1.37e+04	8.79e+04	Phenol →CharPhen
b.t	3.5	5.08e+04	Benzene →0.5Diphenyl + 0.5H_2
b.p	15.6	5.81e+04	Benzene + O →Phenol
b.ga*	0.1	3.36e+04	Benzene + 4.929H_2O →0.875H_2 + 0.017CO + 2.456CO_2 + 3.527CH_4
b.ga**	0.1	3.36e+04	Benzene + 5.546H_2O →2.172H_2 + 0.08CO + 2.733CO_2 + 3.186CH_4
b.na	391	6.92e+04	Benzene →0.5Naphtalene + 0.5C_2H_4
na.ch	1.9	3.72e+04	Naphtalene →CharNaph
b.ch	50.9	6.27e+04	Benzene →0.5Diphenyl + CH_3 + O
oc.t	0.0063	0	oCresol →0.5Diphenyl + CH_3 + O

*Gasification stoichiometry at 500°C

**Gasification stoichiometry at 600°C

Table A6: Arrhenius parameters for reactions of protein in sub-critical water

Name	**A** (s^{-1})	**Ea** ($kJ\,mol^{-1}$)	**Equation**
as.a	7.75e+09	1.28e+05	AspAcid + 0.667H_2O →0.333AceticAcid + 0.333PropAcid + 0.333Alanine + 0.333H_2 + 1.333CO_2 + 0.667NH_3
as.g	1.75e+10	1.31e+05	AspAcid + 0.34H_2O →0.34AceticAcid + 0.34Glycine + 0.681CharAspAcid
al.et	1.4e+12	1.56e+05	0.47Alanine + 0.235H_2O →0.235LacticAcid + 0.235EthAmine + 0.235NH_3 + 0.235CO_2
g.met	3.6e+11	1.6e+05	0.78Glycine + 0.39H_2O →0.39GlyAcid + 0.39MethAmine + 0.39NH_3 + 0.39CO_2

Table A7: Arrhenius parameters for reactions of protein in supercritical water

Name	**A** (s^{-1})	**Ea** ($kJ\,mol^{-1}$)	**Equation**
al.et	1.4e+12	1.56e+05	0.47Alanine + 0.235H_2O →0.235LacticAcid + 0.235EthAmine + 0.235NH_3 + 0.235CO_2
g.met	3.6e+11	1.6e+05	0.78Glycine + 0.39H_2O →0.39GlyAcid + 0.39MethAmine + 0.39NH_3 + 0.39CO_2
al.gas*	7.37e+05	1.31e+05	Alanine + 0.757H_2O →0.982H_2 + 0.008CO + 1.374CO_2 + 1.617CH_4 + 0.486N_2 + 0.028NH_3
al.gas**	7.37e+05	1.31e+05	Alanine + 1.421H_2O →2.341H_2 + 0.042CO + 1.69CO_2 + 1.268CH_4 + 0.485N_2 + 0.029NH_3
g.gas*	7.37e+05	1.31e+05	Glycine + 0.146H_2O →0.765H_2 + 0.006CO + 1.07CO_2 + 0.924CH_4 + 0.489N_2 + 0.023NH_3
g.gas**	7.37e+05	1.31e+05	Glycine + 0.648H_2O →1.79H_2 + 0.029CO + 1.309CO_2 + 0.661CH_4 + 0.488N_2 + 0.023NH_3
et.gas*	7.37e+05	1.31e+05	EthAmine + 0.646H_2O →0.745H_2 + 0.003CO + 0.322CO_2 + 1.675CH_4 + 0.483N_2 + 0.033NH_3
et.gas**	7.37e+05	1.31e+05	EthAmine + 1.097H_2O →1.665H_2 + 0.019CO + 0.539CO_2 + 1.442CH_4 + 0.484N_2 + 0.032NH_3
met.gas*	7.37e+05	1.31e+05	MethAmine + 0.123H_2O →0.684H_2 + 0.001CO + 0.061CO_2 + 0.938CH_4 + 0.479N_2 + 0.042NH_3
met.gas**	7.37e+05	1.31e+05	MethAmine + 0.412H_2O →1.284H_2 + 0.008CO + 0.202CO_2 + 0.79CH_4 + 0.484N_2 + 0.031NH_3

*Gasification stoichiometry at 500°C

**Gasification stoichiometry at 600°C

Table A8: Arrhenius parameters for reactions of intermediates in sub- and supercritical water

Name	A (s^{-1})	Ea ($kJ\,mol^{-1}$)	Region*	Equation
f.ga1	1.6e+06	8.5e+04	sub	FormicAcid →CO_2 + H_2
f.ga2	0.004	0	sub	FormicAcid →CO + H_2O
levu.lacet	6.59e+07	9.4e+04	both	LevuAcid + H_2O →LacticAcid + Acetalde
la.lacet	2.37e+09	1.48e+05	both	LacticAcid →Acetalde + CO_2 + H_2
acet.aa	0.0325	0	both	Acetalde + H_2O →AceticAcid + H_2
la.acry	689	6.88e+04	both	LacticAcid →AcryAcid + H_2O
acry.la	0.2	3.54e+04	both	AcryAcid + H_2O →LacticAcid
acry.pa	0.6	3.49e+04	both	AcryAcid + H_2 →PropAcid
acry.hpa	4.13e+03	8.01e+04	both	AcryAcid + H_2O →HPA
hpa.acry	0.0265	0	both	HPA →AcryAcid + H_2O
hpa.glyco	0.00131	0	both	HPA + $2H_2O$ →GlyAcid + CO_2 + $3H_2$
f.ga1	4.8e+12	1.68e+05	sup	FormicAcid →CO_2 + H_2
f.ga2	3.4e+17	2.44e+05	sup	FormicAcid →CO + H_2O
aa.ga	2.5e+04	9.4e+04	sup	AceticAcid →CO_2 + CH_4
pa.ga	1.4e+05	8.94e+04	sup	PropAcid + H_2O →3CO + $4H_2$
glycol.ga	2.5e+04	9.4e+04	sup	GlyAcid + H_2O →$2CO_2$ + $3H_2$
fal.ga	4.8e+12	1.68e+05	sup	Formalde →CO + H_2
mf.aa	7.5e+23	2.51e+05	sup	MethForm →AceticAcid
wgs	3.8e+05	1.16e+05	sup	CO + H_2O →CO_2 + H_2

*Reaction present in either sub-critical ('sub') or supercritical ('sup') region only, or both regions

Table A9: Nomenclature of Chemical Species in Kinetic Model

Shorthand	Longhand	Formula
Cellobiose	Cellobiose	$C_{12}H_{22}O_{11}$
GlyEryt	Glucosyl Erythrose	$C_{10}H_{18}O_9$
Glycolal	Glycolaldehyde	$C_2H_4O_2$
GlyGly	Glucosyl Glycolaldehyde	$C_8H_{14}O_7$
Erythrose	Erythrose	$C_4H_8O_4$
H_2O	Water	H_2O
Glucose	Glucose	$C_6H_{12}O_6$
Fructose	Fructose	$C_6H_{12}O_6$
AnhyGlu	Anhydroglucose	$C_6H_{10}O_5$
HMF	5-(Hydroxymethyl)furfural	$C_6H_6O_3$
Glyceral	Glyceraldehyde	$C_3H_6O_3$
Dihydrox	Dihydroxyacetone	$C_3H_6O_3$
Pyruval	Pyruvaldehyde	$C_3H_4O_2$
LacticAcid	Lactic Acid	$C_3H_6O_3$
AceticAcid	Acetic Acid	$C_2H_4O_2$
LevuAcid	Levulinic Acid	$C_5H_8O_3$

Continued on next page

Table A9 – *Continued from previous page*

Shorthand	**Longhand**	**Formula**
FormicAcid	Formic Acid	CH_2O_2
Furfural	Furfural	$C_5H_4O_2$
Formalde	Formaldehyde	CH_2O
Xylose	Xylose	$C_5H_{10}O_5$
WSHS	Water Soluble Humic Species	$C_2H_4O_2 + C_3H_4O_2$
AcryAcid	Acrylic Acid	$C_3H_4O_2$
PropAcid	Propionic Acid	$C_3H_6O_2$
GlyAcid	Glycolic Acid	$C_2H_4O_3$
Acetalde	Acetaldehyde	C_2H_4O
HPA	3-Hydroxypropionic Acid	$C_3H_6O_3$
MethForm	Methyl Formate	$C_2H_4O_2$
Guaiacol	Guaiacol	$C_7H_8O_2$
oCresol	oCresol	C_7H_8O
Catechol	Catechol	$C_6H_6O_2$
Diphenyl	Diphenyl	$C_{12}H_{10}$
Phenol	Phenol	C_6H_6O
Benzene	Benzene	C_6H_6
Naphtalene	Naphtalene	$C_{10}H_8$
AspAcid	Aspartic Acid	$C_4H_7NO_4$
Alanine	Alanine	$C_3H_7NO_2$
Glycine	Glycine	$C_2H_5NO_2$
EthAmine	Ethylamine	C_2H_7N
MethAmine	Methylamine	CH_5N
CO	Carbon Monoxide	CO
H_2	Hydrogen	H_2
CO_2	Carbon Dioxide	CO_2
CH_4	Methane	CH_4
C_2H_6	Ethane	C_2H_6
CharFurf	Char (Furfural)	$C_5H_4O_2$*
CharGuai	Char (Guaiacol)	$C_7H_8O_2$*
CharBenz	Char (Benzene)	C_6H_6*
CharDiph	Char (Diphenyl)	$C_{12}H_{10}$*
CharPhen	Char (Phenol)	C_6H_6O*
CharNaph	Char (Naphtalene)	$C_{10}H_8$*
CharAspAcid	Char (Aspartic Acid)	$C_4H_7NO_4$*

* *Solid char species*

Appendix B

H

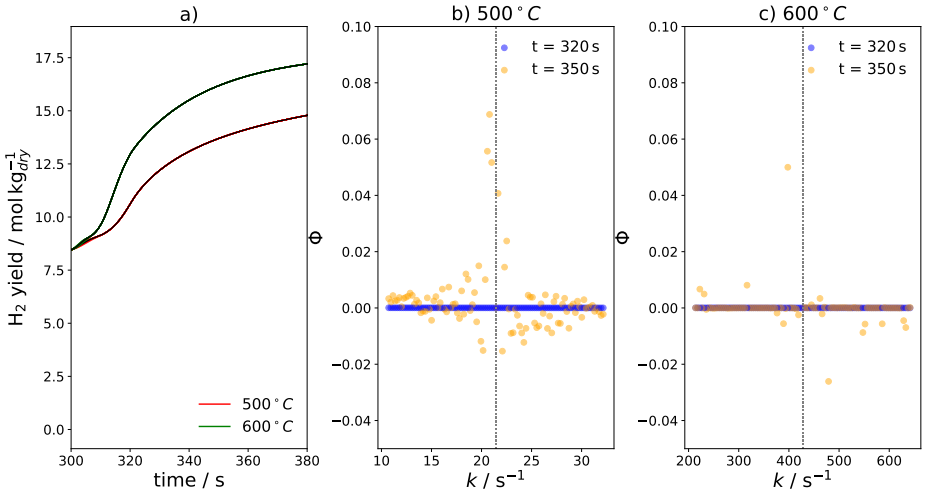

Figure B1: Sensitivity of H_2 formation to `fal.ga`.

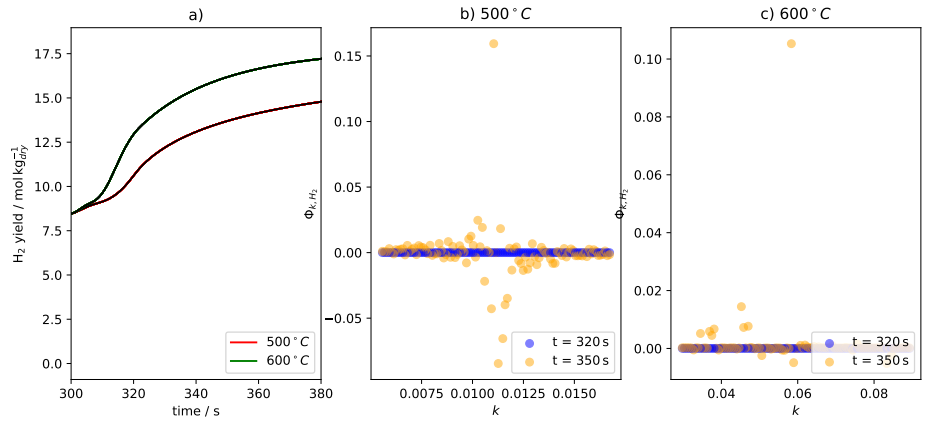

Figure B2: Sensitivity of H_2 formation to `glyco.ga`.

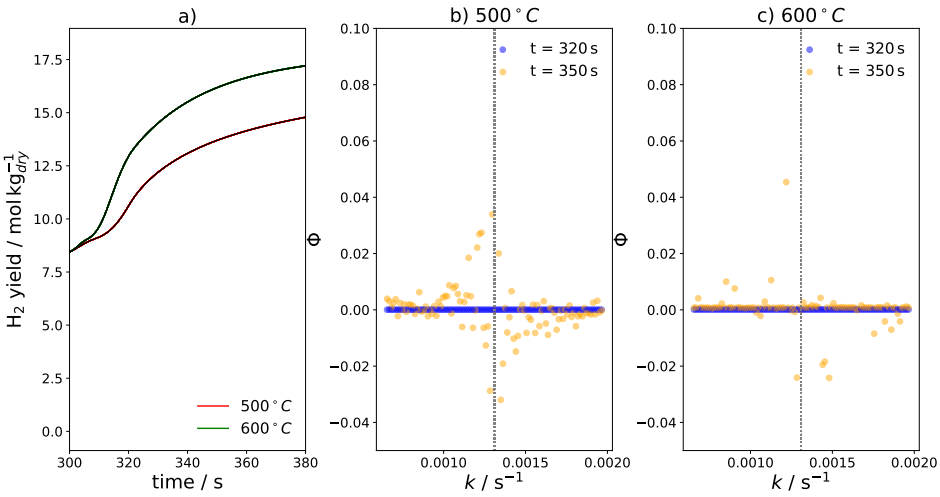

Figure B3: Sensitivity of H_2 formation to `hpa.glyco`.

Appendix C

Table C1: N_2 GC-TCD calibration data.

Run	Gas Conc. (mol.%)	Peak Area	R^2
1	100	5.6624	0.9981
2	100	5.9106	0.9983
3	100	6.0260	0.9982
4	100	6.1695	0.9982
5	100	6.0710	0.9984
6	100	6.0411	0.9984
7	100	5.9992	0.9983
8	100	6.0244	0.9983
9	100	5.9662	0.9983
10	100	5.9317	0.9983
1	90	5.6654	0.9983
2	90	5.6095	0.9983
3	90	5.4293	0.9980
4	90	5.6998	0.9983
5	90	5.5682	0.9984
6	90	4.1687	0.9980
7	90	5.6037	0.9984
8	90	5.6378	0.9982
9	90	5.5831	0.9981
10	90	5.5295	0.9984
1	80	5.0063	0.9983
2	80	4.9941	0.9982
3	80	4.9977	0.9983
4	80	4.9950	0.9983
5	80	4.8940	0.9982
6	80	4.9503	0.9983
7	80	4.9474	0.9983
8	80	4.9805	0.9983
9	80	4.9668	0.9981
10	80	4.7880	0.9983

Table C2: H_2 GC-TCD calibration data.

Run	Gas Conc. (mol.%)	Peak Area	R^2
1	10	5.6686	0.9983
2	10	5.6121	0.9983
3	10	5.4289	0.9980
4	10	5.7048	0.9983
5	10	5.5755	0.9983
6	10	3.5831	0.9993
7	10	4.8059	0.9998
8	10	5.0575	0.9998
9	10	5.1906	0.9998
10	10	5.1117	0.9999
1	20	11.0363	0.9997
2	20	10.9395	0.9997
3	20	10.9880	0.9997
4	20	11.1098	0.9997
5	20	10.6436	0.9997
6	20	10.9552	0.9997
7	20	10.9450	0.9997
8	20	10.8572	0.9997
9	20	10.9112	0.9997
10	20	10.4327	0.9997

Table C3: CH_4 GC-TCD calibration data.

Run	Gas Conc. (mol.%)	Peak Area	R^2
1	10	2.3678	0.9032
2	10	2.1898	0.9888
3	10	2.2746	0.9677
4	10	2.1133	0.9905
5	10	2.1577	0.9841
6	10	2.0733	0.9698
7	10	2.0083	0.9903
8	10	1.9493	0.9900
9	10	1.9870	0.9895
10	10	2.0850	0.9789
1	100	22.5556	0.9960
2	100	23.0427	0.9961
3	100	18.6125	0.9953
4	100	22.8462	0.9954
5	100	17.6886	0.9949
6	100	19.5721	0.9955
7	100	22.5143	0.9959
8	100	21.9364	0.9960
9	100	22.2686	0.9960
10	100	20.9240	0.9959
11	100	17.4462	0.9956
12	100	21.0742	0.9959
13	100	21.2834	0.9956
14	100	20.8408	0.9959
15	100	21.5386	0.9959
16	100	22.1990	0.9955
17	100	21.9250	0.9960
18	100	21.5047	0.9959

Table C4: CO_2 GC-TCD calibration data.

Run	Gas Conc. (mol.%)	Peak Area	R^2
1	10	2.46153315	0.99403626
2	10	2.60177145	0.99393789
3	10	2.72617328	0.99194825
4	10	2.64957227	0.99311444
5	10	2.57096833	0.99395153
6	10	2.50010427	0.98618805
7	10	2.58614875	0.99425304
8	10	2.65923219	0.98661450
9	10	2.58036821	0.99350147
10	10	2.58427251	0.99407126
1	100	31.3513234	0.99775360
2	100	26.6171579	0.99721505
3	100	30.1240560	0.99731182
4	100	30.3430365	0.99735870
5	100	30.1266878	0.99733955
6	100	29.0349154	0.99732014
7	100	30.7263796	0.99752893
8	100	30.7629843	0.99746672
9	100	30.6842429	0.99774456
10	100	30.1922915	0.99770026

Table C5: CO GC-TCD calibration data.

Run	Gas Conc. (mol.%)	Peak Area	R^2
1	100	62.0821	0.9989
2	100	61.6325	0.9987
3	100	58.7959	0.9988
4	100	59.6577	0.9988
5	100	59.7935	0.9988
6	100	59.4342	0.9988
7	100	60.3010	0.9988
8	100	59.6030	0.9988
9	100	58.0778	0.9988
10	100	58.7984	0.9988
11	100	59.0833	0.9988

GC-TCD Methods

Method 1 - Helium

```
Data File  : C:\Chem32\1\DATA\CALIBRATION(JAN'25)\100%CH4-HE-4.D\
Acq. Method: SPL 1-10 (CARBO SUP 25C SLOW TO FAST).M
The Acq. Method's Instrument Parameters for the Run were :
================================================================================
                                  6890 GC METHOD
================================================================================
OVEN
   Initial temp:  25 C (On)                  Maximum temp:  250 C
   Initial time:  15.00 min                  Equilibration time:  1.00 min
   Ramps:
     #   Rate  Final temp  Final time
     1    0 (Off)
   Post temp:  25 C
   Post time:  0.00 min
   Run time:  15.00 min
FRONT INLET (SPLIT/SPLITLESS)             BACK INLET (UNKNOWN)
   Mode:  Split
   Initial temp:  230 C (On)
   Pressure:  2.2 psi (On)
   Split ratio:  10:1
   Split flow:  20.0 mL/min
   Total flow:  24.7 mL/min
   Gas saver:  On
   Saver flow:  15.0 mL/min
   Saver time:  1.00 min
   Gas type:  Helium
COLUMN 1                                  COLUMN 2
   Capillary Column                          (not installed)
   Model Number:  25461
   Description: Carboxen 1006 Capillary
   Max temperature:  250 C
   Nominal length:  30.0 m
   Nominal diameter:  530.00 um
   Nominal film thickness:  30.00 um
   Mode:  ramped flow
   Initial flow:  2.0 mL/min
   Initial time:  7.00 min
     #   Rate  Final flow  Final time
     1   4.00     14.0         5.00
     2    0 (Off)
   Nominal init pressure:  2.2 psi
   Average velocity:  18 cm/sec
   Inlet:  Front Inlet
   Outlet:  Back Detector
   Outlet pressure:  ambient
FRONT DETECTOR (FID)                      BACK DETECTOR (TCD)
   Temperature:  230 C (Off)                 Temperature:  230 C (On)
   Hydrogen flow:  40.0 mL/min (Off)         Reference flow:  15.0 mL/min (On)
   Air flow:  450.0 mL/min (Off)             Mode:  Constant makeup flow
   Mode:  Constant makeup flow               Makeup flow:  7.0 mL/min (On)
   Makeup flow:  15.0 mL/min (Off)           Makeup Gas Type: Helium
   Makeup Gas Type: Helium                   Filament:  On
   Flame:  Off                               Negative polarity:  Off
   Electrometer:  Off
   Lit offset:  2.0
SIGNAL 2
   Save Data:  Off
   Type:  back detector
```

Save Data: On

POST RUN
Post Time: 0.00 min

TIME TABLE
Time(min) Parameter & Setpoint

Column(s)

Column Description : Carboxen 1006 Capillary Column
Inventory# :
Model# : 25461 Manufacturer: Sigma
Diameter : 530.00 µm Length : 30.0 m
Film thickness : 30.00 µm Void time : 2.802 min
Maximum Temperature: 250.0 °C
Comment :

Method 2- Argon

```
    Data File  : C:\Chem32\1\DATA\CALIBRATION(JAN'25)\20%H2-AR-10.D\
Acq. Method: SAMPLE RUN (AR) JAN 25.M
The Acq. Method's Instrument Parameters for the Run were :
================================================================================
                                   6890 GC METHOD
================================================================================
OVEN
   Initial temp:  35 C (On)                  Maximum temp:  250 C
   Initial time:  15.00 min                  Equilibration time:  1.00 min
   Ramps:
     #   Rate  Final temp  Final time
     1    0 (Off)
   Post temp:  50 C
   Post time:  0.00 min
   Run time:  15.00 min
FRONT INLET (SPLIT/SPLITLESS)             BACK INLET (UNKNOWN)
   Mode:  Split
   Initial temp:  230 C (On)
   Pressure:  3.1 psi (On)
   Split ratio:  50:1
   Split flow:  150.3 mL/min
   Total flow:  155.6 mL/min
   Gas saver:  On
   Saver flow:  15.0 mL/min
   Saver time:  2.00 min
   Gas type:  Nitrogen
COLUMN 1                                  COLUMN 2
   Capillary Column                          (not installed)
   Model Number:  25461
   Description: Carboxen 1006 Capillary
   Max temperature:  250 C
   Nominal length:  30.0 m
   Nominal diameter:  530.00 um
   Nominal film thickness:  30.00 um
   Mode:  constant flow
   Initial flow:  3.0 mL/min
   Nominal init pressure:  3.1 psi
   Average velocity:  27 cm/sec
   Inlet:  Front Inlet
   Outlet:  Back Detector
   Outlet pressure:  ambient
FRONT DETECTOR (FID)                      BACK DETECTOR (TCD)
   Temperature:  250 C (Off)                 Temperature:  230 C (On)
   Hydrogen flow:  40.0 mL/min (Off)         Reference flow:  15.0 mL/min (On)
   Air flow:  450.0 mL/min (Off)             Mode:  Constant makeup flow
   Mode:  Constant makeup flow               Makeup flow:  7.0 mL/min (On)
   Makeup flow:  45.0 mL/min (Off)           Makeup Gas Type: Nitrogen
   Makeup Gas Type: Nitrogen                 Filament:  On
   Flame:  Off                               Negative polarity:  Off
   Electrometer:  Off
   Lit offset:  2.0
SIGNAL 2
   Save Data:  Off
   Type:  back detector
   Save Data:  On
                                          POST RUN
                                             Post Time: 0.00 min
TIME TABLE
   Time(min)      Parameter & Setpoint
================================================================
                               Column(s)
```

```
=========================================================================
Column Description :  Carboxen 1006 Capillary Column
Inventory#         :
Model#             :  25461              Manufacturer: Sigma
Diameter           : 530.00 µm           Length :   30.0 m
Film thickness     : 30.00 µm         Void time :    1.858 min
Maximum Temperature:  250.0 °C
Comment            :
```

GC-TCD SOP

Start-Up

1.1: Set the gas selection valve to either helium (Method 1) or argon (Method 2), depending on the method in use (Fig. C1a).

1.2: Open the appropriate gas cylinder and adjust the regulator to deliver a pressure of 80 psi.

1.3: Power on the GC-TCD unit using the main switch (Fig. C1b). Wait until the LCD screen displays `"POWER ON RESTART"`.

1.4: Launch the `Instrument 1 online89` program on the computer. Once the software starts, the GC-TCD fan oven will activate which can be heard.

1.5: Using the software GUI, select the appropriate start-up routine: `STARTUP (HELIUM).M` or `STARTUP (Ar) OCT 24.M`. This will initiate heating of the gas inlet and TCD, which requires approximately 15 min.

1.6: When the system status in the GUI changes to `READY` (Fig. C1c), select the run method corresponding to your gas choice (Method 1 for He, Method 2 for Ar). Upon selection, the TCD will activate; this can be identified by a ticking sound at a rate of approximately 2–3 beats per second.

1.7: Allow the system to stabilize. Wait approximately 40–60 minutes until the signal trace on the GUI displays a consistent baseline (Fig. C1d). Once stable, the system is ready for sample injection.

Sample Run

2.1: Select `Sample Info` from the GUI and in the pop-up window provide an appropriate file name and comment (Fig. C1e). E.g., GasA-1-Ar.D; "Sample run of Gas A using Ar carrier with Method 2 on 30.06.26."

2.2: Using a precision gas syringe, draw in ambient air and inject it into a small beaker containing acetone. Observe for bubbles at the needle tip as this confirms the needle is unobstructed.[1]

2.3: With the needle in the closed position, insert the needle through the gas bag septum. Open the needle and draw in a sample. Remove the needle and purge it to flush residual air. Repeat this process three times to ensure the needle is properly flushed.

[1] If the needle is blocked, remove the plunger from the rear of the syringe and force a full volume of air through the needle to clear the obstruction. Exercise caution to avoid drawing acetone into the syringe.

2.4: After flushing, draw precisely 50 µL of sample gas into the syringe.

2.5: As quickly as possible, inject the sample into the GC-TCD inlet (Fig. C1f). Simultaneously, start a timer and select `RUN Method` in the software GUI.

2.6: After exactly 30 s has elapsed on the timer, press the `Start` button on the GC-TCD unit (Fig. C1g).

2.7: Allow the chromatographic run to proceed for 15 min.

Shut Down

3.1: Select the approprate shut-down method: `SHUTDOWN (HELIUM).M` or `SHUTDOWN (AR) OCT 24.M`. This will turn the TCD off and start cooling all components.

3.2: Open the GC-TCD ventilation door on the top of the machine to help speed up cooling (Fig. C1h).

3.3: After roughly 1 h, use the GC-TCD buttons to check the temperatures of the `Front Inlet` and `Back Detector (TCD)`. They should both be below 100°C.

3.4: Turn OFF the GC-TCD from the main switch and close the appropriate gas cylinder.

Post-Processing

4.1: Data files are stored in the 'offline' version of the software, `Instrument 1 (offline)`

4.2: A `.csv` file for each run can should be exported to a relevant directory. Ensure to select the ASCII delimiter code of `44` make the signal trace and time stamps separated by commas.

4.3: Samples should be exported to an appropriate

GC Servicing and Maintenance

To get the GC into working condition, a number of routine services were carried out. They are listed as follows

- TCD Bakeout at 375°C for 5 hours.
- Column conditioning (as per manufacturers recommendations)
- Inlet liner, o-rings, and septum
- Inlet and detector graphite ferrules
- The inlet-column connection gold seal.

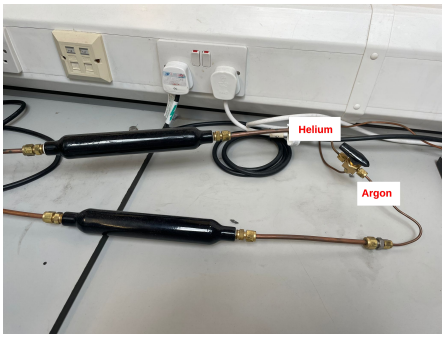

(a)

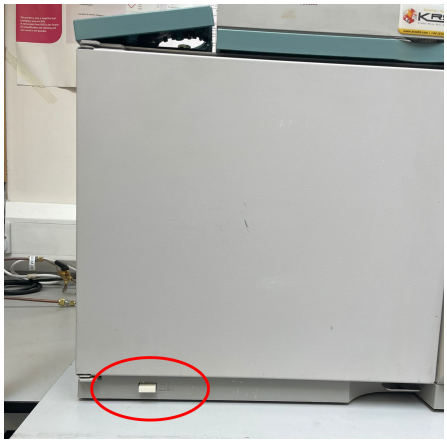

(b) Dynamic Viscosity

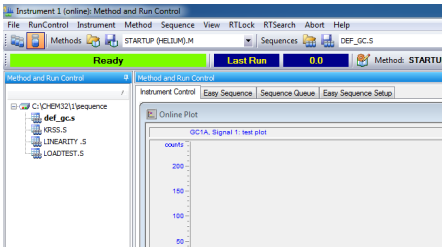

(c)

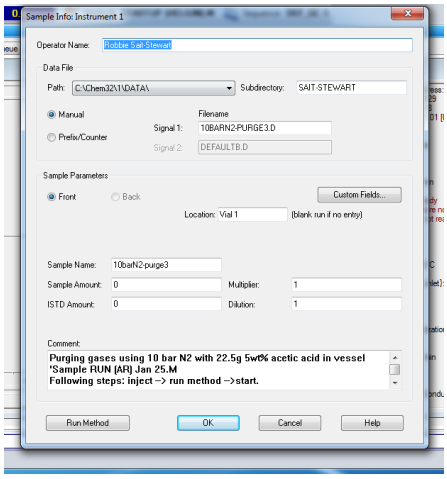

(d) Ionic Product

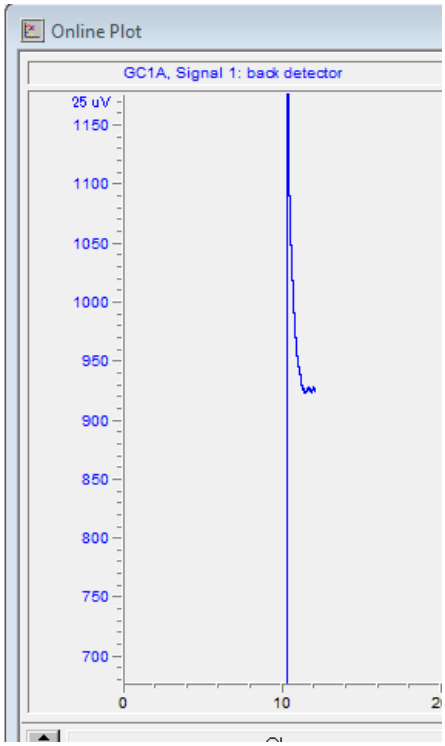

(e)

(f)

Figure C1: GC SOP

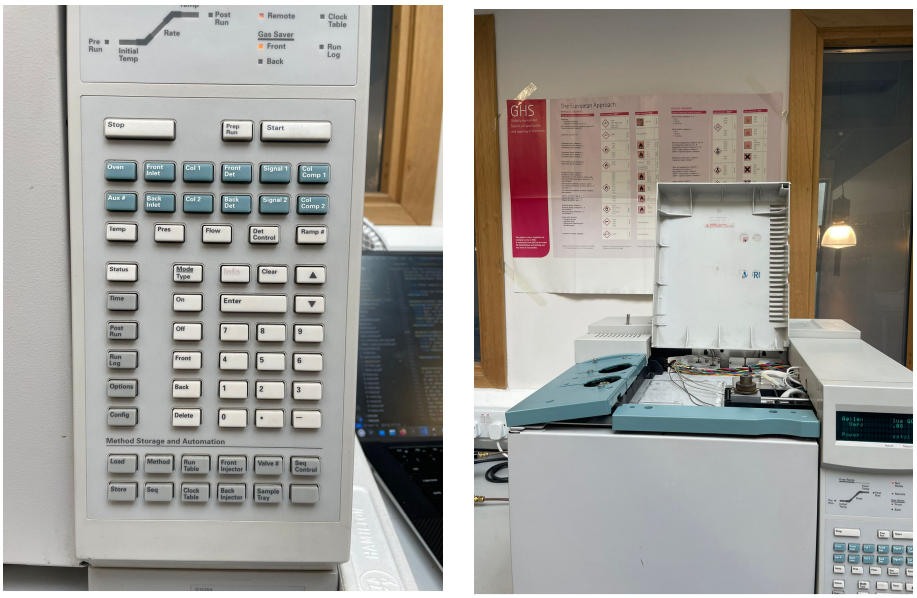

g) h)

Figure C2: Figure C1 continued.